Doctoral Dissertation
Doctoral Program in Mechanical Engineering (35th Cycle)

Graphene in Tribological Applications: Experimental Approaches

By

Edoardo Goti

******

Supervisor(s):
Prof. Luigi Mazza, Supervisor
Prof.ssa Francesca Maria Curà, Supervisor

Doctoral Examination Committee:
Prof. Dario Croccolo, Referee, University of Bologna
Prof. Josu Aguirrebeitia, Referee, University of the Basque Country, Bilbao

Politecnico di Torino
2023

Declaration

I hereby declare that the contents and organization of this dissertation constitute my own original work and does not compromise in any way the rights of third parties, including those relating to the security of personal data.

Edoardo Goti

2023

* This dissertation is presented in partial fulfillment of the requirements for **Ph.D. degree** in the Graduate School of Politecnico di Torino (ScuDo).

I would like to dedicate this thesis to my parents, who supported me and allowed me to reach this milestone.

Acknowledgement

And I would like to acknowledge prof. Andrea Mura for his valuable input during numerous discussions and his help in many laboratory activities, Luca Corsaro for the work done together, and all of my friends for supporting me in times of discouragement.

Abstract

Graphene is a nanomaterial of great interest in many research fields due to its unique properties different from bulk graphite. Recently, graphene has also found potential applications in the field of tribology. Graphene has been exploited to synthesize innovative atomically thin coatings, produce composite materials, or as an additive to functionalize traditional lubricants. Despite the great interest at the research level, the massive industrial application of graphene is still missing because proven benefits compared to the traditional solutions have not been fully substantiated yet. This PhD thesis aims to bridge this gap and further investigate whether graphene can positively affect friction and wear by comparing the results of simplified laboratory tests with component tests in close-to-service conditions. Graphene was investigated in two forms for this research: as a lubricious 2D coating and as a nano-additive for lubricating grease.

Graphene-based nano-coatings are intended for tribological applications in electrical environments. The main asset expected from these coatings is to combine high lubricity and high electrical conductivity while leaving the mechanical strength of the substrate unaffected. Different types of graphene coatings were deposited on conductive substrates for electro-mechanical applications (Cu and Al alloys) and tested to correlate their tribological performance with the deposition method. The deposition method affects the crystalline structure of the carbon film, indeed, which in turn affects the durability of the coating itself at the contact interface. The results of pin-on-disc tests revealed that the performance of the tribological system is improved as long as the nano-coating can withstand the shearing action of the sliding interface. However,

adhesion to the substrate and durability are still issues to be dealt with for scalability to industrial applications.

Graphene-based additives into lubricants are expected to improve both the thermal properties of the lubricant and its tribological performance in demanding operating conditions, for instance, when boundary lubrication prevails. Graphene-grease compounds were prepared with a commercial, high-performance, fully synthetic lubricating grease for bearings and commercial graphene nanoplatelets (GNPs). Several compounds were prepared by increasing the percentage of the nano-additive from 0.5% and 5% wt. The effect of the solid nano-additive on the reduction of sliding wear, rolling friction and grease useful life was investigated to assess whether the presence of the additive is beneficial for the lubricant. Pin-on-disk tests and simplified rolling friction tests were carried out to investigate the impact on friction and wear under conditions of grease lubrication. Grease endurance tests were also carried out through a dedicated test rig for bearings to assess whether the presence of the additive is beneficial for the lubricant itself.

Results revealed that graphene could stabilize and strengthen the boundary lubrication film in sliding contacts, thus smoothening the friction curve and reducing the likelihood of severe lubricant shortage events. Sliding wear may be significantly reduced as well. The quantity of nano-additive is a major factor in optimising grease performance; the optimum percentage for the selected grease was between 0.5% GNPs and 1% GNPs. On the other hand, rolling friction tests revealed that the presence of graphene is detrimental to rolling friction, and the higher the percentage of nano-additive, the higher rolling friction.

In grease endurance tests, the presence of a lubricious layer rich in graphene inside the rolling track of the spheres systematically correlated with the increase of lubricant life. Grease life doubled during bearing tests with 5% GNPs grease because this layer always formed. The 0.5% and 1% GNPs greases brought about a slightly reduced grease life, except when the lubricious layer could originate.

Few repetitions of the long-lasting endurance tests make these results a preliminary assessment of the effect of graphene on the useful life of lubricating grease because grease lubrication is known to be a chaotic phenomenon.

Contents

Abstract 2

Contents 1

1. Theory background on Tribology 1

    1.1 Lubrication 1

        1.1.1 Solid Lubrication 1

        1.1.2 Grease Lubrication 3

    1.2 Wear 11

        1.2.1 Sliding Wear 13

        1.2.2 Rolling wear 17

    1.3 Friction 19

        1.3.1 Sliding Friction 20

        1.3.2 Rolling Friction 22

2. Graphene nano-coatings in tribological applications 24

    2.1 Short review of production methods of graphene 26

        2.1.1 Scotch tape-exfoliation 27

        2.1.2 Chemical Vapor deposition-based graphene 28

        2.1.3 Self-assembly of graphene nano-platelets 32

    2.2 Review of graphene nano-coatings in sliding contact 35

3. Tribological characterization of graphene nano-coatings 42

    3.1 Materials and methods 44

    3.2 Aluminum samples 47

        3.2.1 Coating deposition and spectroscopic inspection 47

3.2.2 Pin-on-disc tests 51
3.3 Copper samples 64
3.3.1 Coating Deposition and spectroscopic inspection 64
3.3.2 Pin-on-disc tests 69
3.4 Conclusions and future perspective 86
4. Graphene-enriched greases in tribological applications 90
4.1 The Role of Graphene-based additives in greases 92
4.2 Literature review of laboratory tests on grease enriched by graphene nano-additives 98
4.3 Bearing rating life calculation and according to standards 126
4.4 Grease life calculation 134
5. Friction and wear performance of graphene-enriched greases 141
5.1 Thermal and rheological properties of graphene-enriched greases 141
5.1.1 Experimental determination of thermal conductivity 144
5.1.2 Characterization of the bulk electrical conductivity of grease compounds 145
5.2 Pin-on-disc tests 147
5.2.1 Correlation between friction, thermal response and ECR curves 151
5.2.2 Reduction of sliding wear 162
5.3 Rolling-in-raceway simplified tests 165
5.3.1 Special test setup 165
5.3.2 Friction results of rolling-raceway tests 169
5.3.3 Validation of the testing method 175
5.4 Conclusions and future perspectives 178
6. Grease life modification by graphene nano-additive 181
6.1 Review of the rolling bearing grease testers 184
6.1.1 FE 8 Rolling bearing grease tester 184
6.1.2 FE 9 Rolling bearing grease tester 186

6.1.3 R0F/R0F+ Rolling bearing grease tester 190
6.1.4 LFT Rolling bearing grease tester 192
6.1.5 SNR-FEB2 Rolling bearing grease tester 194
6.2 Design of a test rig for grease life tests 196
6.2.1 Mechanical layout.....197
6.2.2 Data Acquisition and control system 207
6.3 Grease endurance tests 214
6.3.1 Estimated Wohler curves 218
6.3.2 Results of Preliminary tests.....225
6.3.3 Results with base grease.....229
6.3.4 Impact of Graphene on the grease performance 241
6.4 Conclusions and future perspective.....255
7. Conclusions.....257
8. References.....260

List of Figures

Figure 1: Fundamental modes of solid lubrication; (a) lubrication by lamellar solid with weak interlamellar bonding; (b) lubrication by soft, thin films deposited on rigid substrates. Modified from [1]. 2

Figure 2: The rheological behavior of greases depends on the thickener content. The dashed line shows the *Carreau fluid* behaviour as a reference. Modified from [1]. 4

Figure 3: Film thickness profile inside contact in the starved regime. Modified from [4]. 8

Figure 4: Evolution of the grease film thickness as the lubrication mechanism evolves 9

Figure 5: Typical film thickness versus speed curves of greases obtained by interferometric measurement at rolling point contacts. Modified from [16]. 10

Figure 6: Fundamental wear mechanisms as per DIN 50320:1979 (now retired). From [22]. 12

Figure 7: Failure mechanisms of adhesive junctions. Modified from [1]. 13

Figure 8: Abrasion wear mechanism. From [22]. 14

Figure 9: Abrasion modes. From [22]. 15

Figure 10: Indirect tribo-oxidation at low sliding speed and under low loads (limited flash temperature). From [1]. 16

Figure 11: Relative influence of the fundamental wear mechanisms in rolling wear in proportion to lubrication regime and lubricant quantity. Modified from [23]. .17

Figure 12: Nucleation and propagation of a subsurface fatigue crack. From [23]. 18

Figure 13: (a) Rabinowicz model of abrasive particles; (b) Free-body diagram of a particle causing three body abrasion). From [23]. 22

Figure 14: (a) Forces actin gon a rolling body; (b) Schematic of a body rolling on a flat plane. From [23]. 23

Figure 15: Beneficial characteristics of 2D materials relevant for tribological applications. From [30]. 25

Figure 16: Peeling of multilayer graphene by scotch-tape exfoliation. Adapted from [40] 27

Figure 17: Schematic of an hot wall furnace for CVD synthesis of carbon structures. From https://www.sputtertargets.net/blog/what-is-chemical-vapor-deposition-cvd.html 28

Figure 18: Overview of the stages of the CVD growth of graphene on the catalytic metal substrate. The general mechanism involves: (1) mass transport of the reactant, (2) reaction of the precursor (gaseous) species, (3-4) adsorption of the precursor molecules, (5) diffusion into the substrate, (6) surface reaction and solubilization of C atoms, (7-8) desorption and removal of the side products. The continuous film is formed at cooling down. From [48]**.** 31

Figure 19: Typical process parameters of the APCVD (a) and LPCVD (b) graphene growth on thin metal foils. Adapted from [46] 31

Figure 20: (a) Schematic of the spit furnace of the PECVD systems; (b) Example of a commercial PECVD furnace where the growth chamber is on the left and the RF plasma source is on the right. From [48]. 31

Figure 21: Transfer process of SLG after growth by LPCVD on a Cu foil. From [50]. 32

Figure 22: Comparison of three main cost-effective methods for graphene synthesis: drop-casting, spin-coating, and self-assembly. Adapted from [51]. 34

Figure 23: Example of the chemical structure of GO where the carbon lattice is disrupted by heteroatoms, i.e., oxide-based functional groups. From [61]. 43

Figure 24: Hot wall furnace for CVD at MIT Laboratories. 45

Figure 25: Self-assembly process to prepare a graphene sheet from an ethanol solution with suspended graphene fakes. Adapted from [50]. 46

Figure 26: (a) Anton Paar TRB tribometer at Laboratories of Mechanics (DIMEAS); (b) test setup to perform rotating pin-on-disk wear test with graphene-coated aluminium and copper samples. 46

Figure 27: SEM images of the sample surfaces before tribological tests. From [50]. 48

Figure 28**.** Raman spectra were collected on the surface of the three coated samples in different positions. (a) Aluminium with transferred CVD graphene; (b) Aluminium coated by 3h-sonicated graphene. (c) Aluminium coated by 6h-

sonicated graphene. The optical images show the corresponding points where the spectra were collected. From [50].....49

Figure 29. Friction curves which were measured during the pin-on-disc tribological test. (a),(c) The signals acquired up to the end of the tests (30m). (b),(d) Zoomed view of the trend in the first 2m of sliding where the coating-to-substrate transition occurs.....52

Figure 30. Typical CoF trend in the first few meters from sliding onset measured with the coated sample: in Part 1, the graphene coating is working, and in Part 2, the graphene coating has been removed. From [50].....53

Figure 31. Average values of the CoF in the first and second parts of the tests, according to Figure 30. The average CoF value for the uncoated sample is calculated over the whole test only since no transition was there. From [50].....54

Figure 32. The average lifetime of the three-graphene coating in terms of rotating cycles before the transition of the CoF curve. From [50].....55

Figure 33. Typical wear track profile recorded by stylus profilometry on the 3h-Sonicated graphene-coated sample.....56

Figure 34. Low magnification SEM images of wear tracks at r =4.5mm and below the appearance of the sample surface after the tribological tests. Adapted from [50].....57

Figure 35. 3D topography and height map of steel sphere after the tests against the graphene-coated aluminium samples. The same sphere was used to perform all the tests and rotated each time to expose a fresh unworn region towards the flat sample. Where the sphere slid against the samples, there is evidence of material transferred from the sample to the sphere.....57

Figure 36. Determination of the wear volume for each sample. The error bars are determined as equal to the standard deviation σ. A systematic effect is associated with the wear track radius because the removed material is always higher at r = 2.3mm w.r.t. r = 4.5mm for all the samples.....58

Figure 37. Details of debris found outside the wear track. It is possible to appreciate that the debris shows graphene coating. From [50].....59

Figure 38. Raman spectra were collected inside and outside the wear tracks on the samples coated by transfer graphene (a), the 3h-sonicated UGF (b), and the 6h-sonicated UGF. From [50].....60

Figure 39. Friction curves were recorded during the two additional wear tests of the nano coating: a) 3h-sonicated graphene and b) 6h-sonicated graphene. Some spikes indicate the onset of adhesion due to graphene coating failure at the end of the test. 61

Figure 40. Microscopic inspection of the Aluminium sample surface at the end of the short-term wear tests. 62

Figure 41. The sphere surface at the end of the short-term wear tests before and after cleaning with acetone. Yellow arrows indicate accumulation of black debris (probably carbon-based matter), shining aluminium debris and individual scratches on the steel surface. 63

Figure 42. The surface profile of the Aluminum samples at the end of the short-term wear tests: a) 3h-sonicated graphene, b) 6h-sonicated graphene. 63

Figure 43. (a) Surface morphology of the samples before the tribological tests. (b) Inspection under the optical microscope of the sample surface before the tribological test. Interestingly, the surface of the samples with direct growth graphene features a pattern of platelets or grains which resembles the morphology of multiplayer CVD graphene on Ni substrate reported by Bhowmick et al. [30]. They are probably crystalline grains of copper after annealing....65

Figure 44. SEM Imaging of transferred and directly grown graphene with magnification 500X, 2.5kX and 25kX. SEM imaging of Bare copper and self-assembled graphene nano-coatings with magnification 500X and 15kX. Inset shows defective recombination of GNPs resulting from the production process of the UGF....67

Figure 45. 43kX FESEM image of the surface of the direct growth sample (on the left); 10µmx10µm AFM height map in the centre of the sample coated with direct growth graphene (on the right). The line profile shows the characteristic dimensions of the globular structure. 68

Figure 46. Friction curves measured on the graphene-coated samples at the median radius of 3mm. (a) Frictin curves recorded thrughout the whole test duration; (b) Detail of the friction curves in the first 7 m of sliding. 70

Figure 47. Friction curves from pin-on-disc tests on the graphene-coated samples. 72

Figure 48. Average CoF values are measured in Part 1 and Part 2. The error bars are three times the standard deviation of the average CoF of the three tests carried

out with each sample. (Lower part) The average lifetime of the coatings is determined as the beginning of the friction ramp between Part 1 and Part 2. 73

Figure 49. (a) Region of the samples scanned with the 3D microscope, (b) masks applied to the topographic data, (c) binary trace of the masked region. 76

Figure 50. Void and Material volume parameters of the Abbott-Firestone curve.76

Figure 51. Samples after pin-on-disc tests. (a) bare sample, (b) directly grown CVD graphene, (c) transferred CVD graphene coating, (d) 3h-Sonicated graphene, (e) 6h-Sonicated graphene. A transparent film adhered to the central part of the metal surface is noticeable on the sample with transferred CVD graphene. The sample with direct growth graphene, whose results will be presented separately in section 3.2, featured a pattern of bright patches similar to grains visible to the naked eye, probably the contour of the copper grains after annealing. 77

Figure 52. Comparison of the topography acquired with the FV 3D microscope: (a) Bare Cu, (b) transferred graphene, (c) 6h-sonicated graphene, (d) 6h-sonicated graphene. 78

Figure 53 (a) Removed material volume and (b) deposited or plastically displaced material volume measured at the end of the pin-on-disc tests. 79

Figure 54. Analysis of the wear tracks morphology. The wear tracks of the tests performed at a radius of 3mm were considered for this comparative analysis.....81

Figure 55. Wear scars on the steel balls (left) and wear tracks on the copper samples (right). (a-b) Bare Cu, (c-d) transferred graphene, (e-f) 3h-sonicated graphene, (g-h) 6h-sonicated graphene. 82

Figure 56. (a) Friction curves were measured with the sample treated by direct growth CVD and compared to the other samples at the median radius of 3mm. (b) Set of friction curves measured with the direct growth sample. 84

Figure 57. (a) Removed material volume and (b) deposited or plastically displaced material volume for the direct growth sample. 84

Figure 58. Morphological analysis of the wear track after the tribological test with the sample treated by direct growth CVD. 86

Figure 59. (a) SEM and (TEM) image of pristine graphene platelet used as nano-additive for grease. Adapted from [95]. 92

Figure 60. Schematic of carbon nanosheets participating in the lubrication mechanism. Modified from [98]. 93

Figure 61. Schematic diagram of the lubricating mechanism involving GNPs inside the grease proposed by Niu et al. for the titanium complex grease they tested. (a) The effect of graphene on the physical boundary lubrication film with interlayer slip effect on friction reduction and load carrying capacity. (b) The chemical interaction between the soap molecules and GNPs. (c) The synergistic effect of the boundary lubrication film and the chemical reaction film rich in oxides. Modified from [94].....94

Figure 62. (a) The efficient flowing of nanoparticles into the contact at low concentrations of additive; (b) agglomerations of nanoparticles into larger clumps and accumulation at the contact inlet with high concentrations of the additive into the grease. From [102].....96

Figure 63. (a) Typical evolution of friction coefficient and film thickness for different classes of greases and their base oils; (b) Experimental measurement of the CoF and film thickness for a polyurea grease and its base oil. Modified from [16].....97

Figure 64. The schematic diagram shows the influence of the thickness of the graphene platelets on frictional properties and the interaction with the lubricating mechanism. From [99].....98

Figure 65**.** (a) Evolution of the material lost due to wear and (b) average friction coefficient vs the graphene concentration into the grease under increasing load. Raman spectra of the worn surfaces at (a) 100N, (b) 200N and (c) 400N. Adapted from [101].....99

Figure 66**.** Measured friction curves with the three testing setups. (a) Four-ball tribometer, (b) Rotating tribometer, (c) Linear reciprocating tribometer. Adapted from [104].....102

Figure 67**.** Friction and wear results were obtained by Fan et al. by lubricating the contact with graphene-enriched bentone grease. Adapted from [95].....104

Figure 68**.** CoF, sound pressure level, and vibration level were measured by Singh et al. with ball-on-flat test tests. (a) 0.3% SRR and (b) 27% SRR w.r.t. a fixed rotational speed of the sphere equal to 0.3m/s. Adapted from [98].....106

Figure 69**.** Evolution of the average friction coefficient and wear scar diameter (WSD) as a function of graphene nanosheet concentration under 400N load. From [105].....108

Figure 70. Impact of the applied load on the wear scar diameter (a) and friction coefficient (b) with the lubrication by pure calcium grease 3% wt. GNS calcium grease. From [105]. 109

Figure 71. Friction and wear behaviour obtained by Lin et al. testing lithium grease with graphene nano-additive in SMHL (a-b), MLS (c-d) and HSLL (e-f) contact conditions. Adapted from [106]. 111

Figure 72. (a) The average coefficient of friction, (b) WSD and (c) thermal conductivity values obtained by Mohamed et al. with Merkan 23 grease admixed with increasing content in graphene nano-sheets and multiwalled carbon nanotubes. From [107] 114

Figure 73. Viscosity vs Shear rate curves by Mohamed et al. for the nano-grease they prepared [107]. 115

Figure 74. Results of the friction test under ramp increase of load (a) and wear test under constant load (b,c,d). Adapted from [93]. 117

Figure 75. Results of the friction tests under ramp increase of temperature (a), and wear tests under constant high temperature (b,c,d). Adapted from [93]. 118

Figure 76. (a-b) AFC and WSD obtained by Niu et al. with Grease A (350SN oil + 150BS oil) and Grease B (650SN oil) under fixed 392N load at increasing concentration of graphene additive; (c-d) Evolution of AFC and WSD with increasing load for pure grease A and Grease A + 0.06%GN. Adapted from [94]. 120

Figure 77. (a) Dynamic yield stress and (b) cross stress of grease compounds at increasing temperature; Evolution of apparent viscosity versus shear strain at (c) 30 °C; (d) 70 °C; (e) 130 °C. Adapted from [97]. 121

Figure 78. (a) Friction curves; (b) Average wear scar diameter and average COF with an increasing percentage of graphene into grease. Adapted from [97]. 123

Figure 79. The coefficient of friction versus sliding speed cures in tests carried out with the MCR tribometer by Pape and Poll. From [99]. 125

Figure 80. Results of the friction tests carried out with the bearing test rig [99]. 126

Figure 81: $\eta b(\kappa)$ curve adopted by the ISO 281:2007 standard (bold green curve). From [111]. 131

Figure 82: Diagram for the values of the reference kinematic viscosity $\upsilon 1$ provided by the ISO 281:2007 standard. 132

Figure 83: Chart of the life modification factor $aISO$ for thrust ball bearings and the related system approach equations that define the curves as per ISO 281:2007. 133

Figure 84: Basic grease operating life chart as a function of the parameter $n \cdot dm \cdot kf$. Modified from [116].....136

Figure 85: Grease life correction factor for high temperature. Modified from [116].....137

Figure 86: Grease life correction factor for high load. ① is K_p for thrust bearings; ② is the range of spherical and other special roller bearings; ③ is for tapered and cylindrical roller bearings; ④ applies for deep-drove, angular contact and self-aligning ball bearings. From [116]. 138

Figure 87: Grease life correction factor for oscillating movement. Modified from [116].....138

Figure 88. (a) Overview of the four grease compounds, the black ones are those functionalized with GNP; (b), (c), (d), (e) Inspection under the microscope of the pure grease, 0.5% graphene grease, 1% graphene grease, and 5% graphene grease, respectively. Interestingly, adding 5% wt. of graphene makes the grease grainy, meaning the nanoplatelets cannot disperse evenly. 143

Figure 89. Transmission optical microscope image of the graphene-grease compound prepared for this research. Some clustering of the nanoplatelets in larger carbon particles is visible in transmitted light microscopy. 144

Figure 90. (a) Special grease box for Hot Disk test on graphene-grease compound; (b) experimental setup of the tests. 145

Figure 91. Thermal conductivity of the four graphene-grease compounds (λ) estimated by Hot Disk method.....145

Figure 92**.** (a) Experimental setup for the static non-contact ECR measurement with the four grease compounds. (b) Overview of the grease contact sites after the static ECR tests on the same sample.....146

Figure 93**.** Average values of bulk electrical resistance across an 8 μm thick film of grease with confidence intervals. Adding 0.5% wt. of graphene flakes increased the electrical conductivity significantly. The value related to pure MULTEMP ET-C is not displayed because the measuring range of the DMM (100 MΩ) was saturated. 147

Figure 94. Experimental layout for the tribological tests. 148

Figure 95. Position of the two thermocouples (a) before greasing, (b) after grease build-up is formed. The pin thermocouple was installed with thermo-conductive paste to improve the accuracy of the measured value and protect the sensing region of the probe from direct convective effects. 149

Figure 96. (a) Samples prepared for ECR measurements with an external wire welded on the side for connection to the rotating copper ring; (b) Schematic of the ECR measurement circuit. 150

Figure 97. Wear damage on the sphere. (a) Example of a spherical cap diameter measurement under the microscope at the end of a test lubricated with the base grease (the grey dashed line is the location of the profilometric inspection); (b) Profilometric inspection of the flattened region on the sphere; (c) Calculation of the spherical cap volume as per ASTM G99-17. 151

Figure 98. Comparison among the average friction value measured with the four grease compounds. The error bars represent the 95% confidence level for the estimated average values. 152

Figure 99. Friction and thermal curves were recorded during four tests to compare the tribological performance of the four graphene-rich grease compounds. The values recorded by the pin thermocouple close to the contact region are labelled $\Delta T_{contact;}$ those recorded by the thermocouple inside the grease build-up are labelled ΔT_{grease}. 154

Figure 100. ECR curve recorded during four tests lubricated with different graphene-grease compounds. Additional information about the grease ECR limit of inset (d) is reported in Section 5.1.2. 156

Figure 101. (a) Average ECR values recorded during pin-on-disk tests; (b) Ratio between the average ECR value and the grease bulk conduction value. 160

Figure 102. (a) Average temperature rise on the pin; (b) average temperature rise inside the grease build-up; (c) $Pf\Delta T$ ratio. 161

Figure 103. (a) The volume of removed material from the pin due to wear with the four grease compounds. 162

Figure 104. The worn region and waste grease on the steel sphere right after the tribological tests with the four grease compounds. 163

Figure 105. The appearance of the wear traces on the AISI 52100 flat sample under the optical microscope. Insets show the micro topography visible with SEM

analysis corresponding to the position in the wear track highlighted by the white squares. 165

Figure 106: (a) Special setup of the rolling test installed on the pin-on-disk tribometer; (b) Sector cut from the upper ring of the thrust ball bearing by EDM. From [121]. 166

Figure 107: (a) Free-body diagram of the spheres in contact with the upper pad (θ is equal to 47°) in the case of two spheres in symmetrical contact, where α' = ωt – α; (b) Detail of the set of force at the contact site of the sphere against the pad. From [121]. 167

Figure 108: (a) CoF curve acquired during a short-term test with lubrication by the 0.5% graphene grease; (b) CoF curve acquired during a long-term test with lubrication by the 1% graphene grease. The greyed region of the diagram marks the portion of the curve considered to calculate the statistical quantities. From [121]. 170

Figure 109: Average Ff trend measured with increasing load and speed according to Table 35. Uncertainty bands at the 95% confidence level were estimated equal to 3σ, where σ is the standard deviation of the results. The corresponding CoF values ranged from 0.005 to 0.03. From [121]. 172

Figure 110: Setup for monitoring the temperature rise during rolling-raceway tests by IR thermography. From [121]. 173

Figure 111: Average pad friction force measured during long-term tests (30N load and 600rpm speed) with increasing the graphene content into the grease. From [121]. 174

Figure 112: Equivalent friction torque $Tbearing$ calculated by equation (37) corresponding to the outcome of the long-term rolling-raceway tests with increasing GNPs content. From [121]. 175

Figure 113: Equivalent frictional torque of the SKF 51105 bearing under 240 N load and 600rpm speed estimated based on the results of the rolling-raceway tests and compared to the values predicted by the SKF Friction model. T_{SKF} was calculated by the SKF Bearing Select online calculation tool (SKF Bearing Select, s.d.). From [121]. 177

Figure 114: Schematic of the collision of the spheres with the upper portion of the raceway while entering the contact region where the tribometer measures the friction force Ff. From [121]. 178

Figure 115: Classification of the tribological tests according to DIN 50322 (now retired). From [126] 182

Figure 116: Schematic of the FE8 test rig as per DIN 51819 [116]. 185

Figure 117: FE8 test rig equipped with two thrust test bearings, (a) without auxiliary support bearing [127]; (b) with auxiliary support bearing to bear radial loads. From [128].....185

Figure 118: Schematic of the FE9 test rig as per DIN 51821 [129]. Inset (a) is the 3D view of the test rig from [130]. Five independent test heads are installed in the same test rig and driven by the same motor to run multiple tests simultaneously. Adapted from [129]. 187

Figure 119: Assembly A, B and C of the FE9 test rig. Assembly A comply with the standardized testing procedure of DIN 51821-2. Adapted from [129]. 188

Figure 120: Example of a Weibull diagram obtained from a test campaign on 5 bearings with an FE9 test rig. From [129]. 189

Figure 121: R0F rolling bearing grease tester schematic, from [129]. R0F stands for **R**ig with size **0** (i.e. small size) for **F**ett, a Swedish word for “Grease”. Adapted from [129]. 190

Figure 122: R0F industrial test rig with multiple test units. Adapted from [129]. Inset (a): modern SKF R0F+ test unit from [11]. 192

Figure 123: Schematic of the FAG-LFT rolling bearing test rig. Adapted from [116]. 193

Figure 124: Schematic of the SNR-FEB2 rolling bearing fretting test rig. From [129]. 194

Figure 125: Example of laboratory equipment of the FEB2 type. From [131]. ..195

Figure 126: Section view of the test rig. 198

Figure 127: CAD model of the test rig for grease testing. 199

Figure 128: Pictures of the test rig for grease endurance tests at the Laboratory of Mechanics (DIMEAS, Politecnico di Torino). 200

Figure 128: Detailed of the DUT installed on the test rig and connected to the ECR system.....201

Figure 130: (a) Detail of the power system; (b) detail fo the air cooling system of the DUT. 201

Figure 129: (a) Schematic of the test bearing for HS-EMU bearings by Fan et al. [136]; (b) schematic of the loading system of the test bearing designed for this PhD thesis research work. 203

Figure 130: Schematic of the cooling system of the tested bearing to avoid overheating due to accelerated endurance test conditions. 204

Figure 131: Schematic of the reaction forces on the support bearings SB1 and SB2 for the scenario where an external radial load acts on the bearing under test (adapted from KYH Mounted Bearing Units Catalogue, Nippon Pillow Block Co. Ltd., https:// fyhbearings.com) 205

Figure 132: Front Panel of the LabView routine developed to run the tests. 208

Figure 133: Control and data acquisition system of the test rig 209

Figure 134: Section view of the test rig for grease testing. 210

Figure 135: Technical sheet of the Pt100 RTD sensor installed into the test bench 210

Figure 136: Sensorized seat of the bearing under tests featuring a temperature sensor and a uniaxial accelerometer. 211

Figure 137: Series of the average PSD signal in the frequency domain recorded from the beginning to the end of Test 2. 212

Figure 138: ECR wire tin soldered to the static ring of a 51104 bearing. 213

Figure 139: FR4 Vetronite insulting plates for ECR measurement. 213

Figure 140: Profilometric inspection of the bearings before running the tests. (a,b) Four profiles equally spaced were acquired on each ring; (c) analysis of the profiles and measurement of the local osculating circle radius. 216

Figure 141: Weighting with precision scale (resolution 0.1mg, precision 1mg) of the thrust ball bearings. (a) Rolling elements, (b) rotating ring of an SKF 51104 bearing after degreasing in chloroform and acetone bath. 217

Figure 142: (a) Greasing of a 51105 thrust ball bearing installed in its seat on the test rig with 2g of MULTEMP ET-C lubricating grease before starting an endurance test; (b) the corresponding grease quantity measured with precisions scale. 217

Figure 143: L_{50mh} of 51104 thrust ball bearing estimated at a constant temperature of 75 °C considering lubrication with pure MULTEMP ET-C grease. 221

Figure 144: L_{50mh} of 51105 thrust ball bearing estimated at a constant temperature of 70 °C considering lubrication with pure MULTEMP ET-C grease. 221

Figure 145: a_{ISO} of 51104 thrust ball bearing estimated at a constant temperature of 75 °C considering lubrication with pure MULTEMP ET-C grease. 222

Figure 146: a_{ISO} of 51105 thrust ball bearing estimated at a constant temperature of 70 °C considering lubrication with pure MULTEMP ET-C grease. 222

Figure 147: L_{fGh} Grease life curve estimated considering operation with a 51104 thrust ball bearing and constant operating temperature of 75°C. 224

Figure 148: L_{fGh} Grease life curve estimated considering operation with a 51105 thrust ball bearing and constant operating temperature of 70°C. 225

Figure 149: Temperature chart recorded during preliminary test 2. 228

Figure 150: ECR chart recorded during preliminary test 2. 228

Figure 151: (a) Hard deposit on the cage and (b) at the raceway grove sides at the end of Preliminary Test 2 with base grease. 229

Figure 152: Duration of endurance tests with base grease compared to life rating curves. 232

Figure 153: Experimental Weibull probability plot for MULTEMP ET-C grease duration. η and e are the parameters of the Weibull distribution.....233

Figure 154: (a) Grease base oil drained from the spheres in static contact over the ring after the end of a test (Test 3); (b) Oil droplets expelled out of the DUT and accumulated on the safety enclosure of the test rig. 233

Figure 155: Temperature of the test bearing recorded during Test 2. 234

Figure 156: (a) ECR chart recorded during Test 2; (b-c) Detail of the ECR value between 170 h and 190 h where the resistance value followed the fluctuations of the bearing temperature and often dropped to conduction (few hundreds of Ω). 235

Figure 157: PSD of axial vibrations at the beginning and the end of Test 2. 236

Figure 158: Axial load applied to the test bearing during Test 2. Tests were sometimes paused and restarted to manually adjust the value of the applied load in case of excessive drift of the preset value. Inset is the enlarged view of 20 h of test. 237

Figure 159: Inspection under the optical microscope of the rotating ring of the tested bearing (Test 2). (a) Distribution of waste grease just after the stop of the

test; (b) distribution of waste grease on the cage; (c) appearance of the raceway after cleaning in a bath of chloroform and acetone. 238

Figure 160: (a) Different surface finish inside the rolling track of the spheres visible after a deep cleaning with a tissue soaked in acetone to remove residues of the deposited layer; (b) plastically deformed region visible in the middle of the raceway groove under the optical microscope.....239

Figure 161: High magnification inspection of the surface of an unworn 51104 bearing under the optical microscope. 240

Figure 162: Example of profile comparison before and after the endurance test for (a) the rotating ring and (b) the static ring (Test 2). 240

Figure 163: Experimental Weibull probability plot for the 0.5% GNPs grease duration. 243

Figure 164: Experimental Weibull probability plot for the 1% GNPs grease duration. 244

Figure 165: Experimental Weibull probability plot for the 5% GNPs grease duration. 244

Figure 166: Effect of graphene on the average duration of the endurance tests. Error bars correspond to the 95% confidence intervals of the Weibull distribution. 245

Figure 167: State of the raceway at the end of the endurance tests; (a) Test 3; (b) Test 8; (c) Test 10; (d) Test 9. 246

Figure 168: Detailed view of the raceway at the end of endurance tests; (a) Test 3; (b) Test 8; (c) Test 10; (d) Test 9; (e) high-magnification image of the black deposited layer likely composed of degraded thickener and graphene. 247

Figure 169: Effect of graphene on the average temperature of 51104 bearing during endurance tests. 248

Figure 170: Temperature chart of Test 8 lubricated with 0.5% GNPs grease. 250

Figure 171: Temperature chart of Test 10 lubricated with 1% GNPs grease. 250

Figure 172: Temperature chart of Test 9 lubricated with 5% GNPs grease. 251

Figure 173: ECR chart recorded during Test 9. Contact resistance progressively increases as long as the temperature remains stable. 251

Figure 174: Traces of a deposited layer inside the rolling path of the spheres correlates with a longer useful grease life. Test 4 and Test 7 were both lubricated with 1% GNPs grease. 252

Figure 175: Chaotic temperature fluctuations did not occur when a deposited layer settled inside the rolling track. 252

Figure 176: Appearance of the rolling track (in the middle of the raceway groove of the rotating ring) under the optical microscope; (a-b) Test 5, (c-d) Test 7, (e-f) Tests 6. 254

List of Tables

Table 1: Testing parameters from [54] 36

Table 2: Testing parameters from [45] 37

Table 3: Testing parameters from [55] 38

Table 4: Testing parameters from [56]. 39

Table 5: Testing parameters from [57]. 41

Table 6: Nominal technical specification of Al6082 47

Table 7: Testing parameters of the three pin-on-disc tests carried out with each graphene-coated aluminium sample. 51

Table 8: Average CoF values and standard deviations of averages. 54

Table 9: Testing parameters of the additional short-term pin-on-disc tests on graphene-coated aluminium samples. 60

Table 10: Nominal technical specification of Cu-ETP 64

Table 11: Pin-on-disc tests on graphene-coated copper samples 70

Table 12: CoF values measured on pristine graphene (before coating failure) from literature 74

Table 13: Average value of material loss and deposited/displaced material 78

Table 14: Analysis of the roughness inside the wear tracks 83

Table 15: Average value of material loss and deposited/displaced material for the direct growth sample. Comparison of the roughness value before and after the tribological tests 85

Table 16: Testing parameters from [101] 99

Table 17: Testing parameters from [104] 101

Table 18: Testing parameters from [95] 103

Table 19: Rolling-sliding ball-on-flat testing parameters from [98] 105

Table 20: Four-ball testing parameters from [105] 107

Table 21: Maximum non-seizure load (PB value) of pure calcium grease and 3 wt% GNS/calcium grease, from [105] 109

Table 22: Four-ball testing parameters from [106] 110

Table 23: Four-ball testing parameters [107]. 113

Table 24: Testing parameters of reciprocating ball-on-flat tribological test from [93]. 116

Table 25: Test conditions from the paper by Niu et al. 119

Table 26: Test conditions from the paper by Wang et al. 122

Table 27: Testing parameters from the paper by Pape et al. [99]. 124

Table 28: Value of fc for thrust ball bearings. These values apply to bearings with cross-sectional raceway groove radii not larger than 0.54 · Dw according to ISO/TS 16281:2008. 128

Table 29: Life modification factor for reliability a1 from iso 281:2007. 129

Table 30: General guidelines for determining the contamination factor eC based on the level of contamination of the lubricant. A detailed method for estimating the contamination factor is also described in the ISO/TR 1281-1:2008 as an alternative. 130

Table 31: Reference value of factors KU and KS [116]. 139

Table 32: Technical sheet of MULTEMP ET-C high-performance grease from Kyodo Yushi Co. Ltd [118]. 142

Table 33: Bulk electrical resistance across an 8 μm thick film of grease. 146

Table 34: Roughness and hardness characteristics of the static sphere and rotating steel disk for pin-on-disc tests. 148

Table 35: Map of testing parameters for the rolling-raceway tests carried out with the four concentrations of graphene-enriched greases (0%, 0.5%, 1%, 5%). Marks ‘x’ indicate short-term tests; marks ‘#’ indicate long-term tests. 169

Table 36: Testing conditions for FE8 rolling bearing lubricant test rig 186

Table 37: Testing conditions for FE9 rolling bearing lubricant test rig 189

Table 38: Testing conditions for R0F+ rolling bearing lubricant test rig.....191

Table 39: Testing conditions for FAG-LFT rolling bearing lubricant test rig.....193

Table 40: Testing conditions for SNR-FEB2 rolling bearing fretting test rig 195

Table 41: Technical specs of the P2B-GTMAH-50M support bearings from DODGE Industrial Inc. 198

Table 42: Technical specs and calculation parameters of the 51309 thrust ball bearings from SKF [138]. 202

Table 43: Technical specs of the Lafert 3kW asynchronous electric drive installed into the test rig (https://www.lafert.com/it) 204

Table 44: Equivalent bearing life calculations of P2B-GTMAH-50M bearings according to the SKF Bearing Calculations guidelines. A 0.5 kN thrust load was added to account for parasitic axial load due to the thermal expansion of the shaft (the support bearings are both locating by design). 206

Table 45: Bearing life calculations for the thrust bearing SKF 51309 according to the SKF Bearing Calculations guidelines. 207

Table 46: Measuring range and accuracy of the Digital MultiMeter in DC Resistance mode installed into the National Instrument VirtualBench VB-8012 multifunction card. 212

Table 47: Manufacturing data related to the SKF bearings purchased for the experimental campaign. 214

Table 48: Dimensional and mechanical specifications of thrust ball bearings size 51104 and 51105. 215

Table 49: Overview of the input data needed by *SKF Bearing Select, Bearing Solve and ISO 281:2007 formulas* to perform rating life calculation. Grey-shaded regions indicate input data needed by the specific calculation method. 219

Table 50: Main input data for the grease life model proposed by Schaeffler AG [116]. 223

Table 51: Main input data for the grease life model by Lugt and Berens [117]..223

Table 52: Theoretical bearing life rating for the preliminary endurance tests with SKF 51105 thrust ball bearings. “ISO 281” indicates data obtained by directly applying the formulas provided by the ISO281:2007 standard. The conformity value indicated in the tables is the average of the two raceways of the bearing. 226

Table 53: Test conditions and main results of the preliminary tests with SKF 51105 thrust ball bearings.....227

Table 54: Theoretical bearing life rating for the preliminary endurance tests with SKF 51105 thrust ball bearings. “ISO 281” indicates data obtained by directly applying the formulas provided by the ISO 281:2007 standard. The average conformity used for calculations was estimated by averaging the raceway conformities of the 12 bearings under test. 229

Table 55: Test conditions and main results of endurance tests with on SKF 51104 thrust ball bearings. The conformity value indicated in the table is the average of the two raceways of each bearing. 231

Table 56: Test conditions and main results of endurance tests on SKF 51104 thrust ball bearings with 0.5% GNPs grease. Test 11 was suspended before grease failure. 241

Table 57: Test conditions and main results of endurance tests on SKF 51104 thrust ball bearings with 1% GNPs grease.....242

Table 58: Test conditions and main results of endurance tests on SKF 51104 thrust ball bearings with 5% GNPs grease. Just two repetitions were performed due to time constraints. 242

Chapter 1

Theory background on Tribology

This chapter aims to provide some fundamental concepts to introduce the results of the research work presented in the following chapters. The chapter focuses on the main phenomena involved in the experimental activity carried out for this PhD thesis.

1.1 Lubrication

1.1.1 Solid Lubrication

Solid lubricants are typically employed in all those applications where liquid lubricants cannot be used, for instance, when lubrication is required at very high temperatures (hot working of metals). The typical temperature range for liquid and semi-solid lubricants is -20 °C to 120 °C, whereas solid lubricants can operate at temperatures exceeding 250-300 °C. However, the main disadvantages of using solid lubricants are their limited ability to remove heat from the system and their low wear resistance. Moreover, solid lubricants are required when the contact surfaces to be lubricated are inaccessible (equipment working under vacuum) or when it is necessary to ensure the absence of contaminants (food industry and optical equipment).

In the absence of lubrication provided by liquids lubricants, adhesion between the surfaces causes a significant coefficient of friction and wear. *Anisotropic*

lamellar solids and *soft films* provide the two fundamental modes to facilitate shear parallel to the contact surfaces. The two mechanisms are represented schematically in Figure 1.

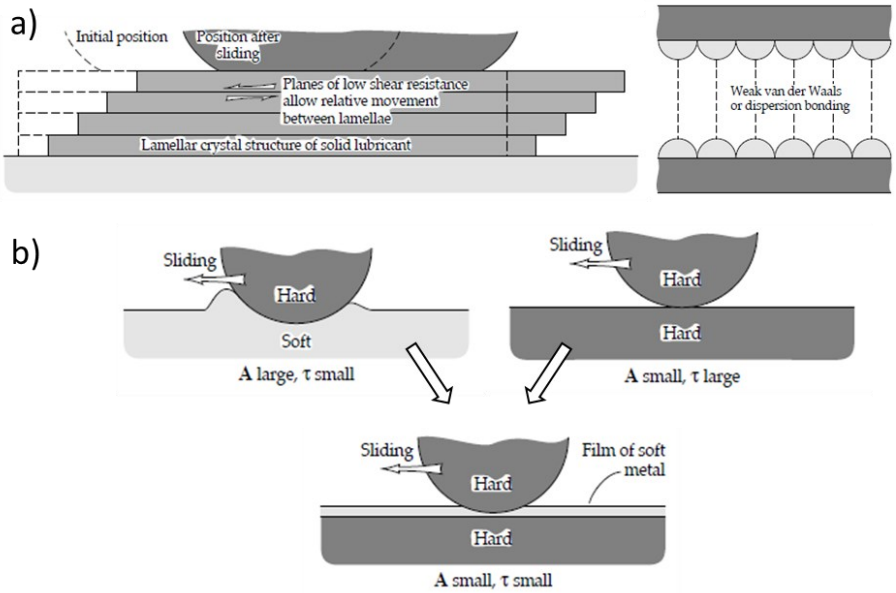

Figure 1: Fundamental modes of solid lubrication; (a) lubrication by lamellar solid with weak interlamellar bonding; (b) lubrication by soft, thin films deposited on rigid substrates. Adapted from [1].

Bragg first proposed the lamellar solid lubrication model [1], which is now commonly accepted even though it has not been demonstrated unequivocally. According to this model, in materials composed of lamellae separated by planes of weakness, i.e. materials with anisotropy of mechanical properties, the lamellae can slide over one another with relatively low shear stress. Not all the materials with lamellar structures are suitable to be used as solid lubricants, though, because it is necessary that the chemical bonding between the lamellae remains very weak both before and after cleavage. It is the case of graphite and MoS_2, whose atomic planes are bonded by weak van der Waals forces. Lamellar solids can be applied to contacts as a powder or deposited as coatings on the surfaces. In both instances, adhesion to the surface is a key feature and should be high enough to prevent ejection from the contact site, like wear debris.

Soft thin films can also act as a lubricating medium through a very different mechanism than lamellar solids, which involves the reduction of the actual area of contact between the rough bodies. Bowden and Tabor [2] theorized this

mechanism within the framework of their adhesive theory of friction. According to their theory, the friction force F_f is scaled by the extension of the actual contact area A_r and the shearing reaction τ_{lim}, determined by the bulk resistance against sliding of the asperities in contact (see equation (1)).

$$F_f = \tau_{lim} \cdot A_r \tag{1}$$

Soft materials with a low shear limit to plastic flow (see also Section 1.2.1) are characterized by tiny values of τ_{lim}. Despite this, the total friction force can be considerably high because the contact area is large and additional effects like pile-up and fringes formation may oppose sliding motion (Figure 1b). When a soft, thin film is deposited onto a rigid substrate, the substrate determines the contact area that remains tiny, whereas the outer film determines the shear strength of the interface. Such a favourable combination of effects produces low frictional forces as long as the thin, soft film can withstand the shearing action without running into wear. Thin films successfully applied are soft metals like Ag, Au, Pb, or In and polymers like PTFE.

1.1.2 Grease Lubrication

Lubricating greases are complex lubricants with semi-solid consistency. They can grab onto the surfaces of the tribological pair and remain long enough in place to feed the contact site. Grease lubrication is applied when a continuous supply of lubricant is needed without the complexity of an active lubrication system, when an extra sealing action by the grease is required, or when long emergency running is required for safety in case of lubrication supply failure. These key features are related to the inherent consistency of grease that must be preserved during operation despite the increase in temperature and the applied mechanical stress. The service life of grease is often determined by the eventual loss of its semi-solid consistency, which can lead to liquefaction or the formation of solid deposits on the contact surfaces.

From the rheological point of view, greases have a pseudoplastic behaviour that can be modelled by the Hershel-Bulkley, i.e. equation (2).

$$\tau = \tau_p \cdot \left(\eta_s \left(\frac{du}{dh}\right) \cdot \frac{du}{dh}\right)^n \tag{2}$$

Where τ is the tangential stress acting on the oil, τ_p is the plastic flow limit, η_s is the dynamic viscosity of the base oil, *du/dh* is the shear rate, and *n* is a characteristic constant (whose value is 1 to 1.2). This rheological behaviour is close to a Bingham fluid, corresponding to *n* equal to unity, where no flow is possible below a limiting shear stress value. Grease behaves as a plastic solid at low shear rates without any plastic flow until a critical yield stress has been reached. At the onset of plastic flows, the rheological properties of grease change as a function of the shear rate and the duration of shearing. This behaviour resembles a Carreau fluid [1].

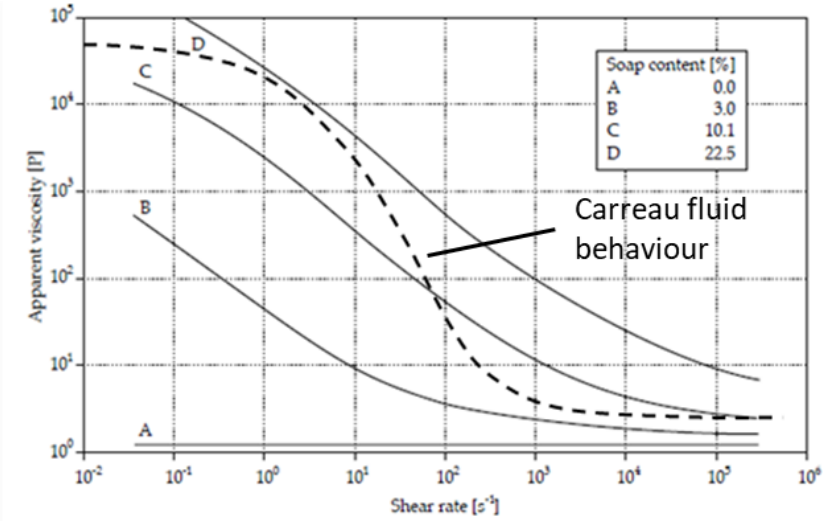

Figure 2: The rheological behavior of greases depends on the thickener content. The dashed line shows the *Carreau fluid* behaviour as a reference. Adapted from [1].

Formulation of grease

Greases are composed of a mixture of three main ingredients: the lubricant oil, the thickening agents and the fillers [1]. In many cases, the base oil plays the most crucial role in determining the tribological performance of the grease, but situations exist where the thickener plays a critical role, especially when the entrainment speed of the lubricant into the contact is low and the applied load is high. Naphthenic oils are the most widely used base stocks for the formulation of commercial general-purpose greases. Despite their low viscosity index, about 99% of the greases on the market are based on mineral oil [1] because they remain in the liquid phase even at low temperatures and combine effortlessly with soaps. Greases for extreme working conditions feature a synthetic base stock and are much more expensive than general-purpose greases. The most commonly used synthetic base stocks are phosphate esters, silicones and fluorocarbons. Moreover,

the base oils formulated to produce greases feature specific packages of chemical additives to implement key characteristics like resistance to rust and corrosion, oxidation resistance, anti-wear properties and extreme pressures (EP) properties.

On the other hand, the physical characteristic of the grease strongly depends on the thickener type and nature. The thickening agent is dispersed inside the oil to jellify the liquid lubricant and create a stable colloidal structure. The thickener forms a soft fibrous matrix of interlocking particles with tiny pockets (about 1 μm in size) where the oil is trapped. This fibrous network locks the base oil in the free spaces at the micro level, thickening the base oil at the macro level. The mechanism which promotes this change from liquid to semi-solid involves the binding of the oil molecules by the thickener molecules (or fibres). The thickener is around 5-20% and is sometimes added together with other fillers (metal oxides, carbon black, molybdenum disulfide, PTFE). The thickener type usually classifies greases into two main classes:

- Soap based
- Non-soap-based (including synthetic greases)

Soaps that are used to produce grease are based on sodium hydroxide (NaOH) or other alkalies, such as lithium, calcium, aluminium, and barium. Thickeners for non-soap greases are made from fine inorganic powders with enough porosity and surface area to absorb oil. Commonly used inorganic thickeners are silica and bentonite clays. Greases with inorganic thickeners are suitable for high-temperature applications because they have no melting point, and their maximum operating temperature depends on the oxidation stability of the base oil. Organic, polymer and synthetic thickeners, such as amides, anilides, and urea-based compounds, can also be used instead of soaps. Greases with synthetic thickeners can operate at extreme temperatures and have a superior performance since they keep their consistency in a wide temperature range and suffer limited side effects due to overheating at very high speeds.

Grease lubrication mechanisms

Despite the practical importance of greases, the understanding of the actual lubrication mechanism is still fragmentary. Practical experience shows that only a tiny quantity of grease applied to a tribological system contributes to lubrication. The surplus accumulates at the borders of the contact within a short time [3] and plays an essential role as a sealing element to prevent contamination of the lubricant inside the contact by dust and debris.

Two main lubrication mechanisms have been proposed for greases to justify the replenishment of the lubricant necessary to maintain the separation between the solid surfaces [4].

According to the so-called *oil bleeding mechanism* proposed by Booser and Wilcock [5], a controlled amount of liquefied lubricant (mainly base oil) is supplied to the contact to sustain the separating film by an almost continuous feed. The flow of liquid lubricant bleeding by bulk grease is poor, and a starved fluid-film lubrication regime is expected. The release of liquid lubricant occurs as the grease close to the contact site is progressively worked by the action of the moving surfaces. The working of grease lying around the contact destroys the thickener structure and lets the base oil trapped into it be released. Bleeding of liquid phase lubricant and transport from the bulk grease to the contact is thus dependent on contact geometry and grease distribution around the contact [6]. Replenishment is supposed here to occur by the combination of spontaneous surface-tension-driven out-of-contact reflow of oil from the side of the track (squeeze flow) [7] or local capillary-driven flow across the contact [6]. It is often intended that the oil-bleeding mechanism involves just the oil fraction that bleeds out of the surplus of grease towards the contact site. This assumption is not valid, however. The results of some experimental investigations on this topic, for instance, O'Halloran et al. [8], proved that grease has to be considered one entity, and the thickener also actively participates in this lubrication mechanism. The availability of oil primarily determines the film thickness, but particles of degraded thickener material can be observed inside the contact site. They contribute to developing the thin viscous layer that controls lubrication [9].

The second mechanism is the so-called *high-viscosity layer mechanism* by Scarlett [10], according to which grease gives rise to a reasonably uniform high-viscosity layer dominated by the thickener structure. The formation of this layer is promoted by wettability and adhesion of the thickener molecules to the solid surfaces. Experimental observations suggest that this layer quickly settles in the early stage of operation of a grease-lubricated contact, and its thickness may be larger than the starved film promoted by oil-bleeding [4]. However, this layer is relatively weak and breaks down easily. Since practical experience suggests that grease-lubricated contacts can effectively separate the solid surfaces, the reshaping of this high-viscosity layer is explained by an intermittent bulk flow of fresh grease from the surroundings into the contact. A grease at low shear rates behaves as a plastic solid, and once expelled from the contact, it remains in its position unless there is an external action to return it to the inlet. Replenishment

of the track should occur by side slip of the contact surfaces, vibrations, and release of grease lumps because of thermal softening. However, any continuous supply of bulk grease is not considered since experimental observations disprove it.

In real applications, these two mechanisms often interplay, which may appear at different times of the contact history. For rolling contacts, the most widely accepted grease lubrication model foresees two successive phases dominated by the abovementioned mechanism: the *churning phase* and the *bleeding phase* [11]. The *churning phase* starts immediately after the relative motion between the mating surfaces is introduced and mainly involves the high-viscosity layer mechanism. Fresh grease is deposited on the rolling track while the bulk of the grease is cleared from the contact site. The grease film thickness is relatively thick (about 110 nm), even thicker than the theoretically possible value of the base oil [12]. Experimental tests proved that for most grease types, film thickness distribution inside the contact is similar to that of a fully flooded EHL film, and higher shear stability and base oil viscosity promote thicker films as for the fully flooded EHD regime [4]. In this transitory phase, high friction and a steep increase in temperature are experienced since a significant quantity of grease is churned by the surfaces (the cage also plays a role in rolling bearing), suggesting that the deposited material onto the rolling path has high viscosity. The shear stress resulting from continued overrolling damages the physical matrix of the deposited layer, and irreversible loss of viscosity occurs. The initial thickness of the high-viscosity layer rapidly decays due to the breakdown of the fibrous thickener structure with the outflow of some base oil. The decline of the film thickness usually continues for some time until an equilibrium film thickness is reached as the bleeding mechanism activates.

In the *bleeding phase,* the microflow of liquid lubricant from the bulk grease becomes predominant and provides starved replenishment of the contact [13]. Elastohydrodynamic film equations do not usually apply because the hypothesis that sufficient lubricant is available at the inlet does not apply. The bleeding of liquid phase lubricant into the contact promotes the stabilization of the lubricating film thickness at about 10-40 nm. The thickness of the lubricating film may even halve compared to the reference case of lubrication with the grease base oil alone [4]. The film thickness profile inside the contact in the starved regime is also very different compared to the fully flooded case, and it features a minimum thickness in the central part of the Hertzian contact footprint instead of the typical flat plateau (Figure 3).

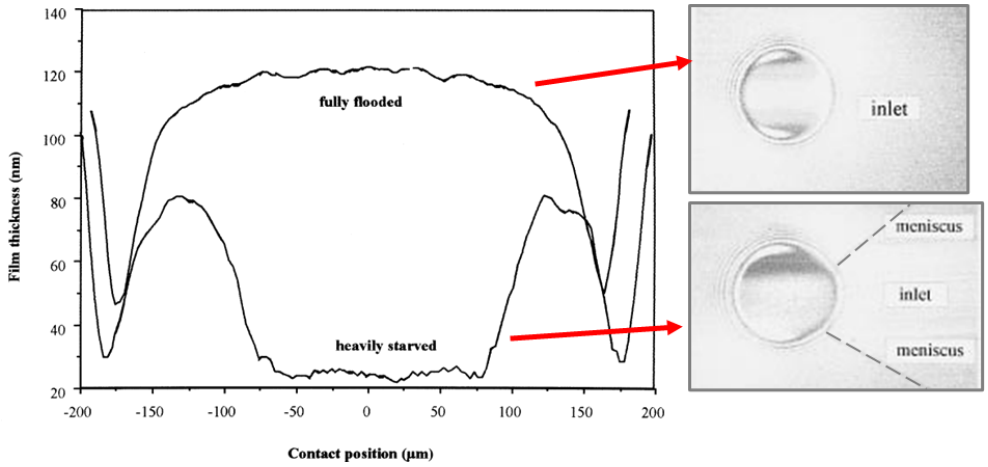

Figure 3: Film thickness profile inside contact in the starved regime. Adapted from [4].

The equilibrium film thickness is determined by the balance between the loss mechanism, i.e. back-flow from the inlet and cross-flow from the contact, and the surface-tension-driven and capillary-driven replenishment mechanisms. These peculiar replenishment mechanisms justify the intensified hydrodynamic effect localized at the edges of the contact area (Figure 3). The film formation depends on the oil availability and the oil transport to refill the contact, where the latter is controlled by the physical properties of the base oil (viscosity, surface tension, amount) and the surface properties of solid bodies (chemical reactivity, roughness). For this reason, the factors that promote the film build-up in fully flooded EHL conditions often hamper it in the starved regime [4]. Reducing the viscosity of grease base oil is beneficial rather than increasing its viscosity, as conventionally suggested by the fully flooded EHL models because the reduction in viscosity promotes capillary reflow.

Similarly, increasing speed may surprisingly decrease the film thickness. The lubricant intake mainly comes from the side, thus being speed insensitive. Whereas the inlet loss due to squeezing back-flow is speed dependent, at least until the inlet meniscus has disappeared (Figure 3).

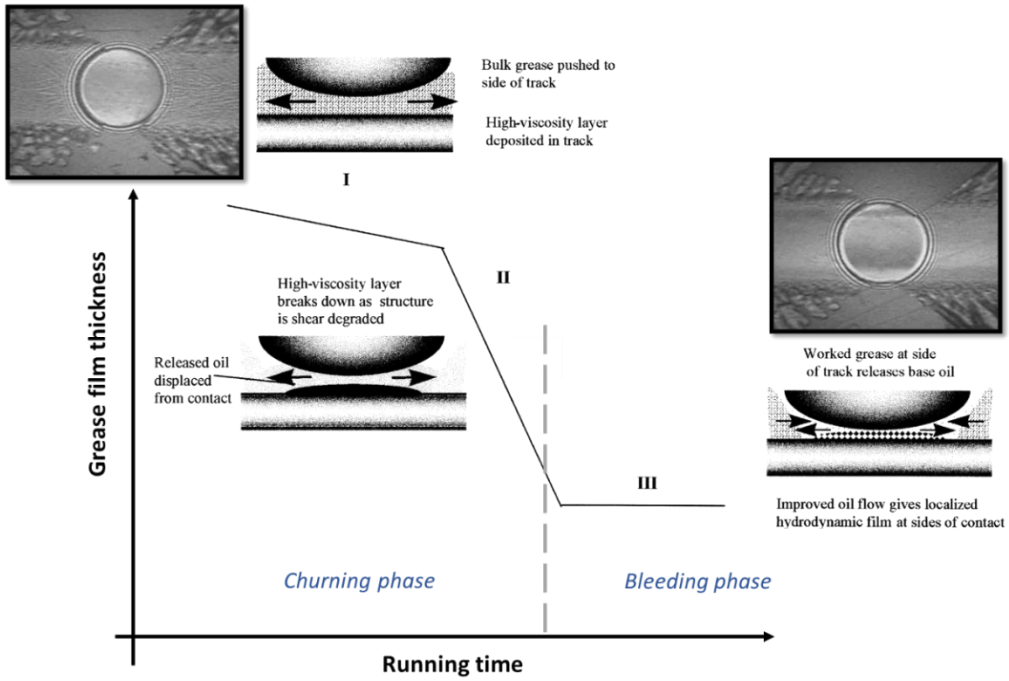

Figure 4: Evolution of the grease film thickness as the lubrication mechanism evolves

The churning phase and bleeding phase sequence usually correspond to a decay curve of the film thickness where three distinct regions are identified: I fairly constant film thickness at the onset of motion, II rapid decay, and III stabilization (Figure 4).

The bleeding phase is delicate, in any case. The contact replenishment mechanism deteriorates progressively in time as the grease ages. The film thickness generally decreases with time until the order of or less than the surface roughness, where it can no longer entirely separate the surfaces. Therefore, the system can run into film breakdown, leading to heat development [3]. As soon as the temperature of the contact region increases, grease accumulated outside the contact softens. It is well known that grease bleeding increases with temperature, and the increased mobility of base oil with temperature helps to limit starvation. Thus, a film breakdown event may lead to the subsequent reflow of liquid lubricant, the restoration of the starved lubricating film, and a corresponding temperature drop. The probability that this sequence of events repeatedly occurs during the lifetime of the contact is high. The bleeding phase is said to survive through *feed and loss* [14], which makes the grease lubricant film relatively unsteady.

However, additional instances may cause occasional replenishment of fresh grease involving the high-viscous layer mechanism. These make the deterioration process less dramatic [11]. Replenishment may even occur in combination with the release of fresh grease lumps that smear onto the moving surfaces, and this occurrence feeds the lubricant films with both oil and thickener fibres. A high viscosity layer may even be transitorily restored with a renewed separation of solid bodies. The release of a small lump of grease creates a new grease surface that enhances the bleeding rate of oil just because the oil concentration gradient is higher at the new surface than at the old [3].

Moreover, the experimental evidence suggests that sometimes the stabilisation of the film thickness over an extended life is attained even if the bleeding mechanism remains of subordinate importance and the bleeding phase never starts. In rolling bearings, for instance, the dominant lubrication mechanism depends on the bearing design, the type of grease (composition, rheology) and the operating conditions. Ball bearing operated at low speeds typically endures long thanks to the high-viscosity layer mechanism, whereas roller bearing cannot but rely on oil bleeding due to sealed line contacts [4].

Stribeck curves measured with different grease types proved that the thickener plays a significant role in the film formation under low speeds, overcoming the bled oil effects [15]. An example of film thickness versus speed is reported in Figure 5, where straight lines correspond to the film thickness with the base oil alone and the markers to grease.

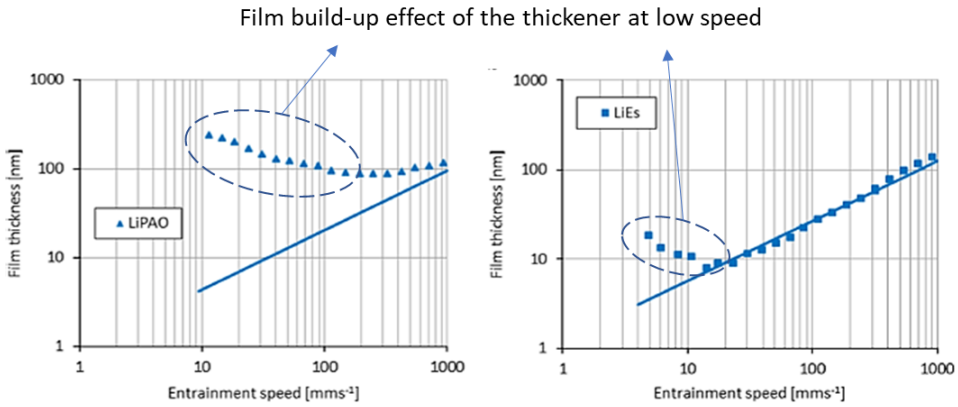

Figure 5: Typical film thickness versus speed curves of greases obtained by interferometric measurement at rolling point contacts. Adapted from [16].

Curves have a characteristic ‘V-shape’ since a thicker film is noticeable at low speed compared to the base oil alone. This build-up effect of the thickener on the lubricating film is most likely associated with settling a highly viscous layer on the tracks. At higher speeds, the film thickness of the grease is close to that of its base oil, meaning that the beneficial effect of the thickener structure vanishes as oil-bleeding dominates [16].

Eventually, it is essential to mention that the grease formulation concerning base oil and thickener affects the lubrication mechanisms. In other words, the formulation should be optimized in light of the predominant mechanism for the target application. For a deposited layer to be settled would require good shear stability, high base oil viscosity, high thickener content and good surface adhesion. On the contrary, low base oil viscosity, moderate thickener content, poor shear stability and low wettability of surfaces are desired to optimize the oil bleed mechanism. Formulating all-purpose greases with a good balance of these conflicting requirements is challenging.

1.2 Wear

According to ASTM G40-17, wear is any damage to a solid surface, generally involving progressive material loss due to relative motion between that surface and a contacting substance or substance. DIN 50320:1979 (now retired) defined wear as the progressive loss of material from the surface of a solid body due to external mechanical actions, i.e. the contact and the relative motion against a solid, liquid or gaseous counter-body. The research group on wear of engineering materials of the Organization for Economic Co-operation and Development (OECD) defined wear as the progressive loss of substance from the operating surfaces of a body occurring as a result of relative motion at the surface [17].

These definitions suggest that wear involves three key features: the contact between a solid surface and another substance, relative motion at the interface [18] and the damage caused by material loss from the solid surfaces. However, from the design and quality engineering viewpoint, surface damage is not necessarily limited to material loss. Other ways to cause surface damage is by the plastic flow of material without loss of mass or the growth of deposited third layers [19]. Therefore, wear can be addressed more comprehensively as the *progressive change to a part that adversely affects its performance caused by*

relative motion with respect to another substance [19]. The latter understanding of wear best fits the engineering use because it focuses on any surface modification resulting from the mechanical interactions, not necessarily the loss of material implied in the earlier material-science-oriented definitions of wear. In other words, it shifts the focus towards any topography modification that may alter the proper functioning of the components.

Wear with corrosion and fatigue failure is one of the primary reasons for engineering systems malfunctions, reduced operational efficiency and components replacement [20]. Understanding the causes of wear and the physical phenomena involved allows the engineers to limit its adverse effects on the mechanical systems, e.g. the increase in vibration and noise, misalignments and overstresses, impulsive loads, or the increase of the backlash in mechanical connections. Wear is experienced by all the mechanical components in machines due to use, and it often leads to the formation of fragments (or debris) that either leave the tribological system or remain trapped inside. This latter case is addressed by the theory associated with the so-called *third-body concept* [21].

Various *wear processes* may arise depending on the nature and the geometry of the materials in contact and the type of interaction, e.g. sliding wear, rolling wear, fretting wear, erosive wear, lubricated or dry wear, impact wear, and others. However, the wear processes combine one or more fundamental *wear mechanisms*. A commonly accepted classification distinguishes between four fundamental wear mechanisms [22], summarized in Figure 6.

- Adhesive wear
- Abrasive wear
- Tribo-chemical wear
- Fatigue wear

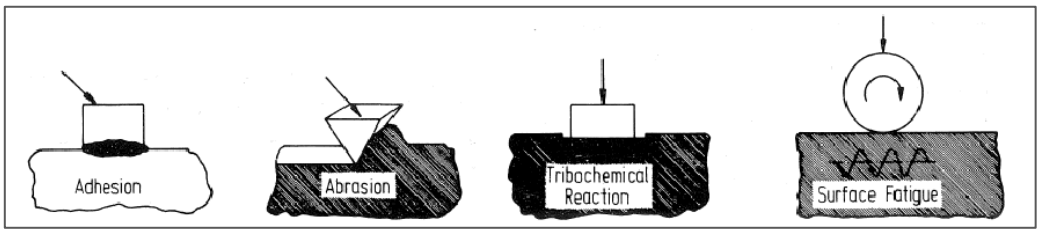

Figure 6: Fundamental wear mechanisms as per DIN 50320:1979 (now retired). From **[22]**.

1.2.1 Sliding Wear

The mechanisms determining the surface damage in sliding systems are mainly adhesion, abrasion and tribo-oxidation. Abrasion dominates if the tribological system is characterized by the presence of hard particles (harder than the surfaces in contact) or when one of the surfaces of the tribological system is much harder than the other one [23].

Adhesive wear is a mechanism in which the adhesion of surface ridges plays a predominant role. Recalling the theory of adhesive friction by Bowden and Tabor [2], failure occurs within the asperities material if the strength of a micro-junction between two asperities is greater than the strength of the surface material itself. In materials with marked plastic behaviour and limited hardening, plastic flow is activated as soon as the shear stress approaches the yielding shear stress τ_y of the weaker material (Figure 7a). In brittle materials, a micro-crack nucleates and propagates as the shear stress reaches the limit for crack initiation τ_m, with debonding and fragmentation of one asperity (Figure 7b). If the applied pressure is above the critical value p_c larger cracks (whose dimension exceeds that of asperities) may propagate towards the bulk material affecting larger portions of the material.

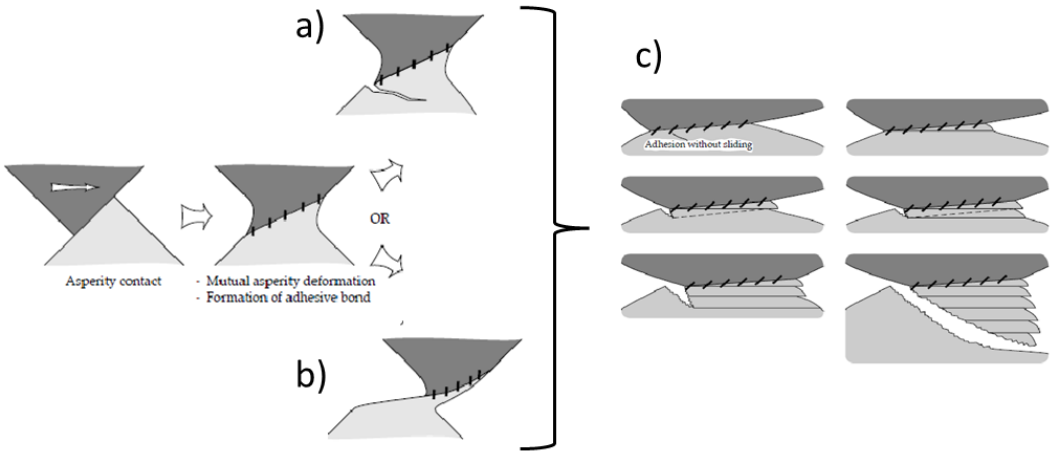

Figure 7: Failure mechanisms of adhesive junctions. Adapted from **[1]**.

The actual behaviour of many materials combines these two limiting cases. As suggested by the slip bands model (Figure 7c), material transfer results from the failure of the micro-junction in both cases. Material transfer contributes to the amount of material the system loses if the transferred debris is detached at some

stage. However, the probability of cleavage at the junction plane is greater than the probability of bulk asperity failure. The junctions releasing wear fragments are thus a limited share of the total number of adhesive junctions between the bodies in contact [24].

Abrasive wear is connected to abrasive agents in the tribological system, either from surfaces or outside. Abrasive wear leads to considerable material removal, and its presence is indicated by characteristic longitudinal grooves and scratches along the sliding direction. Two abrasive wear mechanisms can be distinguished: two-body abrasion and three-body abrasion, depending on whether the abrasive bodies are constrained or free to roll between the mating surfaces. Figure 8 shows the difference between abrasion of an asperity versus abrasion from hard debris between the surfaces. Two-body abrasion occurs when hard particles embedded in one of the two contacting bodies penetrate the partner surface. Typical abrasive particles are ceramic reinforcing particles (Al2O3, SiC) or carbides in steels (FeC, CrxCy). Two-body abrasion can appear between homogeneous materials too, provided that a significative difference in hardness is there. In this case, the asperities of the harder surface act as abrasive bodies.

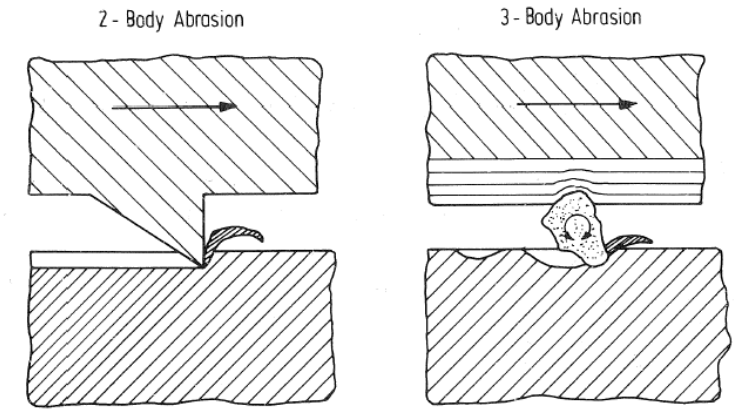

Figure 8: Abrasion wear mechanism. From **[22]**.

Abrasion involves four fundamental modes of surface damaging (Figure 9): micro-ploughing, micro-cutting, micro-fatigue and microcracking. Micro-ploughing appears when each abrasive particle produces a groove without (ideally) any wear volume, i.e. the material flows sideways. On the contrary, micro-cutting appears when a chip whose volume is equal to the groove volume is removed without any other material displacement, like a cutting tool. The incidence of one or the other condition depends on the attack angle of the abrasive

particles, which in turn depends on the attack angle of the abrasive particles [23]. If simultaneous or successive scratches from micro-ploughing occur in the same area, the cumulation of plastic deformation from ratcheting may lead to the detachment of little material portions. This mode is called micro-fatigue, and it is typical of ductile material. Microcracking is typical of brittle material for which the mechanism of spalling dominates

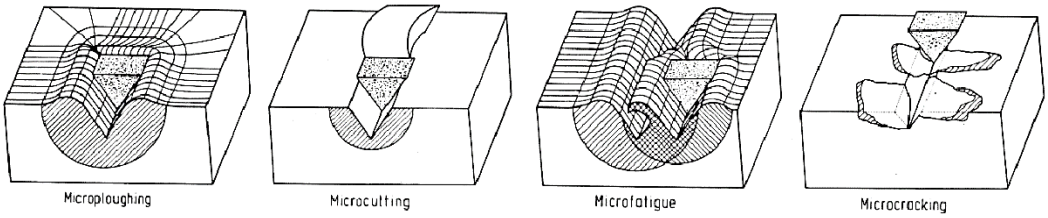

Figure 9: Abrasion modes. From **[22]**.

It has been experimentally observed that the entity of wear phenomena strongly depends on the ratio between the hardness of the surfaces undergoing abrasion and the hardness of the abrasive particles $r = H_{surface}/H_{particles}$. Based on this evidence, Richardson [22] proposed a parallel classification of abrasive phenomena where *abrasion by hard particles* occurs if $r \leq 0.5 \div 0.8$ (hardness of abrasive bodies is higher than that of worn surfaces) with a high wear rate; abrasion by soft particles occurs if $r \geq 1 \div 1.4$ (hardness comparable to the surfaces) and wear rate is associated to it.

Tribo-Oxidative wear is a particular form of corrosive wear where the aggressive agent is the atmospheric oxygen that promotes surface oxidation. Tribo-oxidative wear is more complex than other wear mechanisms as it involves chemical and mechanical action. At room temperature, if the sliding speed and the applied load are such that the flash temperature at the asperity tips is lower than the activation temperature of oxidation, oxidation takes place on already detached debris. This kind of tribo-oxidation, called *indirect tribo-oxidative wear*, is usually triggered by initial adhesive effects involving higher energy w.r.t. abrasive effects (Figure 10). Fragments from adhesive wear are fractured, progressively oxidized and eventually agglomerated in a layer of compacted debris adhered to the surfaces [1]. This coating also provides lubricity to the interface, thus reducing friction and protecting the underneath material. However, friction forces lead this

oxidized tribological layer to failure contributing to the production of wear debris, and a new metal surface is periodically exposed to adhesion.

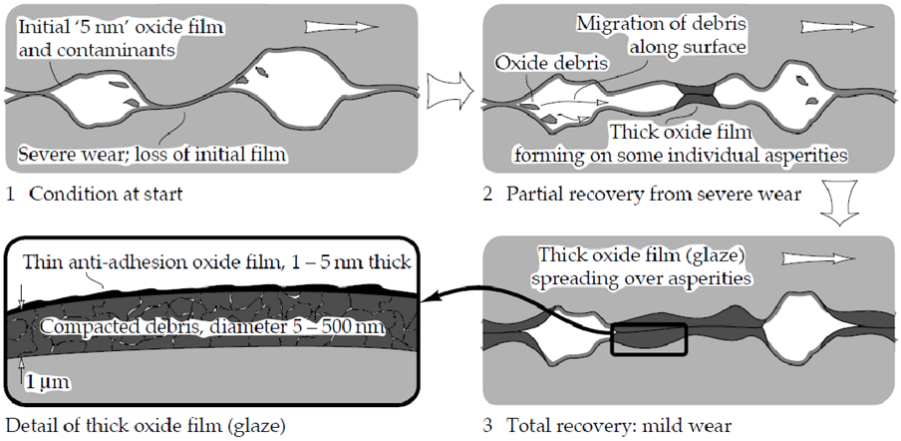

Figure 10: Indirect tribo-oxidation at low sliding speed and under low loads (limited flash temperature). From [1].

In the case of high temperature or very high sliding speed, oxidation may start on the surface. The mechanism is called *direct tribo-oxidative wear,* and the loss of material results from the fragmentation of the layer of oxides that continuously grows on the mating surfaces in contact with oxygen.

The wear rate of a tribological system under sliding motion can be generically expressed as per equation (3), where V is the total volume of material removed from the system, F_N is the applied load, s is the sliding distance that produced the volume V, and H is the hardness of the softer material in contact. The interplay of the different wear mechanisms affects the value of the dimensionless wear coefficient K, also called the *Archard wear coefficient,* after the name of the researcher who first proposed this empirical linear equation for wear. Although equation (4) states the wear coefficient as the sum of individual contributions from each wear mechanism, coefficient K is often determined experimentally as one aggregate value. The contribution of each wear mechanism cannot be easily separated from the others.

$$V = \frac{K \cdot F_N}{H} \cdot s \tag{3}$$

$$K = K_{adh} + K_{abr} + K_{ox} \tag{4}$$

1.2.2 Rolling wear

Rolling wear occurs when two surfaces are in repeated contact as one rolls over the other. Pure rolling is never attained in real applications since some micro slip in the contact region is always present, especially in the case of tractive rolling. Conditions of near-pure rolling occur in mechanical components such as rolling bearings or roller-cam systems. Rolling wear is dominated by surface fatigue when the other fundamental wear mechanisms are inhibited (or significantly reduced), for instance, due to lubrication (Figure 11).

This wear mechanism originates from repeated cyclic stress on the surfaces, which triggers the nucleation and propagation of cracks leading to the detachment of debris after a given number of cycles. Unlike the others, this mechanism does not accumulate continuously from the beginning of the interaction but suddenly appears just like any other fatigue failure. Little importance is usually given to the actual volume of material removed, also because it can be very tiny. The useful life of the tribological system, i.e. the duration before fatigue emerges, is far more significant.

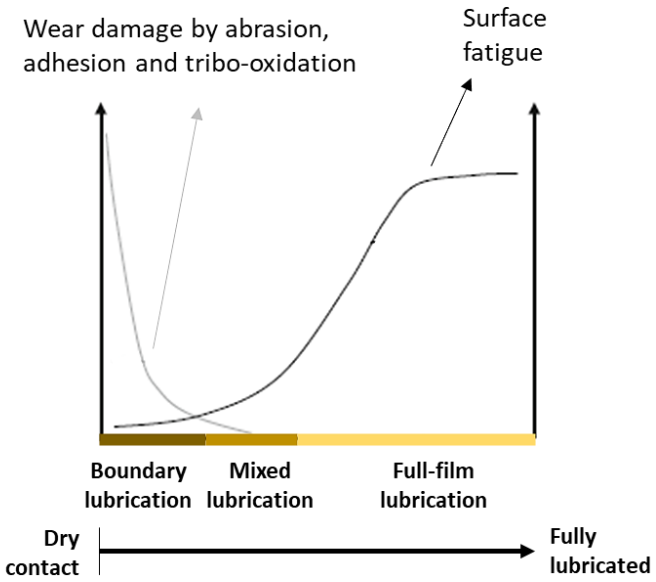

Figure 11: Relative influence of the fundamental wear mechanisms in rolling wear in proportion to lubrication regime and lubricant quantity. Adapted from [23].

Two different conditions of surface fatigue can be distinguished compared to the lubrication regime:

- Microscopic fatigue
- Macroscopic fatigue

Macroscopic fatigue results from fluid-film lubrication conditions where a thicker lubricant layer separates the surfaces. Direct contact between asperities is totally or mostly avoided, but cyclic elastohydrodynamic loads remain. Unlike microscopic fatigue, cyclic loading covers a larger area of the surfaces according to the Hertzian stress distribution of non-conforming contacts. Nucleation of cracks occurs at a depth close to z_m, i.e. the depth of maximum Von Mises stress along the axis of symmetry of the contact. Crack nucleation is favoured by stress concentration induced by non-metallic inclusions (oxides, sulphides), precipitates (carbides, nitrides) or microporosities. Alternatively, it may also occur at soft spots in the microstructure. From a mechanical viewpoint, the nucleation stage is characterized by a local microstructural alteration with dislocation build-up, and nucleation generally occurs after an elastic shakedown has been reached [23]. Subsurface crack propagation is driven by the stress field and proceeds by mixed mode II (predominant) and mode I (tensile mode) propagation. The contribution of mode I propagation also comes from the pumping effect of the lubricant that opens the edges of the crack due to hydrodynamic pressure. It can be assumed that cracks initially propagate along the plane of maximum shear stress at 45° relative to the surface. After some propagation, the crack changes direction and propagates parallel to the surface, driven by the τ_{yz} shear stress. Debris is released when the ligament between the crack tip and the surface fractures by plastic collapse [23]. This process, also called *spalling,* is schematized in Figure 12. The wear fragments are large, typically over 100 µm in diameter.

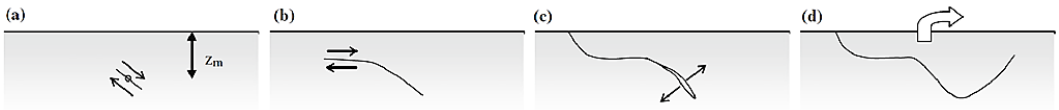

Figure 12: Nucleation and propagation of a subsurface fatigue crack. From [23].

Microscopic fatigue is experienced in the mixed lubrication regime. Due to the thin lubricant film, part of the load is carried by the asperities in direct contact or in contact with debris. In the presence of an adsorbed layer of lubricant molecules on the solid surfaces, direct metal-to-metal contact is avoided, preventing adhesive and abrasive wear. However, repeated rubbing of the

asperities results in some asperity-scale ratcheting and crack nucleation at the surface is made easier [25]. Geometrical discontinuities, such as grinding marks, are preferential sites for surface micro-crack nucleation. Cracks may then propagate inside the material due to the local stress intensity factor, and friction further increases the local stress level beneath the surface.

In most cases, after some propagation, the crack deviates towards the surface because of the instabilities of mode II. Fragments from microscopic surface fatigue are small, in the order of 10 μm in diameter. This phenomenon is often called *pitting* and may anticipate failure by spalling if the lubrication regime is poor.

1.3 Friction

Frictional is dissipative process in which the mechanical work is lost by the sysstem and mostly degraded to heat. Two distinct friction phenomena are usualy identified: *external friction* and *internal friction*. The former identifies actions exchanged between two distinct bodies, the latter includes those friction actions due to deformations into materials. Based on the kinematics of the relative motion external friction is classified as *sliding friction* and *rolling friction*. The microscopic cause of both phenomena is found in chemical-mechanical adhesive interactions between asperites of surfaces, whose quantity and nature depends on the materials involved and the environemnt.

In a very general case, many phenomena may contribute to the overall friction. Assuming that the superimposition of effects holds, the coefficient of friction of a specific tribological system should be predicted as per equation (5), where contributions from adhesion, abrasion, hysteresis of materials, rolling motion, viscous/viscoelastic deformations of solid material, viscous losses due to lubricants are considered.

$$\mu = \mu_{ad} + \mu_{abr} + \mu_{hys} + \mu_{roll} + \mu_{vic} \tag{5}$$

Historically, the Coulomb and Morin's model represents the first quantitative approach to the friction problem. It is based on the following assumptions formulated by Da Vinci and Amontons [1].

- There is proportionality between the maximum tangential force Q_s, acting on a body without altering its state of quiet, and the normal force F_N playing at the body-environment interface.
- In the state of motion, the tangential friction force F_T is proportional to the normal load F_N.
- The friction force is independent from the apparent contact area.
- The friction force is independent from the relative speed.

Coulomb-Morin's model is phenomenological and empirical. It introduced the concept of *static coefficient of friction* and *dynamic coefficient of friction* throught equations (6) and (7). Two bodies adhere to one another because the reaction generated by the interface maintains the static equilibrium of the system until the force applied F_T reaches the limiting value Q_s. Once Q_s is exceeded relative motion is triggered: from this moment on a new dynamic equilibrium is achived with F_T stabilizing at a value lower than Q_s. This model is useful to study the frictional problems from an engineering point of view, but it is inadequate when questions concerning the physics of the phenomena arise.

$$F_T < |Q_s| = \mu_s \cdot F_N \tag{6}$$

$$F_T/F_N = \mu \tag{7}$$

1.3.1 Sliding Friction

Adhesion and abrasion are the two most important source of friction in dry sliding contacts. This section will focus on these two fundamental friction mechanisms.

The *Bowden and Tabor's adhesive theory* of friction, already introduced in Section 1.2, is one of the earlier mechanical theory which traces back the cause of friction to the adhesive-cohesive interactions at the level of the surface asperities [22]. The adhesive theory affirms that the tangential force F_T, required to maintain a dynamic equilibrium with constant sliding speed, is directly proportional to τ_m, i.e.,the critical shear stress required to breake the junction between the asperities in contact, and the real contact area $A_{r,\tau}$, i.e., the effective surface carrying the applied load (equation (8)). In no way the value of τ_m can be greater than the

yielding shear strength τ_y of the softer material, which can be approximated by equation (9), being H the surface hardness.

$$F_T = \tau_m \cdot A_{r,\tau} \tag{8}$$

$$\tau_y \approx H/(5{,}2 \div 6) \tag{9}$$

If the shear strength of the junctions is lower than the shear strength of both the materials, sliding takes place once the shear stress at the junction plane reaches τ_m. If the adhesion is so strong that it results in a strength ideally greater than the one of neighboring materials, then τ_m corresponds to the shear limit of the softer material and a wear particle is generated, as described in Section 1.2.

In the theory of adhesion τ_m can be expressed as a function of the work of adhesion per unit area W_{12} [23]. The work of adhesion represents the energy that must be theoretically supplied to separate two surfaces in contact, and it is related to the surface energies of the bodies.

$$W_{12} = \gamma_1 + \gamma_2 - \gamma_{12} = c(\gamma_1 + \gamma_2) \tag{10}$$

Where γ_1, γ_2 are the surface energies of the interfaces with the surrounding environment [J/m^2]; γ_{12} is the surface energy of the interface that the two bodies form when they are in contact [J/m^2]; c is a coefficient called tribological compatibility.

Alongside with adhesion, *abrasion* is a major source of friction in tribological sliding interfaces, in the form of tow-body abrasion or three-body abrasion. The reason why an abrasive friction force originates is the interpenetration of surfaces which results in the displacement or removal of material. A simplified model for two-body abrasive friction was proposed by Rabinowicz, and reads as equation (11) [26]. Abrasive particles are modelled as non-deformable conical bodies with a certain attack angle Θ, as shown in Figure 13a. The normal load F_N is calculated considering that one half of the lateral surface of the cone (the ploughing side) is able to support the load; the tangential force F_T is supposed proportional to the yielding pressure of the material and the cross-sectional area of the groove. This model works for both ductile and brittle materials, regardless of whether particles remove the material or let it plastically flow sideways. The influencing parameters

of the phenomenon are just the penetration depth and the attack angle of the abrasive body.

$$\mu_{abr} = F_T/F_N = 2\tan\Theta/\pi \tag{11}$$

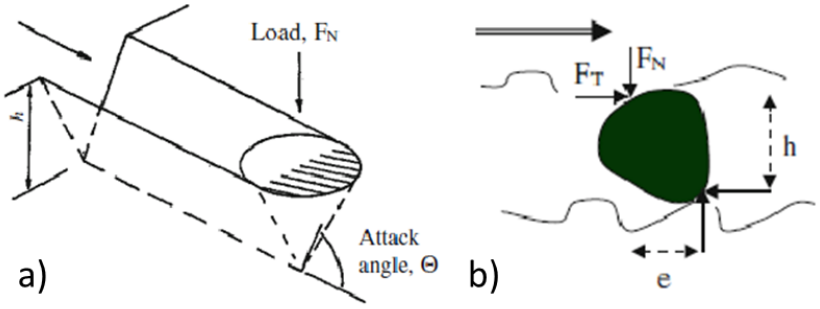

Figure 13: (a) Rabinowicz model of abrasive particles; (b) Free-body diagram of a particle causing three body abrasion). From [23].

As to three-body abrasion, it originates when hard particles are free to roll between the mating surfaces. Particles may either be unleashed by one of the contacting materials (including wear debris) or come from the environment (dust, sand and other inorganic debris). The theoretical evaluation of the coefficient of friction is much more problematic in this case because the type of motion of such particles is unknown: they might roll or undergo a mixed rolling-sliding motion. It can be argued that if pure rolling is there, equation (12) must apply, where *e* and *h* are characteristic dimension defined in Figure 13b.

$$F_T/P = \mu_{abr} < e/h \tag{12}$$

1.3.2 Rolling Friction

The rolling friction coefficient is defined through equation (13), similarly to the sliding friction coefficient, according to the Columb-Morin's model.

$$\mu_v = F_T/F_N \tag{13}$$

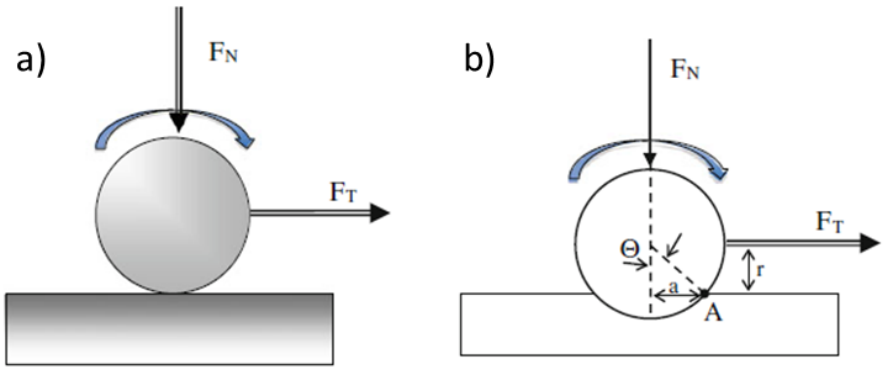

Figure 14: (a) Forces actin gon a rolling body; (b) Schematic of a body rolling on a flat plane. From [23].

The elastic deformations in the contact region are responsible for the resistance to rolling. The dynamic equilibrium about point A as per the schematic in Figure 14 reads as equation (14). A torque $F_T \cdot R \cdot cos\Theta$ is needed to overcome the resisting torque $F_N \cdot a$, where a is the half-width of the contact region, and Θ is very small.

$$\mu_v = R \cdot cos\Theta \,/a \approx R \,/a \tag{14}$$

During rolling some localized micro-slip may also occur because the nominal area of contact has a finite extension also in the case of nonconformal contacts. As a consequence, pure rolling is attained in just one point, i.e., the istantaneaous rotation point, whereas a combination of rolling and micro-slip establishes elsewhere. When micro-slip occurs the mechanism of adhesive and abrasive friction presented in the previous section appear at the contact region.

Chapter 2

Graphene nano-coatings in tribological applications

2D materials or nanosheets are characterized by having the thickness dimensions nano-sized, i.e. close to the atomic layer thickness. Magnificent electronic, optical, physical, and chemical properties are ascribed to these materials due to the effect of their spatial confinement in one dimension, which is usually absent in their bulk counterparts.

They usually possess strong in-plane bonds that let them exhibit a remarkable combination of thermal and electrical properties, high in-plane mechanical strength, and high out-of-plane flexibility which can, in turn, result in unusual frictional behaviour. [27]. Other beneficial characteristics of 2D materials relevant for tribological applications are the conformability to the substrate surface with high roughness, the easy shearing between the atomic planes, and the impermeability to liquids and gasses. The strength of the in-plane bonds between the atoms of one layer usually comes with weaker van-der-Waals forces and/or electrostatic or intermolecular interactions between stacked layers, which produces easy sliding the layers in response to the applied force. This feature is the basis of the outstanding lubrication performance and low friction of these layered materials when slid against themselves or other counter surfaces, both at the nanoscale and macroscale [28]. The regular atomic arrangement is also believed to give these materials the potential to achieve superlubricity [29].

2D materials are promising candidates for solid lubrication of machine components due to their encouraging properties and outstanding tribological performance. One of the major advantages is that they do not impair tolerances of machined because the involved thin layer/coating is so thin that it does do not impair the function. Moreover, the high conformality and thin nature of 2D materials lead to these materials being applicable to both hard and soft substrates according to the specific operational requirements. The potential application fields of nano-coatings range from sliding and rolling bearings to gears, seals, and other components [30].

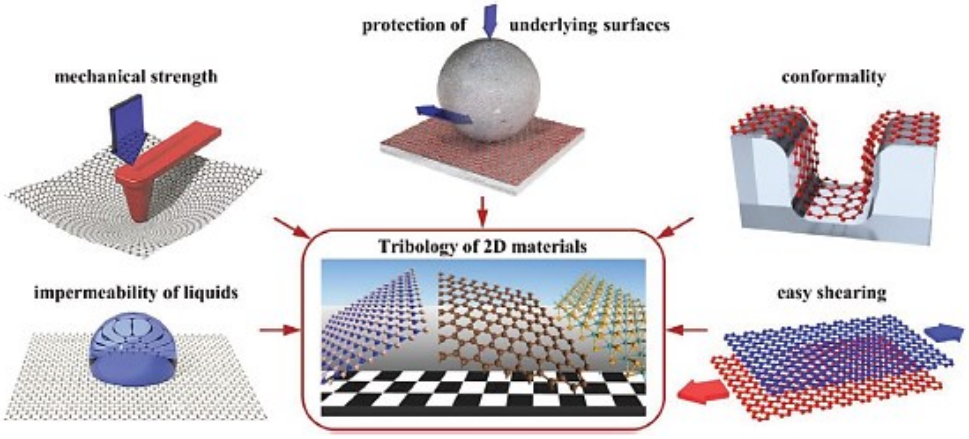

Figure 15: Beneficial characteristics of 2D materials relevant for tribological applications. From **[30]**.

On the other hand, when a bulk counterpart comes in contact with and slides against a nanomaterial, local puckering of the layer may appear because of the low bending stiffness of the sheet compared to its in-plane stiffness. Sometimes this out-of-plane puckering might be the source of increased friction because the contact area increases due to the extra work required to shift the puckered region. As the sheet thins, the puckering effect becomes more significant, suggesting that the best performance is obtained with a structure of a few stacked layers [27].

The 2D material which have attracted significant research work for their tribological performance are graphene and its derivatives, such as hydrogenated or fluorinated, graphene, graphene oxide (GO), and reduced graphene oxide (rGO), thin transition metal dichalcogenides (TMDs) like molybdenum disulfide (MoS_2) and tungsten disulfide (WS_2), silicenes, hexagonal boron nitride (h- BN), black phosphorous (BP), halide structures, metal-organic framework nanosheets and MXenes [30]. These nano-coatings may be sensitive to the test environments.

Some of them, like MoS_2, will not lubricate or last long if oxygen and/or water molecules are present, whereas graphene and boric acid cannot express their potential without humidity in the surrounding air [31].

2.1 Short review of production methods of graphene

The scientific literature reports several techniques developed since the discovery of graphene in 2004 to produce either graphene flakes or continuous graphene sheets for various applications. Many exfoliation techniques of bulk graphite are successfully applied to the production of flakes, i.e. shear exfoliation, chemical and electrochemical exfoliation [32], and liquid-phase exfoliation [33]. Other innovative processes rely upon unrolling/unzipping of carbon nanotubes (CNTs) [34], arc-discharge evaporation of pure graphite electrodes in an inert gas [35], or ball-milling of graphite particles [36].

Among the techniques that allow obtaining a continuous graphene layer, it is worth mentioning the mechanical exfoliation of graphite followed by transfer onto the desired substrate [37], the chemical vapour deposition (CVD) from hydrocarbons source, the inkjet printing of graphene flakes solutions [38], or the self-assembly of graphene nano-platelets (GNPs) via sonication. Drop-casting of a graphene film via the solution-processing of flakes [39] is a cheap and time-effective alternative to depositing a few-layer semi-continuous graphene coating directly onto the substrate. A small amount of solution (usually 10–15 drops per 1 cm^2) containing mostly single-layer suspended graphene flakes is applied on the solid surface in a colloidal liquid state. Then the liquid fraction (usually ethanol) is evaporated in dry nitrogen to prevent graphene oxide formation.

Although many efforts have been made to introduce new production processes, many limitations still exist, either in the scalability of the processes from the laboratory level to the industrial level or in achieving continuous carbon sheets large enough or regular enough to be applied to mechanical and electrical components. Sometimes, the cost and the complexity of these processes are the main issues preventing the mass production of graphene coatings.

The following sections provide details on three techniques suited to give shape to continuous graphene layers.

- Scotch-tape exfoliation

- Low-pressure Chemical Vapor Deposition (LPCVD)
- Self-assembly of graphene nano-platelets (GNPs) via sonication

Scotch-tape exfoliation is presented for historical reasons since it was the first production route through which atomically thin graphene layers were first isolated by Gejm and Novosëlov. Low-pressure CVD and self-assembly of graphene nano-platelets are worth dealing with since they promise to meet many future industrial production requirements.

2.1.1 Scotch tape-exfoliation

Historically, the first efficient way to have atomically thin carbon layers was obtained by mechanical delimitation [37], also known as 'scotch-tape' exfoliation or micromechanical cleavage. Following this technique, single-layer graphene is cleaved from graphite crystals by exerting a normal force with the aid of a piece of scotch tape, which is applied to the graphite surface, as shown in Figure 16.

Highly oriented pyrolytic bulk graphite (HOPG) is the preferred carbon source because of the ease of cleaving thin graphite layers. By continuously repeating this peeling force against another chunk of scotch tape, the graphitic layer gradually thins out until it becomes an even ultra-thin carbon layer [27]. The coatings transfer is achieved by pressing the tape onto the desired substrate. Even though this method to peel graphene is simple and cost-effective since commercially available adhesive tape can be used, it is suitable only for coating small surfaces, e.g., for laboratory testing on graphene samples at the nanoscale. Besides, the process is manually controlled with meagre reproducibility in terms of size and thickness of the coating and slow output rate, making it hardly scalable to industrial applications and very little used nowadays [27].

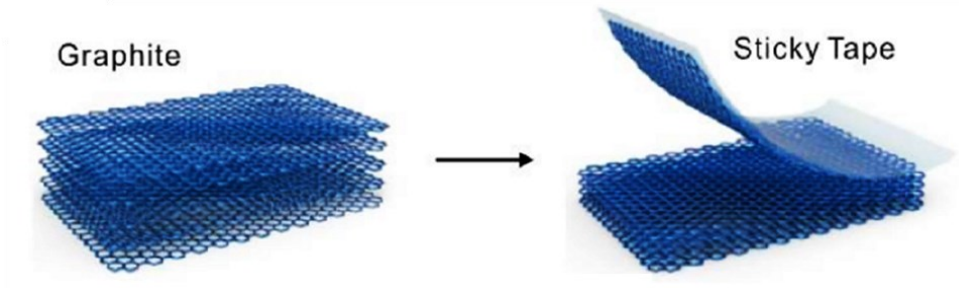

Figure 16: Peeling of multilayer graphene by scotch-tape exfoliation. Adapted from **[40]**

2.1.2 Chemical Vapor deposition-based graphene

The chemical vapour deposition (CVD) method is considered by researchers the most promising method for the large-scale synthesis of high-quality single-layer graphene (SLG) or multi-layer graphene (MLG). CVD graphene is synthesized by forcing a hydrocarbon species, usually in the gaseous state, to react with thin metal foils at high temperatures (typically between 800°C and 1100°C) and low pressure. A typical reactor to grow CVD graphene consists of a hot wall furnace, with a 40-mm fused silica tube heated in a split tube furnace, as Figure 17 shows.

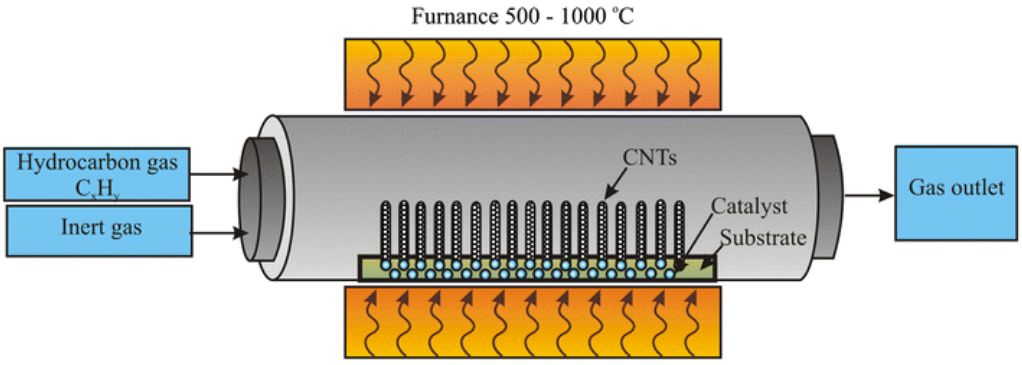

Figure 17: Schematic of an hot wall furnace for CVD synthesis of carbon structures. From https://www.sputtertargets.net/blog/what-is-chemical-vapor-deposition-cvd.html

The thin metallic foil exposed to the carbon precursors under controlled reaction conditions acts as a catalyst body resulting in the decomposition of the carbon-rich species and the growth of a continuous carbon layer with sp^2-hybridized bonds and hexagonally arranged lattice. Methane, acetylene and ethylene are the most common gaseous carbon precursors to synthesize graphene [27]. Methane is widely employed being a cost-effective carbon source, while ethylene is sometimes preferred over methane because it has higher reactivity and requires lower furnace temperature for chemical decomposition [27]. Some researchers tried solid or liquid carbon-rich precursors as an alternative to gaseous precursors for cost-reduction or process simplification. For instance, Somani et al. grew few-layer graphene on a nickel substrate by thermal CVD using low-cost solid camphor, and Dong et al. produced large-sized single- and few-layered graphene by chemical vapour deposition on copper foils using liquid ethanol and pentane [41]. As to the catalyst, several suitable metals have been proposed by researchers, such as Ni, Cu, Ir, Ru, Co, Pt, Pd and Re. Among the others, polycrystalline Cu foils have been widely employed because high-quality single-

layer graphene can be produced at low cost by adequately controlling the furnace parameters and transfer to any other substrate is easily achieved.

Several factors, including the nature of the precursor, the carbon solubility limit of the substrate, the lattice structure, and the thermodynamic parameters like pressure and temperature of the furnace, determine the growth of graphene on the metal catalyst. By adjusting these conditions, the growth of the graphene can be controlled with a tunable number of layers, high crystallinity and a reduced number of wrinkles or folding. The synthesis of graphene is confined at the catalyst surface, and different growth mechanisms have been attributed to the characteristic carbon solubility of the metal substrates. The graphene synthesis proceeds via a combination of diffusion into the thin metal film at the growth temperature and precipitation of carbon from bulk to the surface of the metal upon cooling after CVD synthesis [42].

Usually, increasing the partial pressure and the temperature of the reaction substances in the furnace drives homogeneous gas-phase reactions to be stronger with a faster graphite-like solid carbon matter growth rate. This homogeneous reaction must be controlled and sometimes minimized to grow high-quality single-layer graphene [43]. For this reason, conditions of high temperature and low partial pressure of the precursor species are usually preferred for deposition. The higher temperature allows more carbon to solubilize and diffuse into the metal catalyst with easy activation of many nucleation sites of graphene; the partial pressure of the precursor species is exploited as the self-controlling parameter to limit the growth rate and prevent stacking of many graphene layers. However, insufficient carbon supply may drive the crystallization of graphene to abort after activation of nucleation sites with the formation of amorphous carbon instead of graphene [44]. The synthesis of highly crystalline graphene is still not that straightforward, though, for instance, the surface roughness of the catalytic metal surface may still be an issue [27].

A typical deposition procedure follows the main stages listed below [45].

I. After loading the thin metal foil into the furnace, the chamber is evacuated to 1×10^{-1} Pa to remove moisture, dust, oxygen and other atmospheric gases that can affect the graphene quality.
II. The chamber is backfilled with hydrogen or a mixture of H_2 and another carrier inert gas (e.g. He or Ar). The pressure of backfilling of the chamber depends on the type of CVD process. The total pressure equals the ambient

pressure for the so-called ambient-pressure chemical vapour deposition (APCVD). In low-pressure chemical vapor deposition (LPCVD), the total pressure is kept at a few hundred Pascals, e.g. at 100 Pa [46]. The chamber can sometimes be evacuated and backfilled once again to ensure the complete removal of residuals.

III. The heating of the chamber to the desired temperature is carried out typically at 25 °C/min under a constant flow of H_2 or hydrogen plus another inert gas (from 30 sccm to 100 sccm).

IV. The metal target is annealed at a high temperature for 5 to 10 min to remove residual surface oxides. It was observed that suitable annealing of the metal foil before the graphene growth also promotes the growth of crystalline grains up to a favourable size and enhances the quality of graphene since it increases the single-crystal graphene domain size.

V. The carbon precursor is introduced into the chamber for the desired time (or *growth time*). 10 sccm to 35 sccm of CH_4 are introduced to allow the precursor to react with the catalyst. Carbon solubilizes into the metal target during this period.

VI. The furnace is cooled (e.g., the cooling rate is 140 °C/min) down to room temperature in an inert or reducing atmosphere to promote the segregation of C atoms and the nucleation activation. The role of hydrogen is crucial in this stage because it can saturate the edges of the growing graphene island and stabilize them [47]. Figure 18 resumes the main stages of the growth mechanism of CVD-based graphene, and Figure 19 exemplifies the typical process parameters of the hot wall furnace.

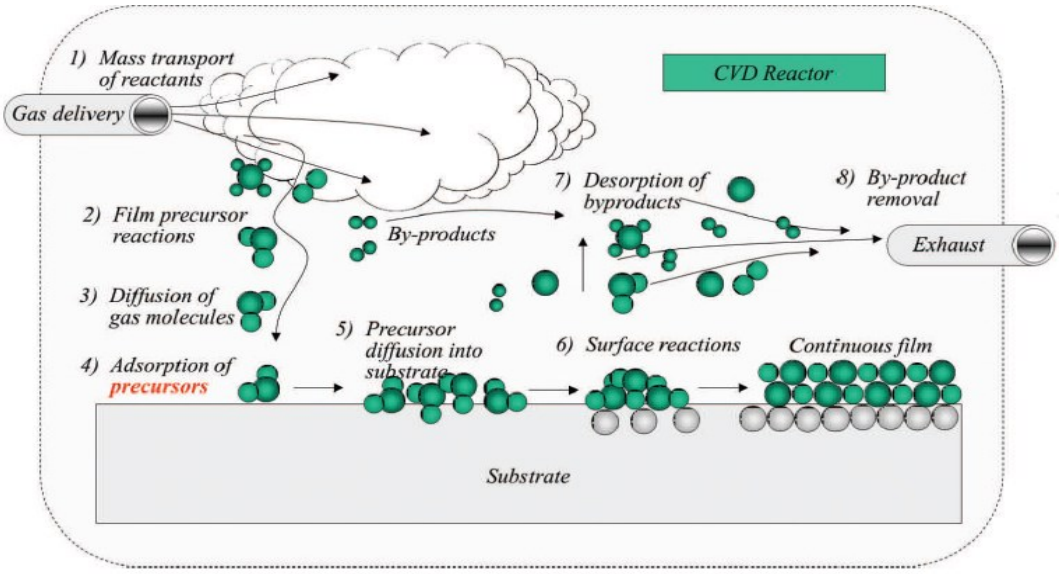

Figure 18: Overview of the stages of the CVD growth of graphene on the catalytic metal substrate. The general mechanism involves: (1) mass transport of the reactant, (2) reaction of the precursor (gaseous) species, (3-4) adsorption of the precursor molecules, (5) diffusion into the substrate, (6) surface reaction and solubilization of C atoms, (7-8) desorption and removal of the side products. The continuous film is formed at cooling down. From [48].

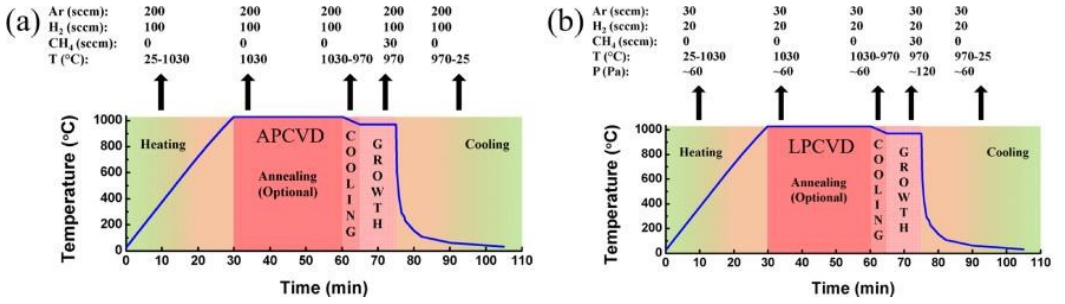

Figure 19: Typical process parameters of the APCVD (a) and LPCVD (b) graphene growth on thin metal foils. Adapted from [46]

It is worth mentioning that sometimes deposition is performed with the contribution of plasma produced by radio frequency (RF) within the silica tube. The process, called Plasma-enhanced chemical vapor deposition (PECVD), takes advantage of the rapid dissociation of hydrocarbons by plasma that fosters the growth rate of graphene on the metal foils. This process allows the deposition of high-quality and large-size graphene films at lower temperatures (400-600°C) than traditional CVD. The experimental setup for the growth of monolayer graphene films using PECVD is depicted in Figure 20.

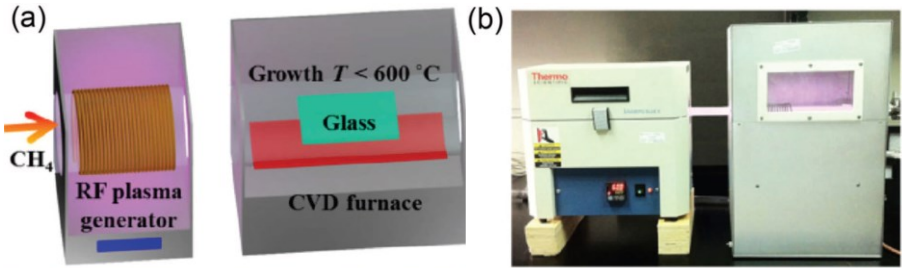

Figure 20: (a) Schematic of the spit furnace of the PECVD systems; (b) Example of a commercial PECVD furnace where the growth chamber is on the left and the RF plasma source is on the right. From [48].

Now, to use graphene sheets synthesized by CVD, it is necessary to detach them from the thin metal foils that serve as catalyst bodies. A transfer process is needed except when the metal foils are directly mounted on a substrate, or the

deposition is directly performed onto the end surface. Transfer processes are rather complicated and unavoidably induce some defects, residues, and tears that may degrade the performance of graphene sheets.

The so-called 'wet etching and transfer' process is the most widely used transfer approach. The process requires encapsulating the graphene sheet with a backup polymer coating as a support media to make transfer onto the end samples possible and subsequent etching of the metal catalyst in an etching bath. After transferring the polymer/graphene film onto the desired substrate, the polymeric supporting layer is removed, and graphene naturally grabs onto the solid surface (Uzoma). A typical transfer process route requires the stages resumed in Figure 21. A thin polymeric layer of ethylene-vinyl-acetate (EVA) or poly-methyl-methacrylate (PMMA) is spin-coated on the graphene/metal foil sandwich and baked in an oven at 80°C. The metal foil is removed through an etchant and rinsed away with DI water. The EVA/graphene layers are transferred onto the desired substrate by immersion of the end substrate into the DI water bath. The coated system is then baked for one hour at 80°C into N_2 to avoid oxidation so that graphene grabs onto the surface. The last step is removing the polymeric support layer by rinsing it with a strong solvent, like acetone or xylene. [49]. This procedure was followed to prepare the CVD graphene for tribological tests presented in Section 3.

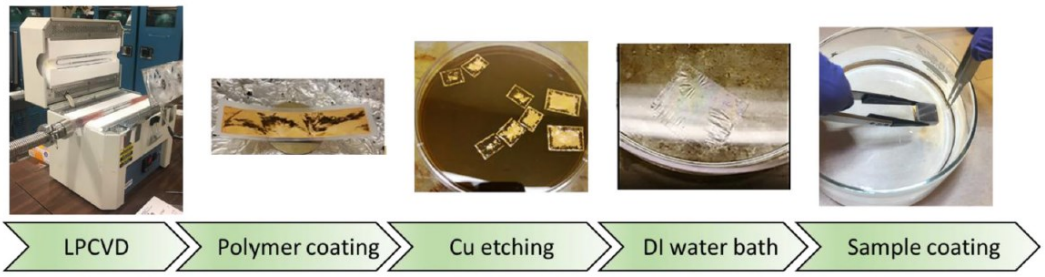

Figure 21: Transfer process of SLG after growth by LPCVD on a Cu foil. From [50].

2.1.3 Self-assembly of graphene nano-platelets

Graphene nano-coatings can also be prepared with graphene flakes or nano-platelets (GNPs). These carbon flakes are prepared by electrochemical exfoliation from a bulk graphite rod, using a platinum wire as the grounded electrode and applying a 10 V bias. Once the graphite rod is dissociated into flakes, the flakes

are dispersed in dimethylformamide. The obtained solution is centrifuged to remove side products and thick graphite particles to get high-quality flakes with narrow thickness distribution. Centrifuged flakes are re-dispersed in ethanol, and then the graphene dispersion is injected beneath the surface of a DI water bath. Ethanol quickly spreads on the DI water surface upon injection because of the Marangoni effect, but its distribution is non-homogeneous. The graphene flakes naturally move from the low surface tension regions (those rich in ethanol) to the high surface tension regions (where the content in DI water is higher). This dynamics lets the graphene flakes collide and bind with each other via π–π interactions on the surface of the DI water bath as ethanol evaporates. With the increase of the percentage of graphene flakes dispersed into the bath, the assembled graphene flakes are pushed forward towards the bare surface of DI water, where the surface tension is higher so that the surface covered in graphene flakes grows. Finally, the assembled graphene films are driven to pack tightly at the liquid/air interface as ethanol evaporates, and a continuous graphene layer, called Ultrathin Graphene Film (UGF), takes shape. The UGF comprises two or three graphene layers with an average of 4-5nm thickness because flakes are partially bounded and stacked.

This environment-friendly method is cost-effective and fast. Areas as large as 150 cm^2 can be covered in a few seconds, and the scalability is up to 1000 cm^2 in one synthesis process [51]. The assembly of flakes is facilitated by sonicating the DI bath with flakes floating on top [52]. Compared to other cost-effective solution processes proposed in the scientific literature (e.g., drop-casting and spin-coating), the unique feature of this method is the extraordinarily structural uniformity of the graphene film. Drop-casting processes suffer from the so-called coffee-ring effect upon the evaporation of ethanol, i.e., when a drop of graphene-ethanol solution dries, the flakes precipitate with high concentration along the edge and low concentration in the middle. Similarly, graphene flakes would be dragged outward in the spin-coating processes due to the centrifugal effect, and wave-like edges form into the graphene film (see Figure 22).

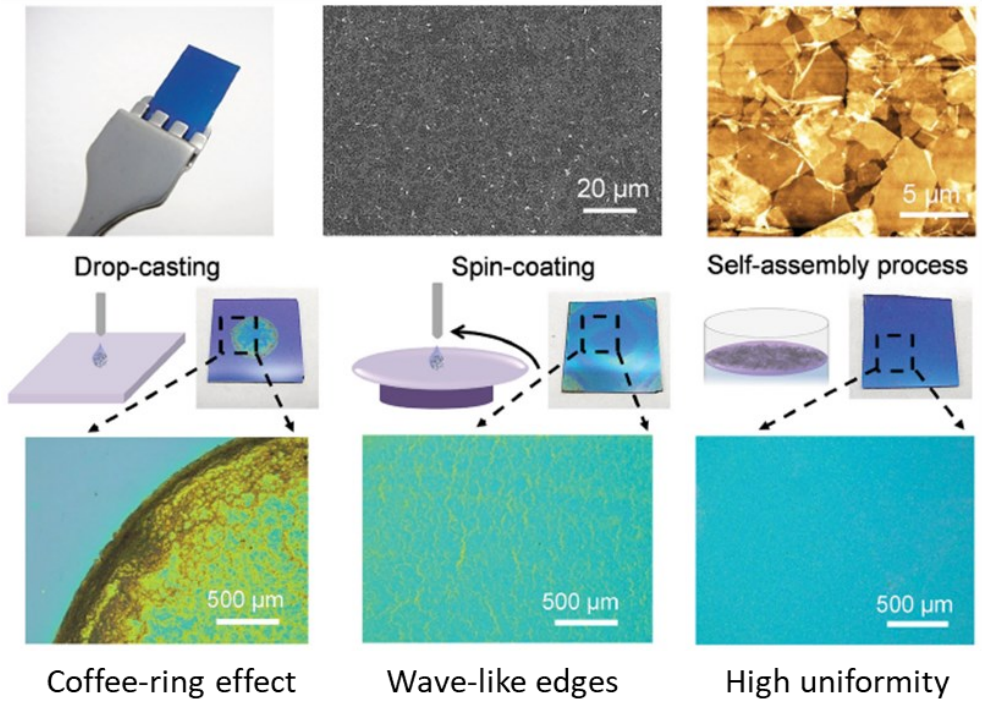

Figure 22: Comparison of three main cost-effective methods for graphene synthesis: drop-casting, spin-coating, and self-assembly. Adapted from [51].

The mass concentration of flakes in the ethanol solution affects the compactness and uniformity of the graphene layer thus produced. Li et al. proved that 1 mg/ml is the minimum concentration of flakes to have a continuous graphene sheet. Lower concentrations make the UGF defective and porous, whereas higher concentrations are useless because, once the whole DI water surface is covered in graphene and the maximum compactness is reached inside the film, the excess of flakes remain suspended in the bath without altering the thickness of the UGF (Li & al., 2016).

The graphene sheet floating on the DI water bath can now be transferred onto a substrate. The process is here similar to the transfer process of CVD graphene sheets. The sample is immersed into the DI bath so that the graphene film can adhere to the sample surface, like in water transfer printing techniques. Samples are finally dried (sometimes in an inert gas atmosphere), allowing graphene to grab onto the surface by Van-der-Walls bonding. With this process, it is possible to obtain a multi-layer graphene structure with thicknesses from three to a dozen atomic layers.

The *self-assembled multi-layered graphene* structure thus obtained is sometimes called *percolative graphene,* and it is thought to have good structural uniformity even though it may suffer from clamping-up of flakes due to imperfect binding. The process is much cheaper and easier to carry out than CVD because of the high cost of the experimental equipment and the raw materials of the latter. However, it is more prone to contamination of the carbon structure with other chemical species, and several factors may play a role in the overall quality of the graphene coating, e.g. the size of the flakes, the crystalline quality of the flakes, and the sonication time.

2.2 Review of graphene nano-coatings in sliding contact

The 2D graphene layer has been extensively investigated for the past few years by many authors in the scientific literature [31] for both mechanical and electrical applications. Graphene is ideal for all those applications where it is desired to reduce interfacial wear while preserving extremely high electrical conductivity. It is the case, for instance, of electrical connectors that need to be protected from tribo-oxidation damage due to frequent engaging-disengaging cycles to preserve proper electrical conduction through the connection pair [53].

Penkov et al. [42] collected and revised in their paper many results from the early tribological investigations at the nanoscale and macro-scale of graphene deposited on several substrates. Extensive research has been carried out to investigate the friction mechanism of graphene at the nanoscale, e.g. exploiting AFM (in Lateral Force Microscopy mode) to measure friction with near-atomic resolution. Fewer investigations have addressed graphene nano-coatings for macroscale dry sliding contacts. To the best of the author's knowledge, the essential literature on this topic is represented by the papers referred to below, whose main findings are summarized.

Yildiz et al. [54] tested graphene transferred to a connecting rod journal bearing. They observed that even single-layer graphene could protect the rough substrate surface and reduce macroscale wear even under severe conditions despite a relatively high coefficient of friction compared to the bare material. Especially under higher load, the bare substrate material performed better in friction than the graphene-coated specimen. The maximum wear reduction was

observed under 15N after 250m sliding, where the wear rate was 9 times lower; in the worst case, the wear rate was reduced by 16%.

The authors also compared the results of the macro-frictional tests with the nano-frictional characterization by Lateral Force Microscopy (LFM). The graphene-coated samples showed a stable coefficient of friction equal to about 0.13 regardless of the applied load, whereas the bare substrate showed a progressive decrease of the COF under applied normal loads from 5 to 30 nN. Graphene-coated specimens exhibited better frictional behaviour, up to 10 nN, whereas friction was lower for the uncoated journal bearing under the highest loads. Table 1 lists the main testing parameters of the tests conducted by Yildiz et al.

Table 1: Testing parameters from **[54]**

Contact mode	**Lateral force microscopy**	**Pin-on-disk**
Deposition method	CVD (Copper foil 20um)	
Substrate	Bearing steel	
Load	5 to 30 nN	10, 15, 30 N
Speed	10 μm/s	2.8 m/s
Temperature [°C]	25	25
Sliding distance	n.d.	250 to 700 m
Track radius /stroke	10 mm	n.d
Sphere diameter	-	Steel, 10 mm
Maximum Hertzian Contact pressure		n.d.

Won et al. [45] investigated the effect of growth time on the CVD process to synthesize graphene at atmospheric pressure on polycrystalline Cu substrates. Interestingly, they reported that the growth time does not significantly affect the

maximum number of graphene layers, and a longer growth time increases the spatial uniformity of the coating.

The friction and wear characteristics of graphene-coated copper were investigated at the microscopic scale, and the results proved that a graphene coating of a few layers could protect the substrate from wear and reduce friction in dry sliding. Table 2 presents the parameters of the friction tests carried out by the authors. Graphene-coated specimens showed a stable friction coefficient of approximately 0.18 up to several thousand sliding cycles. The eventual failure of the coating occurred due to the degradation of graphene to amorphous carbon. Traces of amorphous carbon were found inside the wear track at the end of the test. Moreover, the coating lifetime was well correlated with the initial uniformity and the amount of defect in the graphene layer.

Table 2: Testing parameters from **[45]**

Contact mode	**Pin-on-disk**
Deposition method	CVD
Deposition time	5, 10, 15, 20 min
Substrate	Polycrystalline Copper substrate, 1 mm thick
Load	20 mN
Average Speed	1 mm/s
Temperature	25 °C
Sliding cycles	9000
Stroke	1mm
Sphere diameter	Steel, 1.6 mm
Maximum Hertzian Contact pressure	220 MPa

Berman et al. [55] investigated how solution-processed multi-layer graphene (SPG) can affect the tribological behaviour of steel. A series of experiments were conducted to test the wear and friction behaviour of graphene-coated steel against steel in humid air, graphene-coated steel with a supply of droplets of SPG at the tribological interface, and graphene-coated steel lubricated by the ethanol-graphene solution bath. In ambient air tests, a continuous graphene supply is needed to maintain a graphene film inside the wear tracks. The supply of droplets of the graphene-rich solution to the interface revealed the most effective method to extend the duration of the nano-coating. In this condition, the wear loss of steel surfaces was reduced by 3 orders of magnitude and friction was reduced by 6 times. Table 3 resumes the testing conditions of pin-on-disc tests.

Raman spectroscopy indicated that the presence of graphene suppressed the iron oxide peak. A passivation effect was attributed to the graphene layers, which reduced tribo-corrosion and provided easy shearing at the contact points of asperities.

Table 3: Testing parameters from **[55]**

Contact mode	**Pin-on-disk**
Deposition method	solution processing (SPG)
Substrate	Steel 440C
Load	2 N
Speed	9 cm/s
Temperature	25 °C
Sliding distance	190 m
Stroke	1mm
Sphere diameter	Steel 440C, 9.5mm
Maximum Hertzian Contact pressure	341 MPa

In another paper, **Berman et al.** [39] compared the performance of stainless-steel substrates coated by single-layer graphene (SLG) synthesized by CVD and solution-processed multi-layer graphene (MLG). Both types of graphene drastically reduced friction and wear rate in a hydrogen environment; monolayer graphene was reported to endure at the interface for as long as 6400 cycles. Their results showed that a single graphene layer could last longer the tearing off action of the counter body in an atmosphere of H_2 than in humid air due to the passivation of dangling bonds corresponding to defects of the graphene structure.

Shi et al. [56] investigated the combined effect of graphene coatings and surface texturing with M2 steel. They claimed that the friction-reducing effect of graphene was enhanced by surface texturing. Grooves covering 35% of the specimen area were particularly effective in the presence of graphene. The friction coefficient was stable at about 0.22 for 1400 s when the specimens were prepared with grooves covering 35% of the surface area. For comparison, the bare M2 steel surface with equivalent grooves covering ratio showed low CoF only for 180 s. The wear resistance was also significantly improved, with an 80% reduction in the wear rate. The main testing conditions are summarized in Table 4.

Table 4: Testing parameters from **[56]**.

Contact mode	**Pin-on-disk**
Deposition method	solution processing (SPG)
Substrate	M2 steel Texturing with grooves of 140 µm width, 2–3 µm depth, 14% - 35% - 56% coverage
Load	0.5 N
Speed	3 mm/s
Temperature	25 °C
Sliding time	4000 s

Stroke	3 mm
Sphere diameter	AISI 52100, 4mm
Maximum Hertzian Contact pressure	680 MPa

Surface analysis revealed that the microgrooves could play as reservoirs for the solid lubricant and promoted the stacking of graphene along the sliding direction in the form of an amorphous matrix. This protective carbon layer prevented steel from coming into direct contact with the counter body during the sliding process.

Bhowmick et al. [57] investigated the role of humidity in reducing the sliding friction of multilayered graphene deposited on Ni substrate sliding against a Ti–6Al–4V sphere. Table 5 reports the main testing conditions of pin-on-disc tests. The tests conducted in a dry N2 atmosphere produced the highest CoF (0.52) and the most unsteady friction curve. The CoF was significantly reduced when the same tests were conducted in an air atmosphere. The higher the humidity, the lower the CoF observed, equal to 0.18 with 10% RH and 0.11 with 45% RH on average.

The authors hypothesized that defects in the carbon structure were introduced because of sp^2 to sp^3 hybridization due to graphene amorphization. Amorphization could be, in turn, promoted by the chemisorption of H and OH molecules by the C atoms and the formation of C–H and C–OH bonds during sliding. Raman and XPS analyses revealed that friction reduction was possible because some material with an amorphous structure transferred to the counter face.

In the works of **Mura et al.** [52], [49] single-layer CVD graphene was compared to graphene produced by the self-assembly method presented in Section 2.1.3. Graphene layers were deposited on steel and polymer substrates. The results of these papers showed that highly defective multi-layer graphene produced with cost-effective self-assembly methods usually outperform high-quality and high-purity CVD graphene in terms of tribological performance.

Table 5: Testing parameters from **[57]**.

Contact mode	**Pin-on-disk**
Deposition method	Commercial graphene on 0.5 Ni foil (CVD)
Substrate	Ni foil glued to steel holder
Load	1 N
Speed	0.05 m/s
Temperature	25 °C
Humidity	0% (Nitrogen), 10%, 32%, 45% RH
Sliding cycles	1000
Sphere diameter	Ti-6Al-4V, 4mm
Maximum Hertzian Contact pressure	n.d.

Chapter 3

Tribological characterization of graphene nano-coatings

Among the materials used as solid lubricants and low-friction coatings, graphene has drawn interest for mechanical and electrical applications since it was first isolated by Novoselov—[58]. Traditional low-friction coatings have many advantages compared to fluid lubricants, but troubles may arise when applied to electrical components like connectors or switches. Many of them are insulating materials, such as ceramics or polymer composites, and their presence would impair the fundamental function of the systems to conduct electricity. Efforts are being made to develop conductive low-friction and hard coatings to improve tribological properties and reduce wear in electrical devices without impairing their conductive properties [59]. Graphene is prone to exhibit low shear stress at the contact interface, like graphite, and it is also expected to be well suited for electrical applications thanks to its extremely high electrical conductivity.

Multilayer graphene coatings are similar to graphite except for their thickness. Also, the mechanism by which the graphene acts as lubricant is similar to that of graphite. However, experimental evidence showed that graphene and graphite disclose different tribological behaviour in humid air and dry environments. Graphite achieves the highest performance in a humid environment because the intercalation of water molecules between the carbon sheets allows easy shearing of graphite and provides low friction. Additionally, previous tribological studies

indicated that a mechanism unique to graphite is the formation of graphite scrolls favourable for decreasing the surface energy of the interface [60]. Berman et al. [31] showed that graphite powder exhibited higher friction anwear losses in dry nitrogen than in a humid atmosphere, while graphene performed significantly better in humid air and dry nitrogen environments.

In the family of graphene-based materials, chemically modified graphene structures, namely, graphene oxide (GO) and reduced graphene oxides (rGO), have been investigated too. GO contains oxygen-based functional groups in the carbon lattice, whereas reduced graphene oxide is a nearly pure carbon structure like graphene. Monomolecular sheets of GO can be produced by treating bulk graphite with strong oxidizers; the presence of these functional groups affects the properties of the nano-layer, for instance, its solubility in solvents which is higher than graphene even with high concentrations, and electrical conductivity, which is poorer than graphene.

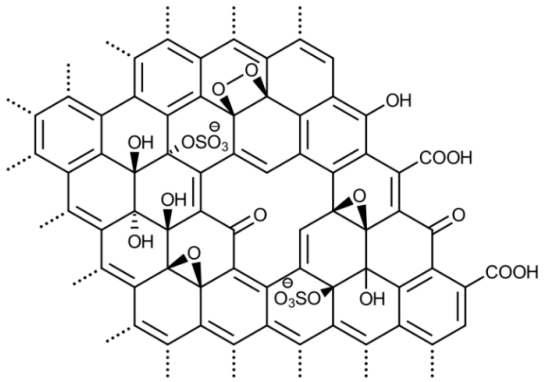

Figure 23: Example of the chemical structure of GO where the carbon lattice is disrupted by heteroatoms, i.e., oxide-based functional groups. From [61].

GO can be reduced to rGO, i.e., the reduced form of monomolecular graphene oxide sheets, to produce nearly-pure graphene sheets. Reduction of GO to rGO is regarded as a more effective and cheaper method than those presented in Section 2.1, which exploit graphite as the source material to produce graphene. Although rGO has a virtually identical structure to pure graphene, it usually contains more defects and is of lesser quality. There are several ways to reduce graphene oxide; the most important techniques are thermal, chemical, or electrochemical methods. Chemical methods allow to better scale-up the production of graphene sheets or flakes. The reduction process has a crucial role in determining the properties and quality of the product.

Similar tribological behavior was observed for GO and rGO at the macroscale and based on a similar lubrication mechanism. Studies carried out at the nano-scale and micro-scale indicated a different mechanism at play for GO and rGO compared to pure graphene, whose understanding is still limited. In both cases, the experimental results [31] confirmed that graphene oxide might also be used to lubricate steel with friction lower than 0.2. However, the wear rate is 1–2 orders of magnitude larger than that for unmodified graphene. This difference was attributed to the worse two-dimensional coverage of the substrate by GO compared to graphene and the oxygen presence that may cause steel corrosion.

In this research work, technically pure copper and aluminium alloy were used as substrates to investigate the tribological performance of different kinds of graphene coating by deposition methods. This research did not consider GO and rGO due to their poorer electrical properties. Copper and Aluminum substrates were selected because there are commonly used materials for mechanical and electrical purposes and electromechanical applications. Graphene nano-coatings were synthetized according to the deposition methods presented in Sections 2.1.2 and 2.1.3. The aim is to compare the performance of the different nano-coatings to identify the most promising one for those industrial applications where improved friction and wear behaviour are required. Among the others, the performance of a APCVD graphene layer directly grown on a bulk thick copper substrate was explored. This kind of sample preparation has been explored so far only by Pham et al. for a dielectric substrate [48] and Mura et al. for a steel substrate [49].

As indicated by Berman et al. [31], a few research works in the scientific literature have investigated the tribological properties of graphene-coated systems at the macroscale compared with miniaturized scale and nano-scale investigations. For this reason, a standard tribological test method was selected to explore the effect of graphene on sliding friction and wear.

3.1 Materials and methods

The graphene-coated samples were prepared and inspected at the Research Laboratory of Electronics (Massachusetts Institute of Technology, USA). Tribological testing was conducted in the Laboratory of Mechanics (DIMEAS, Politecnico di Torino).

Figure 24: Hot wall furnace for CVD at MIT Laboratories.

The furnace used for the deposition of the LPCVD graphene film is shown in Figure 24. Except for the case of direct deposition on the copper substrate, a copper foil was used as a catalyst element. A layer of ethylene-vinyl-acetate (EVA) was deposited onto the graphene layer as a support layer for transfer to the end sample. The copper foil was etched and rinsed away with DI water. The EVA/graphene layers were transferred to the end surface and heated at 80 °C into nitrogen for one hour to let graphene grab onto the metallic surface. The thin EVA film was eventually removed by rinsing with xylene [50].

As to self-assembled graphene films, graphene flakes were prepared by electrochemical exfoliation from bulk graphite. Flakes were collected by filtration and dispersed in dimethylformamide. The solution was then centrifuged to remove side products and thick graphite particles and get high-quality flakes. Centrifuged flakes are re-dispersed in ethanol with a mass concentration of 1 mg/mL, and the solution is dropped into DI water with a syringe. An Ultrathin Graphene Film (UGF) is formed by a self-assembly process on the DI water surface, and assembly is facilitated by sonicating the solution. Two sonication times were used, i.e., 3 hours and 6 hours. The UGF was transferred onto the end samples by immersion into the DI water solution, and the samples were dried at 75 °C for 1h to let graphene grab onto the surface. The process is schematized in Figure 25.

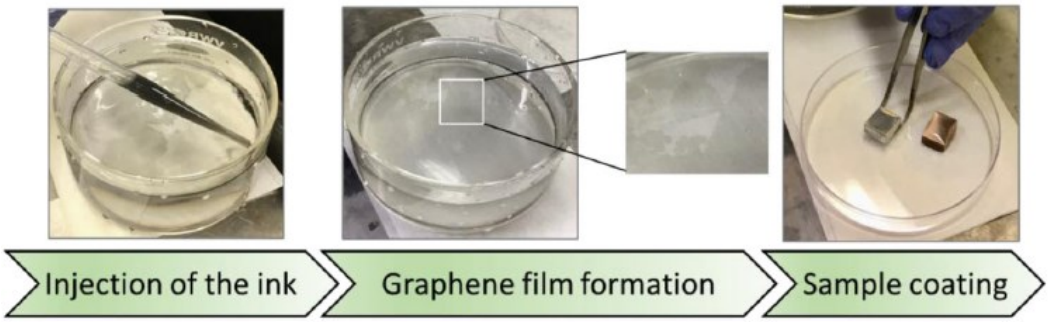

Figure 25: Self-assembly process to prepare a graphene sheet from an ethanol solution with suspended graphene fakes. Adapted from [50].

The tribological tests were performed in ambient air with a TRB pin-on-disc tribometer from Anton Paar TriTec (Corcelles, CH) against 6mm AISI 52100 steel spheres for bearings. Pin-on-disk setup complies with the ADTM G99 standard [62]. Unidirectional rotating wear tests run with constant speed, and the friction coefficient (CoF) was recorded throughout the tests. Figure 26 shows the tribometer used to conduct the tests in the Laboratories of Mechanics (DIMEAS). The load and speed selected for the tests aimed to avoid overload of the substrate material and excessive shear stress on the graphene layer. Detailed information about testing conditions is reported in Sections 3.2.2 and 3.3.2.

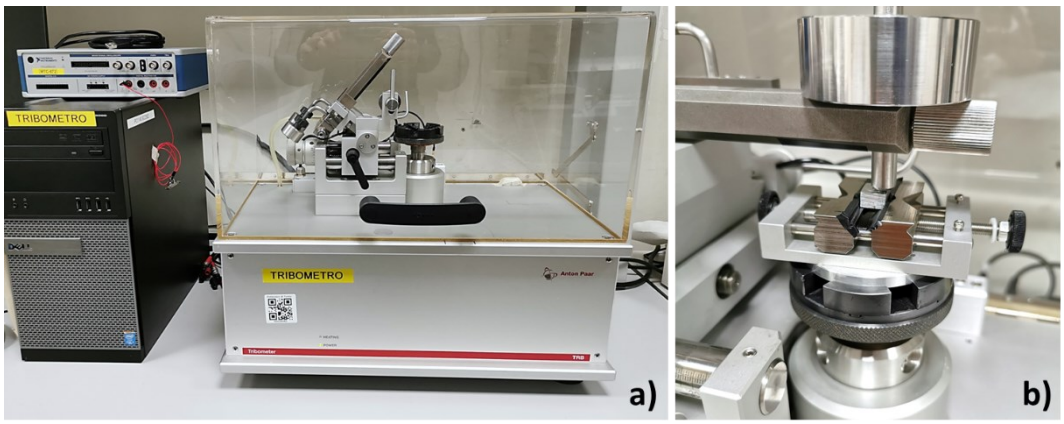

Figure 26: (a) Anton Paar TRB tribometer at Laboratories of Mechanics (DIMEAS); (b) test setup to perform rotating pin-on-disk wear test with graphene-coated aluminium and copper samples.

3.2 Aluminum samples

3.2.1 Coating deposition and spectroscopic inspection

The material selected for the substrate was the Al6082 aluminium alloy known by the trade name *Anticorodal*. The chemical composition and nominal mechanical properties are reported in Table 6. Samples of about 12x12mm^2 area and 5mm thickness were cut from a square bar and coated with graphene. Samples were polished before the coating deposition to achieve a high surface finish with an average surface roughness of Ra 0.22 um and cleaned in an ultrasonic bath. Three kinds of graphene-coated aluminium alloy samples were tested, and one sample was prepared for each graphene coating.

- 1 sample was coated with a high-purity graphene sheet synthesized by LPCVD and transferred onto the sample.
- 1 sample was coated with a self-assembled graphene layer after 3 hours of sonication in the DI (see Section 2.1.3), referred to as 3h-sonicated.
- 1 sample was coated with a UGF graphene after 6 hours of sonication, referred to as 6h-sonicated

Table 6: Nominal technical specification of Al6082

Chemical composition

Cu	Fe	Mn	Mg	Si	Zn	Cr	Ti	Al
0.1 %	0.5 %	0.4 - 1 %	0.6 - 1.2 %	0.7 - 1.3 %	0.2 %	0.25 %	0.1 %	Balance

Mechanical properties

Tensile strength	Yield strength	Elongation at break	Specific weight	Elastic modulus	Hardness
275-310 MPa	230-260 MPa	4-10 mm	2.71 kg/dm^3	69 GPa	81 HV/0.5

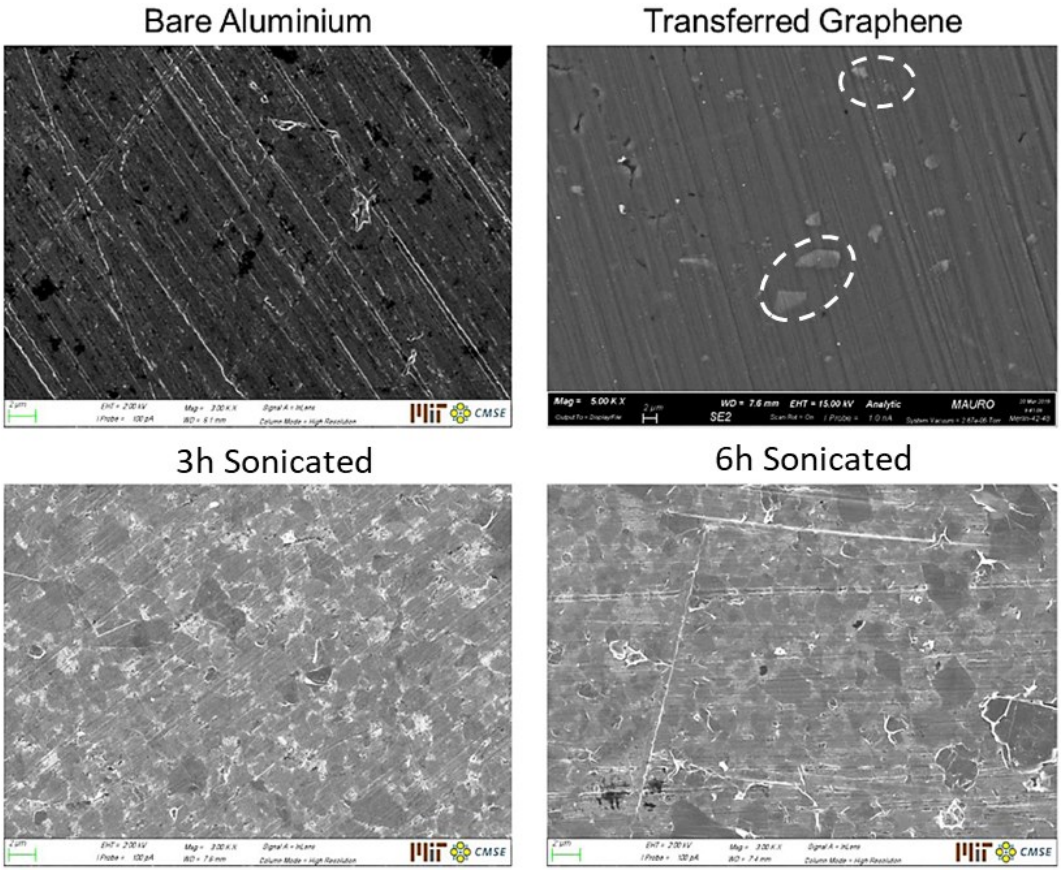

Figure 27: SEM images of the sample surfaces before tribological tests. From [50].

The three coated samples were inspected by SEM and Raman analysis to check the coating quality and the degree of coverage of the substrate. Figure 27 shows the SEM images of the samples before the tribological tests. Transferred graphene is barely visible on the surface of the aluminium substrate because of its atomically thin thickness, which makes the graphene layer nearly transparent [63]. The nano-coating appears uniform except for some regions of localized higher thickness, probably due to folds or contaminations from the transfer process. The two self-assembled coatings appear as a patchwork, and the borders of the graphene nanoplatelets stitched together are evident in the high-magnification images. The UGF results as a continuous layer after 3h of sonication and 6h of sonication, as confirmed by the Raman analysis. Some agglomerations of graphene flakes are visible in the image of the 6h-sonicated coating, i.e., darker patches where the flakes rolled up and clumped together during the assembling process.

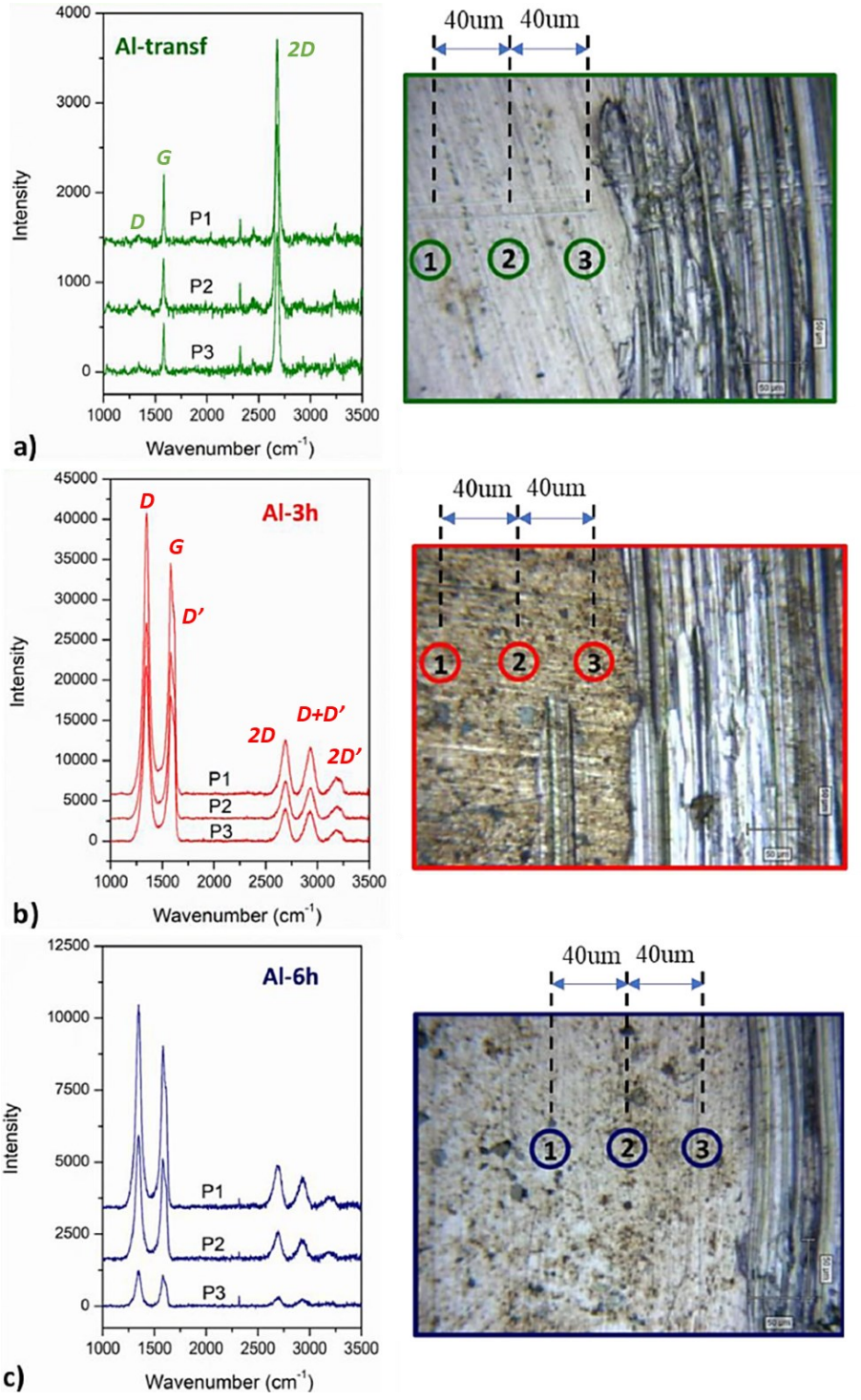

Figure 28. Raman spectra were collected on the surface of the three coated samples in different positions. (a) Aluminium with transferred CVD graphene; (b) Aluminium coated by 3h-sonicated graphene. (c) Aluminium coated by 6h-sonicated graphene. The optical images show the corresponding points where the spectra were collected. From [50]

Raman spectroscopy was performed at DISAT Laboratories (DISAT, Politecnico di Torino) through a Renishaw InVia Reflex micro-Raman spectrometer (Renishaw plc, Wottonunder-Edge, UK). A cooled CCD camera was coupled to the Raman spectrophotometer for combined spectroscopic and microscopic inspections. The Raman source was a green-light diode laser (λ = 514.5 nm), and the inspection was carried out through a 20X microscope objective in backscattering light collection mode. The excitation parameters were 20 W of laser power, 10 s exposure time and 1 accumulation. The micro-Raman spectrometer allowed different regions of the samples to be inspected, and still coated areas could be distinguished from areas where coating failed due to the tribological interaction. The combined spectroscopic and optical evaluation was performed by collecting three spectra in 3 different points (P1, P2 and P3) 40 µm apart along a straight line to assess the uniformity of the coating coverage. Figure 28 shows the Raman spectra acquired at the investigated areas, highlighted by circles in the optical images. If some inhomogeneity in the surface coverage is present, it should be revealed by comparing the shape and position of the peaks in the spectra acquired in a different position on the same sample.

A sharp G peak at 1581 cm^{-1} and a narrow 2D peak at 2679 cm^{-1} with a high-intensity response indicated that the transferred graphene coating is a uniform ultra-thin sheet with the typical hexagonal crystalline lattice of graphite. The integrated peak ratio I_{2D}/I_G close to 3 confirmed that single-layer graphene was obtained [41] [64]. The overall quality of this graphene layer was relatively high because the D peak at 1339 cm^{-1} was hardly discernible, which is a sign of disorder and defects in the graphene structure when its intensity is high [65].

The red and blue diagrams in Figure 28b and Figure 28c are the typical spectra given by highly defective multilayer graphene structures originating from the self-assembly of flakes [66]. In these spectra, additional peaks appeared, i.e. D, G, D', 2D, D+D' and 2D' peaks positioned at 1350 cm^{-1}, 1583 cm^{-1}, 1614 cm^{-1}, 2694 cm^{-1}, 2932 cm^{-1} and 3187 cm^{-1}, respectively. The prominent D-peak confirmed that these nano-coatings had highly disordered structures, as expected by the imperfect assembly of the graphene flakes. The integrated peak ratio I_{2D}/I_G is between 0.2 and 0.3 for the 3h-sonicated and 6h-sonicated UGF, suggesting that MLG originated [50]. The Raman analysis also shows that the amount of graphene agglomerations increased with increasing the sonication time. The peak of the 2D-band was weaker on average for the 6h-sonicated UGF compared to the 3h-sonicated one.

The three spectra being compared were qualitatively similar for every sample, thus providing evidence that the coverage of the nano-coating was uniform. Just for the 6h-sonicated graphene, a variation in the peak intensity was observable in different positions of the sample, which correlates to the higher variability in the thickness of the multi-layered graphene structure. The roll-up and clustering of the graphene flakes likely caused this poor uniformity.

3.2.2 Pin-on-disc tests

The parameters of the pin-on-disc tests are summarized in Table 7. Three tests were performed overall on each sample. Two long-term tests were performed at two different radial positions (2.3 mm and 4.5 mm radius). The tiny dimensions of the samples and the width of the wear tracks prevented running more rotating pin-on-disc tests with each sample.

Table 7: Testing parameters of the three pin-on-disc tests carried out with each graphene-coated aluminium sample.

	Long-term tests	Short-term test
Wear track radius [mm]	2.3 mm, 4 mm	3.4 mm
Load [N]	5	5
Speed [mm/s]	50	50
Sliding distance [m]	30	Up to coating failure
Sampling [Hz]	100	100

Tribological tests were also performed on one more bare aluminium sample to have a benchmark for the tribological performance of the substrate. The corresponding average Hertzian contact pressure at the beginning of the test was 565 MPa, calculated via the *HertzWin* free software considering the effect of roughness on the contact stress state (Ra 0.09 µm for the steel sphere and Ra 0.22 µm for aluminium). One additional short-term pin-on-disc test was performed with the samples coated by 3h-sonicated graphene and 6h-sonicated graphene to

get more insight into the wear behaviour of the system before coating failure (see Figure 30). An unworn location was exploited between the wear tracks of the long-term tests. These additional tests ran under the same load and speed as previous tests.

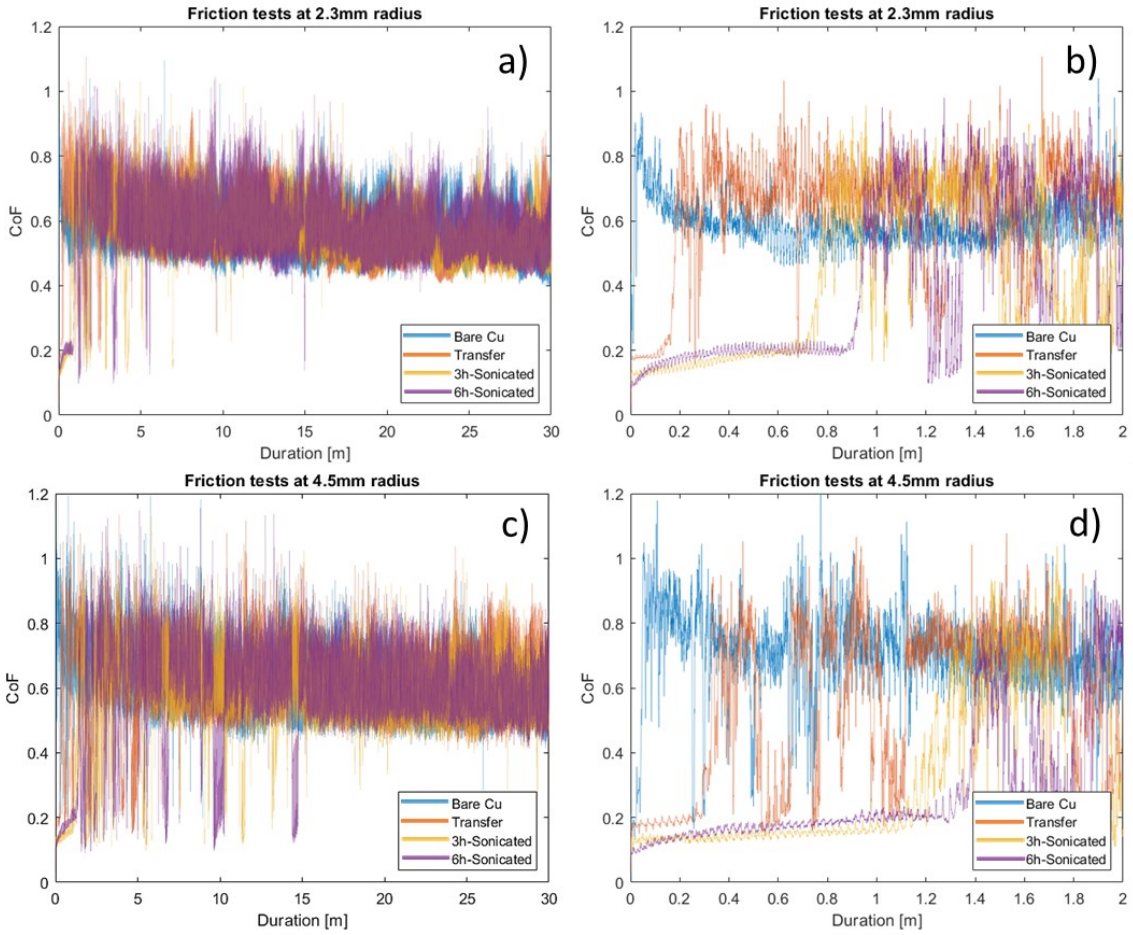

Figure 29**.** Friction curves which were measured during the pin-on-disc tribological test. (a),(c) The signals acquired up to the end of the tests (30m). (b),(d) Zoomed view of the trend in the first 2m of sliding where the coating-to-substrate transition occurs.

Figure 29a and Figure 29c compare the friction curves measured with the four samples at a 2.3 mm and 4.5 mm radius, respectively. The diagram shows that the friction curves are alike for most of the tests, and a peculiar frictional behaviour appears in the first few meters of sliding. Figure 29b and Figure 29d are the zoomed view of the first 2 meters of the tests, which is the most significant part of the tests to understand the beneficial effect of these graphene nano-coatings.

All the friction curves measured with the graphene-coated samples featured the same trend in the first few meters of the tests, outlined in Figure 30. At the onset of sliding, the CoF had a relatively low value compared to the uncoated sample, and the curves had a stable trend with low scattering. After sliding a given distance, depending on the coating type and the wear track radius, a transition occurred, and the CoF quickly increased.

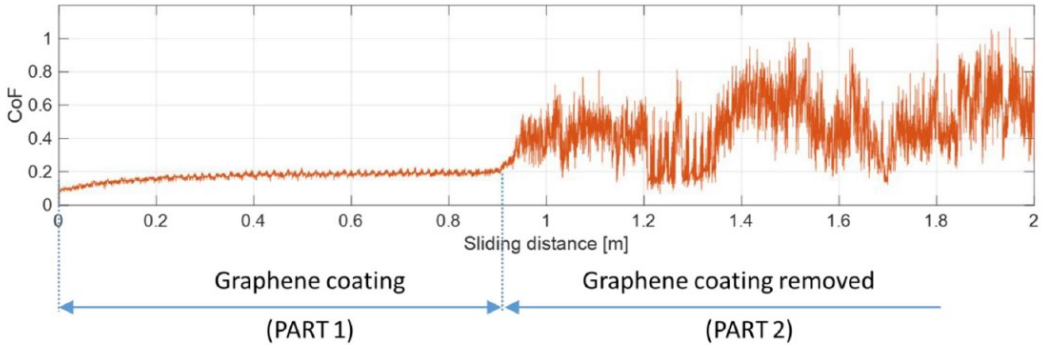

Figure 30. Typical CoF trend in the first few meters from sliding onset measured with the coated sample: in Part 1, the graphene coating is working, and in Part 2, the graphene coating has been removed. From [50].

This transition in the friction curves is likely associated with the graphene coating removal from the sliding path. The scattering and unsteadiness of the signals in Part 2 of the tests made the tribological behaviour very similar to the case where the steel sphere slid over the bare aluminium sample. This evidence proves that the steel sphere directly interacted with the aluminium substrates after the transition.

The CoF averaged over Part 1 and 2 of the two tests per sample are compared in Figure 31 and Table 8. The average CoF value was calculated across the whole test duration. The overall test average and the average related to the Part 2 are very similar, as was expected, because the coating failure occurred just a few meters after the onset of sliding. The results show that the graphene nano-coatings could provide a substantial lubricious effect and strongly reduce friction as far as they withstood the tearing-off effect of the sphere. Figure 31 shows that the CoF dropped from about 0.6 to less than 0.2 in the presence of graphene nano-coatings. The improvement of the frictional performance was attributed to the reduction of shear stress at the contact junctions between surfaces [55] [23]. Interestingly, the three graphene coatings show similar characteristic CoF values. The smallest value corresponded to the 3-hour sonicated coating even though the 6-hour sonicated coating was thicker and thus more protective for the substrate. It may be

due to the higher degree of disorder and unevenness caused by the longer sonication time, according to the results of the Raman analysis (Figure 28).

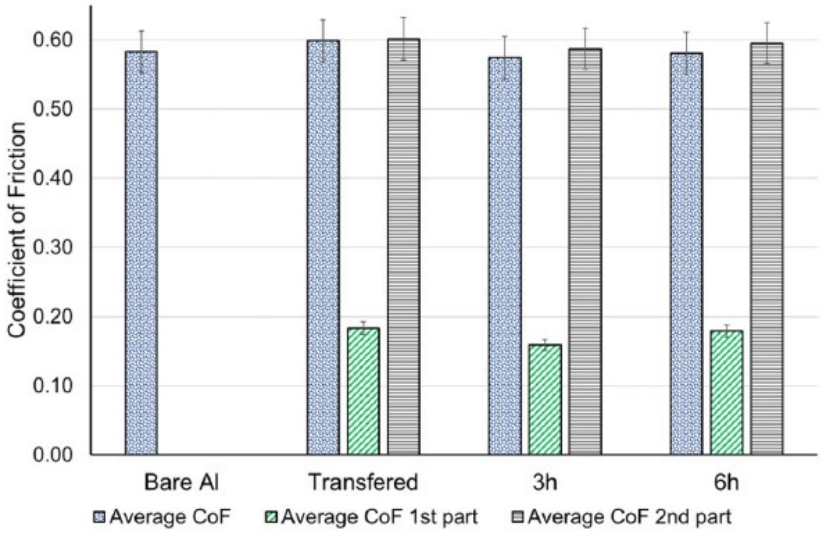

Figure 31. Average values of the CoF in the first and second parts of the tests, according to Figure 30. The average CoF value for the uncoated sample is calculated over the whole test only since no transition was there. From [50].

Table 8: Average CoF values and standard deviations of averages.

CoF	Whole test		Part 1		Part 2	
	Avg	St.Dev.	Avg	St.Dev.	Avg	St.Dev.
Bare Al	0.583	0.030	N.A.	N.A.	N.A.	N.A.
Transfer	0.599	0.032	0.184	0.005	0.602	0.033
UGF 3h-sonicated	0.574	0.007	0.159	0.016	0.587	0.013
UGF 6h-sonicated	0.581	0.006	0.179	0.010	0.595	0.010

Friction curves also provide valuable information to determine the life of each coating, i.e. the distance slid before the coating failure, which is an estimate of their wear strength. Figure 32 collects the average travelled distance at the coating

failure. The number of rotating cycles to failure expresses the coating endurance in the diagram of Figure 32 instead of the cumulated distance. Friction curves from tests performed with increasing track radius are coherently compared only if evaluated against the accumulation of the rotating cycles when the wear damage of the static sphere is negligible compared to that of the rotating samples. In fact, the evolution of the tribological response is driven by how many times the static body slides over any point of the rotating lower specimen.

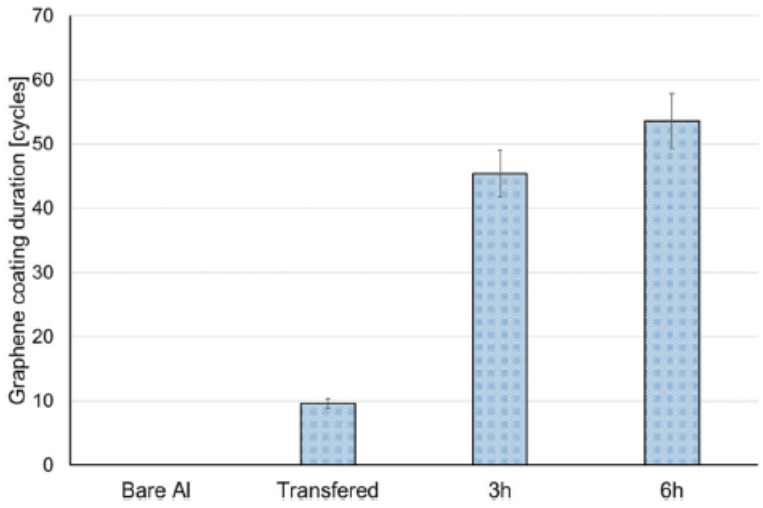

Figure 32**.** The average lifetime of the three-graphene coating in terms of rotating cycles before the transition of the CoF curve. From [50].

The results indicate that the most durable coatings are those prepared by the self-assembly method, whereas the wear strength of transferred graphene is relatively weak. The quality of transferred graphene coating is very high in terms of crystallinity and defectiveness of the carbon sheet (see also Figure 28) with thickness close to the atomic size. The UGFs synthesized by self-assembling flakes have coarse quality form the chemical point of view. The coating structure is more likely to consist of several carbon layers, and each layer is high defective with poor crystalline continuity. However, this relatively thick graphene structure resulted in an enhanced wear strength.

The calculation of the wear volume was carried out as per equation (15) according to the guidelines of the ASTM G99-17 standard, where V is the volume of the removed material, r is the nominal radius of the wear track, and S is the average cross-sectional area of the track.

$$V = 2\pi \cdot r \cdot \bar{S} \tag{15}$$

Wear tracks were profiled in at least eight locations equally spaced to one another with a stylus profilometer (RTP80, SM Metrology System, Volpiano, IT) equipped with a 20 µm tip radius stylus. The standard prescribes at least four cross-sectional profiles to be measured, but high sampling was preferred since the wear tracks looked inhomogeneous along the circumferential direction. $\bar{S}$ is therefore calculated as the average of the cross-section areas underneath the eight wear track profiles. The morphology of the wear tracks was inspected by SEM. Figure 34 shows how the four wear tracks (at r = 4.5 mm) appeared under low magnification. All the wear tracks were strongly uneven and had a similar wear texture composed of large and deep ploughing paths along the sliding direction and protrusions due to material transfer and severe plastic deformation. This peculiar texture, dominated by plasticity, indicated that adhesion was the dominant wear mechanism. Aluminium and steel have a high chemical affinity that easily triggers adhesive phenomena [23]. The presence of craters due to chunks of material transferred to the sphere and large wear debris confirmed adhesion. The high quantity of material transferred onto the sphere surface was also an indicator of adhesive wear. Adhesion and tearing of the adhesive joints are known to increase the flash temperature of asperities because of plastic energy loss so that debris detached from the surface is easily transferred to one of the surfaces. Figure 33 shows one of the wear track profiles acquired after a test with the 3h-sonicated graphene sample. The profile shows a lot of holes and ridges from severe adhesiona and plastic flow.

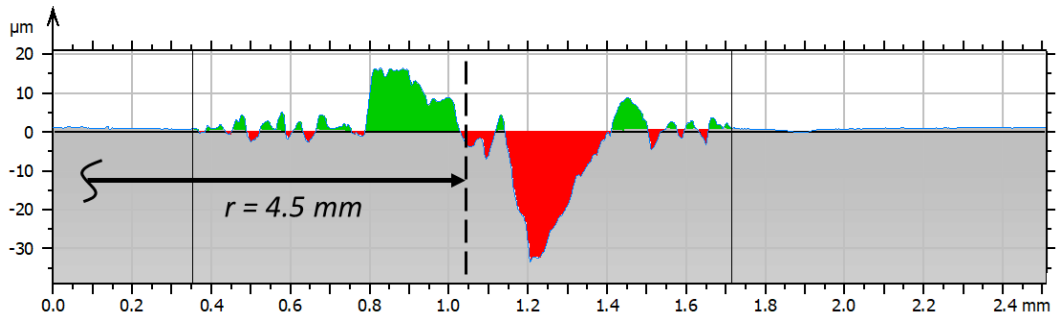

Figure 33. Typical wear track profile recorded by stylus profilometry on the 3h-Sonicated graphene-coated sample.

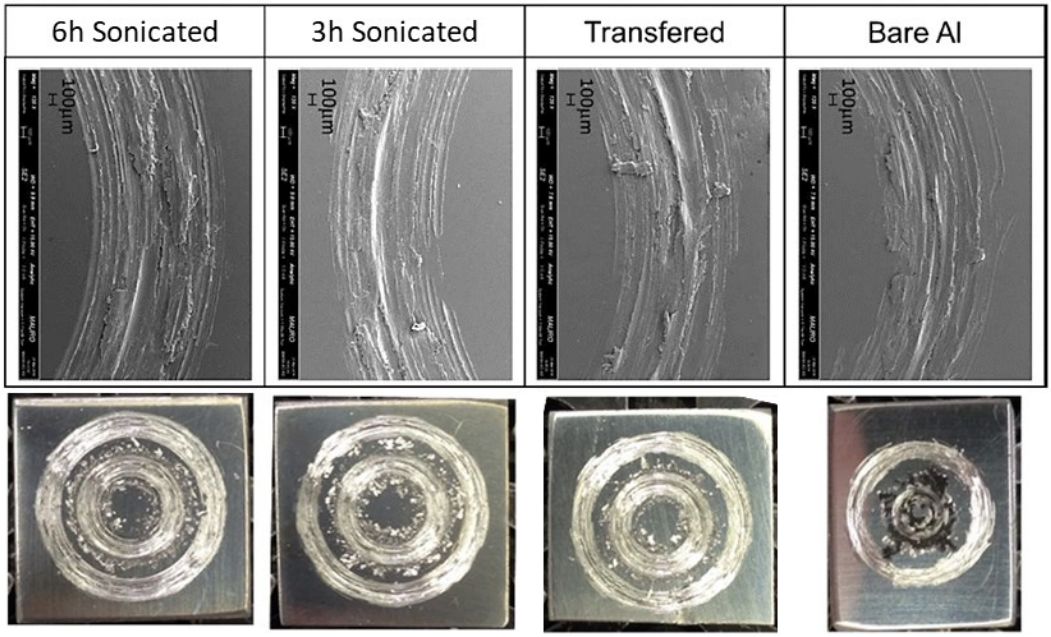

Figure 34. Low magnification SEM images of wear tracks at r =4.5mm and below the appearance of the sample surface after the tribological tests. Adapted from [50].

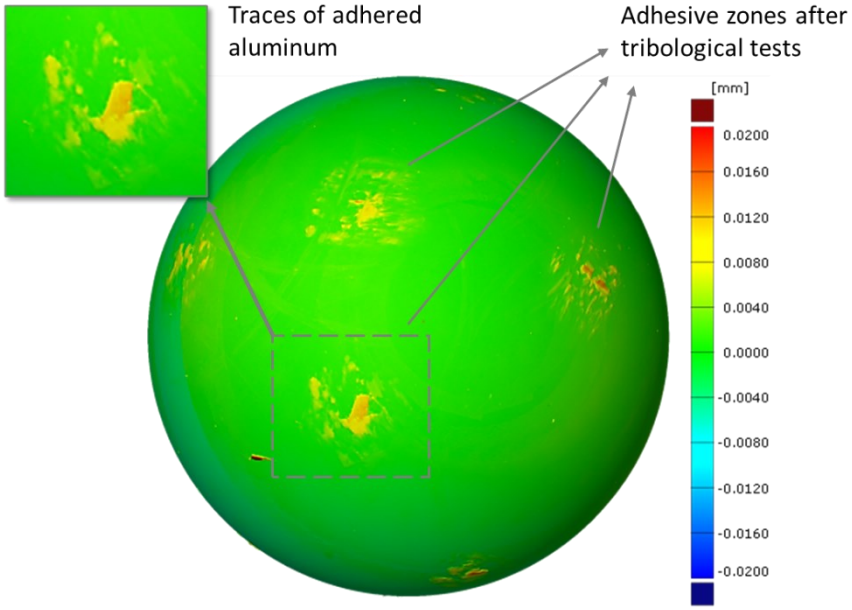

Figure 35. 3D topography and height map of steel sphere after the tests against the graphene-coated aluminium samples. The same sphere was used to perform all the tests and rotated each time to expose a fresh unworn region towards the flat sample. Where the sphere slid against the samples, there is evidence of material transferred from the sample to the sphere.

Being the sphere harder than the aluminium sample, minor damages appeared on the sphere, essentially limited to scratches and traces of transferred material (Figure 35). Therefore, the sphere wearing-out was neglected to determine the total wear volume because the related contribution was not measurable.

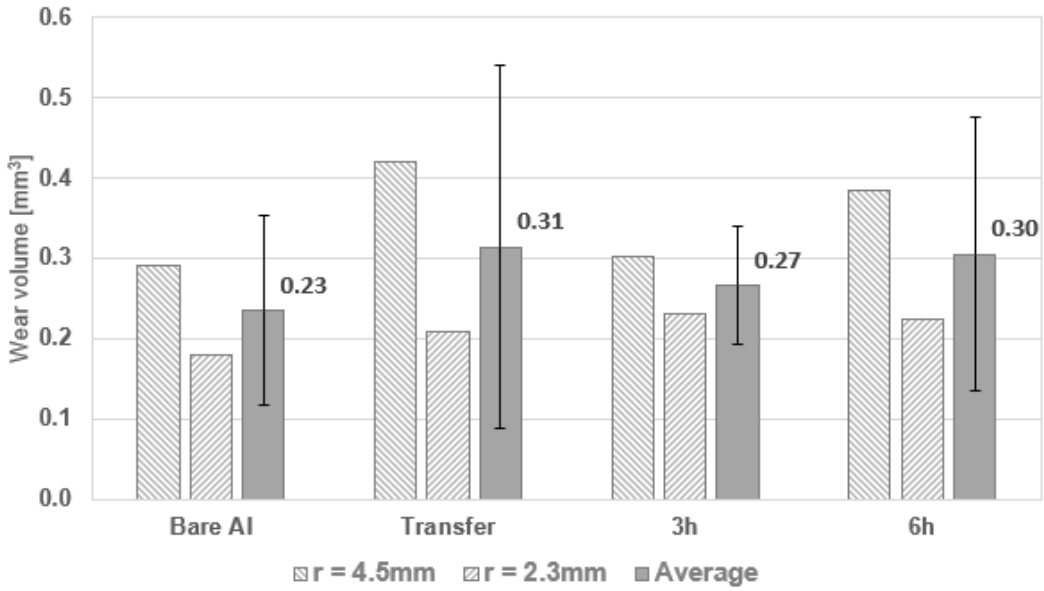

Figure 36**.** Determination of the wear volume for each sample. The error bars are determined as equal to the standard deviation σ. A systematic effect is associated with the wear track radius because the removed material is always higher at r = 2.3mm w.r.t. r = 4.5mm for all the samples.

Figure 36 resumes the wear volumes calculated for each sample. The average material loss of the coated samples is higher than that of the uncoated sample. This phenomenon is hard to explain because earlier evidence of tribological tests in ambient air reported benefits for the tribological system from the presence of graphene also in terms of reduction of the wear volume [52] [49], [67]. However, the increase in the wear volume is not relevant from the statistical viewpoint because the uncertainty bands (the error bars in the diagram) overlap. In addition, it must be considered that the wear volume was measured at the end of 30m sliding tests, and the graphene coating had long been removed by the end of the tests. As the friction curves suggest, the high-lubricity carbon sheet acted only in the first meters of the sliding interaction when it could hold on to the sample surface (Figure 29). Any potential benefits vanished after the transition. Therefore, such early removal might prevent the nano-coatings from bringing about any advantage to total wear volume reduction of the test.

From a detailed SEM inspection, some debris was found inside and outside the wear tracks of coated samples. Figure 37 shows the debris identified on the surface of the three coated samples. The areas identified by the red circles correspond to the magnified view in Figure 37e, Figure 37f, and Figure 37g. It was possible to appreciate the presence of residual graphene layers attached to the debris by zooming on the borders of the particles.

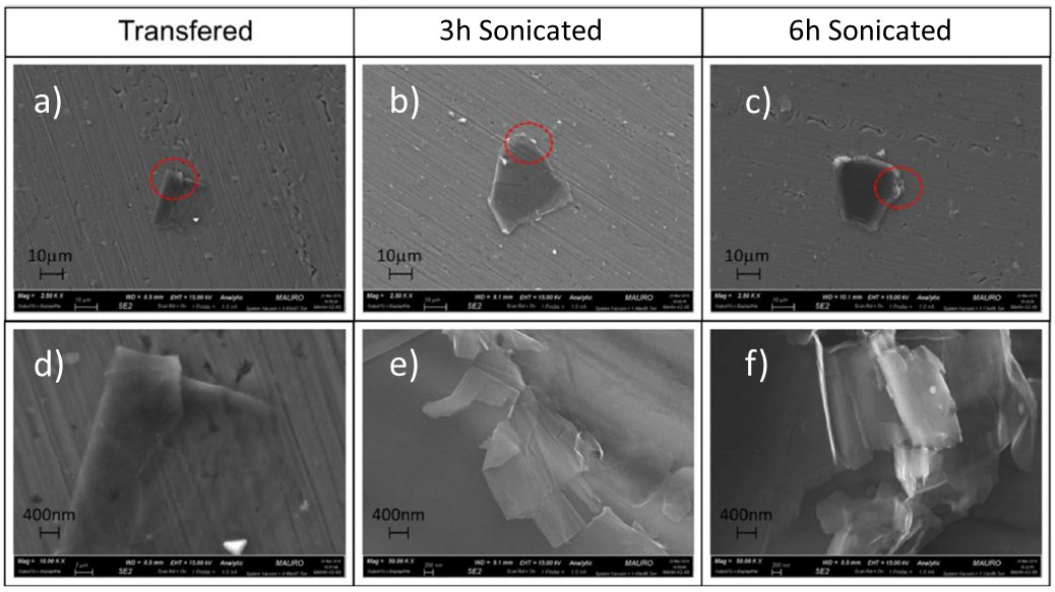

Figure 37**.** Details of debris found outside the wear track. It is possible to appreciate that the debris shows graphene coating. From [50].

To confirm that the transition of the friction curves coincides with the graphene coating failure, a series of Raman spectroscopy was performed inside the wear tracks. Raman spectra inside the wear tracks confirmed that either no graphene or damaged graphene remained inside the wear tracks after the tribological tests. The result reported in Figure 38 showed that the graphene coating removal was inhomogeneous inside the wear tracks. The solid blue lines represent the typical vibrational modes of an area where some remains of a graphene structure still exist. The carbonic structure is a little more defective than the ones lying outside the wear track, represented by the solid black line. This effect is most apparent for the transferred graphene sheet (Figure 38a), where the D peak at 1339 cm-1 appears in the spectrum acquired inside the wear track, whereas for the two self-assembled graphene films (Figure 38b,c), the D peak grows in intensity. The blue-dashed lines are spectra collected in regions where the graphene nano-coating failed. This signal is typically obtained in the presence

of amorphous carbon, the typical residual from graphene sheets detached from the substrate and degraded by mechanical shearing at the sliding interface (Chu & Li, 206).

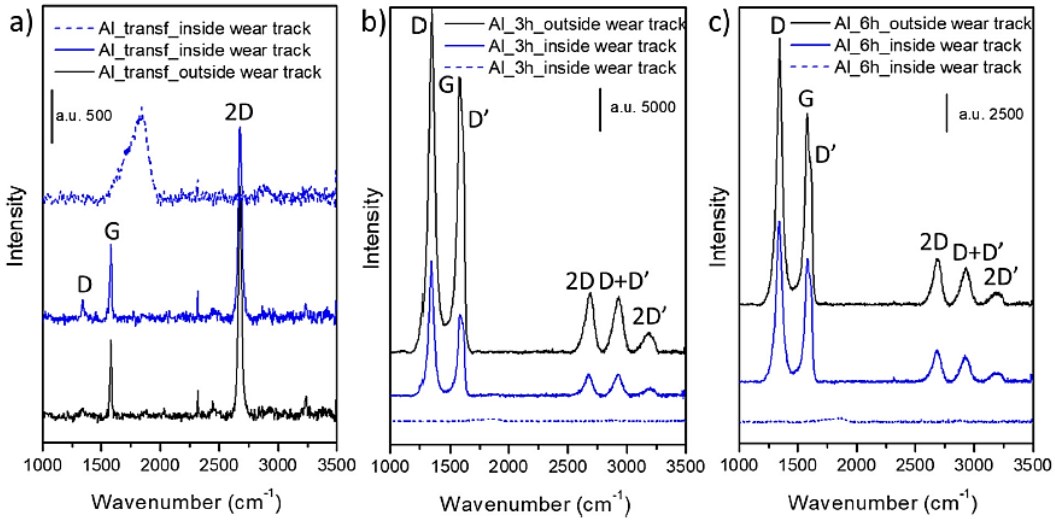

Figure 38**.** Raman spectra were collected inside and outside the wear tracks on the samples coated by transfer graphene (a), the 3h-sonicated UGF (b), and the 6h-sonicated UGF. From [50].

Some additional short-term pin-od-disc tests were performed to get more insight into the wear behaviour of the system before the steep increase of friction (see Figure 30). An unworn location was exploited between the former wear tracks on the samples coated by 3h-sonicated graphene and 6h-sonicated graphene. These additional tests ran under the same load and speed as previous tests but were stopped before the abrupt increase in the friction force. Table 9 summarizes the duration and the primary outcome of these additional tests, and Figure 39 shows the friction curves recorded by the tribometer. The sphere and sample surface were inspected under the optical microscope and profiled to look for traces of wear.

Table 9: Testing parameters of the additional short-term pin-on-disc tests on graphene-coated aluminium samples.

Sample	Track radius	Sliding distance at stop	Average CoF	St.Dev.
3h-sonicated	3.6 mm	0.5 m	0.137	0.016
6h-sonicated	3.4 mm	1.45 m	0.183	0.021

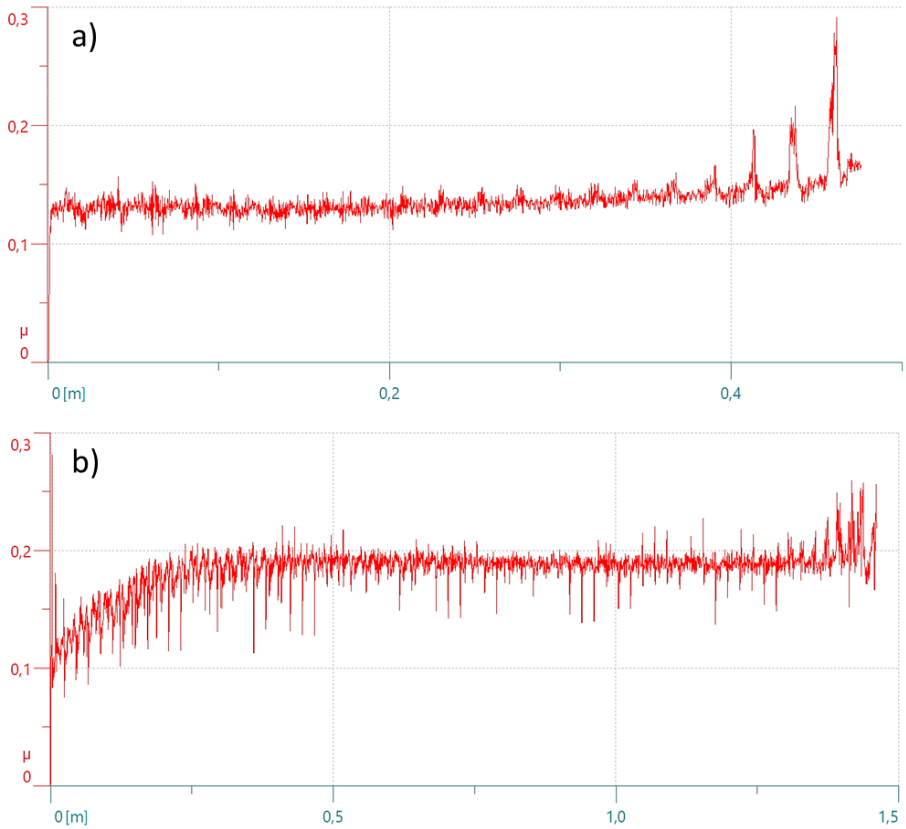

Figure 39. Friction curves were recorded during the two additional wear tests of the nano coating: a) 3h-sonicated graphene and b) 6h-sonicated graphene. Some spikes indicate the onset of adhesion due to graphene coating failure at the end of the test.

Figure 40 and Figure 41 provide the optical microscopic observation of the wear track on the sample and contact site on the sphere. Black matter accumulated inside the contact area before cleaning with acetone, which is likely to be degraded graphene worked with other finer aluminium debris by the shearing action. The sphere disclosed minor damage due to wear. A few scratches were observed on the steel surface and a few shining aluminium debris outside the contact region. Figure 42 shows the sample surface profile taken along a radial direction inside the region where the sphere slid. The sphere carved some grooves, but they are unlikely to be associated entirely with any material loss from the sample. The small amount of debris observed after the tests cannot justify the volume of the grooves at the end of these short tests. Therefore, the grooves are reasonably attributed to plastic flow in the aluminium body, promoted by the combined action of subsurface stress concentration and inhibited surface adhesion with the hard steel sphere. Ridges at the groove sides were another sign of plastic

flow. Their section area (in green in the figure) was almost equivalent to the grooves (in red). These results evidenced that the steel surface and the aluminium substrate were not directly touching during most of the sliding time and that the coting-to-substrate transition coincides with the steep increase in the friction curves. Adhesion was activated only by the end of the test when the coating eventually failed.

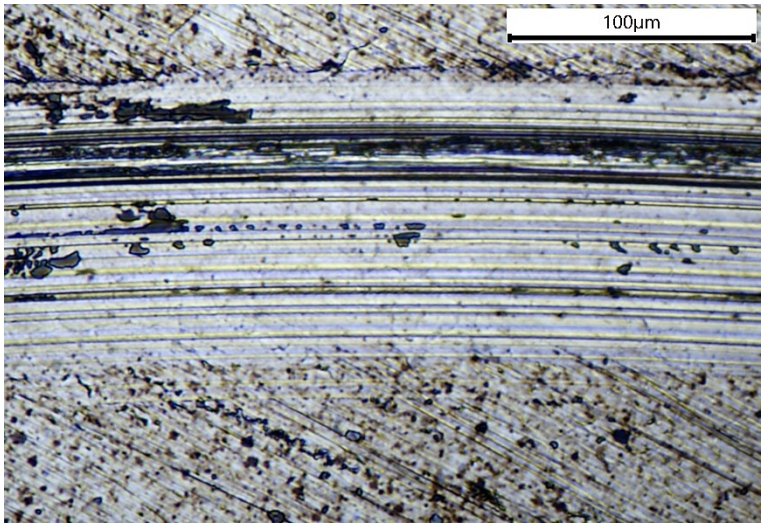

Figure 40**.** Microscopic inspection of the Aluminium sample surface at the end of the short-term wear tests.

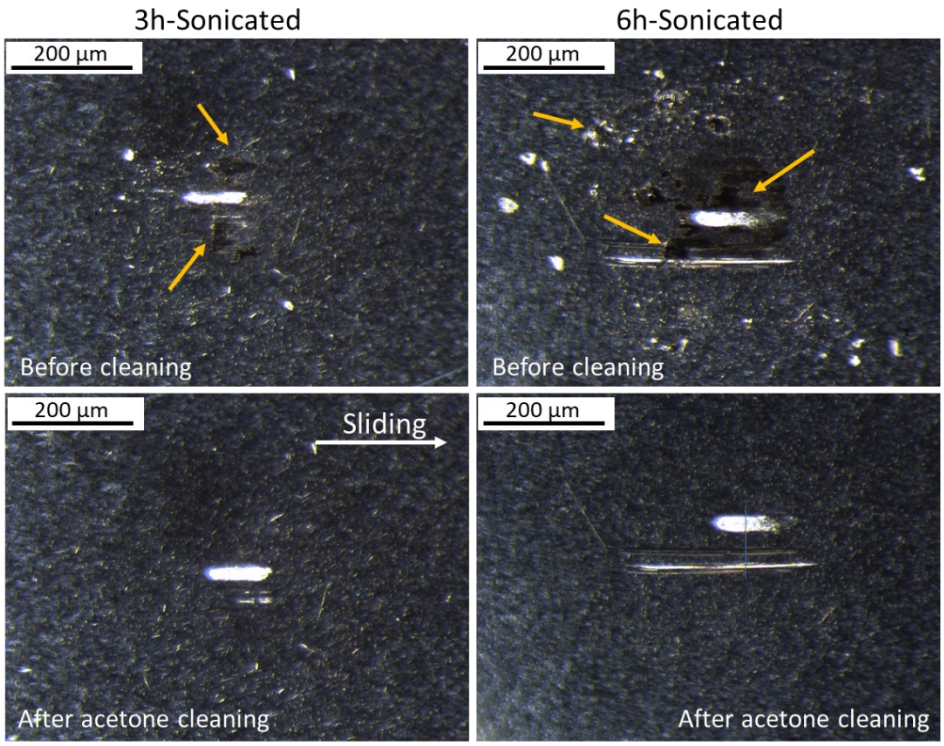

Figure 41. The sphere surface at the end of the short-term wear tests before and after cleaning with acetone. Yellow arrows indicate accumulation of black debris (probably carbon-based matter), shining aluminium debris and individual scratches on the steel surface.

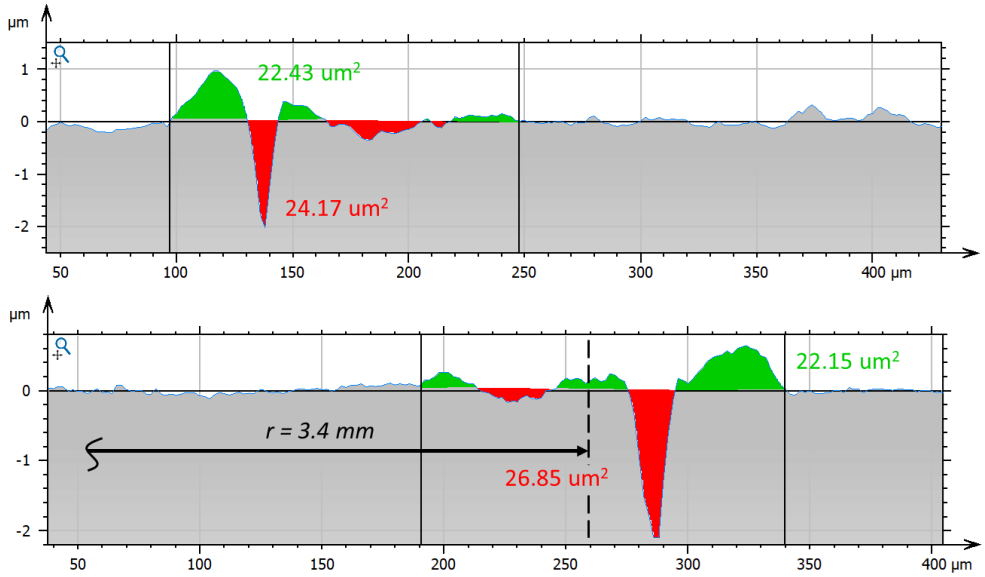

Figure 42. The surface profile of the Aluminum samples at the end of the short-term wear tests: a) 3h-sonicated graphene, b) 6h-sonicated graphene.

3.3 Copper samples

3.3.1 Coating Deposition and spectroscopic inspection

The material for the tribological samples was a technically pure copper Cu-ETP (EN 13599:2014) widely used for electrical purposes. The choice of this copper grade is in line with previous experimental investigations [45] [68]. Table 10 reports the standardized chemical composition of the Cu-ETP copper grade and its mechanical properties. Five rectangular samples of size 12x10 mm2 and about 5 mm thick were cut from a square conductor for electrical cabinets (ItalWeber, Assago, IT) [69]. The surface of the samples was prepared by grinding with sandpaper and polishing with diamond slurries to achieve high planarity and a high surface finish. The average roughness was Ra 0.182 μm.

Table 10: Nominal technical specification of Cu-ETP

Chemical properties			
Cu	**Bi**	**Pb**	**O**
99.90 %	Max 0.0005%	Max 0.005%	Max 0.040%

Mechanical properties					
Tensile strength	**Yield strength**	**Elongation at break**	**Specific weight**	**Electrical resistivity**	**Hardness**
220MPa	160MPa	33%	8.89g/cm^3	0.017μΩ·m	100

Four different type of graphene nano-coating were synthesized and deposited on one sample. Five samples were tested overall, including one bare copper sample to identify the reference tribological behaviour of the substrate.

- 1 sample was coated with graphene directly grown onto the bulk copper substrate by APCVD

- 1 sample was coated with a high-purity graphene sheet synthesized by LPCVD on a *Cu* foil and then transferred to the end copper sample.
- 1 sample was coated by self-assembled graphene flakes after 3 hours of sonication in the DI (see Section 2.1.3), referred to as 3h-Sonicated.
- 1 sample was coated by self-assembled graphene flakes after 6 hours of sonication, referred to as 6h-sonicated

Figure 43a shows the topography of the five samples after preparation and the corresponding value of the 3D areal surface roughness as per ISO 25178. Figure 43b illustrates the appearance of the sample surface under the optical microscope. The significant increment of roughness measured for the sample coated by directly grown graphene is presumably due to the curious globular-like structure observed on the surface of the sample during FESEM analysis (Figure 44a). Some details are provided on this aspect in the following sections.

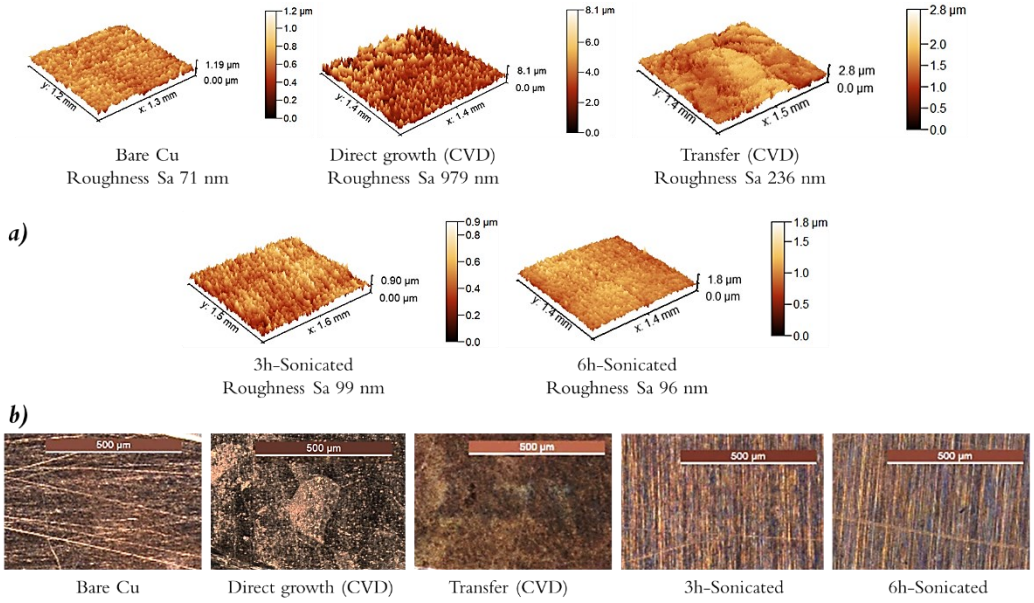

Figure 43. (a) Surface morphology of the samples before the tribological tests. (b) Inspection under the optical microscope of the sample surface before the tribological test. Interestingly, the surface of the samples with direct growth graphene features a pattern of platelets or grains which resembles the morphology of multiplayer CVD graphene on Ni substrate reported by Bhowmick et al. [30]. They are probably crystalline grains of copper after annealing.

The samples were inspected with FESEM (Zeiss, Jena) with an ultra-high-resolution Inlens EsB detector to image the carbon nano-coatings; images are grouped in Figure 44. Except for direct growth graphene, a transparent grainy

structure was perceived on the surface of the sample through which one can see the roughness pattern of the substrate surface. It corresponds to the ultra-thin layer of sp^2-bonded carbon atoms.

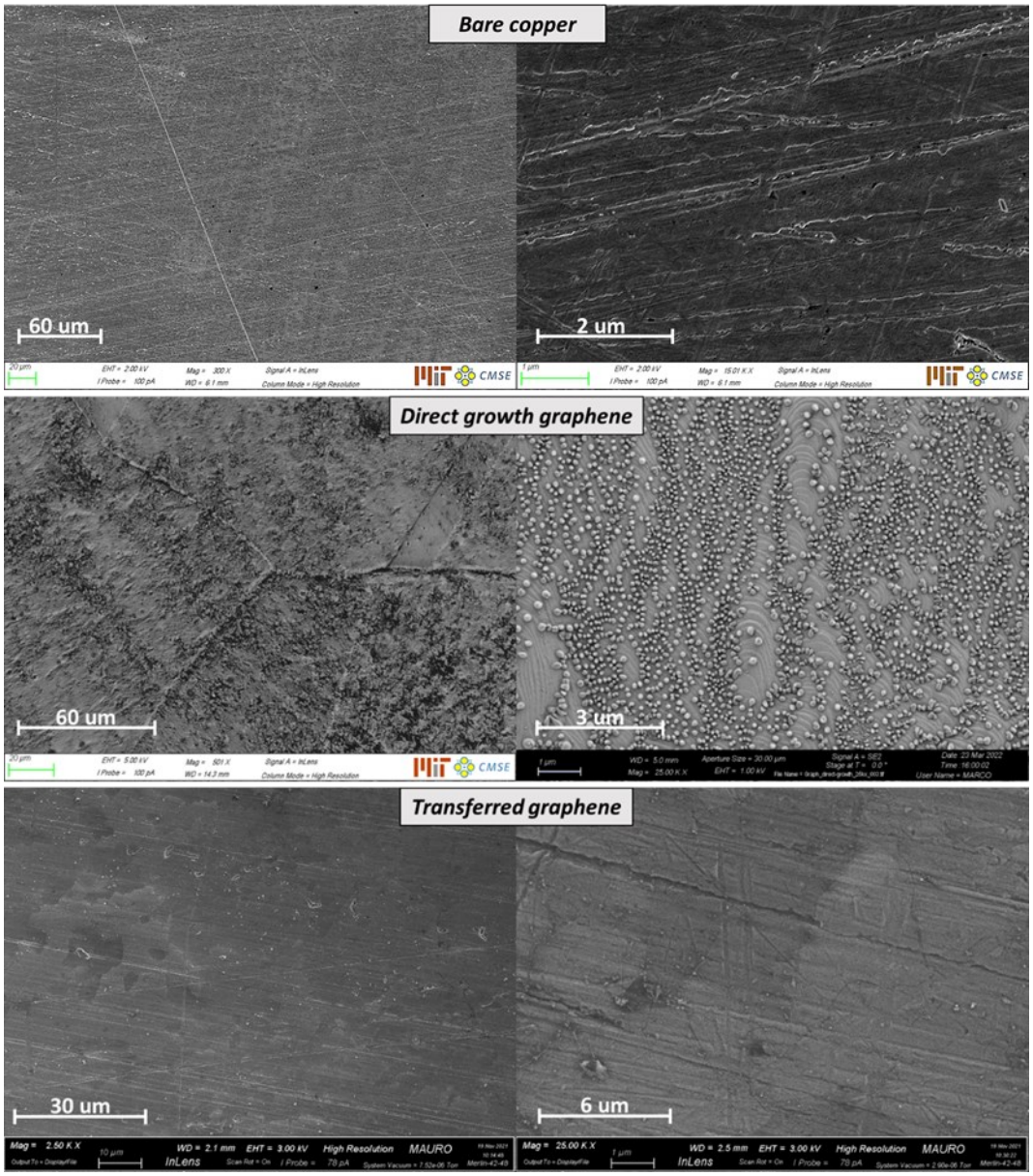

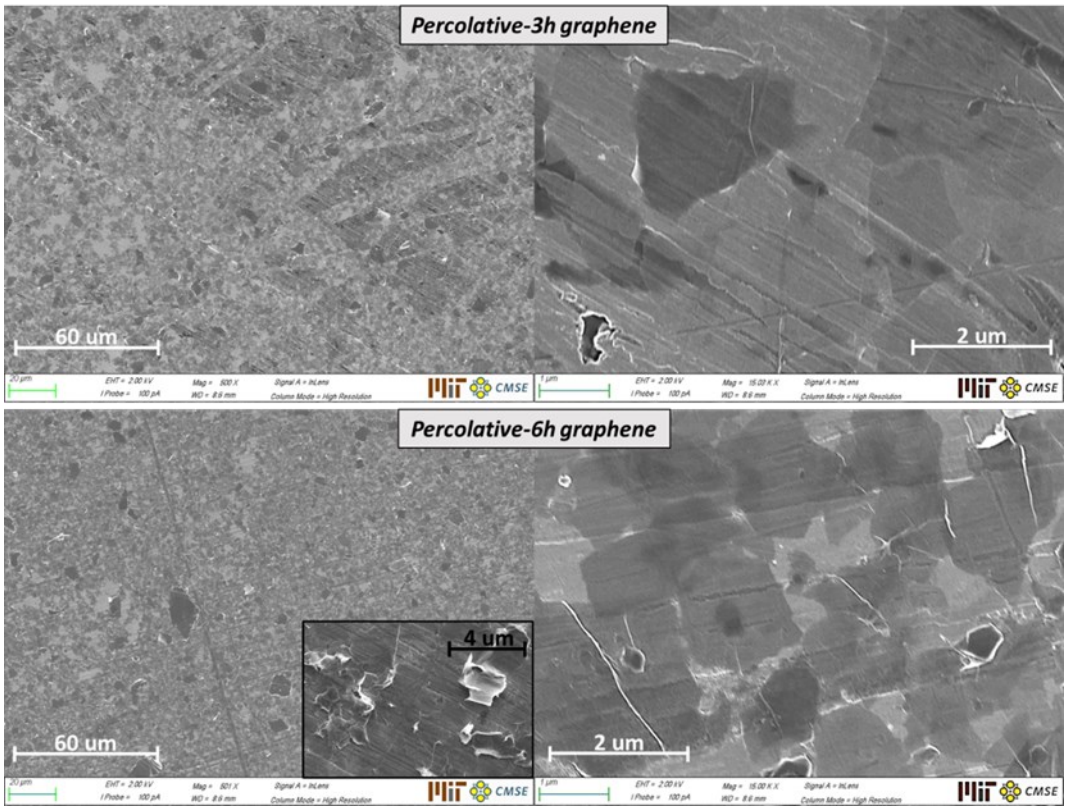

Figure 44. SEM Imaging of transferred and directly grown graphene with magnification 500X, 2.5kX and 25kX. SEM imaging of Bare copper and self-assembled graphene nano-coatings with magnification 500X and 15kX. Inset shows defective recombination of GNPs resulting from the production process of the UGF.

The transferred graphene coating appeared as a uniform patchwork with patches of similar colour, and it looked like the bilayer graphene structure reported by Ullah et al. on copper [46]. The patches are single-crystalline graphene islands grown at nucleation sites on the catalyst foil. As to self-assembled graphene coatings, the enlarged images suggested that the recombination of GNPs was effective in covering the surface of the sample, but the pattern of dark and light patches hints that the carbon layer is uneven, as expected, with regions of locally increased thickness due to folds (see also the inset of Figure 44) or superpositions of many flakes. This graphene structure appeared very similar to the eight-layer graphene reported by Ullah et al. [46].

The surface of the direct growth graphene appeared covered by a structure of spherical nodules protruding from the surface. The authors found no other evidence of CVD graphene on copper with a similar surface texture in the

scientific literature. A possible explanation of this phenomenon could be that this peculiar globular structure is made of relatively hard amorphous carbon nodules. Hu et al. suggested that amorphous carbon can originate on the surface of copper foils during the CVD process if an insufficient flow of precursor gas is supplied and, thus, an insufficient amount of C solubilizes into the substrate [46]. The concentration of the carbon precursor is an important influencing factor in triggering the graphene nucleation, irrespective of the reactor temperature (800–1000°C) and the nature of the catalyst metal. This argumentation led the authors to raise the hypothesis that the globular structure visible under FESEM inspection is some form of agglomerated amorphous carbon grown in place of the pristine graphene layer at the nucleation sites. The reasons for this phenomenon are yet unclear. The flow rate or the partial pressure of CH_4 inside the reactor might have been insufficient to promote the supersaturation of C atoms on the surface of a thicker copper substrate compared to the case of deposition on Cu foils. At the same time, the state-of-the-art understanding of the deposition process evidences that carbon solubility decreases with cooling down, and carbon precipitation triggers the surface crystallization of the graphene lattice [67]. Therefore, it might also be that the cooling of the thick copper target inside the reactor after CH_4 inflation was not fast enough to allow for crystallization at the nucleation sites. Deeper investigations are necessary to clarify these aspects in the future.

The higher magnification tilted-view FESEM image and the results of the AFM analysis in the centre of the sample supported this hypothesis (Figure 45). The height profile allows quantifying the average size of the nodules equal to about 150nm high and 300nm wide.

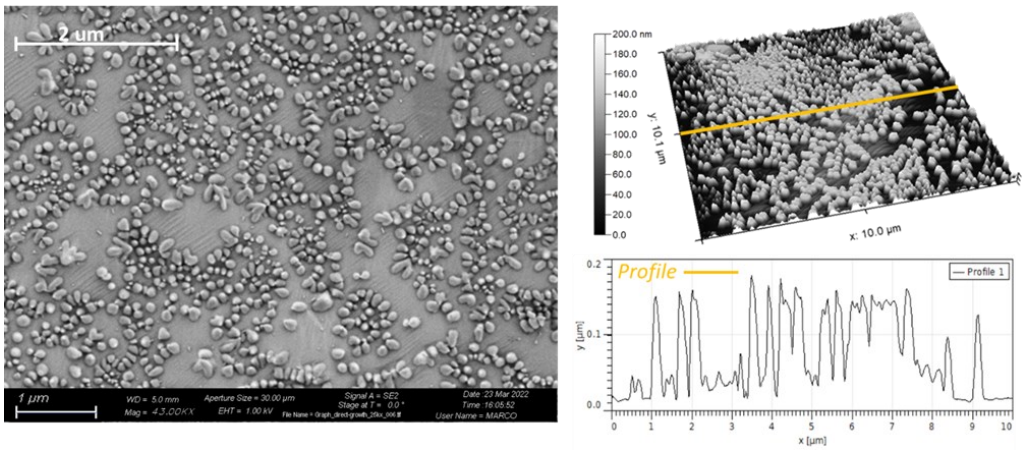

Figure 45. 43kX FESEM image of the surface of the direct growth sample (on the left); 10µmx10µm AFM height map in the centre of the sample coated with direct growth

graphene (on the right). The line profile shows the characteristic dimensions of the globular structure.

Therefore, the direct growth CVD process on bulk copper presented in this research is considered unsuccessful since it did not provide a graphene sheet but a degraded carbonic structure. Nonetheless, the tribological tests performed on the available sample treated by direct growth CVD are presented in the next section, along with the friction and wear performance of the other graphene-coated samples and bare copper. However, the direct growth CVD sample results will not be directly compared to those obtained with actual graphene nano-coatings because it would be meaningless.

Optimization of the direct-growth deposition process is needed because little is known in the scientific literature about the optimum deposition parameters for direct-growth CVD on bulk metal specimens. No researchers have ever tried to produce CVD graphene by catalysing the reaction with a bulk and thick specimen placed inside the CVD furnace. Unfortunately, there was no time to achieve this optimisation goal within the bounds of this thesis work.

This failure gives the feeling of the challenge related to the scalability of this approach intended to avoid the cumbersome transfer procedure of the graphene sheet. The direct growth process would allow synthesising a graphene layer on the surface of the components directly, avoiding the time-consuming transfer process. For that reason, it is of great interest in the perspective of applying high-purity graphene coatings to industrial components directly.

3.3.2 Pin-on-disc tests

Unidirectional rotating wear tests run with the testing parameters summarized in Table 11, and the selected load and speed conditions aimed to avoid excessive graphene layer damage and wear. Three tribological tests were carried out on each sample with an increasing radius of the wear track, i.e., 2mm, 3mm, and 4mm. The dimension of the specimens prevented from running more than three wear tests per sample.

Berman et al. [70] argued that graphene protection is more pronounced at lower loads, while under higher loads, the graphene layer is quickly worn out and removed out of the wear track with a reduced beneficial effect for the system. The

corresponding average Hertzian contact pressure at the beginning of the test was 336 MPa, calculated via the *HertzWin* software considering the effect of roughness on the contact stress state (*Ra* 0.092µm for the steel sphere and *Ra* 0.182 µm for copper). The initial contact pressure was consistent with previous works on the frictional behaviour of graphene coatings [45], [39] , [67].

Table 11: Pin-on-disc tests on graphene-coated copper samples

Wear track radius [mm]	2 mm	3mm	4 mm
Load [N]	2	2	2
Speed [mm/s]	15	15	15
Sliding distance [m]	30	30	30
Sampling [Hz]	100	100	100

Friction

The effect of the different kinds of graphene coatings on the frictional response of the tribopair is visible in Figure 46. The figure compares the friction curves of the five tests recorder with track radius of 3 mm. The friction curve related to the bare copper sample (the blue curve) is the reference trend to understand the impact of the carbon coatings.

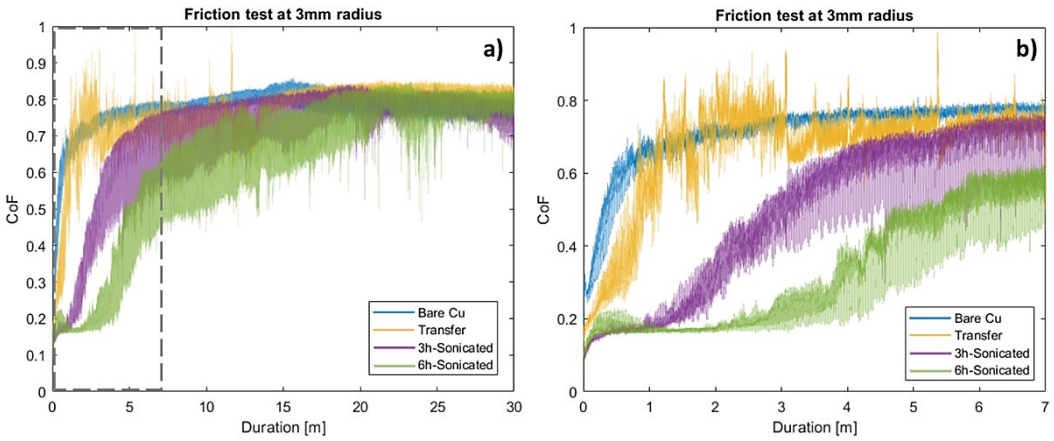

Figure 46**.** Friction curves measured on the graphene-coated samples at the median radius of 3mm. (a) Frictin curves recorded thrughout the whole test duration; (b) Detail of the friction curves in the first 7 m of sliding.

This curve has an initial friction ramp representing the running-in of the sliding contact and brings the CoF to stabilise at about 0.8 after a few meters. Looking at the other curves in the same diagram, it appears evident that the presence of a graphene layer makes the CoF curve deviate from that of the bare copper sample.

A beneficial lower CoF resulted in the first part of the test from the coated samples compared to the uncoated one. The friction curve of these samples featured an initial steady state with low scattering whose duration is strongly correlated to the structure of the coating itself. After this initial steady run, a transition occurred that closely resembles the running-in phase observed with bare copper but delayed by a few meters. This friction ramp was likely associated with the failure and removal of the graphene coating from the contact region. Like in the case of the graphene-coated aluminium samples (see Section 3.2.2), this increase in friction was triggered by the direct contact between the steel sphere and the substrate. Won et al. argued that the increase of friction corresponding to the failure of the coating is followed by the degradation of graphene to an amorphous state [45]. Figure 46b is the zoomed view of the first 7 meters of the tests, where the difference among the curves is most prominent. Interestingly, irrespective of the initial frictional behaviour, all the friction curves levelled off in the second half of the test, and both the uncoated and coated samples had similar friction in the last few meters of sliding. A few traces of carbon matter remained inside the wear tracks by 30m sliding, similar to what was observed in previous investigations [45] and with aluminium samples.

Figure 47 displays the whole set of friction curves, except those of the direct growth CVD specimen, as anticipated in the previous section. Friction curves plotted against the number of rotation cycles allows appreciating the high repeatability of the results despite the different wear track radius[1].

Even after removing the nano-coating, the curves remained relatively smooth with low scattering because the wear mechanisms were less severe than those observed with steel against aluminium. The friction curves of transferred graphene showed the highest scattering of the friction signals, mainly between 200 and 500 rotating cycles, which may indicate severe abrasion and ploughing. Abrasion grooves are evidenced in Figure 55d. The other curves acquired with

[1] As already explained in Section 4.1.2, since the samples experienced more extensive wear damage than the steel sphere, friction curves measured at increasing radial position would not match if plotted against the sliding distance due to a visualisation bias.

bare copper and with the samples coated by self-assembled graphene are much smoother because a transfer layer was established at the interface (Figure 55f, h).

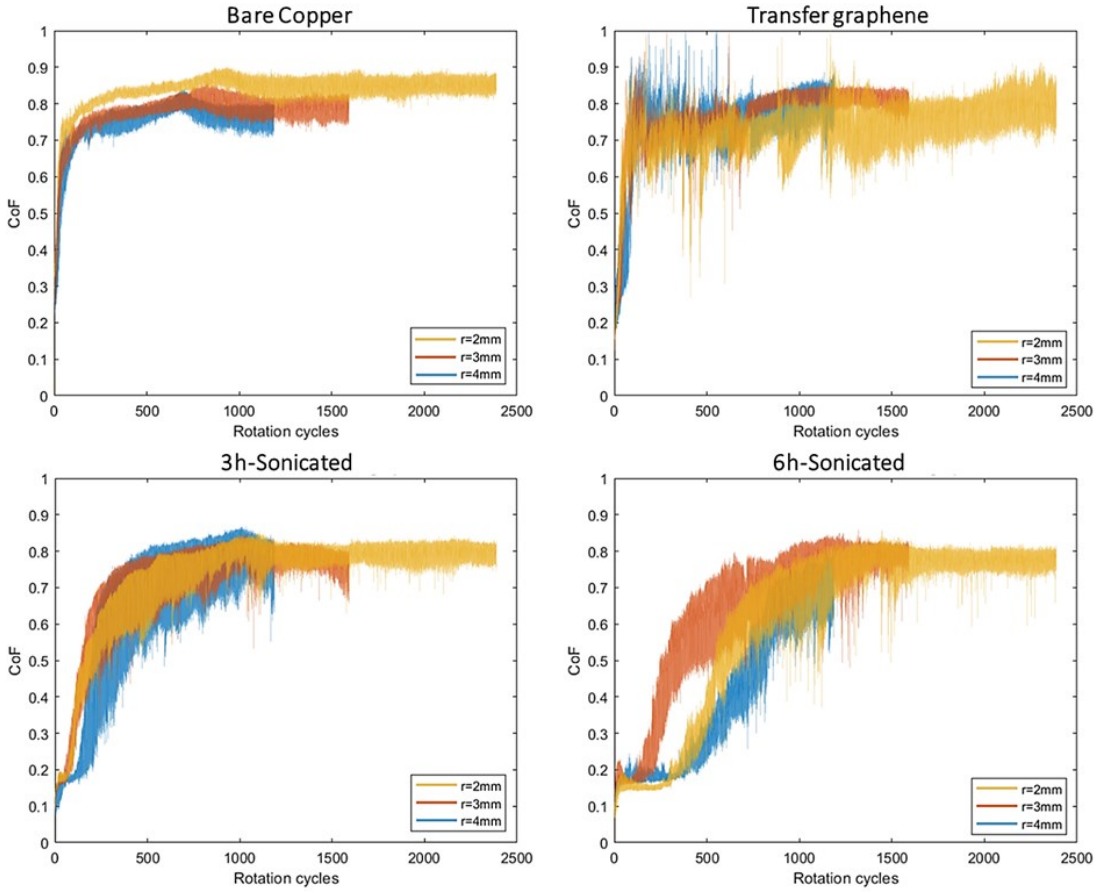

Figure 47. Friction curves from pin-on-disc tests on the graphene-coated samples.

Following the same scheme used for aluminium samples and presented in Figure 30, the friction curve of coated samples can be divided into two parts: Part 1, extending from the beginning of the test to the beginning of the coating-to-substrate transition, and Part 2, from the transition up to the end of the test. The analysis of the curves in Figure 47 also provided valuable information about the travelled distance before the coating failure. The transition was completed within 15÷20 cycles for transferred graphene, whereas the duration was extended to 250 cycles for the self-assembled graphene nano-coatings sonicated 6 hours. The average CoF values measured in Part 1 and Part 2 are compared in Figure 48. The corresponding duration of the nanocoating is expressed by the cycles accumulated at the time the transition started. These results suggested that all the graphene nano-coatings could reduce friction from about 0.6-0.8 to 0.15-0.25. However,

this beneficial effect endured as long as the carbon sheet withstood the tearing-off action of the counter body.

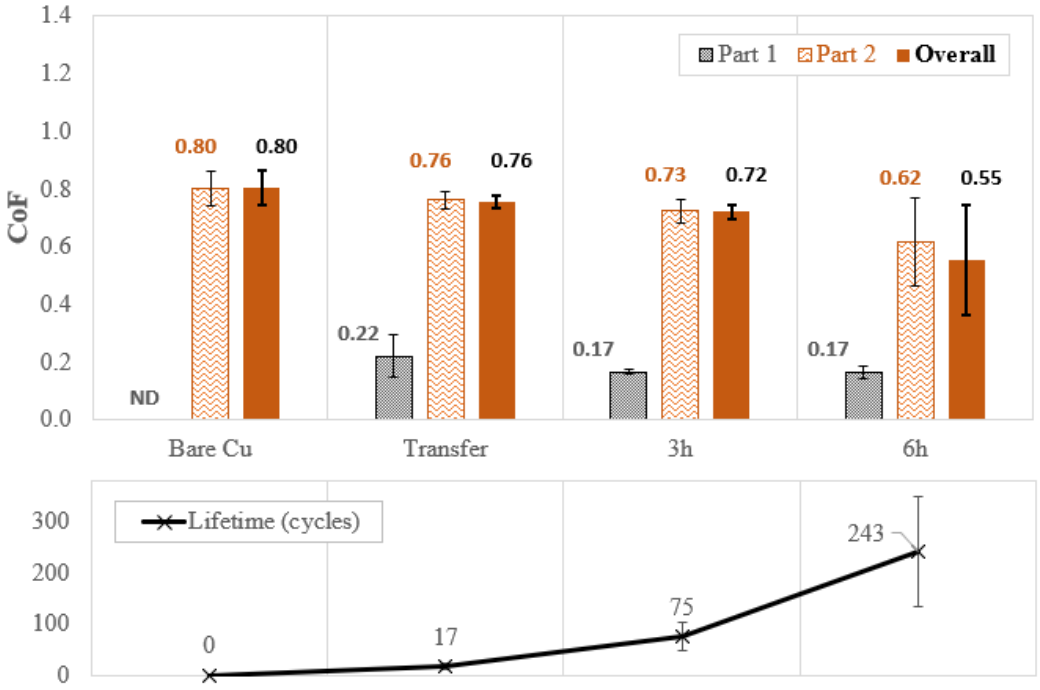

Figure 48. Average CoF values are measured in Part 1 and Part 2. The error bars are three times the standard deviation of the average CoF of the three tests carried out with each sample. (Lower part) The average lifetime of the coatings is determined as the beginning of the friction ramp between Part 1 and Part 2.

The overall friction reduction by transferred graphene coating was vanishing because of its limited duration at the interface. Its thickness is so tiny that Part 1 could not be distinguished from the running-in of the steel-copper pair. The two self-assembled graphene nano-coatings showed the minimum value of the CoF in Part 1, and a significant 11% reduction of the overall friction coefficient was observed with 6h-sonicated graphene. The results of Raman spectroscopy on the same kinds of self-assembled graphene deposited on aluminium (see Figure 28 in Section 3.2.1) revealed that their quality was coarse from the point of view of the crystalline structure. The coating was more likely to consist of a structure of several broken atomic layers imperfectly arranged. Self-assembled graphene was thicker than transferred graphene, and its enhanced wear strength at the macroscopic level made Part 1 longer-lasting. These results support the evidence that the nano-coatings by self-assembly of GNPs are the strongest and most

effective for the tribological system, whereas transferred graphene is relatively weak.

Table 12: CoF values measured on pristine graphene (before coating failure) from literature

	Reference	CoF value	Testing conditions
Shi et a.	[56]	0.22	Pin-on-disc; graphene-coated and textured M2 steel against stainless steel; 0.5N load; Testing in ambient air; solution-processed graphene coating;
Berman et al.	[55]	0.19	Pin-on-disc; graphene-coated 440C steel against 440Csteel; 2N load; Testing in ambient air, in ethanol bath and with the addition of droplets of graphene solution; solution-processed graphene coating;
Berman et al.	[39]	0.16-0.23	Pin-on-disc; graphene-coated 440C steel against 440C steel; 1N load; testing in N_2 and H_2; CVD graphene and solution-processed graphene coating;
Berman et al.	[71]	0.2	Pin-on-disc; graphene-coated steel against steel; 1N to 5N load; Testing in dry Nitrogen; solution-processed graphene coating;
Won et al.	[45]	0.2	Pin-on-disc; graphene-coated copper against stainless steel; 20mN load; Testing in ambient air; CVD graphene;
Yildiz et al.	[54]	0.19 - 0.4	Flat-on-flat; graphene-coated bronze against AISI52100 steel; 10N to30N load; Testing in ambient air; CVD graphene;

The wearing-out of the self-assembled nano-coatings in Part 1 comes with a stable average friction value, and friction was equal to 0.17 for the two self-assembled coatings. Interestingly, very similar values were reported by other

researchers; they are summarized in Table 12. Even with different substrates and environmental conditions, they recorded friction curves with extraordinary similarities to those reported in this research, featuring initial low friction followed by a gradual increase up to the typical CoF of the substrate. Besides, this value was also aligned with the results presented in Section 3.2.2. At the beginning of the tests, the CoF measured with the 3h- and 6h-sonicated UGFs deposited on aluminium was 0.14 and 0.18, respectively. Therefore, 0.15 to 0.2 should be regarded as the characteristic friction coefficient for the graphene-steel pair regardless of the substrate nature and the characteristic scale of the phenomenon.

Wear

The surface of the samples was scanned with an InfiniteFocus G5 Focus Variation (FV) 3D digital microscope by Bruker Alicona with a 20x high-resolution lens to measure the amount of wear. The surface enclosed in the square area around the three concentric wear tracks in Figure 49 was acquired at once to have a single reference plane to estimate the wear volume of the three tracks.

The volume of removed material and deposited or plastically displaced material were calculated with the Volume Parameters Topographic Method based on the Abbott-Firestone curve. The method is schematically represented in Figure 50 and relies on equations (16) to (18)[2]. Further details are reported by Leach [72], Waterworth [73], and Maculotti et al. [74]. This calculation method of the wear volume was proved by Maculotti et al. to be the most robust from a statistical point of view. It has higher accuracy and lower uncertainty than the method suggested by the standard ASTM G99-17 and ISO 18535 based on the profilometry of the wear tracks.

[2] V_m and V_v are the material volume and the void volume, respectively, V_{VP} is the total damage volume, h is the surface height, S_{mc} the cumulative probability distribution of the surface heights (i.e. the Abbott-Firestone curve), and K is a conversion factor that represents the area of the projected surface topography on a horizontal plane. Given a specific horizontal section plane representing the average position of the unworn surface whose height is h_0, V_m represents the volume of material enclosed below the measured surface and above this plane, whilst V_v is the volume of missing material above the surface and below this plane.

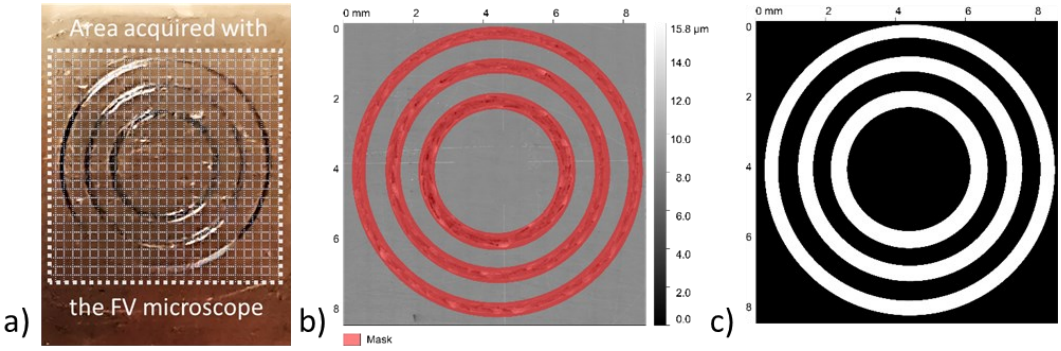

Figure 49. (a) Region of the samples scanned with the 3D microscope, (b) masks applied to the topographic data, (c) binary trace of the masked region.

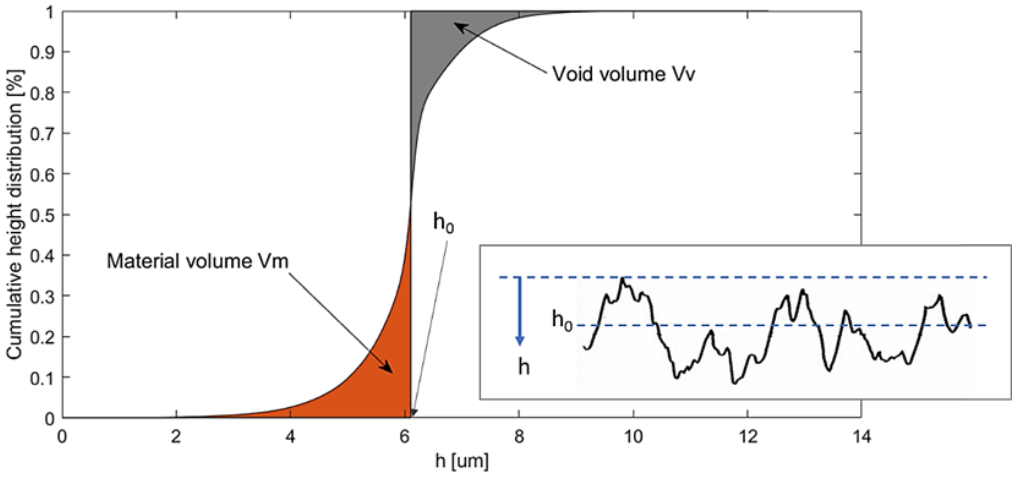

Figure 50. Void and Material volume parameters of the Abbott-Firestone curve

$$V_{VP} = V_m(m_r) + V_v(m_r) \tag{16}$$

$$V_m(h_0) = K \int_0^{h_0} S_{mc}(h)\, dh \tag{17}$$

$$V_v(h_0) = K \int_{h_0}^{1} \left(1 - S_{mc}(\mathrm{h})\right) dh \tag{18}$$

Volume calculations were performed through the open-source software Gwyddion. Rough topographic datasets were imported into Gwyddion, where three annular masks identified three regions of interest (ROI), as Figure 49b shows. Setting suitable ROI was necessary to exclude from the volume computations any contributions from roughness and other topographical features

of the surrounding surfaces that are not related to the tribological tests. The dataset outside the three annular masks, i.e., the region in black in Figure 49c, was exploited to fit a polynomial function through which the rough topographic acquisition was planarized by shape removal. This practice is imperative to correct the residual error of planarity and thus to identify the reference section plane representing the unworn surface accurately. This plane at $z = h_0 = cost$ was identified as the median value of the dataset filled in with black filler in Figure 49c. The Abbott-Firestone curve was computed for each wear track individually by elaborating the data inside each annular region of the mask. The integration of the Abbott-Firestone curve schematically represented in Figure 50 provided the quantification of the material removed and displacement during the sliding interactions.

The worn surface of the samples after the pin-on-disc tests is shown in Figure 51, and Figure 52 collects and compares the corresponding topography of the worn-out region acquired with the FV microscope. Samples were blown with air before the topographic analysis, and the wear tracks were gently wiped with a dry lint-free swab to remove any residual wear debris from the surface. The samples were not further cleaned to avoid physical or chemical damage to the carbon layer.

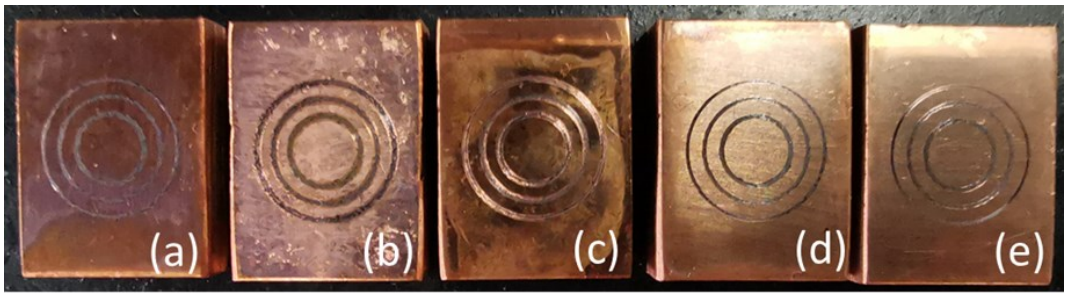

Figure 51. Samples after pin-on-disc tests. (a) bare sample, (b) directly grown CVD graphene, (c) transferred CVD graphene coating, (d) 3h-Sonicated graphene, (e) 6h-Sonicated graphene. A transparent film adhered to the central part of the metal surface is noticeable on the sample with transferred CVD graphene. The sample with direct growth graphene, whose results will be presented separately in section 3.2, featured a pattern of bright patches similar to grains visible to the naked eye, probably the contour of the copper grains after annealing.

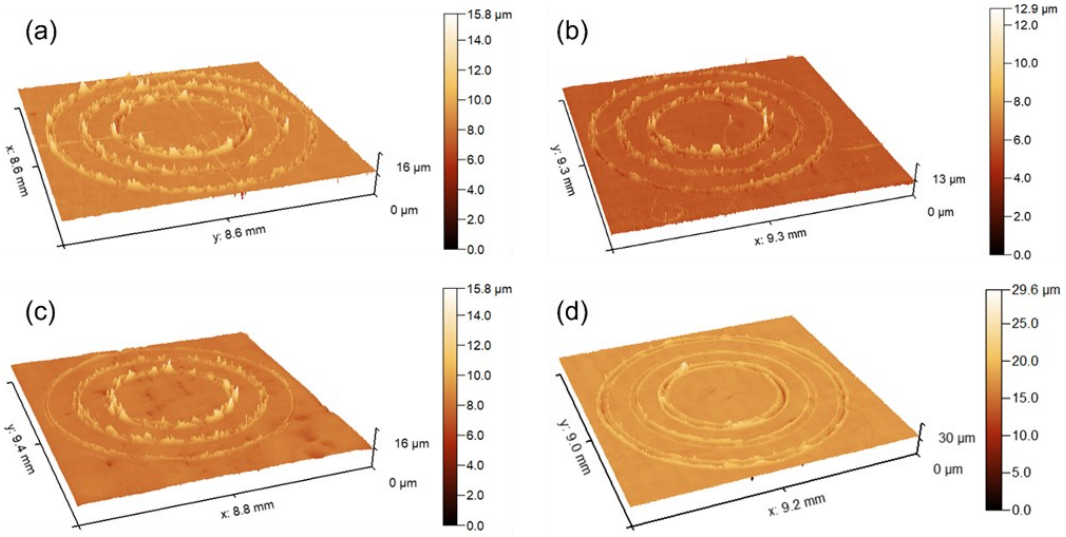

Figure 52. Comparison of the topography acquired with the FV 3D microscope: (a) Bare Cu, (b) transferred graphene, (c) 6h-sonicated graphene, (d) 6h-sonicated graphene.

The calculated volume data are presented in detail in Figure 53 for each test, and the corresponding average values of the sample are listed in Table 13. The result of the wear tests revealed different wear behaviours for the various types of graphene coatings.

Table 13: Average value of material loss and deposited/displaced material

Volume data [mm^3]	Bare Cu	Transfer	3h-sonicated	6h-sonicated
Average volume loss	0.0030	0.0056	0.0019	0.0018
St.Dev. of the volume of material loss	0.0009	0.0022	0.0003	0.0006
Average volume of deposited material	0.0024	0.0045	0.0017	0.0021
St.Dev. of the volume of deposited material	0.0007	0.0014	0.0001	0.0004

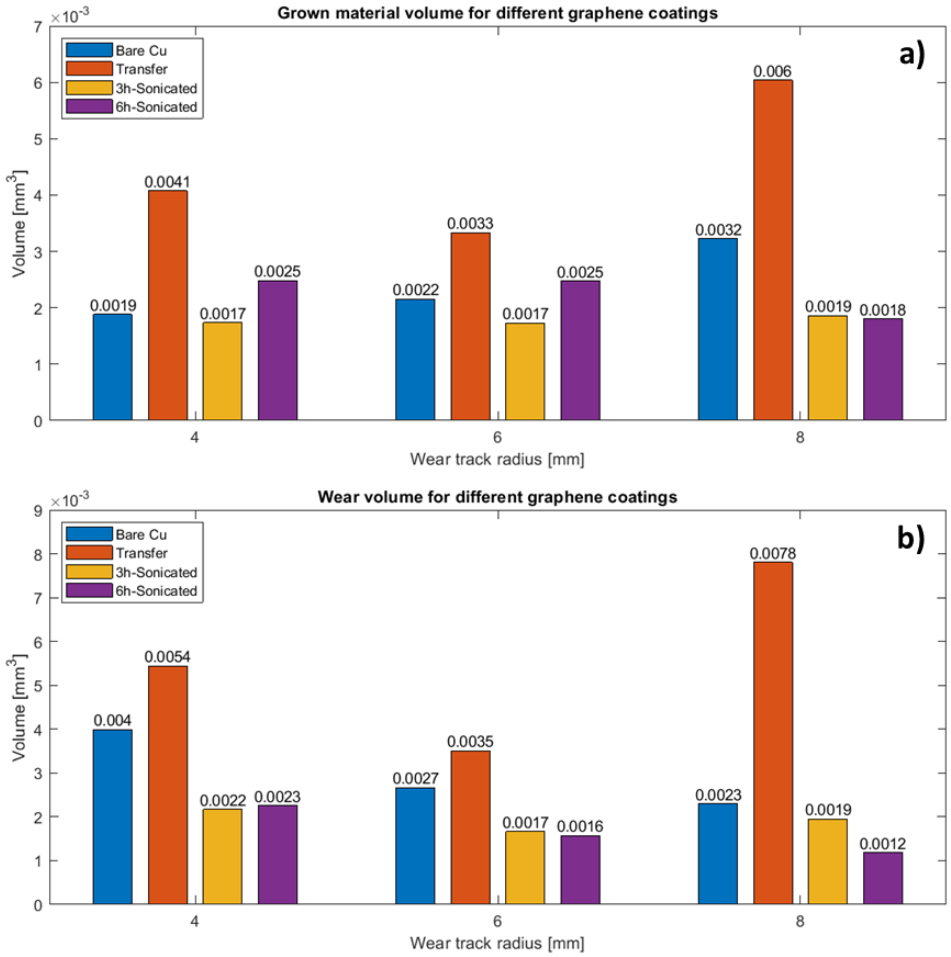

Figure 53 (a) Removed material volume and (b) deposited or plastically displaced material volume measured at the end of the pin-on-disc tests.

The two samples coated by self-assembled graphene performed best, and, in particular, the 6h-sonicated graphene let the amount of removed material decrease by 36%, taking the bare Cu sample as the reference. The adhered or plastically displaced material decreased by 10-15% on average, even though its value was slightly higher for the 2mm and 3mm track radii. These results were remarkably different from those obtained with graphene-coated aluminium samples, where no evident benefit in wear was observed. The relative reduction of wear was substantial, yet the early graphene removal may have hidden the full potential of these coatings if they had endured for a more extended time. In other words, the wear volume was measured only at the end of each test, whilst the coating failure happened on average at 1/6th or 1/10th of the total sliding distance. Therefore, the benefits of these high-lubricity graphene nano-coatings might have proven even

more significant if the wear volume were inspected repeatedly after shorter sliding distances or at the end of shorter tests.

The performance of transferred graphene was mediocre. The average amount of material lost and plastically displaced was two times higher than the bare copper sample. This evidence, however, is not in line with the results of the work by Yildiz et al. [54], who observed a substantial reduction of the wear rate by transferred CVD-graphene. The presence of ripples in the graphene coating might cause such a negative performance. According to Long et al., wrinkles and ripples are relatively common in graphene produced by CVD due to the negative thermal expansion coefficient of graphene. Wrinkles appear during the cooling process as the substrate shrinks while the coating dilates [75]. Paronyan et al. [76] also pointed out that the critical phase of the CVD method is the cooling-down of the Cu-C system since at about 1000°C a thin melted layer is likely to appear on top of the catalyst body and it may run into quenching. Such undercooling is responsible for forming a surface Cu lattice favourable to many graphene ripples, e.g., ripples formed due to cellular and dendritic solidification patterns. Comanescu [77] proved that transfer from the copper foil to a super smooth surface (like SiO2) might make the graphene sheets flatter and less defective. However, if some ripples formed during the CVD process, they could be easily transferred to the end copper sample because the surface finish of these samples was much higher than those employed by Comanescu. The high shear stress experienced by the wrinkles and ripples under sliding contact interactions quickly leads to structural changes from sp^2 to amorphous carbon, according to Huang et al. [78], leading to harsher tribological conditions.

The morphological analysis in Figure 54 was carried out to investigate the wear mechanisms acting at the tribological interface. It seemed that the dominant wear mechanism varied due to the presence of a carbon layer and the structure of the nano-coating. The bare copper and the sample coated by sealf-assembled graphene featured isolated deeps and hills inside the wear tracks, suggesting the detachment of chunks of material due to local adhesion and subsequent deposition of oxidised matter inside the sliding path. Figure 55 shows that a dark grey third layer made of an oxidised matter covered the wear tracks, and it was responsible for the peculiar morphology visible in Figure 54.

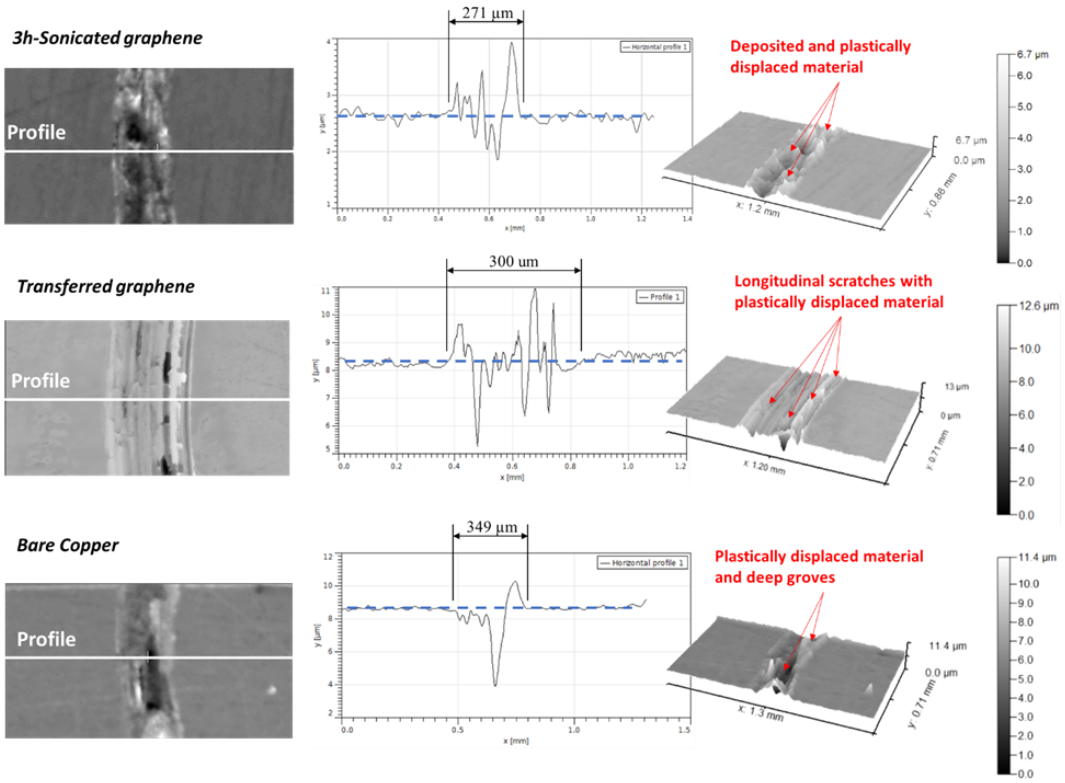

Figure 54. Analysis of the wear tracks morphology. The wear tracks of the tests performed at a radius of 3mm were considered for this comparative analysis.

In the presence of graphene, this layer may have encapsulated lubricious carbon matter and protected the substrate from wear. Therefore, tribo-oxidation activated by initial adhesion was probably the primary wear mechanism here. This was not the case for the transferred graphene. A dark layer only partially covered its wear track, and shining areas were still visible by the end of the test in Figure 55f. No transfer layer stabilized, and thus, tribo-oxidation had a limited effect, probably. The wear track was much more regular in width and featured a pattern of longitudinal grooves and ridges that may point out abrasion as the dominant mechanism. Abrasion was well correlated with the friction curve recorded during the tests, which were erratic and characterized by high scattering of the CoF. Abrasion might be promoted by the presence of wrinkles and ripples in the transferred graphene layer, as discussed above.

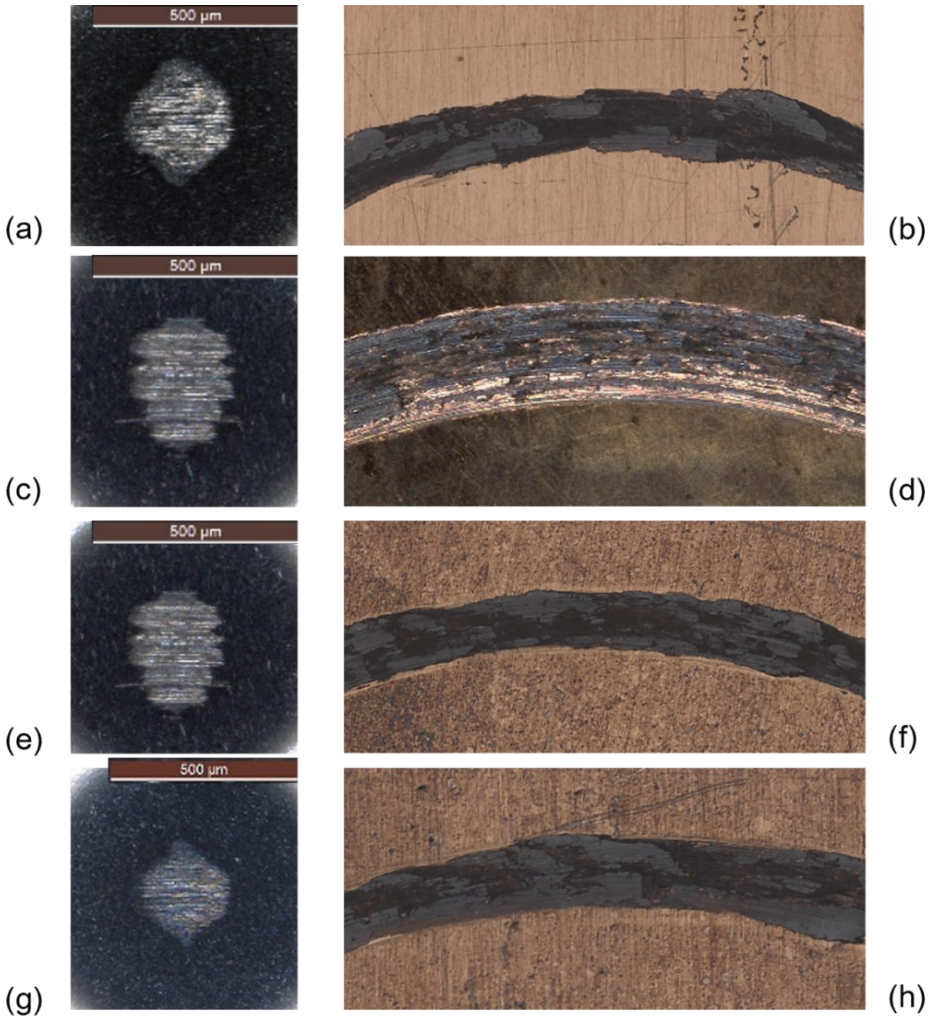

Figure 55. Wear scars on the steel balls (left) and wear tracks on the copper samples (right). (a-b) Bare Cu, (c-d) transferred graphene, (e-f) 3h-sonicated graphene, (g-h) 6h-sonicated graphene.

As to the counterpart, minor damages appeared on it, and the inspection under the optical microscope provided no evidence of transferred or oxidized matter on the ball. The damage was mostly limited to a local pattern of scratches on the sphere. Therefore, the wearing-out of the sphere was neglected because the related wear volume was not measurable confidently (it was limited to minimal deviations from the initial spherical shape).

The analysis of the roughness values measured inside the wear tracks after the tests are presented in Table 14. Interestingly, the roughness values were higher

than the initial ones and correlated with the inherent wear results. Lower S_a values than bare Cu were measured for the two samples with the best tribological performance and higher S_a for the other two, which supports the evidence that graphene had a beneficial lubricious effect only in the form of self-assembled graphene, at least in the sliding contact conditions explored in this research.

Table 14: Analysis of the roughness inside the wear tracks

		Bare Cu	**Transfer**	**3h-sonicated**	**6h-sonicated**
Initial value of roughness	*Sa [μm]*	*0.071*	*0.236*	*0.098*	*0.096*
Roughness inside wear tracks	Sa [μm]	0.671	0.957	0.508	0.525
	Sq [μm]	0.897	1.514	0.641	0.701
Wear track width	[μm]	349	300	271	231

The S_a and S_q surface roughness parameters were calculated after extracting a random region inside the wear track and removing the waviness shape through a polynomial function. This evidence agrees with the results by Won et al. [45], who claimed a reduction in the average roughness and width of the wear tracks when the tribological performance was enhanced by graphene.

Direct growth CVD

As to direct growth CVD, the specimen disclosed a different tribological behaviour against the steel sphere. Figure 56a compares the friction curve of the direct growth sample with the other friction curves of bare copper and graphene-coated copper. High friction was measured at the beginning of the test, with a peak of 1.4 at the onset of sliding. A gradual decrease of the CoF followed and stabilisation at a value slightly lower than the other curves of the diagram. The friction curves in Figure 56(b) suggest that an extra abrasive effect worked at the interface at the beginning of the test, which was detrimental to the tribological system. The amount of material removed and displaced was also distinctly and dramatically higher than the uncoated sample. The wear volume calculations are presented in Figure 57 and Table 15. No previous investigation about samples prepared by direct growth CVD reported a similar result.

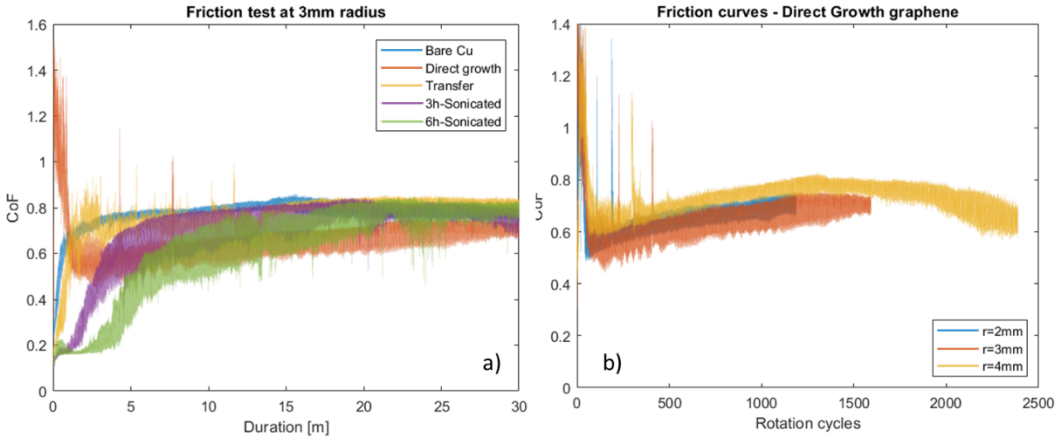

Figure 56. (a) Friction curves were measured with the sample treated by direct growth CVD and compared to the other samples at the median radius of 3mm. (b) Set of friction curves measured with the direct growth sample.

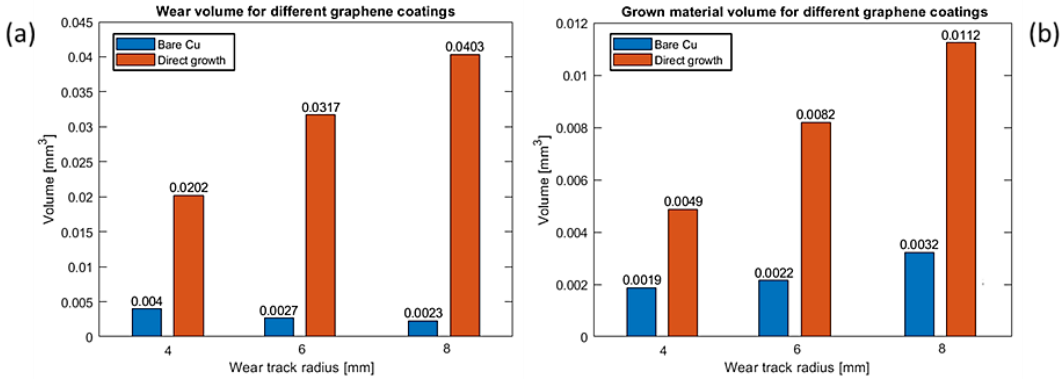

Figure 57. (a) Removed material volume and (b) deposited or plastically displaced material volume for the direct growth sample.

If hard amorphous carbon formed due to anomalous activation of the carbon nucleation sites, as hypothesised, it is likely that a 2-body abrasive effect played a role. Abrasion would justify the peak of the CoF in the very first cycles of the test. During the subsequent downfall of the CoF, the globular structure may have detached and turned into hard debris rolling at the interface. Hard globules may have mixed with copper oxides and strengthened the third layer covering part of the wear track. Some oxidized matter is visible in the middle of the wear in Figure 58b. This scenario would explain, on the one hand, why significant material loss continued up to the end of the test and, on the other hand, would justify the slightly lower friction coefficient observed in the steady-state part of the tests compared to the other samples.

Table 15: Average value of material loss and deposited/displaced material for the direct growth sample. Comparison of the roughness value before and after the tribological tests

Direct growth				
Volume data	**[mm³]**	**Roughness**		**[µm]**
Average volume of material loss	0.0307	*Initial roughness value*	*Sa*	*0.979*
St.Dev. of the volume of material loss	0.0101	Roughness inside the wear tracks	Sa	1.176
Average volume of deposited material	0.0082		Sq	1.636
St.Dev. of the volume of deposited material	0.0032	Wear track width		578

Figure 58 shows that the wear track was large and deep with no longitudinal scratches. Many recesses distributed along the track are shown in Figure 58c, together with chunks of material ripped off the samples (Figure 58a). These pieces of evidence suggest that after the transition of the CoF, the dominant wear mechanism evolved from dominant abrasion to a mix of adhesion, abrasion and tribo-oxidation. The wear tracks of the direct growth sample also feature the largest amount of plastically displaced material forming hills at the borders of the tracks, which explains why the wear scar on the ball has high ellipticity in Figure 58(a). This effect can be related to the substrate softening due to annealing at high temperatures (1000°C) during the CVD treatment.

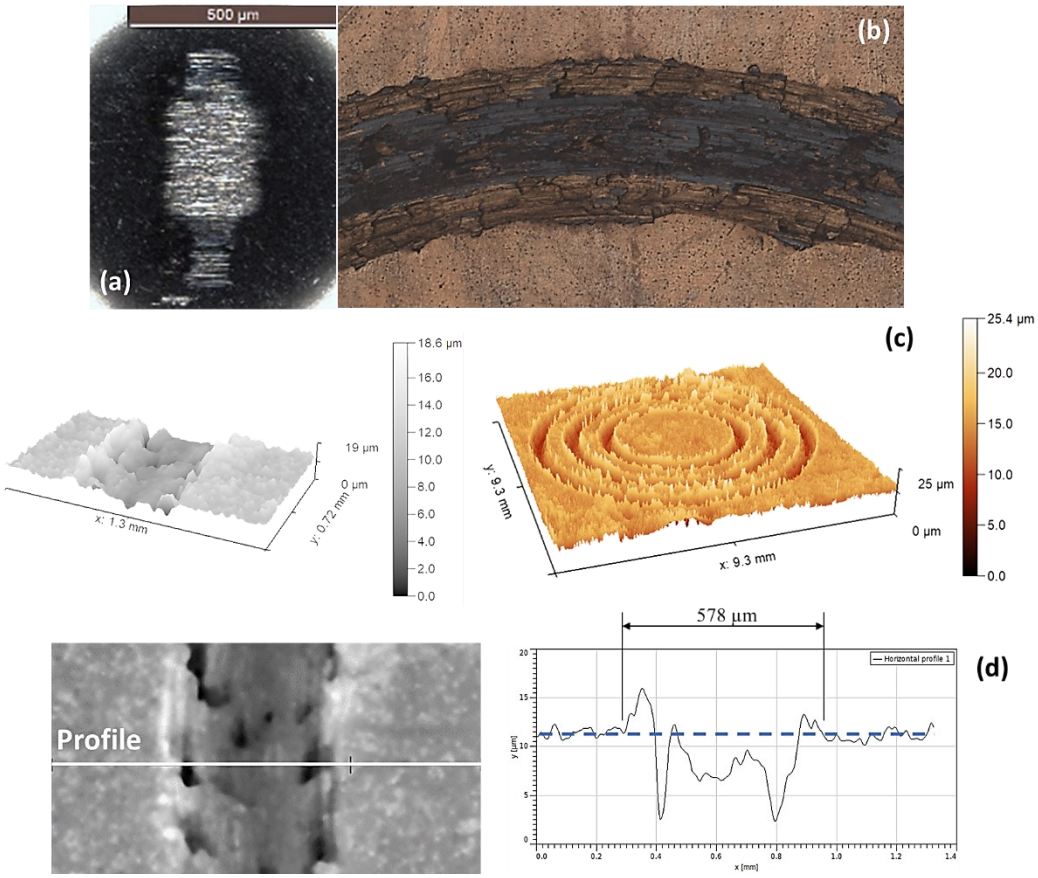

Figure 58. Morphological analysis of the wear track after the tribological test with the sample treated by direct growth CVD.

3.4 Conclusions and future perspective

Sections 3.2 and 3.3 investigated the tribological performance of graphene-coated aluminium alloy and graphene-coated copper. Four synthesis methods were compared to produce 2D carbon coatings by either transfer or self-assembly of flakes. The nature and quality of the graphene structures thus obtained were investigated through Raman spectroscopy and SEM analysis to confirm their thickness, defectiveness, and uniformity of substrate coverage. Direct growth of CVD graphene was possible for copper substrate only since aluminium cannot be a catalytic metal for activating graphene nuclei.

The results of the tribological tests against steel under low load and sliding speed revealed that graphene coatings could serve as a solid lubricant while reducing friction. The CoF dropped from 0.6-0.7 to 0.15-0.25 for aluminium alloy and copper, with a maximum reduction of 72% and 78%, respectively. However, this beneficial effect endured as long as the carbon nano-sheet withstood the tearing-off effect of the counter body sliding against it. The coating duration was limited to just 1/10th to 1/6th of the total sliding distance with copper. The carbon layer lasted even shorter with aluminium alloy, up to a maximum of 1/30th of the total sliding distance. Even though pin-on-disc tests never replicate the actual contact conditions found in real applications, such a duration is overly limited to foresee any reasonable application of these coatings to components subjected to gross sliding.

As to wear, the presence of graphene had a very different impact depending on the substrate material and the synthesis process. Graphene deposited on aluminium alloy did not improve the wear properties of the tribological system compared to bare substrate, regardless of the synthesis method. Duration might have contributed decisively to limiting the beneficial effect of graphene. Also, the unfavourable wear mechanism of the aluminium-steel tribopair prevented graphene debris from laying inside the wear track after the film failure. On the other hand, the reduction in the average wear volume of copper was remarkable in the case of self-assembled graphene coatings (UGFs). The reduction was about 36% and 40% for the 3h-sonicated and 6h-sonicated coatings compared to the bare copper, respectively.

Interestingly, a remarkable performance improvement of wear was achieved, although the duration of the coating at the contact interface was limited. The presence of a transferred sheet of graphene showed no clear benefit instead since the lifetime of the coating was vanishing. This carbon layer (the least defective 2D graphene film considered in this research) turned out to be overly thin and weak to have any impact on macroscale friction and wear phenomena over extended sliding time.

The deposition of direct growth graphene on copper samples failed, and SEM analysis showed that a globular structure (amorphous carbon, probably) formed on the sample surface instead of a 2D carbon layer. Wear experienced by the tribo-system was, therefore, much higher than in the case of bare copper.

In the end, the results proved that graphene obtained from the self-assembly of GNPs is the longer-lasting nano-coating among those investigated. The main benefits are related to its increased thickness (i.e. some tens sp^2-hybridized carbon sheets) and the ability to promote a lubricious third layer in the worn-out region after failure, at least when deposited on copper. Moreover, self-assembled graphene coatings are easy to apply and cost-effective compared to CVD graphene. UGFs are the most promising form of graphene for prospective industrial applications where macroscale tribological interactions are involved, despite their defective and uneven carbon structure.

Nevertheless, some critical aspects have already to be addressed to make these nano-coating suitable for extensive use in mechanical and electrical applications. The main issue remains the low endurance under the tearing-off action of a counter body, which, in turn, is affected by weak adhesion to the substrate. Due to limited adhesion, graphene coatings may be helpful in applications involving friction partners with limited rubbing motion (either in time or amplitude), e.g. where fretting dominates or in cold metal forming processes. Based on these results, component tests with self-assembled graphene nano-coatings deposited on oscillating rolling bearings, spline couplings, and electrical connectors subjected to fretting damage may be performed in the future to explore the behaviour of these coatings in close-to-actual operating conditions.

Regarding adhesion to the substrate, the adhesion of graphene films relies on Van-der-Waals bonds. Previous research on graphene at the nanoscale [79] has proved that when a solid body slides against graphene, the weak bonding cannot prevent ripples and puckers in the out-of-plane direction from arising in front of the contact. Lumping of the carbon sheet is the primary cause leading to the eventual breakdown of the layer. If graphene is deposited on substrates with relatively low stiffness, the local elastic or elastoplastic deformation at the contact site increases the contact area and allows further crumpling of graphene under relative sliding motion. This effect promotes deboning of the 2D nano layer from the substrates, leads to higher friction and increases the failure probability of the nanocoating itself. [80]. The puckering effect would be suppressed if graphene were firmly bound to the substrate. Therefore, enhanced adhesion is expected to allow any graphene to last longer, and thinner graphene layers may also yield better results. In this scenario, the functionalization of the substrate surface to enhance adhesive attraction can be a promising way to improve the performance of graphene as a nano-coating for tribological applications. Zeng et al. reported,

for instance, that plasma etching of the substrate before deposition leads to stronger adhesive attraction of the graphene sheet and less friction [81].

Another good evolution of this research is investigating the performance of composite nano-coatings made of graphene and other nano-materials, e.g. MoS_2 and graphene oxide (GO). Ayyagari et al. [82] have recently proved by pin-on-disc testing that MoS_2-GO nano-coatings deposited by a simple spray-coating technique can last exceptionally long even under high load and moderate sliding speed.

Chapter 4

Graphene-enriched greases in tribological applications

Liquid or semi-solid lubricants such as oils and grease have been traditionally applied to reduce friction and wear of sliding parts. They reduce the adhesion energy between solid surfaces and, possibly, the area of direct solid-solid contact [23].

Although many efforts are being made to replace traditional lubricants with more environment-friendly solid lubricants, for instance, carbon-based [83] or MoS_2-based materials [84] or innovative MXenes materials [85], liquid or semi-solid lubricants are hardly replaceable in many industrial applications. Solid lubricants offer the advantage of avoiding mechanical power waste due to viscous effects, but liquid lubricants are invaluable as debris conveyors or as a means to provide a cooling-down effect at the contact site, for instance, in machining and cutting.

Functionalizing liquid and semi-solid lubricants with particle additives is a promising strategy to improve their performances and increase the life of both components and lubricants [86]. The role of graphene as an additive for oils and greases has been investigated for the last decade and has proven effective in reducing friction and protecting surfaces from wear. For instance, works by Senatore et al. [87] and Mao et al. [88] with graphene-enriched oils. A review of the relevant literature about graphene-enriched greases is presented in Section 4.2.

It was also claimed by previous investigations [89], [90] that graphene, like other carbon solid additives such as carbon nanotubes [91] or graphite, can affect the thermal conductibility of the lubricant with a beneficial effect on the contact temperature and related temperature-induced wear damages. Fu et al. reported an increment of 55% in thermal conductivity by enriching the grease with 4% graphene [92]. Thermal conductivity is an important feature of greases. The grease consistency prevents them from removing heat from the contact site by convection, as oils do, and thermal conduction is the only mechanism to shed heat in grease-lubricated contact. Actually, greases have limited applications at very high speeds because they can contribute decisively to the overheating of the system, and their lubrication mechanism may fail. Conductive solid lubricants added to greases as performance modifiers may improve the stability of greases by protecting them from thermal degradation and therefore extend their life or the time-to-relubrication.

State-of-the-art knowledge of grease lubrication, already addressed in Section 1.1.2, indicates that grease surrounding the contact is a reservoir that feeds the contact region in lubricant. Graphene additives can have a role in the complex mechanisms of grease lubrication: graphene may serve as a solid lubricant supporting the lubricating film when dragged into contact with grease. Grease-lubricated rolling contacts typically operate in starved film lubrication, whereas boundary lubrication is typical of grease-lubricated sliding contacts. In the former case, a thin pressurized film thicker than the characteristic roughness size ensures the separation between the surface asperities. Sliding boundary-lubricated contacts are particularly fragile because lubrication relies on a nanometric film adsorbed on surfaces. Lubrication is governed by the physical and chemical properties of this thin molecular film [93]. Since no hydrodynamic separation occurs between the solid bodies, lubrication works through a chemical mechanism rather than a mechanical action [94]. Scraping by the surface asperities promotes localized desorption of the physically (sometimes also chemically) absorbed layer, and consequently, direct solid-to-solid contact spots are easily restored. The desorption rate may overcome the lubricant feed rate under high loads and limited relative speed or excessive contact temperature. Severe wear may thus appear as a consequence, followed by heating-up driven by adhesion or abrasion [90]. Solid additives like graphene flakes can effectively reduce friction and wear in these extreme conditions. Section 4.1 provides some insight into the role of graphene as an additive for lubricating grease in these operating conditions.

4.1 The Role of Graphene-based additives in greases

In the presence of sliding at the interface, e.g., in the four-ball and pin-on-disc friction and wear tests, the regime of grease lubrication is usually boundary lubrication, even with the high relative speed at the interface. [95]. This is especially true when the surface is rough and the applied load is high because the lubricant bleeding from the grease reservoirs is insufficient to produce a hydrodynamic effect.

Graphene-based grease additives are composed of either graphene nanoplatelets (GNPs), also referred to as graphene flakes, or reduced graphene oxide (rGO) sheets. These nanoparticles usually have a slender laminar shape with very tiny thickness, usually in the range of 2-3 nm to 15-20 nm (comprising a few atomic carbon layers) and in-plane dimensions in the order of a few microns (Figure 59).

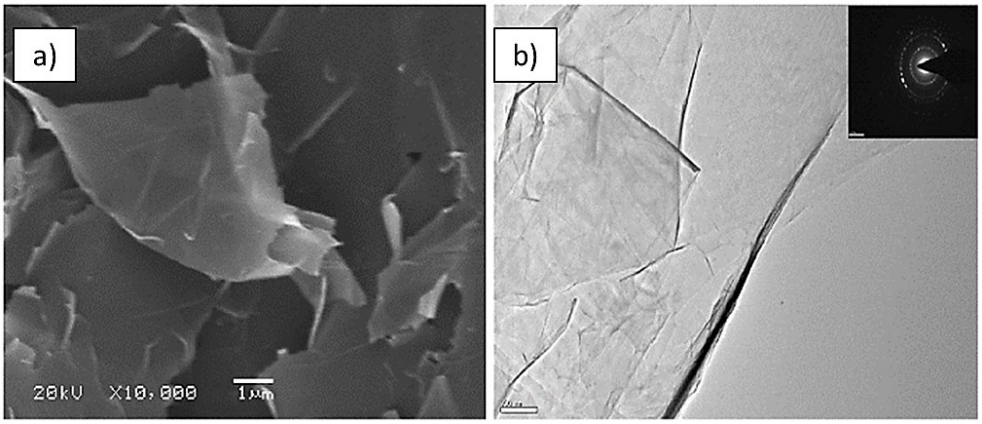

Figure 59. (a) SEM and (TEM) image of pristine graphene platelet used as nano-additive for grease. Adapted from [96].

According to Niu et al. [95] the reduction in the frictional side effects and the improvement of the anti-wear properties of grease by graphene-based additives should be attributed to three main factors:

- Interaction with the thickener molecules into the physical boundary lubrication film
- Physical adsorption of graphene on the tribological surface and shearing of nano-sheets

- ❖ Chemical reactions between graphene, grease molecules, metal debris and oxygen.

Graphene nano-platelets dispersed into the grease could easily enter the contact area due to their thin laminated structure and participate in the lubrication mechanism. The interaction between graphene and the soap molecules fosters such transportation of nanosheets inside the contact [97]. According to Niu et al., an appropriate concentration of graphene nanoplatelets strengthens the physical boundary lubrication film against the scraping effect of the asperities. Complex grease molecules are formed of a polar group (polar head) and a nonpolar hydrocarbon chain (see Figure 60). The polar head grabs onto the worn surfaces, and the nonpolar hydrocarbon chains are oriented away from the metal surface, as per the schematic in Figure 61. A physiosorbed protective boundary film is formed, and poor adhesion is promoted by the interaction among the hydrocarbon chains anchored to the opposite surface. Graphene interacts with the soap molecules (Figure 61 and), thus promoting physisorption [95] and thickening the structure itself of the soap fibres [97]. An appropriate amount of graphene flakes can also make the boundary film more stable so that it can withstand long-term friction without failure [98]

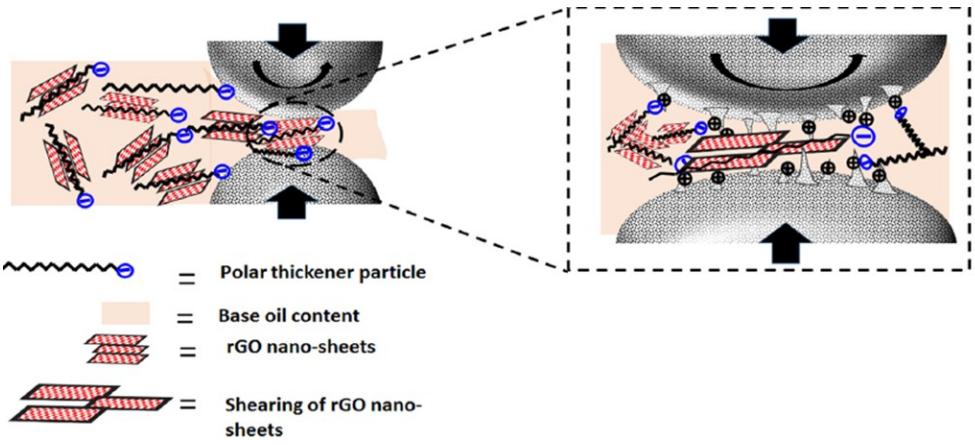

Figure 60. Schematic of carbon nanosheets participating in the lubrication mechanism. Adapted from [99].

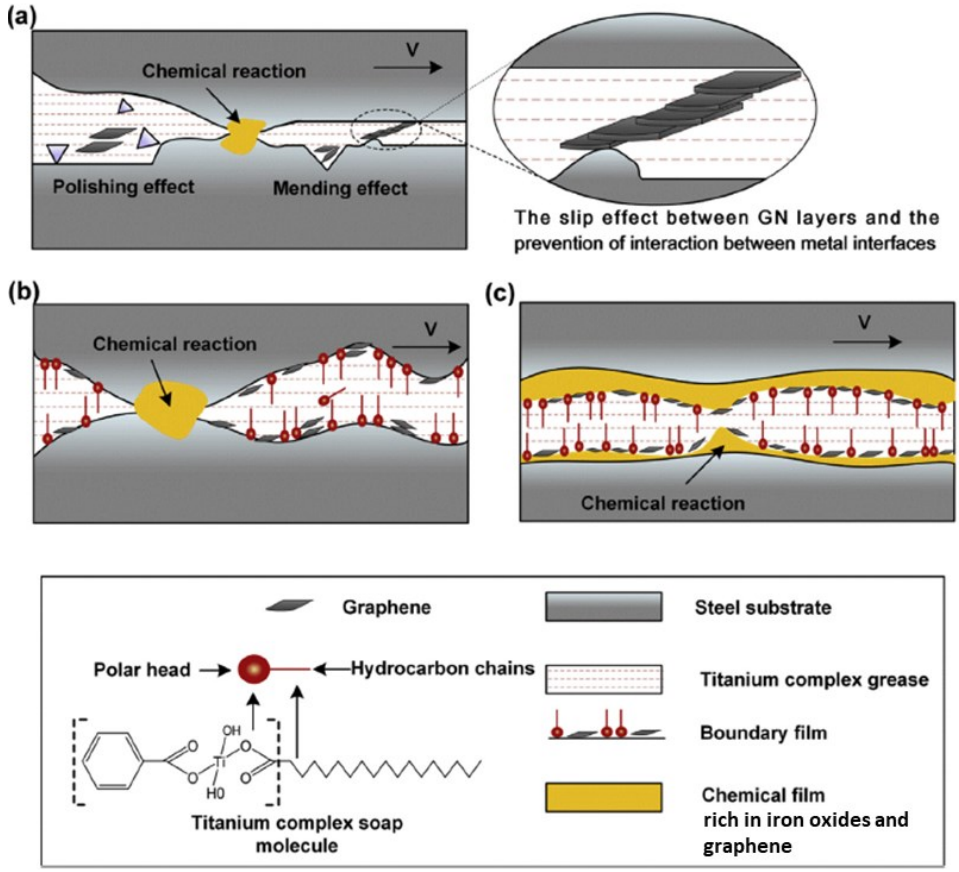

Figure 61. Schematic diagram of the lubricating mechanism involving GNPs inside the grease proposed by Niu et al. for the titanium complex grease they tested. (a) The effect of graphene on the physical boundary lubrication film with interlayer slip effect on friction reduction and load carrying capacity. (b) The chemical interaction between the soap molecules and GNPs. (c) The synergistic effect of the boundary lubrication film and the chemical reaction film rich in oxides. Adapted from [95].

Secondly, carbon nanosheets can participate physically in lubrication as a solid lubricant without any chemical reaction with the metallic surfaces, as they are physically absorbed on the worn surfaces [95]. The mechanical slip effect between graphene layers with laminated structures prevents direct contact between metal interfaces. The mobility of the carbon layers helps the asperities to slide past the others with limited adhesion, even in the event of transitory lubrication shortage under high applied load. Low friction slip can occur both inside multilayer graphene flakes and among thinner individual flakes [100]. While this mechanism is similar to that of conventional graphite additives, the main difference between graphite and graphene additives is to be found in the shape of the additive particles. Graphene platelets have superior performance

because they can easily enter the contact zone and cover the surface asperities with a 2D structure featuring favourable sliding planes. Graphite powder has spherical particles, which cannot contribute to relative motion as effectively as graphene due to the less favourable spatial orientation of sliding planes [100]. Besides, the laminated structure of graphene activates a mending effect by the deposition of graphene flakes onto the worn surfaces (Figure 61). Mending makes surfaces smoother, while the concave micro-holes are progressively filled with graphene [101]. Wang et al. [102] also pointed out, based on the results of SRV tests, that the increase of contact load favours the adsorption of graphene and the formation of a protective deposition layer on the contact surfaces. However, as soon as the contact load becomes overly high, the graphene-rich boundary layer thus formed is destroyed.

Lastly, graphene takes part in a series of chemical reactions involving grease and steel debris triggered by frictional heating of adhesion-abrasion in boundary lubrication. Complex inorganic chemical compounds consisting of oxides and carbides (e.g. Fe_3C) may form at the level of the asperities. Fragmented multilayer graphene retained within the structure of these tribo-reaction products forms a high-lubricity chemical reaction film (a third layer) that plays a synergistic role in protecting the steel from oxidation and improving the anti-wear properties of grease. The literature generally reports that the alleviation of wear in the presence of graphene additive in the grease coexists with a small number of iron oxides and the smoothening of the worn surface [94].

Singh et al. [103] pointed out that the concentration of nanoparticle additives plays a fundamental role in this delicate mechanism. A concentration-dependent trend of friction and wear is observed almost for any conventional lubricant additive. Low additive concentration promotes the formation of homogenous grease compounds in which graphene nanoparticles are evenly dispersed and segregated into the fibrous network, and the impact of the additive is mostly on viscosity [104]. Graphene is then dragged into the contact and released onto the contact surfaces with oil. This scenario is the optimum condition for the graphene flakes to achieve the highest effectiveness as an anti-friction additive since they preserve their distinctive bidimensional shape. However, if the concentration of graphene flakes is overly poor, it is statistically unlikely that graphene participates actively in the lubrication process. At higher additive concentrations, nanoparticles get easily agglomerated, disrupting the grease fibrous network. Degradation of lubricity usually occurs [104]. The motion of the agglomerates of nanoparticles gets restricted with consequent starvation of nanoparticles that

cannot enter the tribological contact (see Figure 62). The accumulation of carbon agglomerates at the contact inlet and the disruption of the grease network may even interfere with the bleeding of lubricating oil into the contact region, and the anti-friction and anti-wear properties of the grease are negatively affected.

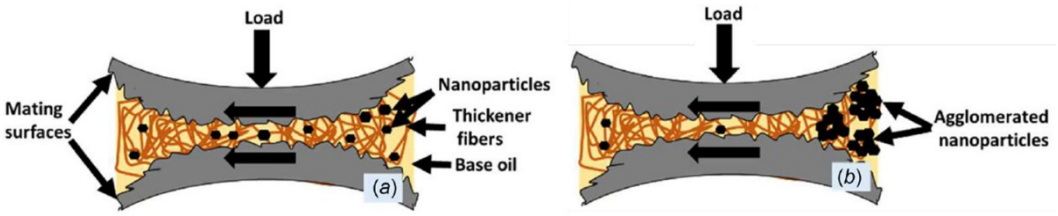

Figure 62. (a) The efficient flowing of nanoparticles into the contact at low concentrations of additive; (b) agglomerations of nanoparticles into larger clumps and accumulation at the contact inlet with high concentrations of the additive into the grease. From [103].

However, the experimental studies in the scientific literature proved that the threshold concentration levels corresponding to ‘low’, ‘optimal’ or ‘high’ quantity depend upon the given base grease. They cannot be defined universally. The combination of applied load, relative speed, and type of motion (rolling or sliding-rolling) may move the threshold for agglomeration of the nano-additive. The influence of the grease thickener structure dominates over separation due to EHL in slow-moving, highly loaded tribological contacts. The typical Stribeck curve of many greases [16] shows that the grease CoF does not increase as much as the base oil without any thickener with decreasing entrainment speed, and the film thickness remains stable or even increases. This behaviour is schematically represented in Figure 63. The grease thickener compensates for the lack of kinematic effect on the build-up of the lubricating film at the interface. It introduces extra load-carrying capacity by forming a highly viscous layer (see Section 1.1.2) deposited on the contact surface. A little graphene additive is needed because the flakes must be thoroughly dispersed into the fibrous thickener soap to actively participate in the lubrication mechanism.

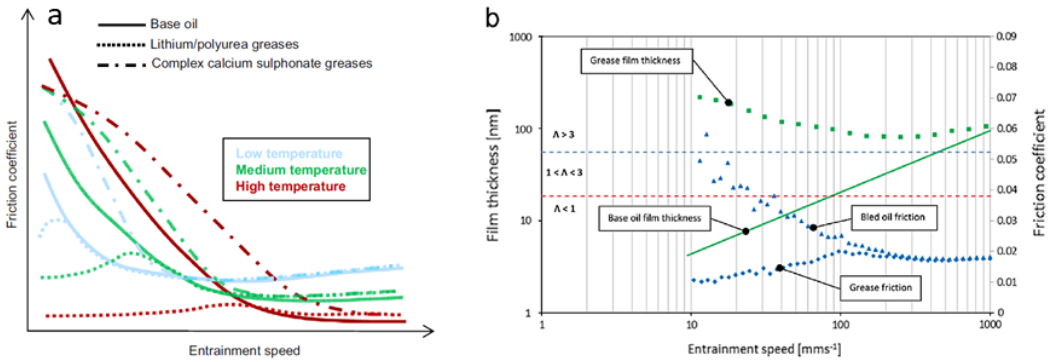

Figure 63. (a) Typical evolution of friction coefficient and film thickness for different classes of greases and their base oils; (b) Experimental measurement of the CoF and film thickness for a polyurea grease and its base oil. Adapted from [16].

In high-speed, lightly loaded contacts, more graphene is needed in grease to overcome the centrifugal force that throws a large part of the thickener fibres away from the contact region. Grease struggles to effectively lubricate the worn surface by oil bleeding, resulting in severe starvation, high local frictional heat and scuffing. A large number of graphene flakes is thus helpful. The graphene nanosheets are restacked/overlapped into thicker layers at such critical speed, and they could form a protective coating between the friction pairs. Besides, the increased amount of nano-additive retains more oil into the contact and easily overcomes severe scuffing.

Shear thinning of lubricant due to sliding promotes the damaging of the grease fibrous structure and increases the interaction between the dispersed nanoparticles leading to the formation of more agglomerates [103]. Pure rolling motion ensures the maximum entrainment speed and the minimum shearing effect on the lubricant. A higher percentage of graphene in the grease is permissible in this tribological condition because slightly larger agglomerated particles may have the chance to enter the contact region.

Together with concentration, the thickness of the graphene layers influences grease performance with nano-additives [100]. Thicker graphene platelets, i.e. those featuring many stacked carbon layers, have many favourable slip planes inside, but fewer could reach inside the contact zone due to their size. Therefore, they are less beneficial in reducing friction losses of grease-lubricated contacts. Very thin graphene platelets can populate the contact zone and cover the friction surfaces, but these flakes can only activate sliding planes between individual

platelets, which are less favourable. When platelets get agglomerated, their shape becomes spheroidal, and the activation of slip planes inside or among the flakes is complicated. This is also the case with graphite nano-particles. According to the results of Pape et al. the graphene platelets featuring the highest friction reduction are those with an average thickness of 6–8 nm.

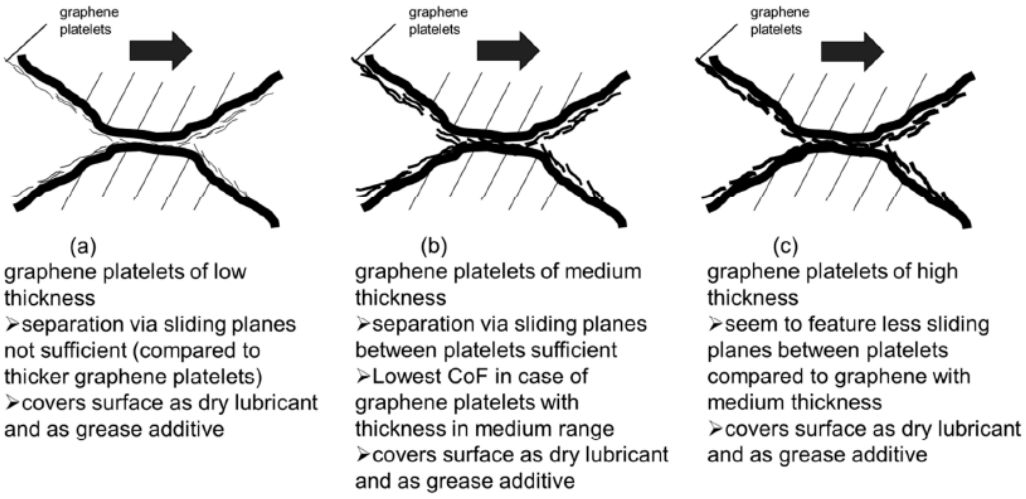

Figure 64. The schematic diagram shows the influence of the thickness of the graphene platelets on frictional properties and the interaction with the lubricating mechanism. From [100].

4.2 Literature review of laboratory tests on grease enriched by graphene nano-additives

Several studies have been published in the scientific literature to investigate the characteristics of grease additives and their ability to improve the performance of lubricants. This section reviews the state-of-the-art knowledge on the tribological behaviour of graphene-enriched greases, and the results of the leading research work on this topic are presented and compared. The results presented in this section are from simplified laboratory testing, such as the four-ball test, pin-on-disc test, and SRV reciprocating ball-on-flat, which reproduce in the most simplified manner the fundamental contact kinematics of mechanical components.

Wang et al. [102] investigated the effect of graphene on lithium grease performance and correlated the effect of the additive with that of applied load and contact geometry. They prepared grease compounds using MVI500 as base oil,

lithium 12-hydroxy stearate as the thickener and liquid-exfoliated graphene flakes in content from 0.2% to 2% wt.

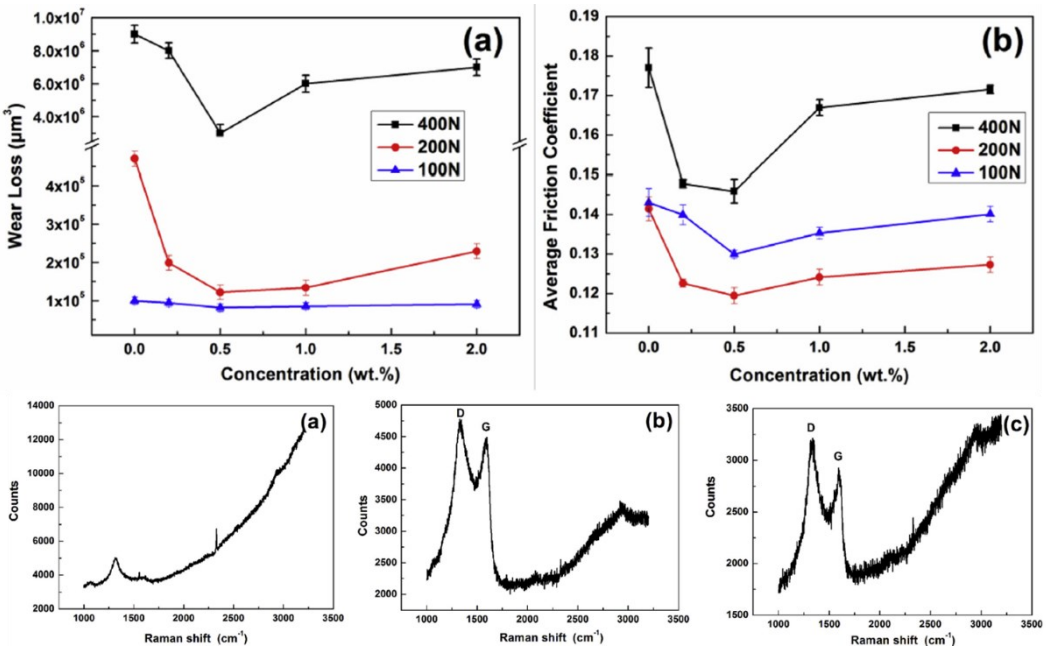

Figure 65. (a) Evolution of the material lost due to wear and (b) average friction coefficient vs the graphene concentration into the grease under increasing load. Raman spectra of the worn surfaces at (a) 100N, (b) 200N and (c) 400N. Adapted from [102].

Table 16: Testing parameters from **[102]**

Contact mode	Ball-on-flat SRV	Block-on-ring	Ring-on-ring
Load	100, 200, 400 N	100, 200, 400 N	1400 N
Speed	-	1200 rpm	1200 rpm
Frequency	50 Hz	-	-
Temperature [°C]	80	25	25
Sliding time	2 h	1 h	1 h
Track radius /stroke	0.9 mm	-	-

Sphere diameter	10 mm (ASTM D5707)	-	-
Sample dimension	-	n.d.	n.d.
Maximum Hertzian Contact pressure	2076 GPa to 3412 GPa	n.d.	n.d.
Grease type	MVI500 base oil, lithium 12-hydroxy stearate thickener		
Graphene concentration [%wt.]	0.2%, 0.5%, 1%, 2%		

Several tests were carried out with different setups, including reciprocating ball-on-disk SRV tests (non-conformal point contact), block-on-ring tests (non-conformal line contact) and ring-on-ring tests (conformal contact) in the condition listed in Table 16. The results (Figure 65) showed a significant reduction in both the average coefficient of friction and the wear loss thanks to the action of graphene. The beneficial effect was maximum with 0.5% wt graphene under any load. The maximum reduction of the CoF and wear was under 200 N, with a 15.5% and 74% reduction, respectively. Interestingly, the load had a stabilizing effect on the tribological behaviour of the system with the optimum quantity of graphene. The CoF was reduced when the load increased from 100 N to 200 N, and the wear loss slightly increased.

Raman spectra acquired on the worn surface revealed that the characteristic D- and G-peak of defective graphene were not detected under the lowest load, indicating that graphene struggles to settle at the interface and its addition into the grease has only minor effects. These peaks appeared instead under 200 N and 400 N in the Raman spectra. This evidence supports the hypothesis that graphene gives rise to a beneficial tribofilm only above a given pressure threshold. Such tribofilm avoids direct contact between metal bodies and inhibits wear by abrasion and adhesion. However, if the load is too high, the protective film is partially destroyed, which would justify why under 400 N friction and wear were higher.

Similar results were also observed under line contact, with a reduction of wear loss by 37.6% and a reduction of the average friction coefficient by 16.8%. In this case, however, the optimum percentage of graphene increased with increasing the

applied load, from 0.2 %wt under 100 N up to 1%wt under 400 N, and the dominant wear mechanism evolved from abrasion to adhesion.

Ouyang et al. [105] admixed lithium grease with 3D hierarchical porous graphene nanosheets (3D HPGS) with concentrations of 0.1 wt%, 0.3 wt% and 0.5 wt%. They focused their investigation on comparing different testing setups for sliding point-contact, i.e. four-ball tribometer (spatial rotating motion), rotating pin-on-disk tribometer (planar rotating motion) and reciprocating pin-on-disk (liner planar motion). Table 17 summarizes the test conditions used by Ouyang et al.

The results obtained by Ouyang et al. showed that a graphene concentration of 0.3 wt% offered the maximum reduction in the average COF, whatever the contact mode (Figure 66). In the case of the rotating pin-on-disk and linear pin-on-disk tests, the CoF was lowered by 20.3% and 16.3%, respectively. Similarly, the wear loss was reduced by 52% and 50.2 %, respectively. The four-ball tests also proved a remarkable performance improvement compared to the pure grease, which was still limited to 20.3% for friction and 23.6% for wear loss. The main beneficial effect on wear by the 3D graphene structure was to make the worn-out regions smoother and with less severe sliding scratches. The reduction of the depth or the width of the wear tracks sometimes complemented this main effect.

Table 17: Testing parameters from **[105]**

Contact mode	**Four-ball**	**Rotating pin-on-disk**	**Linear reciprocating pin-on-disk**
Load	700 N	10 N	20 N
Speed	1200 rpm	9.6 cm/s	2Hz
Distance	1800 m	1800 m	1800 m
Track radius /stroke	-	4 mm	6 mm
Sphere diameter	12.3 mm	3 mm	3 mm
Maximum Hertzian Contact	2.55 GPa	1.5	1.7

pressure	
Graphene concentration [%wt.]	0%, 0.1%, 0.3%, 0.5%

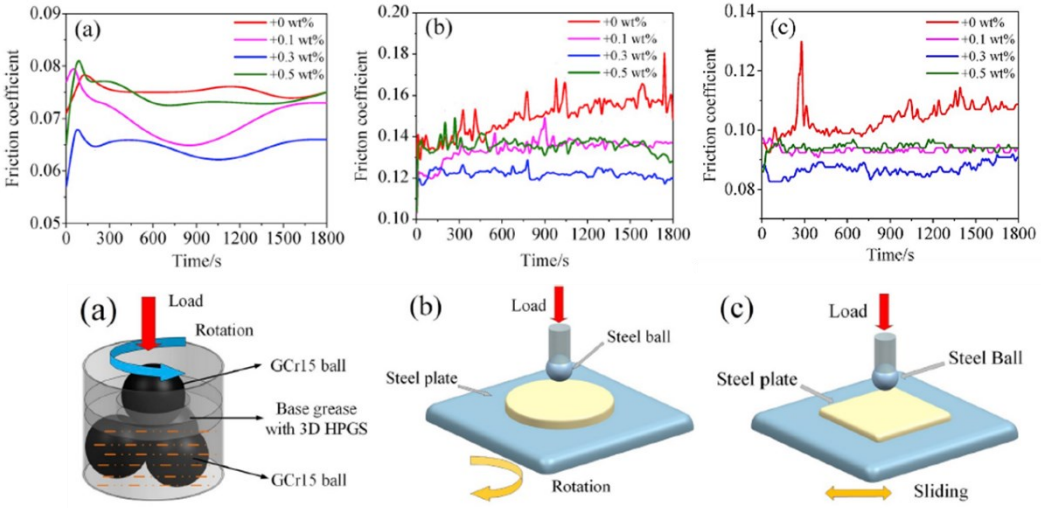

Figure 66. Measured friction curves with the three testing setups. (a) Four-ball tribometer, (b) Rotating tribometer, (c) Linear reciprocating tribometer. Adapted from [105].

Besides, the friction curves suggested that without the help of the additive, the friction trend would have wider fluctuations, perhaps due to the sudden rupture of the adsorbed lubricating film, which causes scuffing. Therefore, the authors concluded that the anti-wear property of the base grease could be enhanced effectively under heavy loads with the addition of 3D HPGS since the additive alleviated the adhesive-abrasive actions by preventing the metallic surfaces from direct contact even in the event of lubricating failure.

The contact surfaces were examined after the tests using EDS and Raman, and the results proved that a significant quantity of carbon matter corresponds to a damaged graphene structure left over from sliding. The typical Raman spectral bands (D-, G- and 2D-peaks) were detected, indicating that the 3D HPGS entered the rubbing interface and participated in the friction process. However, the intensity ratio I_{2D}/I_G decreased significantly compared to the pristine graphene-enriched grease, which was attributed to the trend of graphitization of the 3D HPGS because of tearing and shearing during the frictional process. The D- and G-peaks were more evident in planar rotational and linear reciprocating motion

than in spatial rotational motion (i.e., four-ball tests). The authors explained this finding suggesting that the lubrication mechanism was slightly different, even though it always involved the formation of a carbon tribofilm. The 3D HPGS tended to evolve to 2D graphene flakes in planar motion with more efficient action at the interface, whereas the additive was broken up into smaller pieces in spatial rotational motion but still retained its original porous structure.

Fan et al. [96] investigated the tribological performance of PAO-based bentone grease added with multilayer graphene (MLG) and compared graphene with other two types of grease additives, i.e. 5% wt. graphite and 5wt% of $[C_2OHMim][BF_4]$ ILs (a ionic liquid). Ball-on-flat tribological tests at room temperature were performed with graphene-enriched grease from 0.05 wt% to 0.5 wt%. The details on the testing parameters are provided in Table 18, and the results are reported in Figure 67. Their results suggested that the percentage of graphene which optimizes the performance is 0.1 wt% which outperforms the graphite-enriched grease within the range of load and speed investigated. The authors argued that the MLG persistently existed on the rubbing surface and ensured adequate lubrication because it readily adsorbs on the friction pairs, affecting the shear force magnitude and the heat dissipation at the interface.

Table 18: Testing parameters from **[96]**

Contact mode	SRV
Load	100 N, 200 N, 300 N, 400 N, 500 N
Speed	30Hz, 10 to 50Hz (at 300N)
Sliding time	1800
Stroke amplitude	1 mm
Sphere diameter	10 mm
Maximum Hertzian Contact pressure	2.20 GPa to 3.76 GPa
Graphene concentration [%wt.]	0.05%, 0.1%, 0.5%

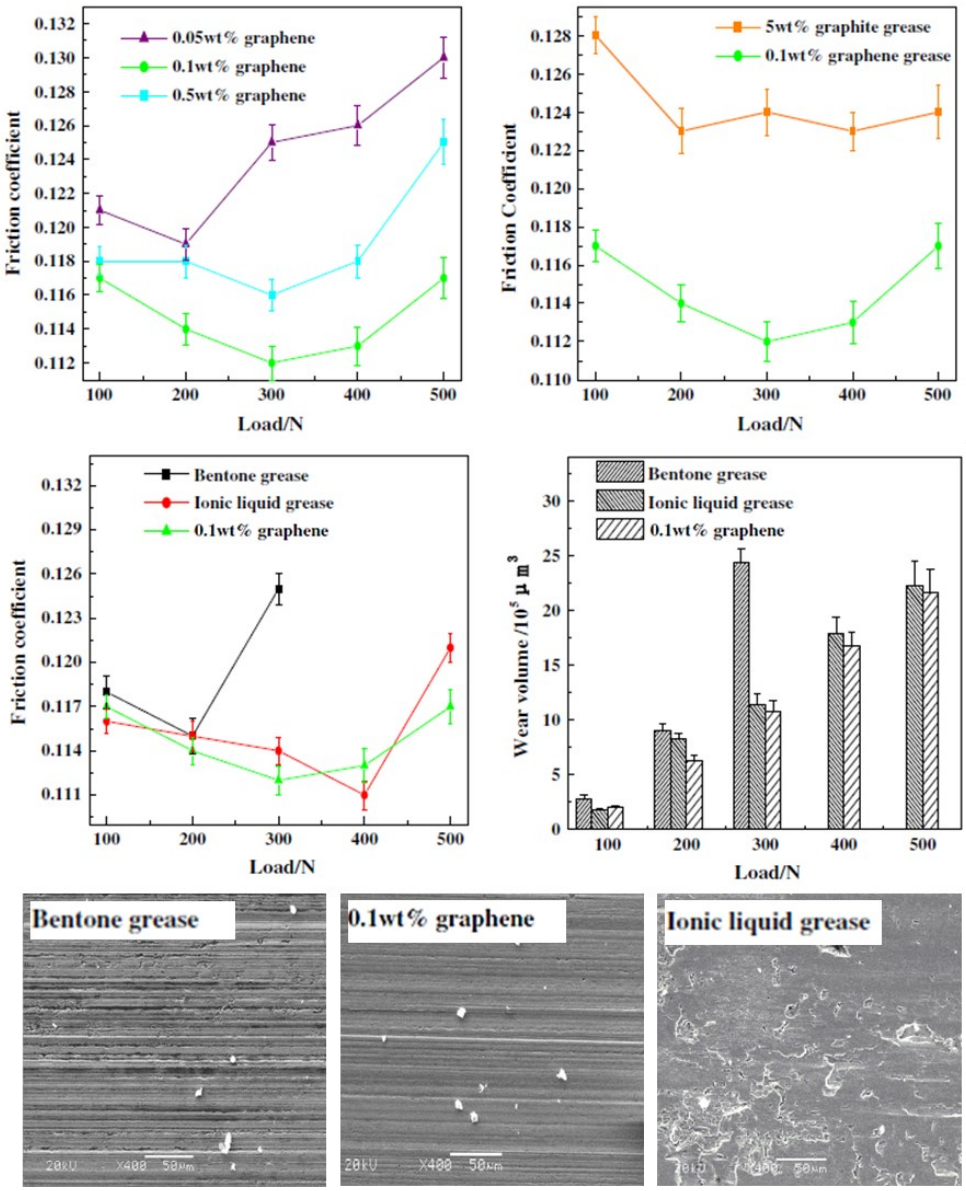

Figure 67. Friction and wear results were obtained by Fan et al. by lubricating the contact with graphene-enriched bentone grease. Adapted from [96].

Yet, an overly large quantity of additive (0.5%) seemed to inhibit the lubricious action of the additive. The reduction in the CoF was strongly dependent on the applied load, similar to what was observed by Wang et al. [102]. The effect of graphene was insignificant up to 200 N, whereas the optimum quantity of graphene (0.1 %) could halve both friction and wear loss under 300N. Friction and wear increased again above 300 N, and the improvement of the behaviour of the base grease was weakened. Overall, the behaviour of the grease with added

0.1% graphene and the ionic liquid grease was somewhat similar, and average CoF and wear loss were only slightly higher in the case of the ionic liquid grease.

SEM analysis and topographic inspection of the contact surfaces revealed that deep grooves from abrasive wear populated the worn-out region if pure bentone grease was applied. Lubrication by graphene-enriched grease produced a smoother wear track with lower depth. The ILs- grease reduced wear but also had a detrimental effect on the system because it induced adhesion as the dominant wear mechanism.

Fan et al. also performed tests at a temperature higher than ambient (150°C) and proved that 0.1% wt of graphene extended the extreme pressure properties of the base grease because it could thermally stabilize the lubricant. The results revealed that the graphene-grease compound had a low and stable CoF of 0.15 under increasing load, up to 500N.

Singh et al. [99] studied the tribological properties of reduced graphene oxide (rGO) added to commercially formulated lithium grease as lamellae. They tested the grease performance with a rolling-sliding ball-on-disk tribometer for testing EHD lubrication, where the sphere could also roll. They investigated the effect of the slide-to-roll ratio (SRR)[3] parameter.

Table 19: Rolling-sliding ball-on-flat testing parameters from **[99]**

Contact mode	**Pin-on-disk (EHD test rig)**
Load [N]	10N, 20N, 30N, 40N, 45N
Speed [m/s]	0.3 (SRR = 0.3% and 27%)
Sliding time [m]	n.d.
Track radius [mm]	n.d.

[3] The slide-to-roll-ratio parameter is the measure of the sliding component in the rolling motion of the ball-disc pair. It is calculated according to the mathematical relation: SRR (%) = $2*(u_1-u_2) / (u_1+u_2) \times 100$, where u_1 is the speed of disc and u_2 the speed of the ball (mm/s). In order to vary the SRR, the speed of ball is fixed, while speed of disc is varied.

Sphere diameter	19.05 mm
Maximum Hertzian Contact pressure [GPa]	0.6 GPa, to 1.2 GPa
Graphene concentration [%wt.]	0.2%, 0.4%, 0.6%

The tests were performed while varying the applied load, the graphene concentration and the SRR value. They also monitored the noise and vibration levels produced by the contact during the tribological tests. Details on the testing parameters are available in Table 19. The results showed a significant reduction in friction, especially with 0.4% of rGO in the grease.

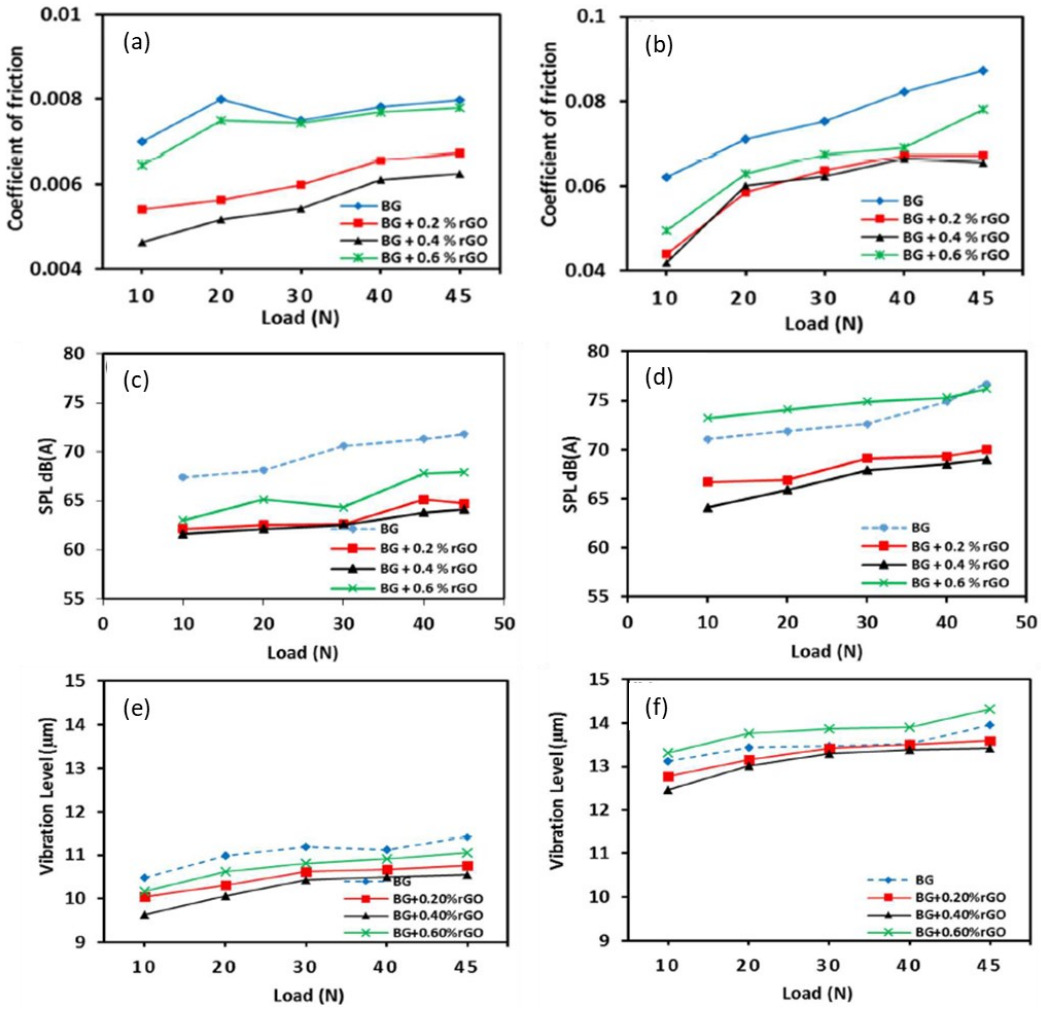

Figure 68. CoF, sound pressure level, and vibration level were measured by Singh et al. with ball-on-flat test tests. (a) 0.3% SRR and (b) 27% SRR w.r.t. a fixed rotational speed of the sphere equal to 0.3m/s. Adapted from [99].

These results confirmed that the improved performance of the composite grease might be attributed to the layered structure of rGO, but an excessive quantity of the nano-additive in the grease may reduce the beneficial effect on friction. This outcome was in line with what was observed by other researchers. With low SRR (i.e. near pure rolling), the system appeared more sensitive to the specific quantity of additive (Figure 68a). The quantity of graphene became less critical when some degree of sliding was present at the interface. The values of the CoF in Figure 68b are one order of magnitude higher than those in pure rolling due to the increased rubbing at the contact site, but the relative difference was lower.

The rGO additive also promoted a significantly smoother operation of the tribological system, with a reduction in the level of noise and vibration (see Figure 68c,d,e,f). 0.4% rGO was confirmed to be the optimum quantity of graphene, but the noise and vibration levels were susceptible to the additive content with high SRR, unlike friction. A higher concentration of rGO than the optimum worsened the operation of the tribological system indeed.

Kamel et al. [106] performed friction and wear tests on a SETA-SHELL four-ball tribometer with calcium grease as a lubricant.

Table 20: Four-ball testing parameters from **[106]**

Contact mode	**Four-ball (ASTM 4172)**
Load	200N, 400N, 600N, 800N
Speed	1200 rpm
Sliding time	60 min
Sphere diameter	12.7 mm
Maximum Hertzian Contact pressure	0.83 GPa to 1.3 GPa
Grease type	Calcium grease (Total MERKAN 23)
Graphene concentration [%wt.]	0%, 0.5%, 1%, 2%, 3%, 4%.

Six grease compounds with increasing concentrations in graphene nano-sheets (GNSs) were prepared by high-speed homogenization and stirring, and the performances were compared to the base grease under the same conditions. Table 20 lists the testing parameter used by Kamel et al.

According to the published results (Figure 69), the recommended concentration of graphene nanoparticles as an additive for calcium grease was 3% wt. The friction coefficient and the wear-scar diameter (WSD) decrease gradually with increasing the GNS content, up to a concentration of 3% by weight. When the GNS concentration reached 3%, thicker films were formed, which reduced wear. This trend is reversed for concentration higher than 3%, and higher friction and wear was observed with GNS concentration equal to 4%. The author attributed this positive effect to a thicker boundary lubrication film rich in GNSs that protected the rubbing surfaces from direct steel-to-steel contact during friction. The EDX analysis on the worn scar surfaces of the spheres supported this explanation. No evidence of carbon element appeared when the tribopair was lubricated by calcium grease, whereas residual traces of C (atomic concentration about 3.52%.) were detected at the contact site with the grease containing 3% of GNSs. According to the authors, the presence of carbon gives strong evidence that the GNSs into the lubricating film deposited onto the rubbing surfaces.

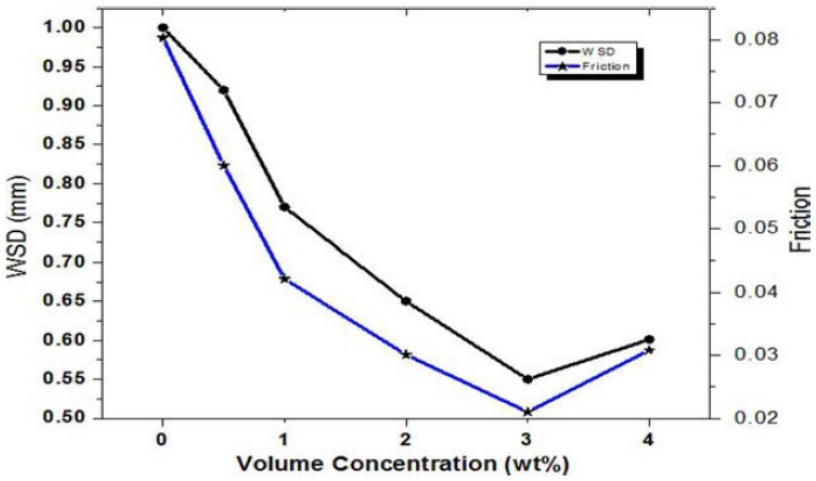

Figure 69**.** Evolution of the average friction coefficient and wear scar diameter (WSD) as a function of graphene nanosheet concentration under 400N load. From [106].

The behaviour of pure grease and the graphene-enriched compounds were compared under increasing applied load, as visible in Figure 70. The increase in the friction coefficient and wear scar diameter with increasing the contact load

was much smaller for the grease containing 3 wt% GNS. This increase indicated that the GNSs could effectively improve the base grease friction–reduction and anti-wear properties. The rubbing surfaces lubricated with grease containing GNS were also smoother than those observed using the base grease.

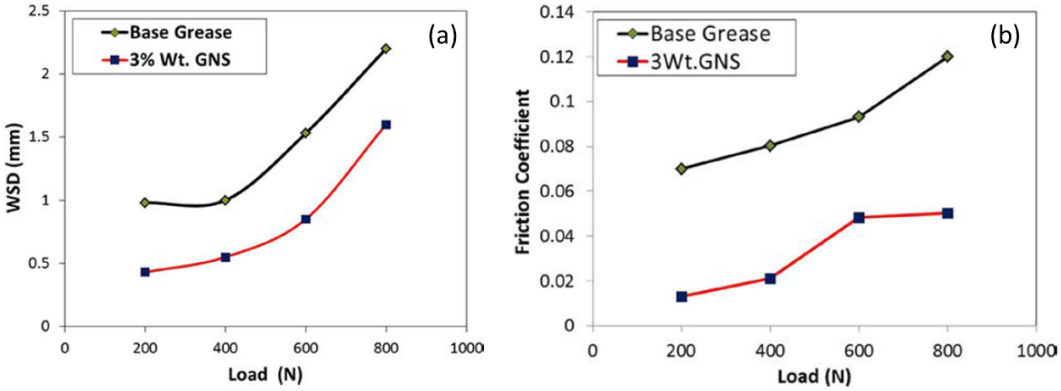

Figure 70**.** Impact of the applied load on the wear scar diameter (a) and friction coefficient (b) with the lubrication by pure calcium grease 3% wt. GNS calcium grease. From [106].

The four-ball tester also allowed the investigation of the maximum non-seizure loads (P_B value) for calcium grease with 3 wt% of graphene. The authors experienced an increase of the P_B value by roughly 60% following the addition of the optimal quantity of graphene, as reported in Table 21, and it meant that the extreme-pressure property of the calcium grease could be improved by graphene.

Table 21: Maximum non-seizure load (PB value) of pure calcium grease and 3 wt% GNS/calcium grease, from **[106]**

	Pure Calcium grease	Calcium grease + 3% wt. GNS
P_B (N)	150	240

Lin et al. [107] modified a commercial lithium grease with graphene in different concentrations. They investigated the modification of the lubrication behaviour using a four-ball tester under slow-moving, heavily loaded (SMHL), moderate load-speed (MLS), and high-speed lightly loaded (HSLL) conditions contact interfaces. Table 22 resumes the testing conditions.

It was evident from the results of this paper, summarized in Figure 71, that adding graphene improved the friction reduction and anti-wear performance of the

grease remarkably. Grease with 0.07% graphene addition exhibited the best performance among all nano-greases for slow-moving, highly loaded (SMHL) contacts. The mean values of CoF and wear scar diameter were reduced significantly by 19.6% and 19.1%, respectively, compared to the base grease. The friction curves were also more stable, and no evidence of lubrication film breakdown appeared, as was the case for the grease with no nano-additives where adhesion and micro-welds occurred.

Table 22: Four-ball testing parameters from **[107]**

Contact mode	Four-ball SMHL	Four-ball MLS	Four-ball HSLL
Load	686 N	392 N	98 N
Speed	800 rpm	1200 rpm	1600 rpm
Sliding time	30 min		
Sphere diameter	12.7 mm		
Maximum Hertzian Contact pressure	2.74 GPa	2.29 GPa	1.44 GPa
Grease type	Lithium grease		
Graphene concentration [%wt.]	0.03%, 0.07%, 0.15%, and 0.3wt %.		

Very similar behaviour was observed in medium load and speed (MLS) contact conditions. The addition of graphene always prevented the friction curves from fluctuating due to local failure of the lubrication mechanism, but the fraction in graphene additive to achieve optimum tribological performance was higher. The grease with 0.15% graphene was found to be the optimum compound. The average CoF was as low as 0.076, resulting in a reduction of 26.9%. Similarly, the most significant reduction in WSD by 20.5% ($p < 0.01$) was achieved with the same graphene concentration.

When the sliding speed was the highest and the load the lowest (HSLL), intense fluctuations of the friction curves with sharp peaks also appeared for some greases with moderate graphene content. This occurrence was probably due to the

centrifugal force, which threw most of the grease out of the contact site, leading to severe lubrication starvation [16]. In this scenario, metal-to-metal contact occurs unless the graphene additive content is sufficient to shield more rubbing surfaces for wear protection. Therefore, for this case, the 0.3% concentration of nano-additive provided the lowest average coefficient of friction (improved by 20.6%) and the lowest amount of wear loss (significantly reduced by 36.1%).

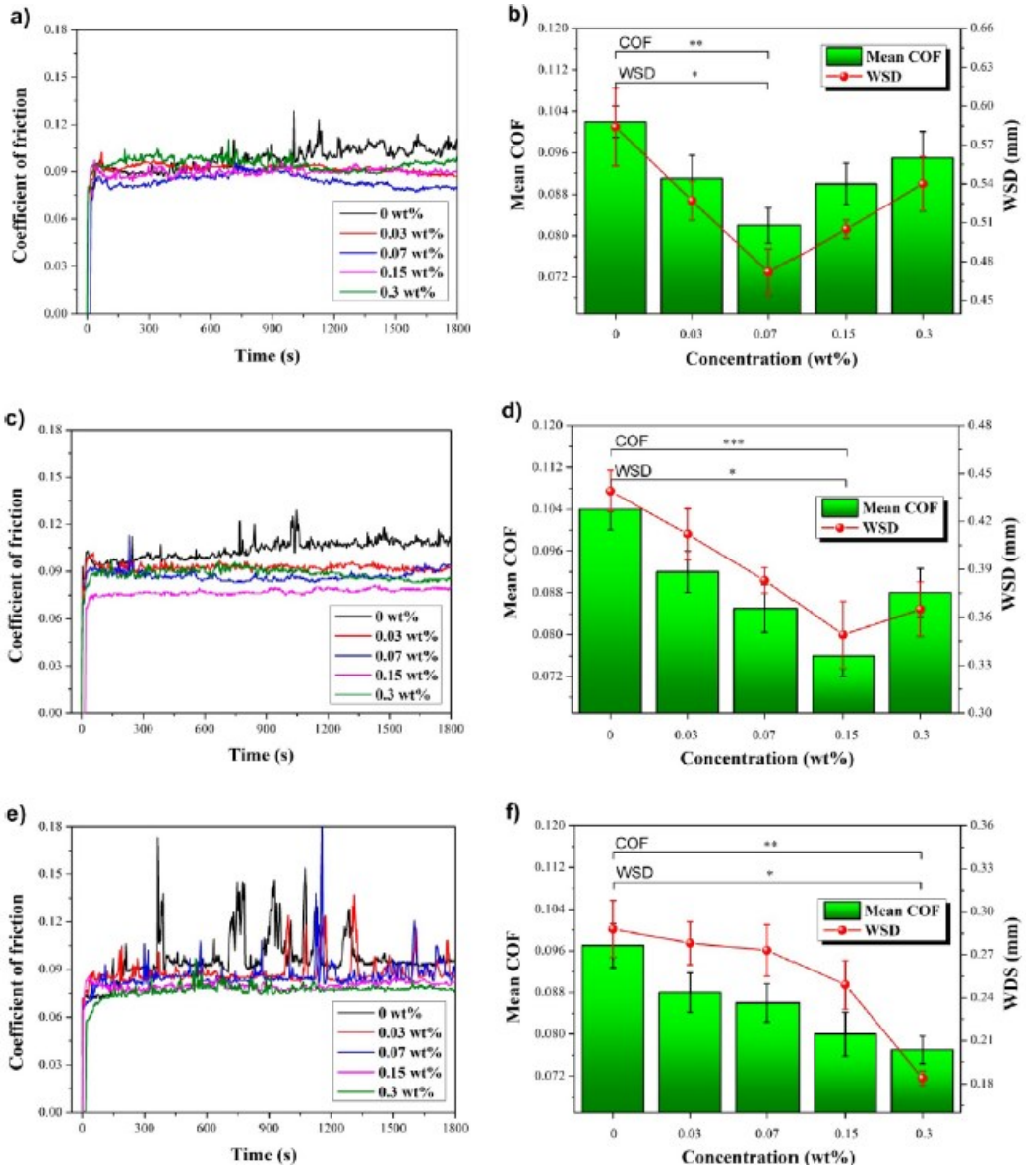

Figure 71. Friction and wear behaviour obtained by Lin et al. testing lithium grease with graphene nano-additive in SMHL (a-b), MLS (c-d) and HSLL (e-f) contact conditions. Adapted from [107].

According to these experimental results, the higher the rotational speed, the larger the quantity of graphene additive required to protect the rubbing surfaces effectively. Interestingly, the authors pointed out from the topographical analysis of the worn scars that the presence of graphene nanoparticles as an additive reduces the depth of furrows and the surface roughness, thus alleviating wear. The optimal percentage for friction and wear resulted in the smoothest and most regular wear scar.

SEM and EDS analysis suggested that with the optimal graphene concentration, the nanosheets prevented direct contact between steel surfaces by forming a physical deposition film and tribo-chemical film. EDS signal detected, indeed, an increased residual quantity of graphene and agglomerated carbon elements inside the wear scar. The easy interlayer sliding due to the weak van der Waal bonds among the graphene flakes promoted the enhancement of the friction performance of lithium grease observed in friction tests. Raman spectroscopy allowed the authors to analyze the structure of the residuals of the graphene deposition layer. The increasing (ID/IG) ratio with increasing the additive concentration in the grease indicated that more sp^3 amorphous carbon and graphitic domains formed in the sp^2 carbon network of graphene during the shearing and tearing process. These findings supported the conclusion that the graphene tribofilm was not easily damaged during sliding because of its excellent structural strength, effectively reducing adhesive wear and accommodating abrasive wear.

Mohamed et al. [108] tested a hybrid calcium grease admixed with multi-walled carbon nanotubes (MWCNT) and graphene nanosheets (GN). They prepared four compositions of 0.5%, 1%, 2%, and 3% by weight, where the two nano additives were taken in a proportion of 1:1. Table 23 resumes the test conditions.

The tribological results obtained with a Seta-Shell four-ball tribometer proved that the coefficient of friction continuously reduced as the additive content in the calcium grease was increased (Figure 72). Adding 3% MWCNT/GN reduced the average friction coefficient by 63.2%. As to the wear-scar diameter (WSD), introducing a small quantity of nano-additives (just 0.5%) reduced the wear loss during the test by 60%. The further increase in the additive content brought about a moderate improvement of the anti-wear properties of the grease with a maximum reduction of the wear loss at 73.6% with the highest quantity of nano-additive in the grease. The improvement of the anti-wear properties of the grease was also reflected in the maximum non-seizure load, which increased from 150 N

in the case of base calcium grease to 250 N for the grease admixed with 2% of MWCNT/GN. Interestingly, the authors investigated the effect of the nano-additive on the base grease thermal conductivity. They observed that the conductivity increases almost linearly as the nano-additives content increases, as visible in Figure 72b.

Table 23: Four-ball testing parameters **[108]**.

Contact mode	Four-ball
Load	20 N
Speed	1450 rpm
Sliding time	60 min
Sphere diameter	12.7 mm
Maximum Hertzian Contact pressure	0.81 GPa
Grease type	Calcium grease (Total MERKAN 23)
Graphene concentration [%wt.]	0.5%, 1%, 2%, 3%

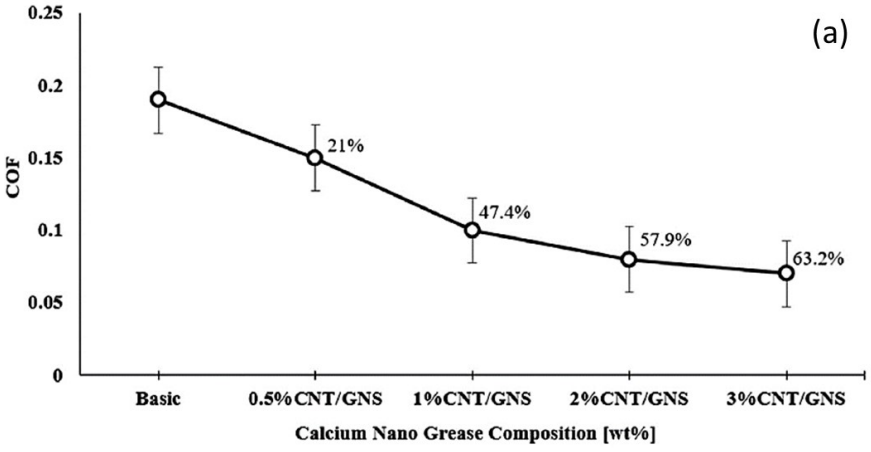

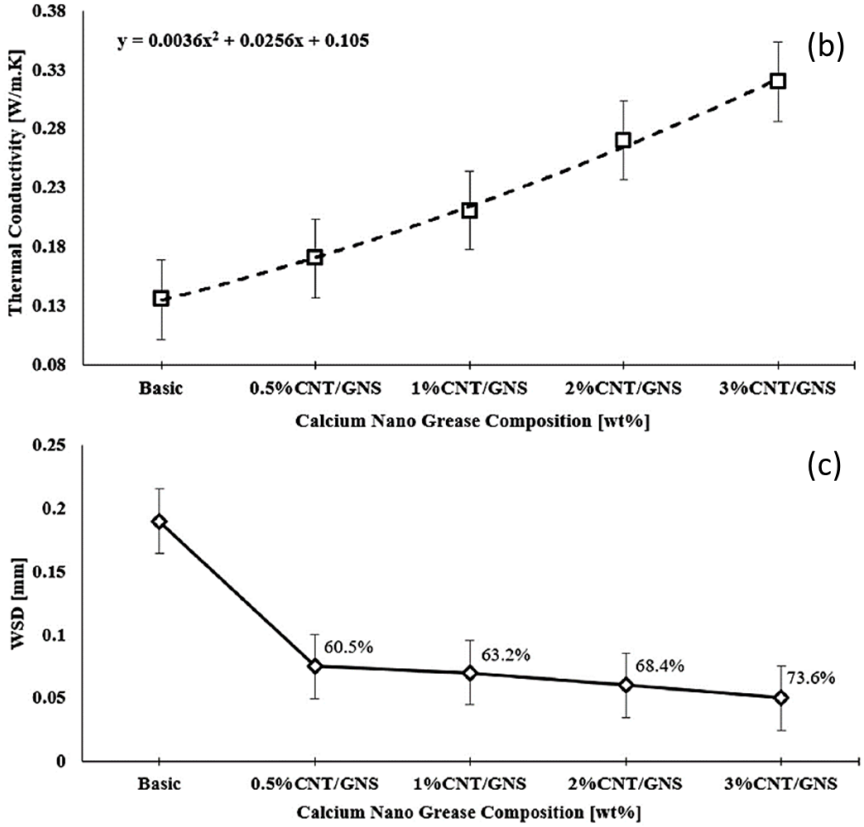

Figure 72. (a) The average coefficient of friction, (b) WSD and (c) thermal conductivity values obtained by Mohamed et al. with Merkan 23 grease admixed with increasing content in graphene nano-sheets and multiwalled carbon nanotubes. From [108]

The authors did not investigate higher quantities of nano-additives purposedly (even though further reduction of the COF and wear might be expected) because problems in the homogenization of the grease compound would be very likely, such as agglomeration and segregation of the additives. The homogenization of the compound gets challenging and may lead to the breakage of MWCNT when the amount of MWCNT/GNS additive exceeds the 2% threshold due to the related increase in shear stress and viscosity (Figure 73). Therefore, the authors selected 2% MWCNT/GNS as the best compromise to obtain better lubrication and tribological performance under severe loads, also considering the costs.

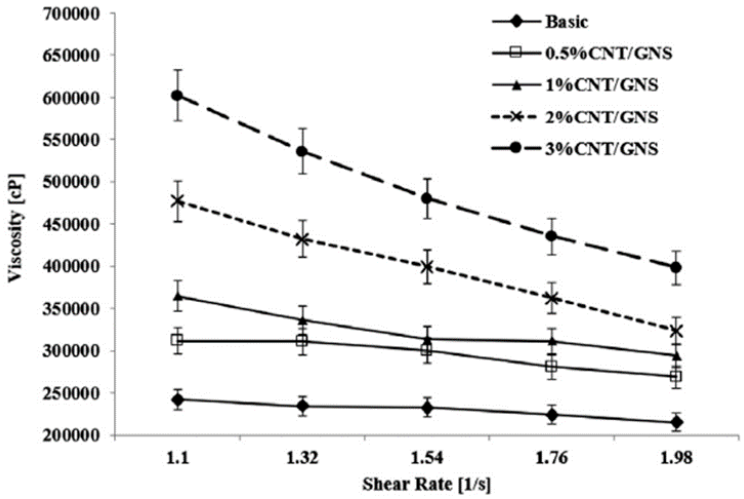

Figure 73. Viscosity vs Shear rate curves by Mohamed et al. for the nano-grease they prepared [108].

Xie et al. [94] explored the effect of multilayer graphene (MGr) as an additive for a lubricating grease composed of esters of fatty acids and triterpenes derived from a plant wax. The performance of the mixture was evaluated on an Optimol SRV-IV tribometer in oscillating high-frequency ball-on-flat reciprocating mode. Testing was carried out under increasing load and temperature through ramp tests, according to the testing parameters listed in Table 24.

The results of the friction test, presented in Figure 74a, showed that the bio-grease admixed with graphene presents stable frictional behaviour over the entire load range. Figure 74b and Figure 74c compare the average friction values and the friction curves obtained under constant 250 N and 300 N with pure bio-grease and enriched bio-grease. A slight reduction of the friction coefficient from 0.13 to 0.123 was observed under 250 N. On the other hand, the behaviour was dramatically different after adding MGr at 300 N. Pure bio-grease ran into lubricant film failure after just a few seconds from the start of the test. At the same time, the presence of the additive stabilized the lubricating film at the contact interface and the CoF.

Table 24: Testing parameters of reciprocating ball-on-flat tribological test from **[94]**.

Contact mode	SRV ball-on-flat test Ambient temperature	SRV ball-on-flat test High temperature
Temperature	R.T.	50°C, 100°C, 150°C, 200°C, 250°C, 300°C
Load	100 N, 200 N, 250 N, 300 N,	100N
Speed	25 Hz (stroke 1mm)	
Sliding time	10 min friction tests, 20 min wear tests	
Sphere diameter	9.6 mm	
Maximum Hertzian Contact pressure	2.47 GPa to 3.56 GPa	
Type of Grease	esters of fatty acids and triterpenes (C. pilosula)	
Graphene concentration [%wt.]	n.d.	n.d.

The authors concluded that the addition of multilayer graphene was favourable to improving the extreme pressure lubrication property of the base grease. Although the additive had a limited effect on the reduction of the wear rate under high loads at room temperature (Figure 74d), the SEM analysis indicated that the worn surfaces of the AISI 52100 steel discs are smoother in the presence of MGr into the grease, and the grooves from abrasion wear were shallow. Composition analysis of the worn surfaces confirmed that the carbon content was much higher than for lubrication with base grease and a small quantity of multilayer graphene debris was also detected. According to the authors, this multilayer graphene debris provided low shear stress and formed a uniform lubricating film.

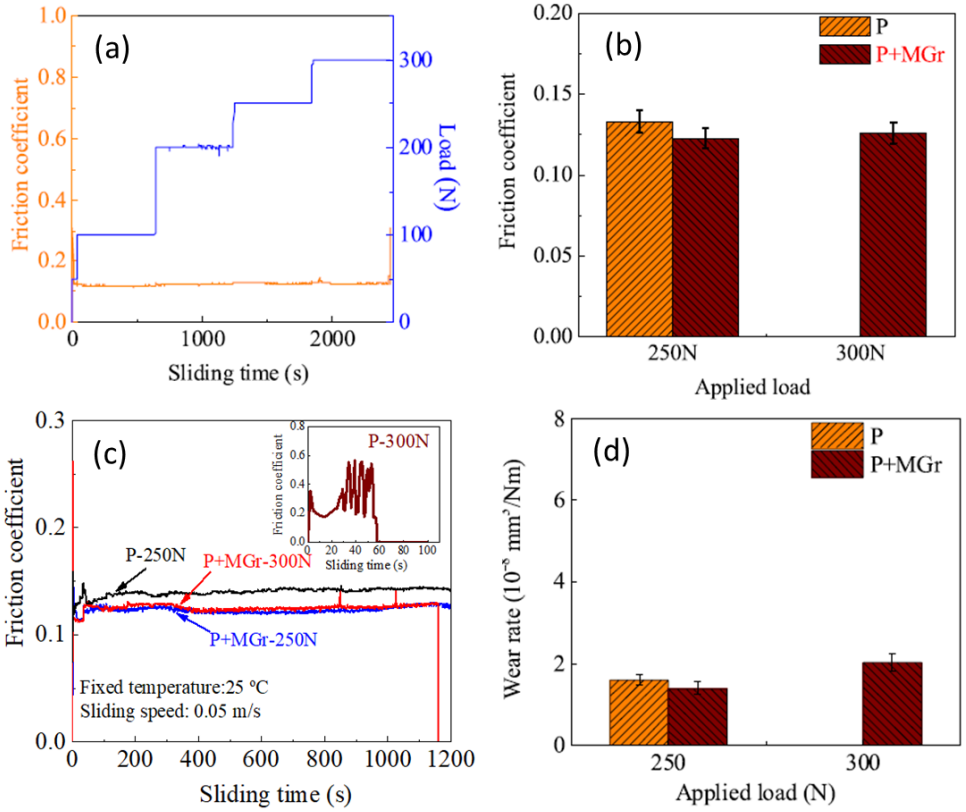

Figure 74. Results of the friction test under ramp increase of load (a) and wear test under constant load (b,c,d). Adapted from [94].

The friction coefficient proved to be very stable during the test with a ramp increase of the temperature within the range from room temperature to 300°C (Figure 74a), which is evidence of good thermal stability and excellent lubricity of the base bio-grease. Adding MGr contributes positively to the performance of the bio-grease at high temperatures in terms of wear rate. The higher the temperature, the more pronounced the wear damage reduction for the tribological pair, up to 35% at 250°C. Despite this, the corresponding average value of the CoF measured during wear tests at 150°C, 200°C and 250°C of Figure 74b was just slightly reduced. The maximum reduction of the CoF appeared at 250 °C, probably related to the accelerated melting of the mixture grease to form a lubricating film.

SEM inspection of the worn surfaces indicated that the worn surfaces at high temperatures exhibit severe oxidation, which justifies the increase in the wear rate with increasing temperature. Traces of deformation or delamination also appeared at 250°C due to the hardness decline and the enhanced tribo-oxidative wear

mechanism. Residual carbon particles were observed in the presence of graphene additive in the grease, contributing to lubrication in this situation.

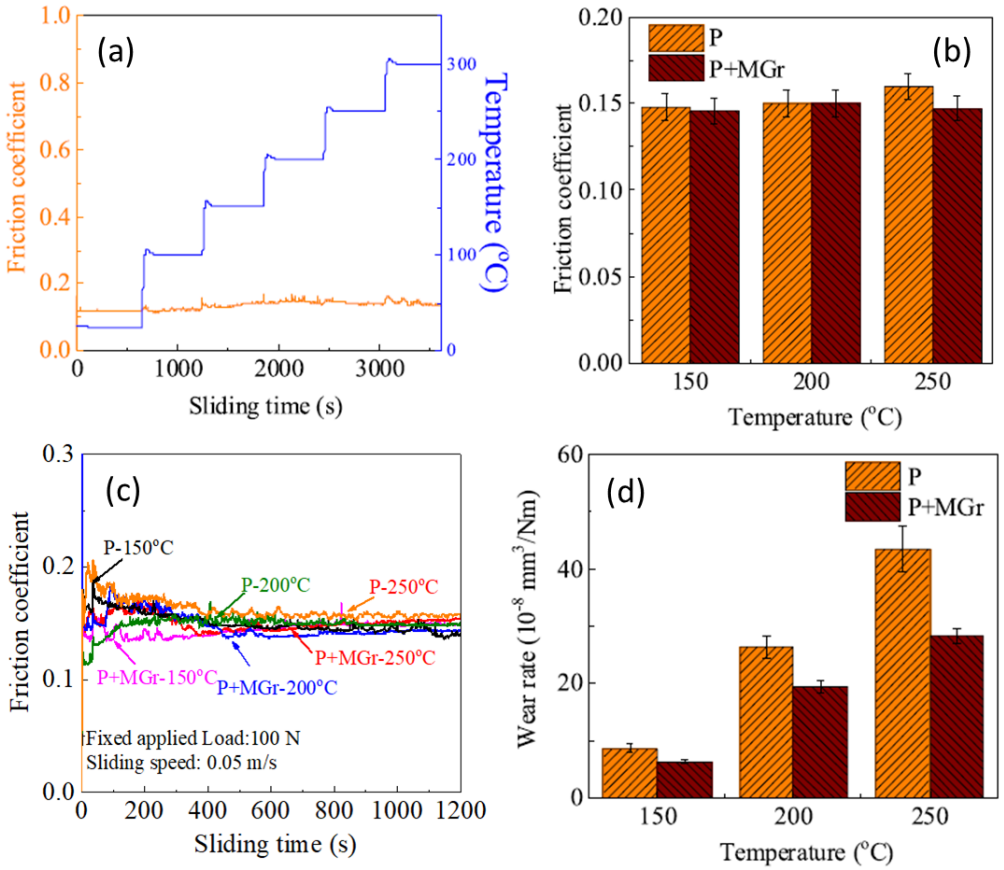

Figure 75. Results of the friction tests under ramp increase of temperature (a), and wear tests under constant high temperature (b,c,d). Adapted from [94].

Niu et al. [95] prepared two titanium-complex greases with a different base oil and investigated the effect of a minimal quantity of graphene nano-platelets, lower than 1%, as an additive package. The experimental activity was carried out using a rheometer for four-ball tribological tests. The test conditions are listed in Table 25. The results of the experimental tests (Figure 76) showed that the additive concentration had a different impact on the tribological properties of the two greases. Grease A was prepared with a mixture of 350SN oil and 150BS oil as base oil; Grease B was with 650SN base oil only. The optimum quantity of graphene was the same for both greases, equal to 0.06%.

Table 25: Test conditions from the paper by Niu et al.

Contact mode	Four-ball
Load	98N, 206N, 304 N, 392 N, 510 N
Speed	1450 rpm
Sliding time	60 min
Sphere diameter	12.7 mm
Maximum Hertzian Contact pressure	2.95 GP to 5.12 GPa
Grease type	Titanium complex grease A (350SN + 150BS oil) Titanium complex grease B (650SN oil)
Graphene concentration [%wt.]	0.02%, 0.04%, 0.06%, 0.08%, 0.1%

As to the average friction coefficient (AFC), the increase in the additive content had a similar impact on grease A and B because the respective base oils have similar anti-friction properties. When the concentration was 0.06 wt%, friction lowered by 21.99% and 21.25% compared to base grease A and B, respectively. A more significant amount of graphene let the AFC increase again, indicating that the antifriction effect was weakened if the dosage of GN was excessive.

On the other hand, the impact of the nano-additive content on the wear scar diameter was very different for the two greases. WSD plot of grease A remained approximately flat for every percentage of graphene, except the optimum 0.06%. The WSD plot of Grease B varied significantly with a similar trend as friction, where any variation from the 0.06% percentage gradually worsened the anti-wear properties. Compared with base greases A and B, the maximum reduction in the wear scar diameter was by 5.0% and 18.4%, respectively. This reduction was due to the better anti-wear properties of the mixture of 350SN and 150BS oil, making

grease less sensitive to any improvement in anti-wear properties driven by graphene.

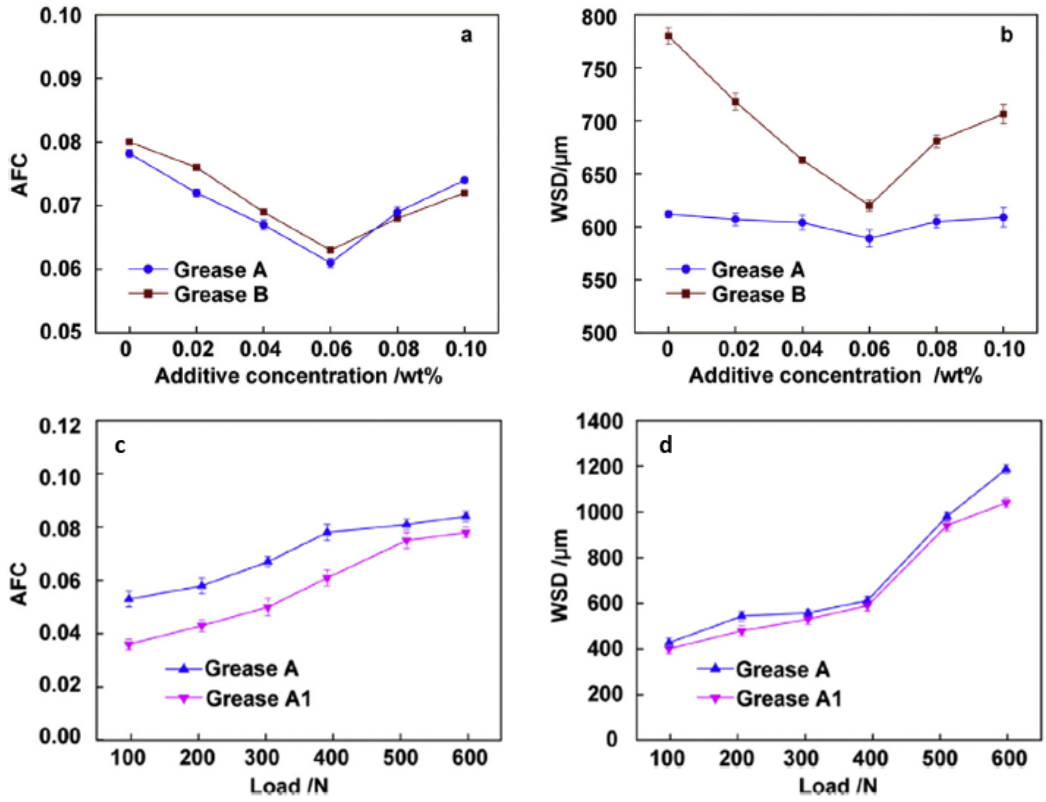

Figure 76. (a-b) AFC and WSD obtained by Niu et al. with Grease A (350SN oil + 150BS oil) and Grease B (650SN oil) under fixed 392N load at increasing concentration of graphene additive; (c-d) Evolution of AFC and WSD with increasing load for pure grease A and Grease A + 0.06%GN. Adapted from [95].

Figure 76c and Figure 76d show the AFC and WSD as a function of the applied load ranging from 98 N to 598 N for pure grease A and grease A enriched with 0.06% graphene. The addition of graphene could significantly decrease the AFC under any load. At the same time, the WSD remained approximately insensitive to the additive irrespective of the applied load. The authors explained the abrupt increase in WSD above 400 N with the fracture of the fibres into the fibrous network. The fracture of fibres may decrease the anti-wear effect if the threshold for maximum compression and deformation of the fibrous structure is exceeded.

The analysis of the worn surface showed that the morphologies of the contact sites were similar in terms of featuring scuffing streaks oriented in the sliding

direction. The main wear mechanisms were abrasion and microscopic adhesion. However, the depths of furrows on worn surfaces were shallower when the tribological contact was lubricated with the graphene-enriched grease because GN probably alleviated adhesion.

Wang et al. [98] prepared graphene-grease compounds using a semi-synthetic base oil (50% mineral and 50% PAO) and measured the rheological properties of the prepared compound with increasing graphene content. Rheological tests were performed with an MCR tribometer.

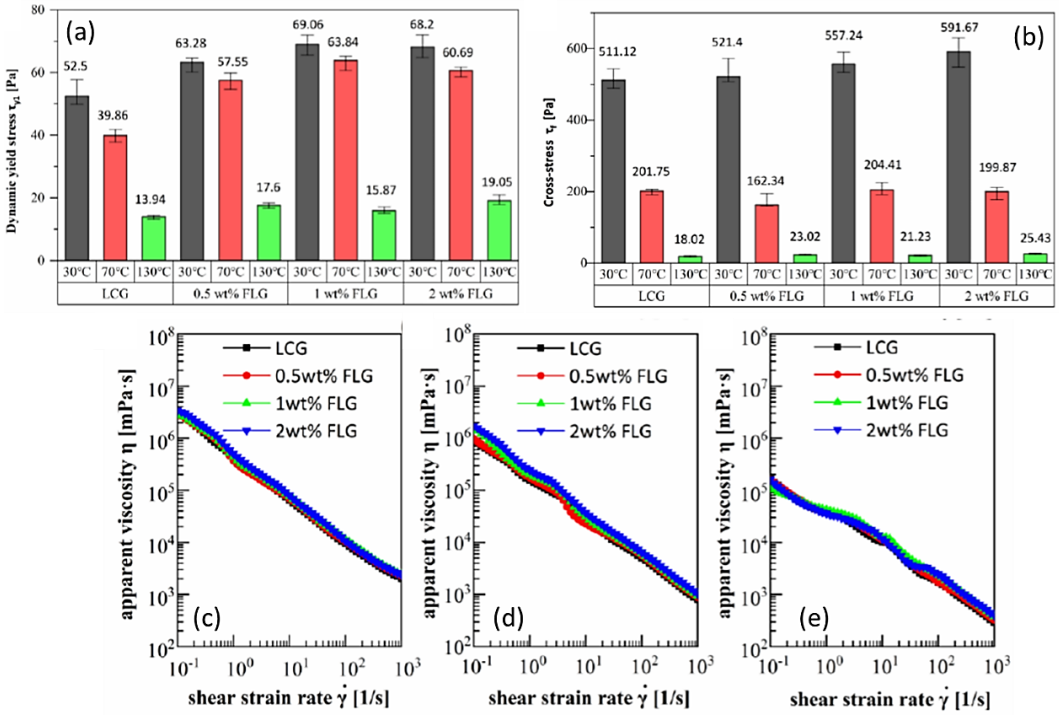

Figure 77. (a) Dynamic yield stress and (b) cross stress of grease compounds at increasing temperature; Evolution of apparent viscosity versus shear strain at (c) 30 °C; (d) 70 °C; (e) 130 °C. Adapted from [98].

Through amplitude sweep shear tests in oscillation mode at three test temperatures, i.e. 30 °C, 70°C and 130°C, Wang et al. proved that graphene increases the density of the fibrous structure of the thickener, thus increasing the ability of the grease to resist elastic deformation and viscous flow. The tangential storage modulus G' and the dynamic yield stress τ_{y1} expressed the elastic deformation, while the energy dissipated during viscous flow was expressed in terms of the loss modulus G'' and cross-stress τ_f. The dynamic yield stress is the

deviation point from linearity (where G' was approximately constant). The cross-stress represents the flow point of grease and is identified as the crossing point between the G' curve and G'' curve. It was found that graphene can improve elastic deformation with temperature by increasing the dynamic yield stress. Temperature mainly affects the viscosity of grease, and graphene was able to significantly modify the viscous response of grease (i.e. the cross-stress value) just at the lowest temperature.

Table 26: Test conditions from the paper by Wang et al.

Contact mode	**SRV test**
Load	90 N
Frequency	10 Hz
Sliding time	30 min
Sphere diameter	10.318 mm
Maximum Hertzian Contact pressure	2.04 GPa
Grease type	Lithium complex grease - 12-hydroxystearic acid as a thickener Base oil: 50% Mineral oil, 50% PAO
Graphene concentration [%wt.]	0.5%, 1%, 2%

The apparent viscosity and steady-state yield stress of grease compounds were also measured through steady-state rotation tests. Increasing graphene flakes resulted in a denser thickener microstructure, increasing the structural strength and flow resistance. Therefore, the higher the content of nano-additive, the greater the apparent viscosity and steady-state yield stress at any temperature. This evidence suggested that graphene could inhibit the temperature decrease of the yield strength and that 70 °C is the most suitable temperature level for graphene flakes to play a role.

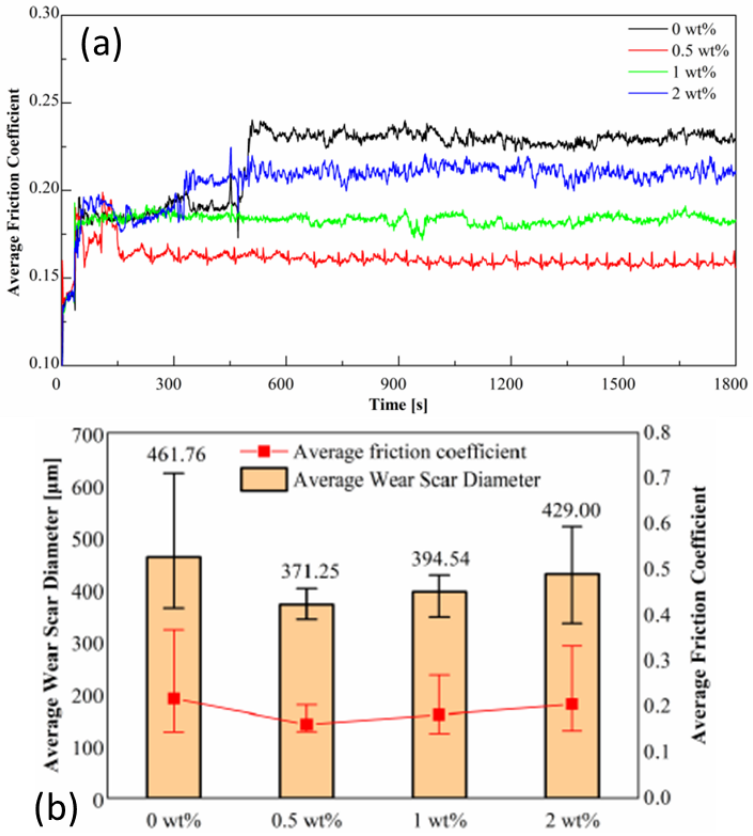

Figure 78. (a) Friction curves; (b) Average wear scar diameter and average COF with an increasing percentage of graphene into grease. Adapted from [98].

Additional tribological tests were performed with an SRV-4 reciprocating tribometer using a plate and a sphere made of GCr15 steel as the lower and upper pair, respectively. Test parameters are listed in Table 26. The results proved that 0.5% of graphene was the optimum quantity of graphene for the selected grease type. Pure grease alone formed a boundary film during the friction process, yet the film was quickly destroyed, resulting in relatively large wear and a fluctuating friction curve. 0.5 wt% graphene disclosed the best friction and wear performance. The amount of wear was minimal, and the friction curve was considerably stabilized due to graphene flakes in the grease. The authors argued that the boundary lubrication film formed faster thanks to the nano-additive and was more stable. Therefore, it could withstand friction without failure up to the end of the test (Figure 78). The flakes covered the friction surface when the percentage of graphene was too high, and the layered graphene structure changed continuously from a state of disordered polymerization to an ordered arrangement during the friction process. This state change affected the anti-wear and anti-

friction effect of the additivities grease, whose performance was just slightly higher than base grease.

Pape et al. [100] investigated graphene as both a dry lubricant and a nano-additive for a Barium complex, synthetic hydrocarbon-based grease. The test conditions are presented in Table 27. Just the results obtained with grease are referred to in this short review. To the best of the author's knowledge, the work by Pape and Poll is the only published research which reports the results of tests carried out with rolling bearings.

Table 27: Testing parameters from the paper by Pape et al. **[100]**.

Contact mode	**Ball against 3 cylinders (MCR302)**	**Two-bearing rig (wear test)**	**Two-bearing rig (friction test)**
Load	n.d.	n.d.	n.d.
Speed	0.00001 mm/s to 1 m/s	5Hz (oscillatory)	0.2Hz (oscillatory)
Duration	n.d.	55h	3h
Maximum Hertzian Contact pressure	1 GPa	1.5 GPa	1.5 Gpa
Grease type	Barium complex soap-thickened synthetic hydrocarbon-based		
Graphene concentration [%wt.]	1% / 2nm, 1% / 6-8nm, 1% / 11-15nm Graphite 1%/3-4nm		

Experiments were performed in pure sliding with an Anton Paar MCR302 rheometer and in reciprocating rolling conditions through a bearing test rig featuring two opposite-arranged angular contact ball bearings operated under oscillating motion. The bearings were grease lubricated with 8 mL grease. The authors compared the performance of spheroidal nano-graphite 3 nm in diameter with 2D-graphene flakes of different thicknesses, from 2 nm to 15 nm. The authors aimed to investigate the specific effect of the bi-dimensional structure of graphene and the impact of the thickness of flakes.

The Stribeck curve (Figure 79) at increasing sliding speed recorded with the MCR rheometer showed that the graphite nanoparticles give rise to little differences in the friction curve compared to the reference base grease curve. On the other hand, the presence of graphene platelets dramatically reduced the coefficient of friction, especially for low sliding velocities. According to the authors, this difference is attributed to the shape of the particle additive. The graphite powder has a nanometric spherical shape, whereas the graphene platelets have nanometric thickness but a few microns in diameter. Such a bidimensional shape favoured the activation of many sliding planes between the flakes that cover surface asperities.

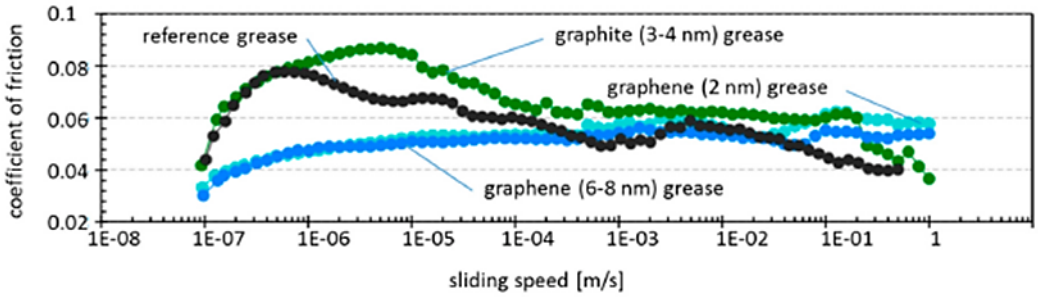

Figure 79. The coefficient of friction versus sliding speed cures in tests carried out with the MCR tribometer by Pape and Poll. From [100].

The friction tests of short duration carried out with the bearing test rig supported the evidence of simplified tribological tests. The friction torque measured with the modified grease was roughly halved in the case of graphene flakes 11–15 nm thick and 2 nm thick, as well as with graphite nanoparticles as a grease additive. The best performance was obtained with flakes of thickness 6–8 nm, thanks to which friction was reduced by a factor of approximately five. Figure 80 resumes the experimental results of the component tests.

The fretting tests on bearings ran for 55 h at 5 Hz with a constant pivoting angle of 48° (±24°). The results proved that wear and fretting corrosion could be detected at the reversal points on the raceway, where the lubrication mechanism of grease is weak. Moreover, a change in the surface colour was visible, and it was associated with the formation of an oxidative tribofilm. Any carbon additive could protect the raceway surfaces; only minor colour changes and small dark spots could be seen on the surface. No other sights of tribofilm formation or direct metal-to-metal adhesive wear appeared since the graphene nano-platelets

separated the solid surfaces, even if the relative motion was null and the lubricating film thickness was vanishing.

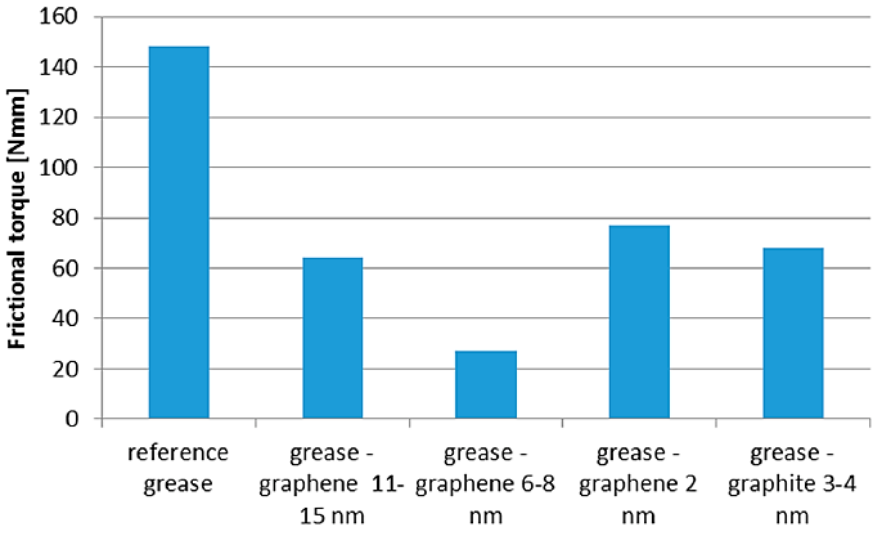

Figure 80. Results of the friction tests carried out with the bearing test rig [100].

4.3 Bearing rating life calculation and according to standards

The bearing rating life model proposed by ISO 281:2007 is based on the original model developed by Lundberg and Palmgren in 1947 [109]. Numerous studies in recent years proved that, although Lundberg and Palmgren's empirical relationship worked reasonably well at the time, it systematically under-predicts the fatigue performance of modern bearing steels of higher quality than those of Lundberg and Palmgren's time and modern lubricants. Hence the need for a modified version of the bearing rating life model able to take many more aspects of the actual operating conditions:

- the bearing loading history
- the fatigue limit of the material
- the extent to which the lubricant separates the surfaces
- the cleanliness of the lubrication gap
- the additive package in the lubricant
- the internal load distribution and frictional conditions in the bearing.

The rating life for a thrust ball bearing, i.e. the predicted value of the life based on a dynamic axial load rating with a given reliability $S = (100 - n)\%$ is given by equation (19) according to ISO 281:2007. The reliability $S = (100 - n)\%$ corresponds to the probability of survival of the bearing, where *n* is the probability of failure expressed as a percentage.

$$L_{nm} = a_1 \cdot a_{ISO} \cdot \left(\frac{C_a}{P}\right)^p \tag{19}$$

Where L_{nm} is referred to as the *modified rating life* expressed in million revolutions and associated with *n*% probability of failure, C_a is the basic dynamic axial load rating for thrust ball bearings, given by equation (20), P is the equivalent axial load applied to the bearing during operation, a_1 is the life modification factor for reliability that depends on the desired reliability (100-*n)%*, p is the exponent of the load-life equation equal to 3 for ball bearings, and a_{ISO} is the life modification factor proposed by the latest release of the standard. Recently, Londhe et al. pointed out that the load-life exponent for ball bearings is material-dependent. The value p = 3 works very well for AISI 52100 bearing steel of standard grade, but modern high-purity, high-performance steels require a higher load-life exponent; for instance, the exponent for ball bearings made of M50 steel bearings was reevaluated at 4.1 [110].

The reference probability of failure according to the standard is *n=10%,* and the related rating life L_{10} is referred to as the *basic rating life*. C_a is also a reference value since it represents the equivalent load a bearing would be able to carry while enduring 10^6 cycles with a failure probability of 10%, i.e. with basic rating life $L_{10} = 10^6$.

$$C_a = b_m \cdot f_c \cdot Z^{\frac{2}{3}} \cdot D_w^{1,8} \quad for \;\; D_w \leq 25.4mm;\; \alpha = 90° \tag{20}$$

In equation (20), Z is the number of balls carrying the applied load P in one direction; D_w is the nominal ball diameter (in millimetres); f_c is a factor which depends on the geometry of the bearing, the accuracy to which the various components are made, and the material; b_m is the rating factor for commonly used high-quality hardened bearing steel in accordance with good manufacturing practices, the value of which varies with the bearing type and design. The recommended value for b_m is 1.3, however each bearing manufacturer is free to

adapt this value to the quality level of their products, such that this factor also serves the purpose of a *safety factor* for metallurgical effects. The values of f_c are given in Table 28 as a function of D_w, D_{pw} (the pitch diameter of the rolling path) and α, i.e. the contact angle w.r.t the plane of the rolling elements and cage.

Table 28: Value of f_c for thrust ball bearings. These values apply to bearings with cross-sectional raceway groove radii not larger than 0.54 $\cdot D_w$ according to ISO/TS 16281:2008.

$\frac{D_w}{D_{pw}}$ [a]	f_c	$\frac{D_w \cos\alpha}{D_{pw}}$ [a]	f_c		
	$\alpha = 90°$		$\alpha = 45°$ [b]	$\alpha = 60°$	$\alpha = 75°$
0,01	36,7	0,01	42,1	39,2	37,3
0,02	45,2	0,02	51,7	48,1	45,9
0,03	51,1	0,03	58,2	54,2	51,7
0,04	55,7	0,04	63,3	58,9	56,1
0,05	59,5	0,05	67,3	62,6	59,7
0,06	62,9	0,06	70,7	65,8	62,7
0,07	65,8	0,07	73,5	68,4	65,2
0,08	68,5	0,08	75,9	70,7	67,3
0,09	71	0,09	78	72,6	69,2
0,1	73,3	0,1	79,7	74,2	70,7
0,11	75,4	0,11	81,1	75,5	
0,12	77,4	0,12	82,3	76,6	
0,13	79,3	0,13	83,3	77,5	
0,14	81,1	0,14	84,1	78,3	
0,15	82,7	0,15	84,7	78,8	
0,16	84,4	0,16	85,1	79,2	
0,17	85,9	0,17	85,4	79,5	
0,18	87,4	0,18	85,5	79,6	
0,19	88,8	0,19	85,5	79,6	
0,2	90,2	0,2	85,4	79,5	
0,21	91,5	0,21	85,2		
0,22	92,8	0,22	84,9		
0,23	94,1	0,23	84,5		
0,24	95,3	0,24	84		
0,25	96,4	0,25	83,4		
0,26	97,6	0,26	82,8		
0,27	98,7	0,27	82		
0,28	99,8	0,28	81,3		
0,29	100,8	0,29	80,4		
0,3	101,9	0,3	79,6		
0,31	102,9				
0,32	103,9				
0,33	104,8				
0,34	105,8				
0,35	106,7				

[a] Values of f_c for $\frac{D_w}{D_{pw}}$ or $\frac{D_w \cos\alpha}{D_{pw}}$ and/or contact angles other than those shown in the table are obtained by linear interpolation.

[b] For thrust bearings $\alpha > 45°$. Values for $\alpha = 45°$ are given to permit interpolation of values for α between 45° and 60°.

As to the life modification factors, the values of a_1 are derived by applying the rules of the Weibull statistics according to ISO/TR 1281-2:2008. Experimental observations confirmed that the two-parameter Weibull statistics describe with sufficient accuracy the scattering of the fatigue life for a reliability of 90% or lower ($L_{\geq 10}$), and a_1 is calculated as per equation (21), where e is the Weibull exponent ($e \leq 1.5$). For higher reliability ($L_{\leq 10}$), the three-parameters Weibull statistic must be introduced, and a_1 is calculated according to equation (22). The values of a_1 accepted by the ISO 281:2007 standard are provided in Table 29.

$$a_1 = \left[\frac{ln(100/S)}{ln(10/9)}\right]^{1/e} \tag{21}$$

$$a_1 = 0.95 \cdot \left[\frac{ln(100/S)}{ln(10/9)}\right]^{2/3} + 0.05 \tag{22}$$

For a_{ISO} practical methods have been developed to determine its value. a_{ISO} considers the fatigue stress limit of the bearing steel and the influence of temperature on it, the influence of lubrication method and lubrication regime related to operational parameters and temperature, and the presence of edge stresses and indentations due to contaminations into the lubricant.

Table 29: Life modification factor for reliability a_1 from iso 281:2007.

Reliability %	L_{nm}	a_1	Reliability %	L_{nm}	a_1	Reliability %	L_{nm}	a_1
90	L_{10m}	1	99	L_{1m}	0,25	99,9	$L_{0,1m}$	0,093
95	L_{5m}	0,64	99,2	$L_{0,8m}$	0,22	99,92	$L_{0,08m}$	0,087
96	L_{4m}	0,55	99,4	$L_{0,6m}$	0,19	99,94	$L_{0,06m}$	0,080
97	L_{3m}	0,47	99,6	$L_{0,4m}$	0,16	99,95	$L_{0,05m}$	0,077
98	L_{2m}	0,37	99,8	$L_{0,2m}$	0,12			

The general equation for a_{ISO} is expressed as per equation (23) [111] where *w* is equal to 1/3 for ball bearings, and *e* is the Weibull's exponent equal to 10/9 for ball bearings according to ISO/TR 1281-2:2008.

$$a_{ISO} = f\left(\frac{e_C C_u}{P}, \kappa\right) = 0.1\left(1 - \left(\eta_b(\kappa) \cdot \frac{e_C C_u}{P}\right)^w\right)^{-\frac{31}{3}e} \tag{23}$$

$$0.1 \leq a_{ISO} \leq 50$$

In equation (23) C_u is the fatigue load limit of the bearing (associated with the fatigue stress limit of the raceway material σ_u reached when the maximum Hertzian contact stress is approximately 1500 MPa), e_C is the contamination factor according to

Table 30, η_b the lubrication factor that includes the effect of the lubricating film thickness and surface roughness.

Table 30: General guidelines for determining the contamination factor e_C based on the level of contamination of the lubricant[4]. A detailed method for estimating the contamination factor is also described in the ISO/TR 1281-1:2008 as an alternative.

Level of contamination	e_C	
	$D_{pw} < 100$ mm	$D_{pw} \geqslant 100$ mm
Extreme cleanliness Particle size of the order of lubricant film thickness; laboratory conditions	1	1
High cleanliness Oil filtered through extremely fine filter; conditions typical of bearing greased for life and sealed	0,8 to 0,6	0,9 to 0,8
Normal cleanliness Oil filtered through fine filter; conditions typical of bearings greased for life and shielded	0,6 to 0,5	0,8 to 0,6
Slight contamination Slight contamination in lubricant	0,5 to 0,3	0,6 to 0,4
Typical contamination Conditions typical of bearings without integral seals; course filtering; wear particles and ingress from surroundings	0,3 to 0,1	0,4 to 0,2
Severe contamination Bearing environment heavily contaminated and bearing arrangement with inadequate sealing	0,1 to 0	0,1 to 0
Very severe contamination	0	0

Figure 81 shows the numerically derived values of η_b for a number of surface topography and lubricant film thickness as a function of the corresponding viscosity ratio κ, together with the reference curve adopted in the ISO 281:2007 standard. The viscosity ratio κ represents the effectiveness of lubrication concisely, i.e. the degree of surface separation between the rolling contact surfaces thanks to the formation of a lubricating film. It is calculated according to equations (24) and (25) and cannot be lower than 0.1 for the validity of this approach to bearing life estimation.

$$\kappa = \upsilon/\upsilon_1 \qquad \textit{for mineral oils and standard raceway surface machining} \qquad (24)$$

$$\kappa \approx \Lambda^{1.3} \qquad \textit{for especially machined raceway surfaces and special lubricants} \qquad (25)$$

[4] The ISO 281:2007 standard considers particle contamination only. Contamination by water or other fluids that may chemically alter either the lubricant or the steel surface is not considered .

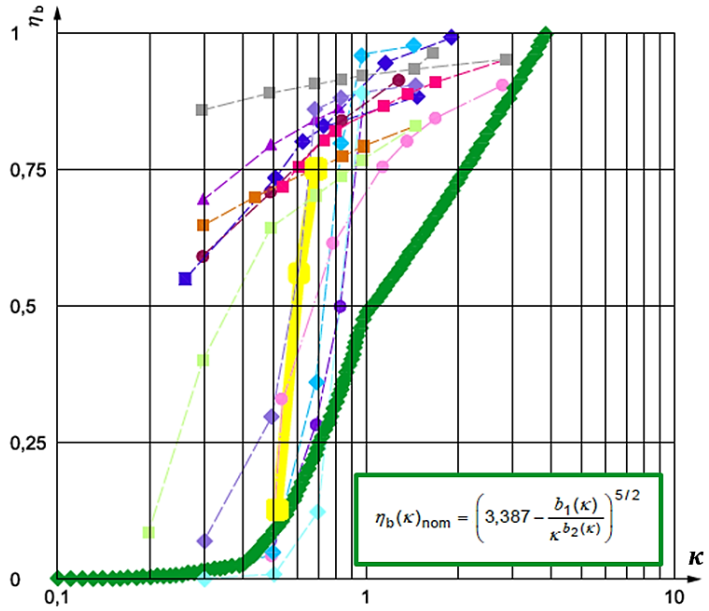

Figure 81: $\eta_b(\kappa)$ curve adopted by the ISO 281:2007 standard (bold green curve). From [112].

Where υ is the actual kinematic viscosity of the lubricant oil (or grease base oil) at the operating temperature, $\upsilon_1 = f(n, D_{pw})$ the reference kinematic viscosity required to obtain an adequate lubrication condition (Figure 82), and $\Lambda = h_{min}/\sqrt{Rz_1^2 + Rz_2^2}$ is the film thickness parameter or Lambda ratio [113]. An adequate lubricating film is formed if the lubricant retains a specific minimum viscosity at the operating contact pressure and temperature and the roughness of the contact surfaces is low enough. The ISO/TR 1281-2:2008 specifies that the minimum film thickness h_{min} is calculated according to the Dowson and Higginson's theoretical film thickness equations [114] for line contacts or according to Hamrock and Dowson's theoretical film thickness equations for point contacts [115]. It should be noted that these semi-empirical equations were derived from oil-lubricated rolling tests and, thus, are strictly valid only for the case of oil lubrication. These equations may provide wrong predictions of the film thickness curve for grease lubrication [116] since the lubrication mechanism of greases is much more complex. Experimental investigations with selective dyes for oil and thickener proved that grease is one entity and involves both the base oil and the thickener [8].

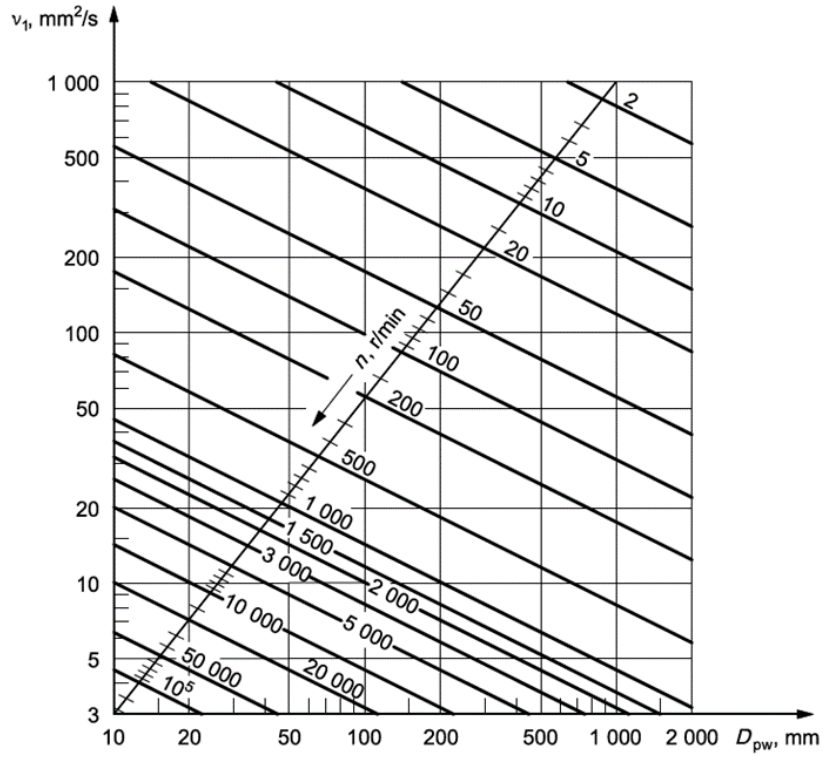

Figure 82: Diagram for the values of the reference kinematic viscosity υ_1 provided by the ISO 281:2007 standard.

a_{ISO} follows a function that asymptotically approaches infinity if the real stress σ is decreased down to the fatigue stress limit σ_u, i.e. if the load is decreased down to or below C_u. Figure 83 shows the chart of the life modification factor a_{ISO} for thrust ball bearings according to the standard.

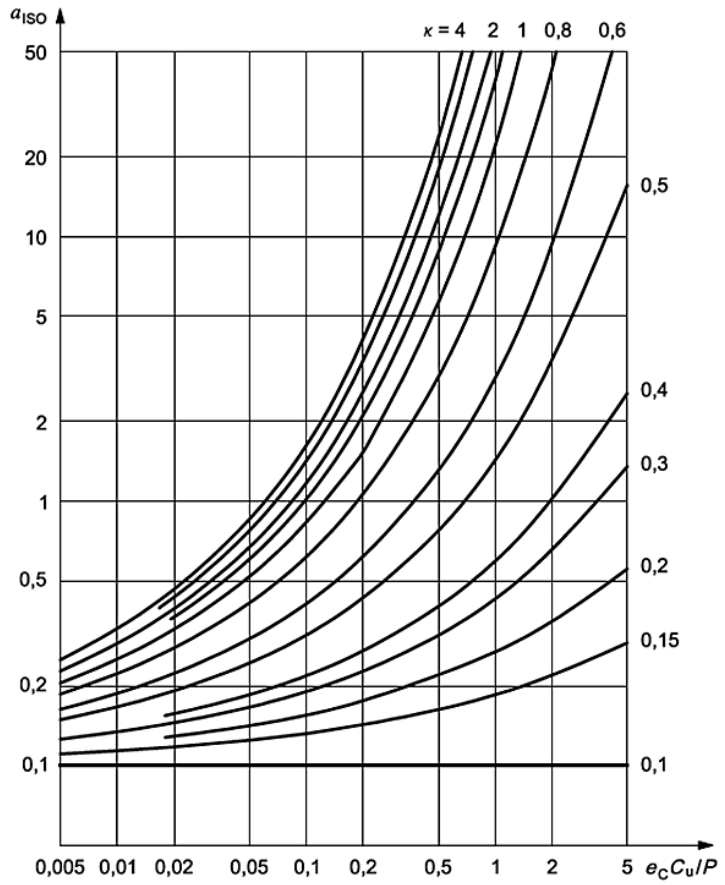

$$a_{ISO} = 0{,}1\left[1-\left(1{,}5859-\frac{1{,}3993}{\kappa^{0{,}054\,381}}\right)\left(\frac{e_C\,C_u}{P}\right)^{0{,}4}\right]^{-9{,}185} \quad \text{for } 0{,}1 \leqslant \kappa < 0{,}4$$

$$a_{ISO} = 0{,}1\left[1-\left(1{,}5859-\frac{1{,}2348}{\kappa^{0{,}190\,87}}\right)\left(\frac{e_C\,C_u}{P}\right)^{0{,}4}\right]^{-9{,}185} \quad \text{for } 0{,}4 \leqslant \kappa < 1$$

$$a_{ISO} = 0{,}1\left[1-\left(1{,}5859-\frac{1{,}2348}{\kappa^{0{,}071\,739}}\right)\left(\frac{e_C\,C_u}{P}\right)^{0{,}4}\right]^{-9{,}185} \quad \text{for } 1 \leqslant \kappa \leqslant 4$$

Figure 83: Chart of the life modification factor a_{ISO} for thrust ball bearings and the related system approach equations that define the curves as per ISO 281:2007.

The life equation proposed by ISO 281:2007 gives satisfactory results for a broad range of bearing loads and typical working conditions of industrial bearings. However, extra-heavy loads may cause detrimental plastic deformations at the ball/raceway contacts that are not considered and cannot be predicted in this model. Heavy loads may also produce cage failure earlier than the failure at the

contact sites between the rolling bodies and the raceways, which the model cannot predict. In general terms, the applicability of this life equation is discouraged in cases where P exceeds $0.5 \cdot C_a$. Similarly, very light loads far below the fatigue limit of the bearing may cause different failure modes that are not covered by the standard.

The STLE Design Guide proposed more specific life modification factors [110]. The modified bearing rating life equation reads as equation (26) according to the STLE Committee. These modification factors were introduced to consider that today's materials, lubricants and testing methods are very different from those when the first bearing life equation was established by Lundberg and Palmgren in the 40s [109].

$$L_{nm} = a_1 \cdot a_2 \cdot a_3 \cdot a_4 \cdot a_5 \left(\frac{C_a}{P}\right)^3 \tag{26}$$

Where a_1 corresponds to the reliability factor of the ISO standard, a_2 is a factor accounting for the specific steel grade, the hardness and the inclusion purity of raceways and rolling elements ($a_2 = 1$ for the standard quenched AISI 52100 of hardness 63 HCR), a_3 is related to the lubrication regime, the surface roughness and thickness of the lubricating film, a_4 accounts for the presence of slip and related frictional effect in boundary lubrication regime ($\Lambda < 1$) and a_5 considers the contamination level of the lubricant and the presence of corrosive agents in the lubricants, e.g. water. It should be noted that a_3. a_5 roughly corresponds to a_{ISO}. For instance, if an M50 steel is used instead of a 52100 grade a_2 is equal to 2; if the production process is VIM-VAR (vacuum induction melt-vacuum arc remelt), the purity of the M50 steel is very high and thus a_2 can be increased by 6 times [110]. If the surface hardness is 65 HRC instead of 63 HRC a_2 can be increased by 1.73 times [110].

4.4 Grease life calculation

The development of the bearing life model proposed by ISO 281:2007 is based on a semi-empirical approach, where computer-supported theory is combined with extensive experimental testing on components and practical experience of the bearing manufactures related to the applications. This standard also defines the

"life" of an individual rolling bearing, i.e. the number of revolutions, or equivalent working hours, which one of the bearing rings can perform with respect to the other (static) ring before the first evidence of fatigue develops on the contact surfaces. Hence, the focus of the model proposed by ISO is mainly on the structural failure of the bearing. In other words, the extensive experimental tests the model relies upon are supposed to be carried out until the first evidence of spalling or degenerative pitting on the contact surfaces.

The standard guidelines do not specify the relationship between such structural duration of the rolling bearing and the lubricants because the approach is very general and applies to both oil-lubricated and grease-lubricated rolling bearings. In endurance tests on bearings is sometimes challenging to separate the endurance of the bearing, meant as the structural limit of the mechanical component, from the service life of the lubricant that allows the component to operate correctly. The latter corresponds to the period during which the lubricant retains its characteristic viscosity and surface protection properties and is capable (without any relubrication) of lubricating the bearing to an adequate extent.

In the case of grease lubrication, the service life of grease-lubricated bearings is very often limited by the life of the grease itself. However, the structural limit of the mechanical component and the lubricant service life might not coincide. The end-of-life condition of grease is typically reached earlier than the structural limit of the bearing, and the latter is promoted by the former if relubrication is lacking. Therefore, the useful life of grease must be assessed separately to determine the proper relubrication interval. In the case of oil lubrication, the scenario is different because the quantity of the lubricant involved is much higher. The continuous recirculation of the liquid lubricant limits the mechanical overstress on the oil, and the structural limit of the bearing can be reached due to circumstances not directly relating to the health of the lubricant.

A guiding value for the grease operating life L_{fG} can be determined in approximate terms by equation (27) [117].

$$L_{fGh} = K_T \cdot K_P \cdot K_R \cdot K_U \cdot K_S \cdot t_f \tag{27}$$

Where t_f is the basic grease operating life in hours of running at 50% failure probability, K_T is the correction factor for increased temperature, K_P is a correction factor for increased load, K_R is the correction factor for oscillation (if

present), K_U is the correction factor for environmental influences, and K_S is the correction factor for an unfavourable oriented shaft according to the bearing class. For instance, a horizontal shaft is unfavourable for thrust bearing without sealing because this orientation lets the lubricating grease pour off by gravity and centrifugal forces.

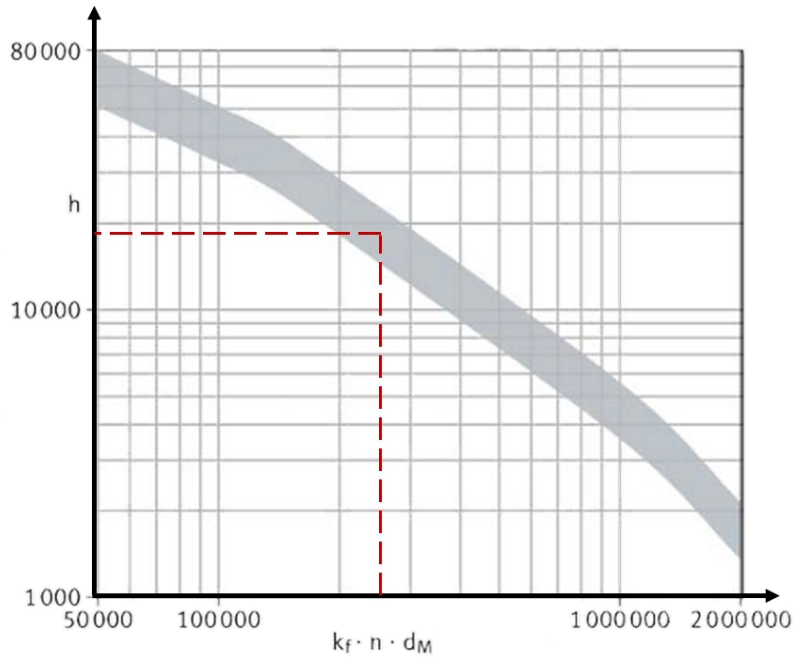

Figure 84: Basic grease operating life chart as a function of the parameter $n \cdot d_m \cdot k_f$. Adapted from [117].

The value of t_f is a function of speed n, average bearing diameter d_m, and a bearing-specific parameter k_f that depends on the bearing class (equation (28)). For thrust deep-groove ball bearings, i.e. the class of rolling bearings of interest for this research work, k_f is equal to 5.5. The grease basic life is evaluated through the diagram in Figure 85, determined by extensive testing of greases with bearing test rigs like those described in Sections 7.1.1 to 7.1.5.

$$t_f = f\left(n \cdot d_m \cdot k_f\right) \tag{28}$$

The values provided by the chart in Figure 84 are, however, valid only if the bearing temperature is lower than the upper continuous limit temperature of the grease $T_{upperlimit}$, the orientation of the bearing and/or the presence of seals

prevents grease from flowing out of the bearing, the bearing is operated under continuous rotation and constant load, and the load is such that the ratio $C_0/P \geq 20$, where C_0 is the basic static load rating. All these circumstances would reduce the service life of grease. Hence the need for some correction factors to extend the validity of this model.

Factor K_T considers the reduction in the grease life that occurs when the grease is operated in a bearing whose stabilization temperature is higher than the upper continuous limit temperature of the grease provided by the technical sheet. As a rule of thumb, the grease operating life is halved each time the temperature increases by 15 °C, as visible in Figure 85.

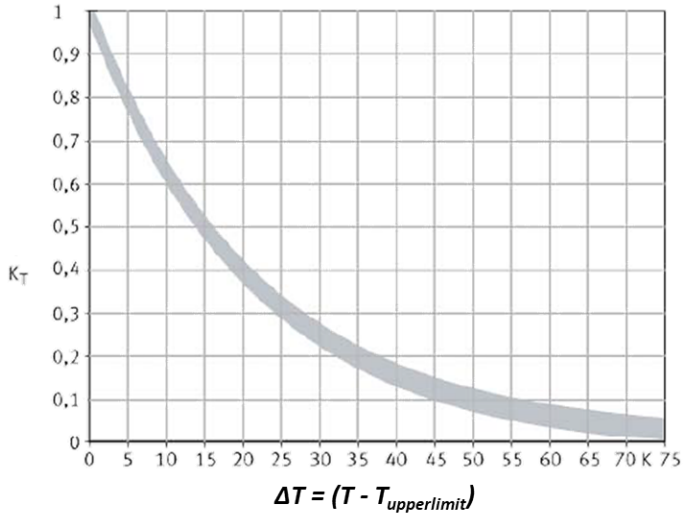

Figure 85: Grease life correction factor for high temperature. Adapted from [117].

K_P corrects the value of t_f for applications where the ratio is lower than 20, i.e. greases are subjected to greater strain. The chart in Figure 86 provides the values of this coefficient evaluated by the class of rolling bearings.

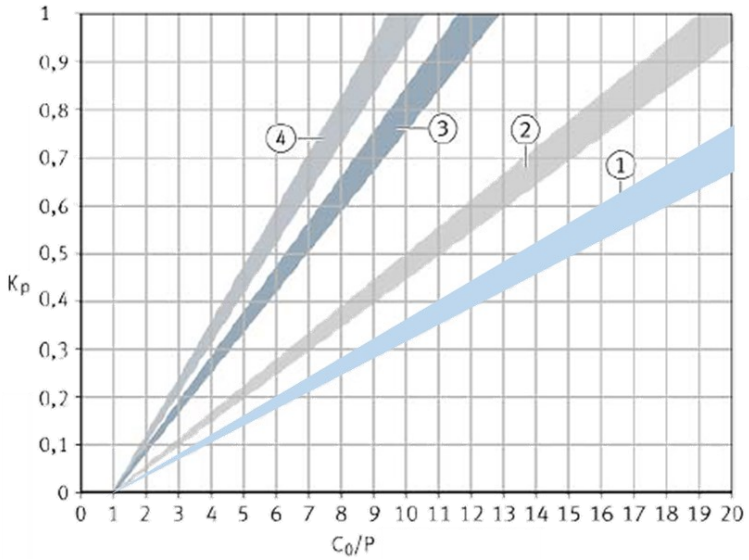

Figure 86: Grease life correction factor for high load. ① is K_p for thrust bearings; ② is the range of spherical and other special roller bearings; ③ is for tapered and cylindrical roller bearings; ④ applies for deep-drove, angular contact and self-aligning ball bearings. From [117].

Grease is subjected to a higher strain if the bearing performs oscillating movements instead of continuous rotation. Moreover, such higher strain is placed continuously on the same grease volume since the oscillating movement disfavors the entrainment of fresh grease into the rolling contact. The grease life is therefore shortened by overload. The oscillation factor is estimated as a function of the angular amplitude as per the chart in Figure 87.

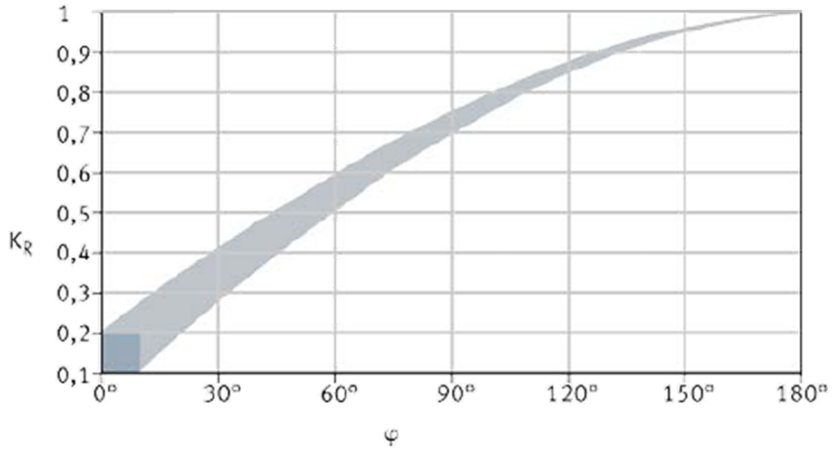

Figure 87: Grease life correction factor for oscillating movement. Adapted from [117].

The factor K_U takes account of the influences of moisture, shaking forces, slight vibration and shocks on grease life, while the factor K_S considers that the grease can leave the contact site due to mounting orientation, so less grease is available for lubrication. Both factors are determined based on the reference value provided in Table 31.

Table 31: Reference value of factors K_U and K_S [117].

Influence factor	Level	Value
Environmental factor K_U	Slight (test rig)	1
	Moderate (standard value)	0.8
	Heavy (outdoor)	0.5
Unfavourable shaft orientation factor K_S	Unfavourable (depending on sealing)	0.5 to 0.7
	Otherwise	1

Another approach for grease life estimation was proposed by Lugt and Berens [118] based on the *Grease Life Factor* (GLF) concept. According to this approach, the GLF is a performance factor that measures how grease provides extended life at a particular temperature depending on its formulation but independently on the bearing type and test rig used for the assessment. Literature results have shown that if the same grease is tested according to different standardized test methods, it would probably last differently. The formula proposed by Lugt and Berens reads as per equation (29).

$$L_{50Gh} = GLF \cdot 52f \cdot \left(\frac{C}{P}\right)^{0.73} \cdot n_R^{-1.09} \cdot \left(\frac{1}{2}\right)^{\frac{T-T_r}{T_A}} \tag{29}$$

$$f = 1 - \frac{V_b - V_g}{V_b} \tag{30}$$

Where f is the fraction of the bearing volume filled with grease calculated by equation (30) (V_b is the free volume of the bearing between the rings and the rolling elements), C is the basic dynamic load rating of the greased bearing, P is

the overall applied load to the rolling elements, n_R is the normalized nd_m product of the bearing with respect to the reference value of 33500 mm/min, T is the operating temperature of the grease, T_r is a reference temperature se to 120°C and T_A is the Arrhenius temperature, i.e. the grease life is halved with every temperature increase equal to T_A. For greases $T_A = 10 \div 20°C$, usually. As already stated above, temperature must remain between the Low Temperature Performance Limit (LTPL) and the High Temperature Performance Limit (HTPL), i.e. within the temperature operating range prescribed by the grease manufacturer, also called the *green zone*. The GLF of each grease type must be estimated through the inverse equation (31) by running a set of grease life tests where L_{50Gh} is determined experimentally.

$$GLF = \frac{1}{52f} \cdot L_{50Gh} \cdot \left(\frac{C}{P}\right)^{-0.73} \cdot n_R^{1.09} \cdot 2^{\frac{T-T_r}{T_A}} \tag{31}$$

The results of the work by Lugt and Berens [118] provided, as an example, the GLF value for a general-purpose lithium grease with a mineral base oil (Li/M) and a high-performance poly-urea grease with a mineral base oil (Pu/M). The average GLF determined experimentally by comparing both FE9 and R0F+ tests results was *1* for Li/M and *5* for Pu/M, which evidences the higher average duration capability of the grease with synthetic thickener.

Chapter 5

Friction and wear performance of graphene-enriched greases

5.1 Thermal and rheological properties of graphene-enriched greases

The base grease selected for this investigation is MULTEMP ET-C by Kyodo Yushi Co. Ltd. This lubricant is a fully synthetic heat-resistant, anti-flaking and low-noise urea grease for bearings featuring a specific package of additives for working in a wide temperature range. As per Table 32, the Low Temperature Performance Limit (LTPL) is -40 °C, i.e., where oil separation practically stops, and the High Temperature Performance Limit (HTPL) is 200 °C, i.e., the point where the grease matrix loses its structure, and excessive leakage occurs. The reason for choosing a high-quality grease is to assess if this innovative carbon nano-additive can outperform the conventional molecular additives currently used by lubricant manufacturers to boost the performance of their greases.

Table 32: Technical sheet of MULTEMP ET-C high-performance grease from Kyodo Yushi Co. Ltd **[119]**.

Product Details

KYODO YUSHI

Franciscusweg 219m NL 1216SE Hilversum, Netherlands
PHONE +31-35-5239152

MULTEMP ET-C

Manufacturer

Kyodo Yushi

Remarks

SKF R0F 10,000 rpm, 170°C : 1989 hrs // BeQuiet+ GN2

Heat-resistant, anti-flaking and low-noise urea grease suitable for outer-ring rotating bearings, recommended for alternator, electromagnetic clutches, cooling fan motor and tension pulley bearings.

temperature range -40 °C <—> 200 °C

Characteristics	Test Method		Typical
Type of base oil	--		synthetic ADE + polyolester
Thickener	--		di-urea
Base oil viscosity			
@ 40 °C	ISO 3104		81.6
@ 100 °C mm²/s	DIN 51562		10.8
Appearance	--		light brown
NLGI Class	DIN 51818		2
Worked penetration	ISO 2137		280
Dropping point, °C	ISO 2176		> 260
Copper strip corrosion 24h/100°C			
Evaporation loss (99°C, 22h), %	ASTM D 972 IP 183		0.47
Oil separation 100 °C 24h	FTMS 791B321 mod.		0.6
Oxidation stability, kPa 100h/99°C	ASTM D 942		
Low temp.torque -40 °C	ASTM D 1478-63	starting	79
N·cm		running	27
4-Ball weld load (N)		W.P.	
Corrosion protection	ISO 11007		0 - 0
Water washout, 1hr at 79°C	ASTM D 1264		
Water resistance	DIN 51807 90 °C 3hrs		0

www.kyodoyushi-europe.com

Three grease compounds with increasing content in Graphene Nano-Platelets (GNPs) were prepared in-house and compared with base grease:

- 0.5% wt. GNPs
- 1% wt. GNPs
- 5% wt. GNPs

Commercial Graphene Nano-Platelets (Cometox Srl, Milan, Italy) with grade C-500 were added to the base grease. GNPs are characterized by a nominal thickness of 2 nm, a maximum diameter of 2 μm and an average specific surface area of 500 m^2/g. The defined amount of graphene was gradually incorporated into the grease by mechanical stirring at room temperature using a Heidolph Hei Torque Precision 400 homogenizer. The compounds were mixed for 30 min at room temperature to achieve uniform nano-particle dispersion into the grease. Figure 88 compares the appearance of the graphene-enriched grease with the pure one. The grease compounds were prepared by mechanical mixing at room temperature. The solid nano-additive was added into the grease by gradually increasing the quantity to the defined percentage to give the solid particles time to spread evenly into the grease. Figure 89 shows the images of the graphene-grease compounds taken under the optical microscope in transmission mode.

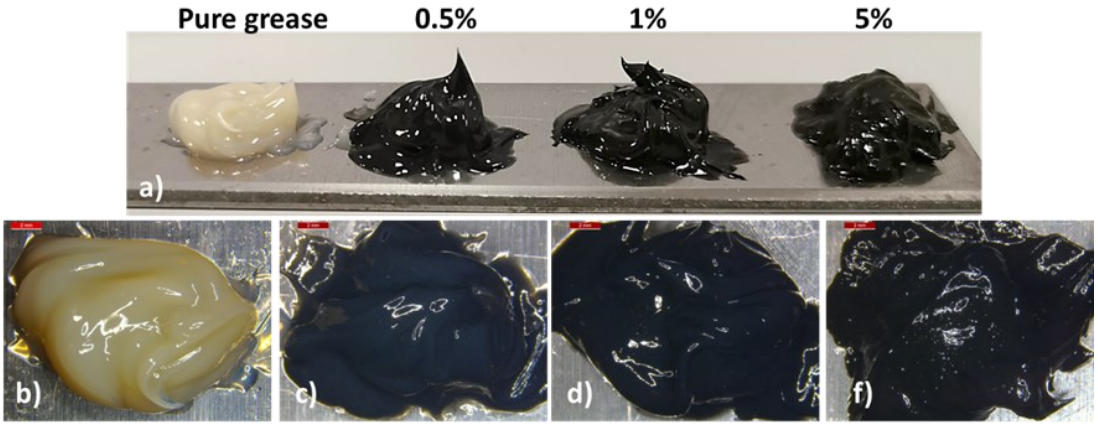

Figure 88. (a) Overview of the four grease compounds, the black ones are those functionalized with GNP; (b), (c), (d), (e) Inspection under the microscope of the pure grease, 0.5% graphene grease, 1% graphene grease, and 5% graphene grease, respectively. Interestingly, adding 5% wt. of graphene makes the grease grainy, meaning the nanoplatelets cannot disperse evenly.

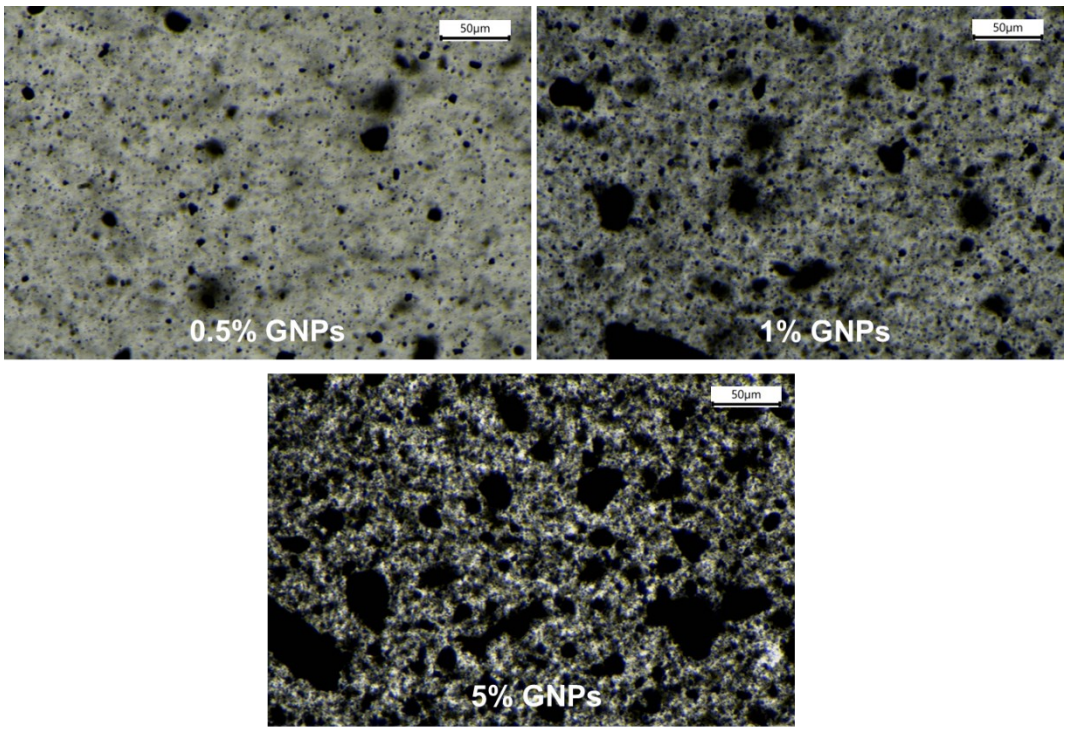

Figure 89. Transmission optical microscope image of the graphene-grease compound prepared for this research. Some clustering of the nanoplatelets in larger carbon particles is visible in transmitted light microscopy.

5.1.1 Experimental determination of thermal conductivity

The thermal conductivity of the grease compounds was experimentally determined through the transient plane source (TPS) technique, also called the Hot Disk method. A special container consisting of two parts (case and cover) was manufactured on purpose to accommodate grease and keep the Kapton sensor in place during the test. The shape and dimension of the container were optimized to allow the thermal wave to propagate uniformly inside the grease. Both the parts were manufactured by 3D printing in PLA.

Figure 90a shows the details of the special grease container and the Hot Disk experimental setup. Figure 90Figure 91 summarizes the measured values of thermal conductivity. The estimated experimental error was about 0.006 W/m/K; therefore, the most appreciable thermal conductivity variation was observed for the 5% GNPs grease compared to the pure MULTEMP ET-C.

Figure 90. (a) Special grease box for Hot Disk test on graphene-grease compound; (b) experimental setup of the tests.

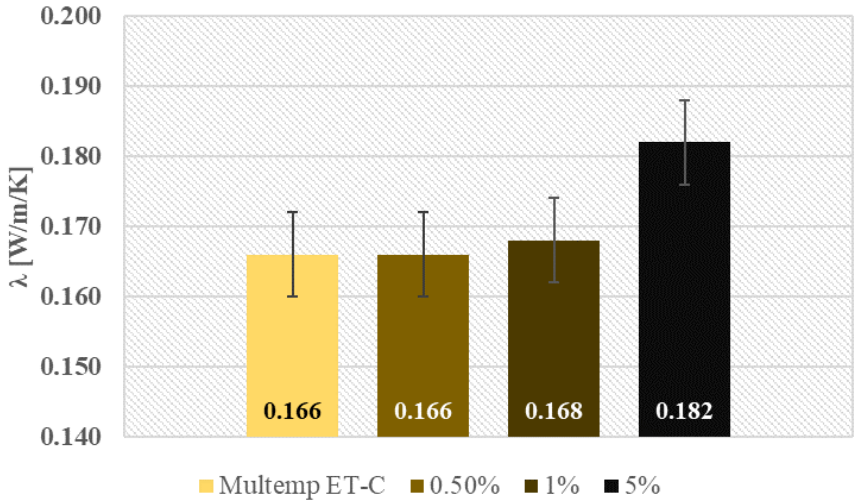

Figure 91. Thermal conductivity of the four graphene-grease compounds (λ) estimated by Hot Disk method.

5.1.2 Characterization of the bulk electrical conductivity of grease compounds

Previous research proved that adding conductive particles to the grease increases the bulk electrical conductivity of the lubricant [120]. As a carbon material, graphene plays a role [121]. Sometimes this effect is desired, for instance, in the case of greases for electrical motors. In the case of monitoring the lubricating film via the electrical contact resistance value, it is necessary to characterize the bulk electrical conductivity of grease to properly analyze the data obtained during tests, i.e. to identify when the measured ECR values indicate conduction through a film of grease.

In order to measure the characteristic value of the electrical conductivity of the four grease compounds, static ECR measurements were performed by exploiting a unique setup. A flat-ended pin was placed 8 µm above the steel sample, and a small quantity of grease was added to fill the gap. Figure 92a shows the measurement setup. A calibrated 8 µm lamina was used to separate the pin and the disc.

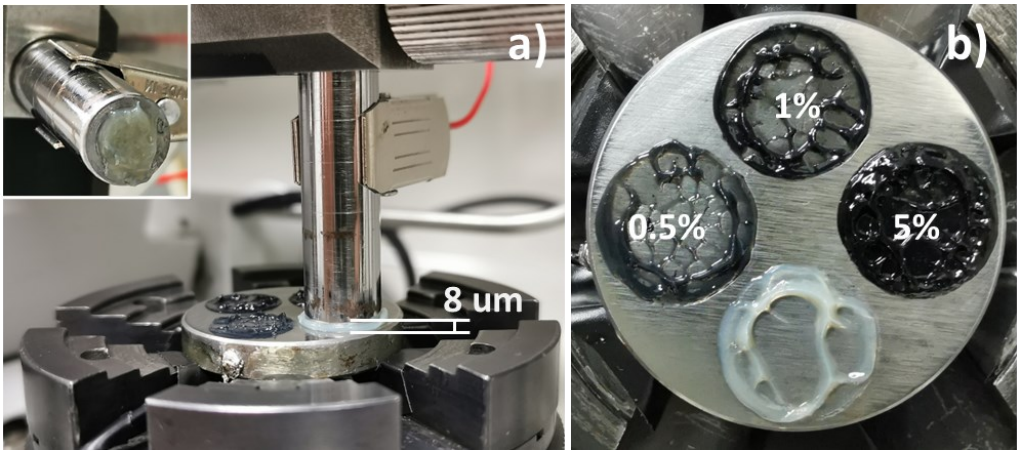

Figure 92. (a) Experimental setup for the static non-contact ECR measurement with the four grease compounds. (b) Overview of the grease contact sites after the static ECR tests on the same sample.

Grease was applied on the pin surface, and the pin moved downward to the desired pre-set distance from the sample so that grease could fill the interspace. The pin was held in place for 10 minutes, and the ECR values were sampled at 0.5 Hz. The average and standard deviation values were estimated across the whole measuring time. The same sample was used to characterize the four grease compounds to make the measured values comparable (Figure 92b). The average values and related confidence intervals are summarized in Table 33 and Figure 93.

Table 33: Bulk electrical resistance across an 8 µm thick film of grease.

	MULTEMP ET-C	**0.5% GNPs**	**1% GNPs**	**5% GNPs**
Electrical resistance	> 100 MΩ	265.2 kΩ	45.9 kΩ	18.2 kΩ

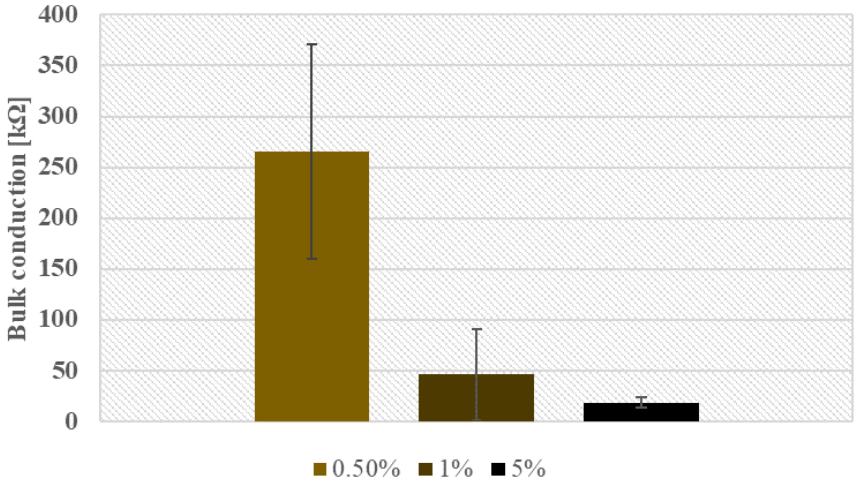

Figure 93. Average values of bulk electrical resistance across an 8 µm thick film of grease with confidence intervals. Adding 0.5% wt. of graphene flakes increased the electrical conductivity significantly. The value related to pure MULTEMP ET-C is not displayed because the measuring range of the DMM (100 MΩ) was saturated.

5.2 Pin-on-disc tests

Lubricated sliding friction tests were performed through a pin-on-disk tribometer (Anton Paar TriTec, TRB). The pin-on-disc testing method ensures sliding motion at the interface as the four-ball method does. Pin-on-disk was preferred over four-ball, although the latter is a standard grease testing method because it is easier to monitor the contact temperature and that of grease accumulated close to the contact. Figure 94 shows the overview of the experimental layout for the tribological tests. Tests were performed on 5 mm thick and 30 mm wide flat cylindrical steel samples of quenched AISI 52100 chromium steel.

The samples were prepared by CNC milling, quenched, and then finished to ensure the parallelism of the upper and lower flat sides within the tolerance of 0.05mm. The friction counterpart was a 6mm AISI 52100 (100Cr6) chromium steel ball for rolling bearings. The amount of grease spread onto the contact surfaces was about *1g*, and it was arranged to cover the whole surface of the sample at the beginning of each test. All the tests ran under 30N load and 0.9m/s speed, and the total sliding distance was 23km (about 7h tests). A very long test duration was chosen to detect any evolution of the grease performance due to ageing or stress degradation. One new sample was used for every test to keep

constant the radius of the wear track equal to 11mm, and the average Hertzian contact pressure was 1290MPa. Each graphene compound was tested at least three 3 times to account for the natural scattering of the tribological phenomena.

Table 34 summarizes roughness and hardness values for the flat samples and the spheres. Roughness was measured through a contact-stylus roughness tester (SM Instruments, RTP80). The average hardness of the sample was measured by quasi-static instrumented micro-indentation tests (Anton Paar, NHT3) under increasing load from 1mN to 400mN.

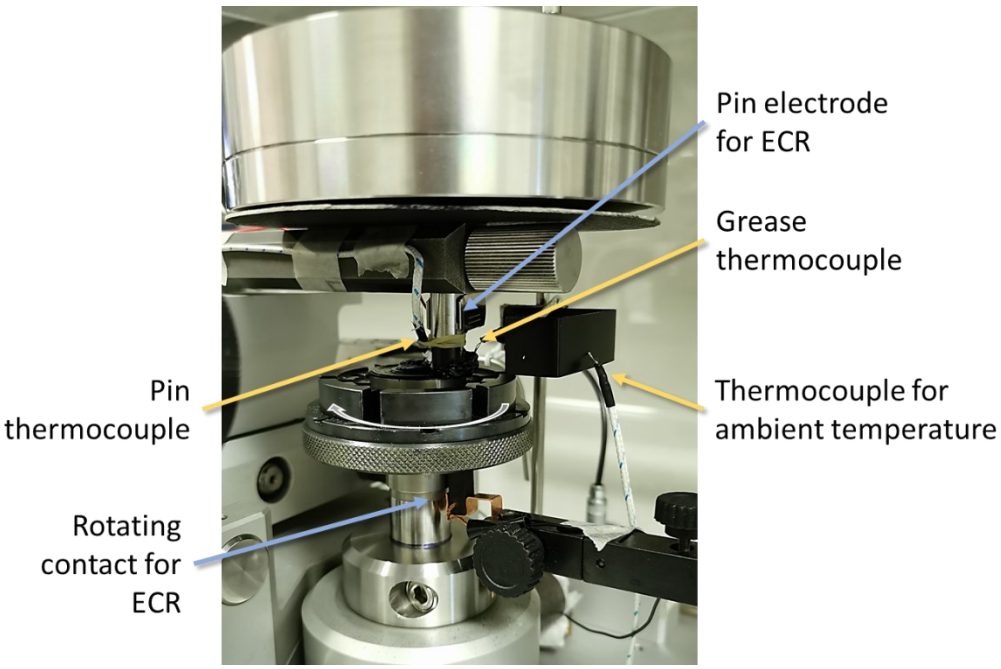

Figure 94. Experimental layout for the tribological tests.

Table 34: Roughness and hardness characteristics of the static sphere and rotating steel disk for pin-on-disc tests.

	AISI 52100 flat samples	**6mm AISI 52100 spheres**
Roughness *Ra*	0.673 μm	0.086 μm
Hardness	15.1 GPa H_{IT}	62 HRC

Two type-K thermocouples (0.5 mm diameter) were installed close to the contact point to monitor the thermal state of the system. One thermocouple was placed in contact with the pin (the ball-holder) as close as possible to the spherical tip; the other was placed inside the grease build-up accumulated at the leading edge of the sliding contact. Both thermocouples were connected to the acquisition card of the tribometer; therefore, the temperature signals were sampled at the same rate as the CoF signal, i.e., 100 Hz. The ambient temperature inside the testing chamber was traced by placing another type-K thermocouple close to the contact site to sense the air temperature in that region. A thin metallic lamina was used to shield the tip of the thermocouple from direct exposure to the whirlwinds caused by the rotating spindle. The trend of the ambient temperature was then subtracted from the temperature values measured by the two thermocouples to compensate for the unavoidable temperature fluctuations inside the testing chamber. Figure 95 provides a detailed view of how the thermocouples were positioned close to the contact point.

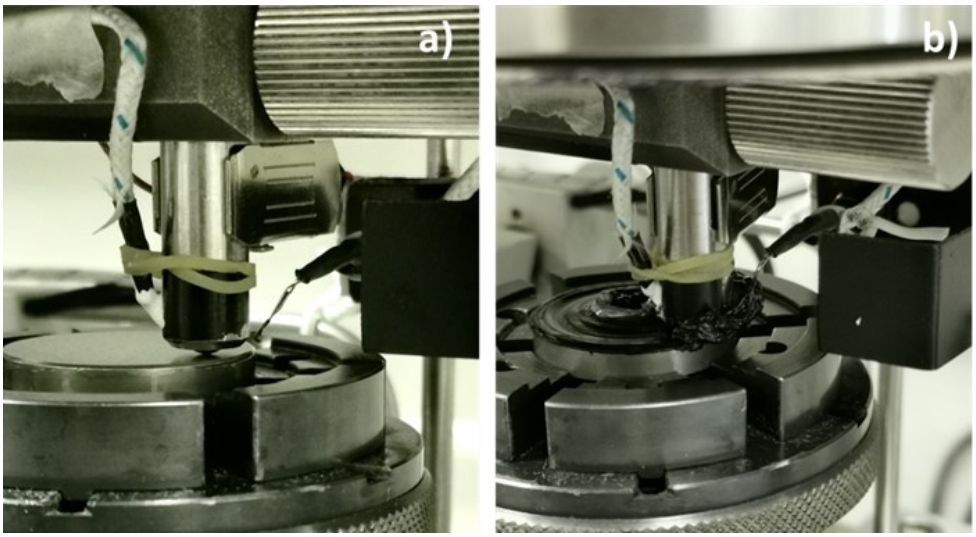

Figure 95. Position of the two thermocouples (a) before greasing, (b) after grease build-up is formed. The pin thermocouple was installed with thermo-conductive paste to improve the accuracy of the measured value and protect the sensing region of the probe from direct convective effects.

The electric contact resistance (ECR) across tribological contact was also measured during the tests. The ball holder and the rotating sample were connected to the digital multimeter (DMM) board of a National Instruments VirtualBench VB-8012 device. The electric resistance was measured with the 2-wire method to obtain the broadest measuring range out of the DMM, i.e. from 0.001Ω to 100

MΩ, with auto-ranging enabled by the control software of the instrument. The ECR values were acquired via a dedicated NI LabView routine. The ball holder and the rotating sample were insulated from the tribometer frame using a high-performance insulating varnish to avoid disturbances due to electric dispersion through the ground. A slip ring system made of a flat copper ring and a carbon brush was installed onto the tribometer spindle, and the copper ring was soldered to the steel sample with an external wire. The electrical circuit of the ECR was closed via the carbon brush pressed against the rotating copper ring by a leaf spring. The carbon-copper sliding pair minimizes the disturbances on the electrical signal at the level of the sliding electrical contact. The schematic of the electrical circuit is shown in Figure 96.

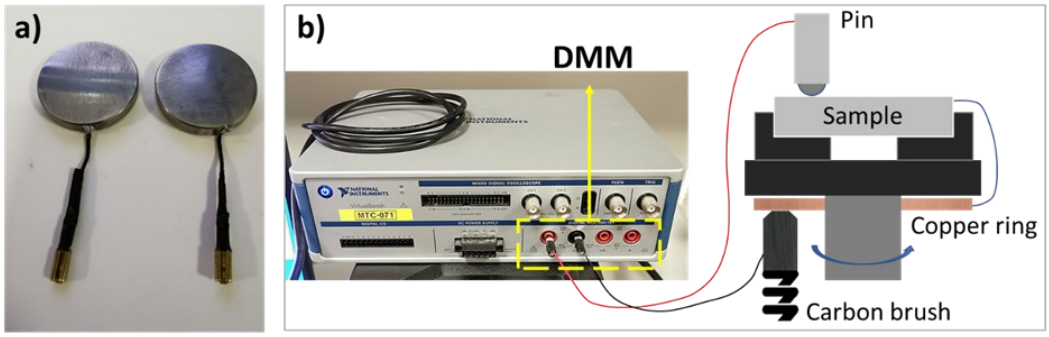

Figure 96. (a) Samples prepared for ECR measurements with an external wire welded on the side for connection to the rotating copper ring; (b) Schematic of the ECR measurement circuit.

The ECR value measured through this setup also includes the bulk resistance of the sample, the resistance of the electrical line, and that of the rotating carbon-copper contact. The contributions read as per equation (32).

$$R_{ECR} = R_{samples} + R_{cables} + R_{connectors} + R_{weldings} + \\ + R_{slip\ ring} + R_{pin-sample} \tag{32}$$

However, any other terms except $R_{pin-sample}$ were deemed to have negligible fluctuations during the tests. The preliminary investigation carried out without lubrication showed that the stationary resistance of the carbon-copper sliding contact ($R_{slip\ ring}$) measured remained stable while increasing the rotating speed of the mandrel. This evidence suggests that R_{ECR} would vary during the

tribological tests according to the evolution of the lubrication and wear regime at the pin-sample sliding interface only.

The pin and the sample were inspected under a digital microscope (Leica Z16 APOA) after the tests, both before and after cleaning with acetone. The material loss was restricted to the sphere only because the quenched sample was harder than the sphere. The wear trace on the spheres was shaped as flattened regions with an almost circular shape (Figure 97), whose diameter was measured under the microscope. Stylus profilometry (SM Instruments, PGS200) on the spheres confirmed that the worn-out region was flat; therefore, the amount of material lost by the system was approximated to a spherical cap with a known base diameter, as per the ASTM G99-17 guidelines.

Figure 97. Wear damage on the sphere. (a) Example of a spherical cap diameter measurement under the microscope at the end of a test lubricated with the base grease (the grey dashed line is the location of the profilometric inspection); (b) Profilometric inspection of the flattened region on the sphere; (c) Calculation of the spherical cap volume as per ASTM G99-17.

5.2.1 Correlation between friction, thermal response and ECR curves

Figure 98 compares the results regarding the average friction coefficient over the whole duration of tribological tests. The lowest friction was achieved with 1% GNPs into grease, which exhibited a 22% reduction compared to base grease. The compound with 0.5% GNPs performed better than the base grease, but the CoF decreased by just 6.5%. On the contrary, a detrimental 94% increase in the average CoF was exhibited by the grease compound with the highest GNPs content, revealing a critical performance loss due to the excess of carbon nano-additive.

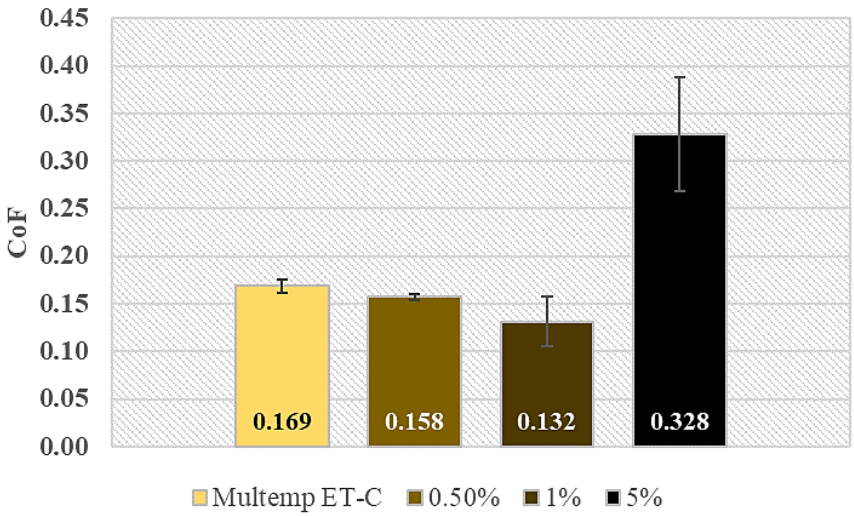

Figure 98. Comparison among the average friction value measured with the four grease compounds. The error bars represent the 95% confidence level for the estimated average values.

Figure 99 shows, as an example, the results of four tests that the author deemed representative of the characteristic tribological response with each grease compound. The diagrams report the set of experimental curves acquired synchronously, including the CoF curve, the thermocouples curves and the online wear depth curve (corresponding to the vertical displacement of the pin). The diagrams give more details on the effect of graphene on the tribological and thermal response of the system. Interestingly, the friction and thermal curves always followed an extraordinarily similar trend due to an obvious cross-correlation.

When pure Multemp ET-C grease was applied to the contact, the frictional behaviour of the tribological system was divided into two phases. After the wear-in, which lasted approximately 700 m of sliding, the friction curve stabilized at about 0.13 with a very low scattering of values. According to Wang to al. [98], a flat, stable friction curve hints that a stable boundary lubrication regime exists at the interface. Boundary lubrication could not rely on any hydrodynamic separation of surfaces, and considerable asperity contact occurs through a thin molecular film adsorbed on surfaces [93]. The corresponding ECR values presented in Figure 100a are relatively low in this first phase and testify that conduction through the nanometric film is relatively easy. Although the test ran smoothly, wear accumulated in this first phase since the linear wear curve increased. Asperities probably scraped off the boundary film due to abrasion, but

it was continuously restored steadily. After a given time, which varied from test to test, this lubrication mechanism ran into instabilities, and a lubricant shortage event occurred.

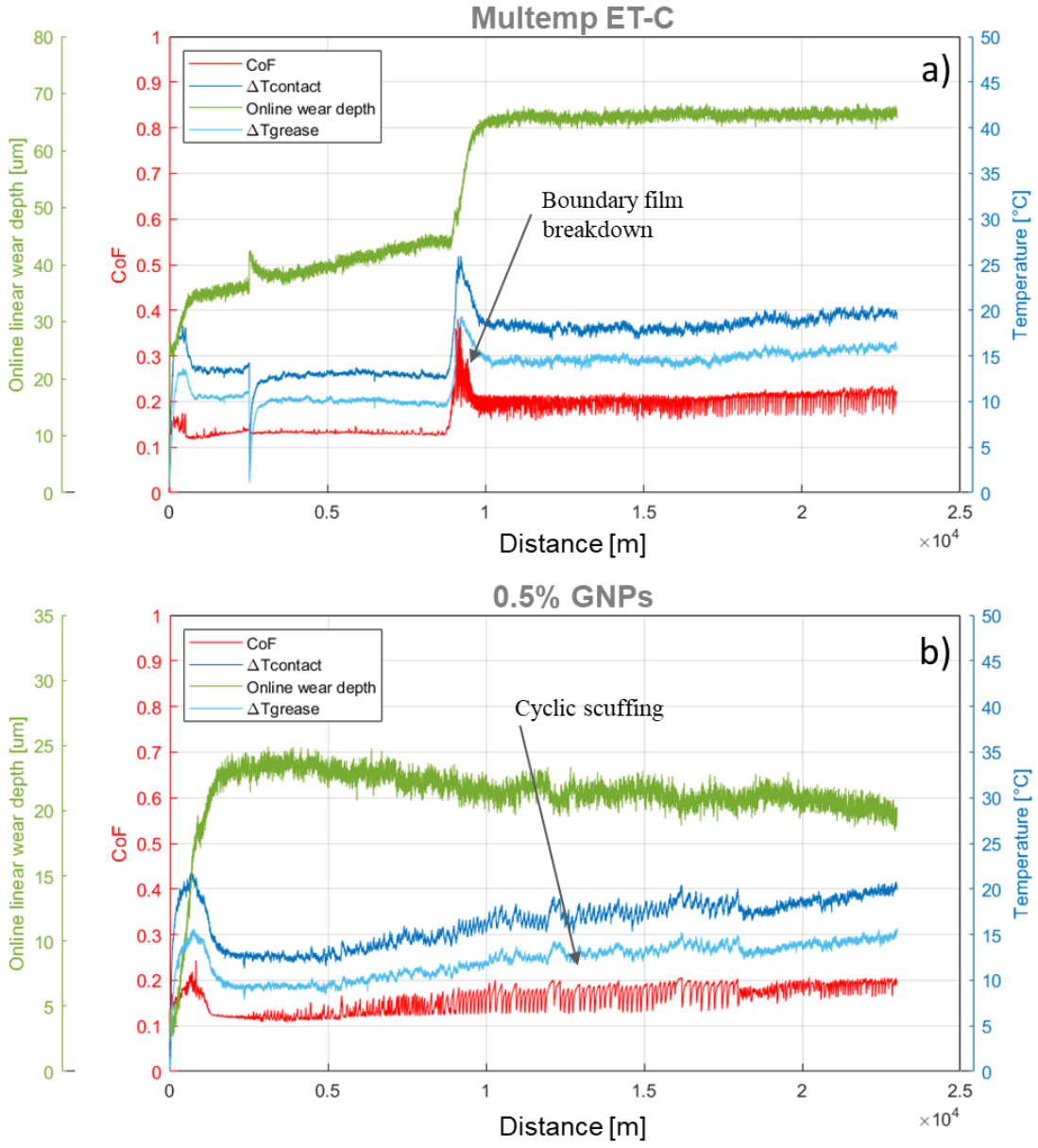

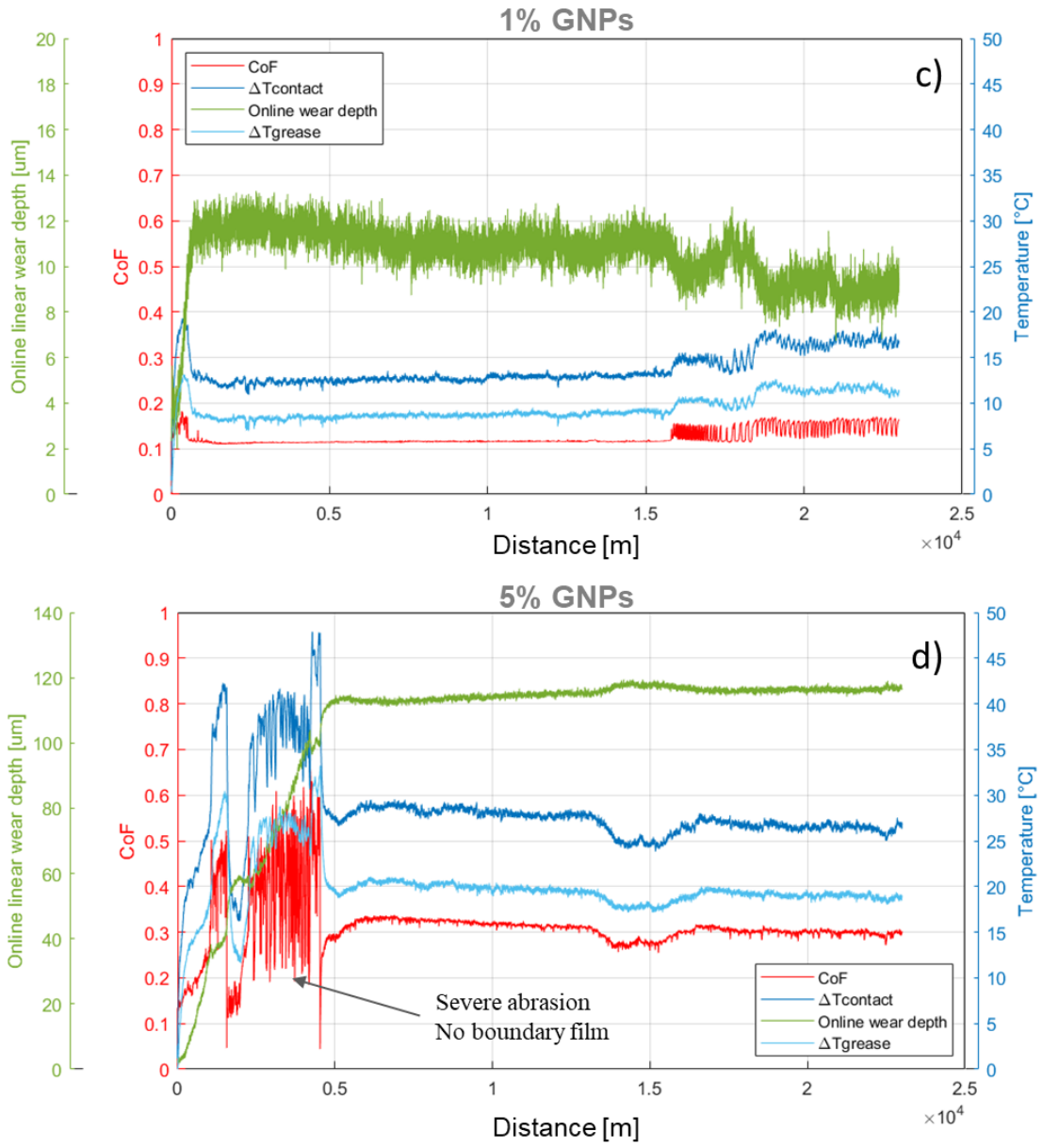

Figure 99. Friction and thermal curves were recorded during four tests to compare the tribological performance of the four graphene-rich grease compounds. The values recorded by the pin thermocouple close to the contact region are labelled $\Delta T_{contact}$; those recorded by the thermocouple inside the grease build-up are labelled ΔT_{grease}.

A peak of the CoF, a steep increase of the linear wear curve and a transient drop of the contact resistance to conduction marked the failure of the boundary film. Lubricant shortage events after some stable running with a boundary film were also reported by Wang et al. in reciprocating pin-on-plate testes with pure

lithium grease [102]. A boundary film grew again in the remaining part of the test but was less stable, and sliding was harsher. The CoF stabilized to a higher level, and the friction curve was more scattered than before. Temperature also rose by 10 °C. The ECR curve slowly increased up to the end of the test with localized peaks of reduced conduction. This trend may be evidence of the accumulation of oxides from tribo-oxidation.

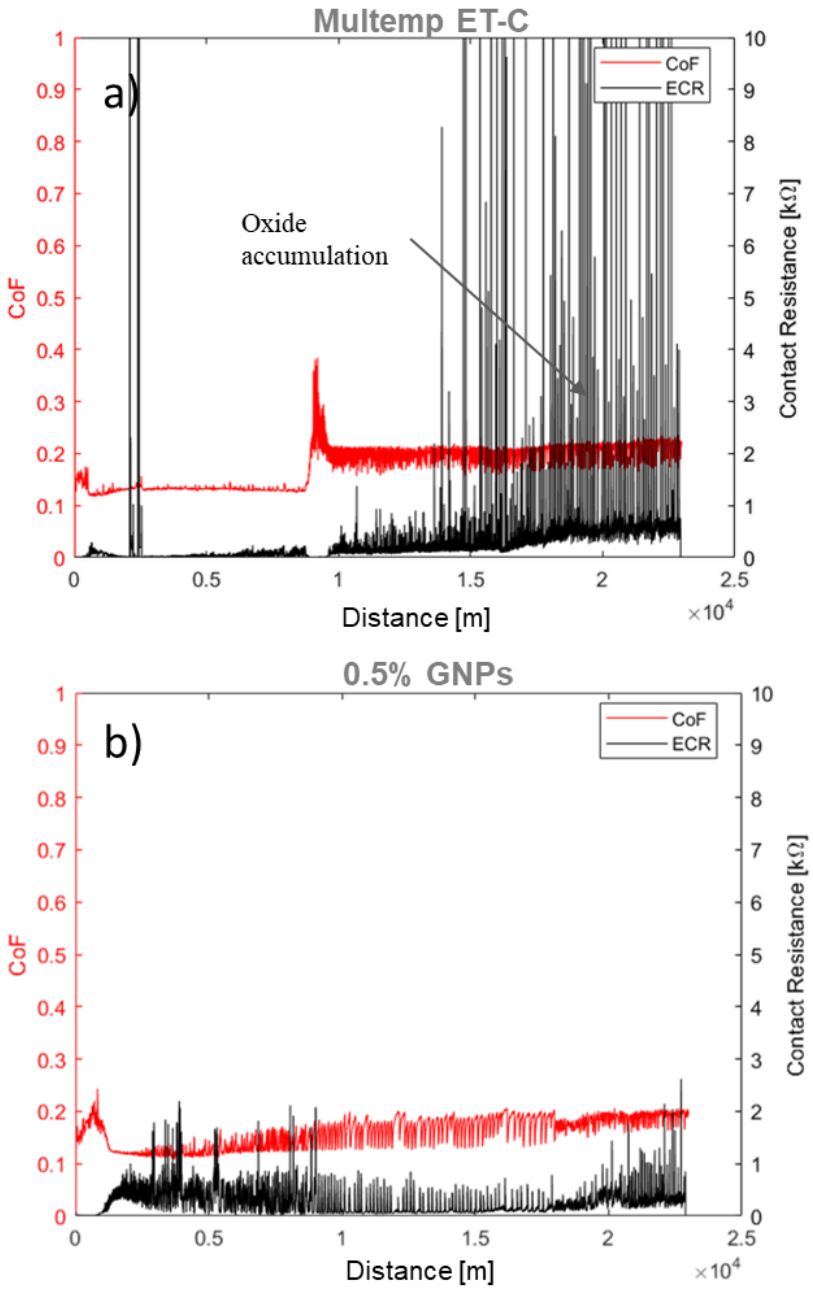

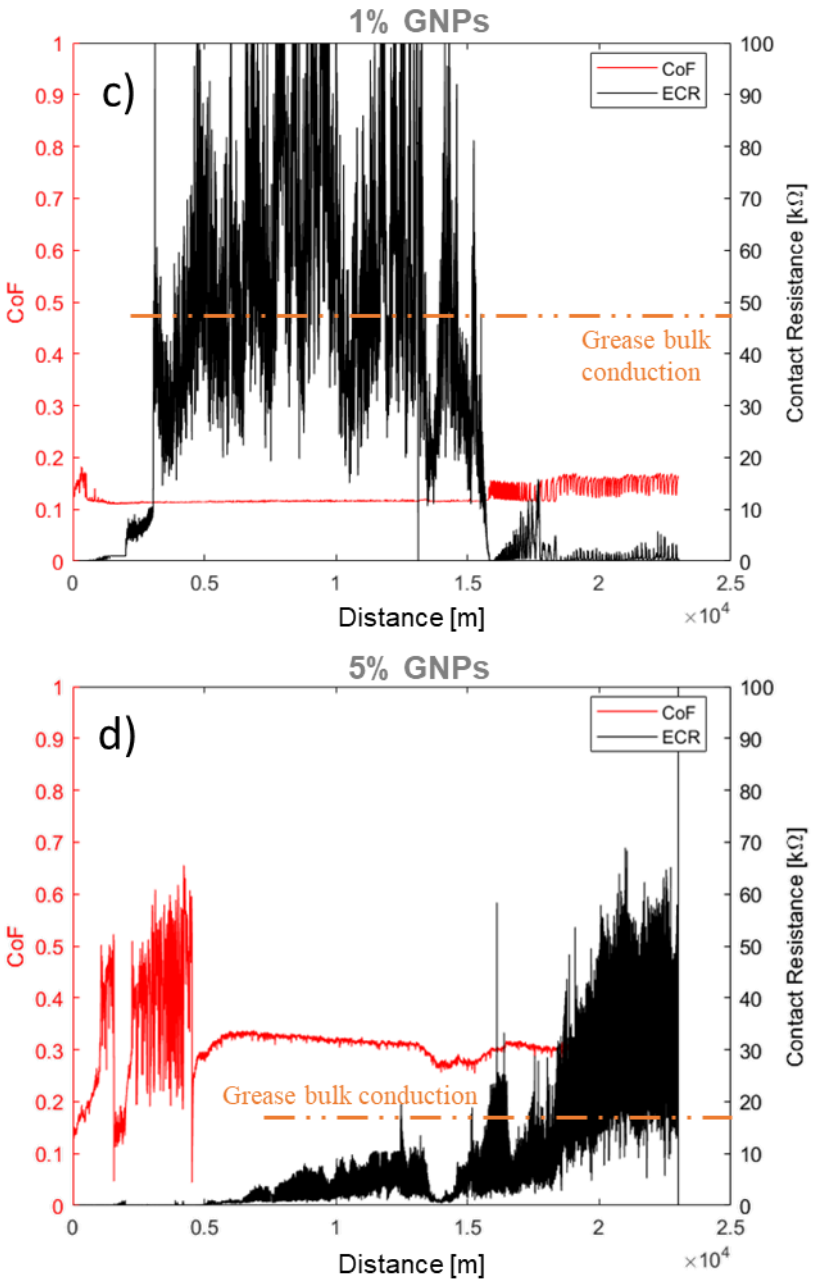

Figure 100. ECR curve recorded during four tests lubricated with different graphene-grease compounds. Additional information about the grease ECR limit of inset (d) is reported in Section 5.1.2.

Oxide particles were found at the trailing edge of the contact (see Figure 104a) and into the waste grease at the border of the wear track. Tribo-oxidation may have been triggered during the lubrication shortage. The linear wear curve was considerably stabilized and increased very gently up to the event stop of the

test. This trend may indicate that the oxides interacted with the newly formed boundary film and contributed to carrying part of the applied load.

The addition of 1% GNPs produced an improvement in the frictional performance of the grease. Results suggested that 1% GNPs allowed the system to run with a stable and low scattered friction curve for an extended time. Wang et al. [98], which reported a similar result by reciprocating pin-on-plat tests, argued that graphene increases the strength of the boundary film when the optimum quantity of graphene is added to grease. As a result, it is more stable and withstands friction longer without failure. This scenario was precisely the case of the test reported in Figure 99c and Figure 100c. Therefore, 1% GNPs can be considered close to the optimum quantity for Multemp ET-C grease. The very smooth running of the test matched high values of the ECR in the first 15000 m. The ECR values of the same order as the characteristic bulk conduction of 1% GNPs grease (see Table 33 in Section 5.1.2) corroborated the inference that a boundary film settled. Since a small quantity of oxidized debris was found in the waste grease (see Figure 104c), oxides were not likely to cause such a high contact resistance. High ECR may indicate that graphene embedded into the adsorbed boundary film according to the interaction mechanism with the fat molecules proposed by Niu et al. [95] and promoted the absorption of a thicker film. The thickening of the boundary film would explain why the linear wear curve followed a decreasing trend, which would be otherwise illogical. No dramatic lubrication shortage occurred, but cyclic fluctuations of the CoF appeared in the last 7000 m of sliding. Localized scuffing with the formation of a few oxides probably started here, and ECR was correspondingly reduced by 10 times due to the less uniform boundary film. The linear wear curve kept decreasing, indicating that the boundary film was probably still growing, although less uniform.

However, 1% GNPs could not always prevent dramatic film breakdown events from occurring in other tests. In one test, a friction curve similar to that of Figure 99a was observed. Yet, if the film breakdown occurred, graphene could alleviate the transient period of severe sliding with an additional solid lubrication action. Moreover, it always regularized the friction curve, it reduced scattering and promoted the fast restoration of the boundary film after any film breakdown.

The 0.5% GNPs grease had a somewhat similar behaviour to 1% GNPs but suffered a long period of cyclic scuffing and repeated fluctuations of friction which started after just 4000 m. The CoF increased continuously throughout the

test, but its value never exceeded 0.2. This behaviour contributed positively to limiting the average friction value. The linear wear curve replicated the trend observed with 1% GNPs and decreased after the wear-in. The wear loss measured on the sphere was probably lost in the wear-in phase only. ECR remained throughout the test at a similar value to part 2 with 1% GNPs (Figure 100c) and base grease (Figure 100a), where oxides were supposed to accumulate. Figure 104b reports a higher quantity of oxides in the waste grease than Figure 104c, which leads to thinking that oxide formation started earlier as soon as the curved started fluctuating. However, less oxides are detected than in Figure 104a and no spikes of the ECR were recorded, as with base grease. Noteworthy, 0.5% GNPs grease also exhibited the highest repeatability over the three repetitions of the tests.

Figure 99d shows that grease struggled to give rise to a stable lubrication mechanism at the onset of sliding when the amount of additive rose to 5% GNPs. The CoF underwent huge fluctuations up to 0.6 in the first 5000 m of sliding, a value dramatically close to the typical values measured in dry sliding contacts of steel [23]. This scenario was in line with the results reported by Singh et al., who argued that the excess of graphene let the nanometric flakes clump together. Larger carbon particles struggled to enter the contact zone and interfered with the feed of lubricant to the contact, thus hindering the formation of a boundary film [103]. The contact suffered severe wear in this first phase, and the noise level was high. Although a lot of oxidized debris was found in the grease accumulated on the pin and at the borders of the track (Figure 104d), oxides did not appear to play a significant role at the interface since ECR indicated metal-to-metal conduction. The wear rate was so high that debris was readily ejected from the contact, and the accumulation into a reaction layer proceeded slowly in the presence of fat molecules. Some stabilization of the friction curve was suddenly observed after 5000 m. At that point, the degree of coverage of the sliding track by oxidized matter was such that wear was mitigated and friction considerably stabilized. The lubricious effect of the reaction layer (visible in Figure 105) and the thermal softening of grease may have fostered more lubricant flow through the contact and the eventual formation of some boundary layer rich in graphene. ECR grew and reached values similar to the characteristic bulk conduction of 5% GNPs grease compound reported in Table 33 (Section 5.1.2). This trend may hint that a layer of grease was settling. However, mild abrasion went on at a reduced rate until the end of the tests because the linear wear curve kept growing.

Let us compare the characteristic values of the bulk electrical conduction presented in Section 5.1.2 and the ECR values averaged across the tribological tests. Average ECR values are presented in Figure 101a, while the ratio of the average ECR to the bulk ECR of greases is presented in Figure 101b. ECR in tests with 1% GNPs and 5% GNP grease was of comparable magnitude to the bulk conduction of grease. In both cases, a boundary film was present for most of the testing time. 1% GNPs grease was the most effective in providing lubrication and its average ECR was the highest. With 5% GNP the relatively thick boundary film (the value is the highest in Figure 101b) formed too late when the system had already suffered severe wear damage and high friciton. The very low values associated to 1% GNPs and 0.5% GNPs in Figure 101a and Figure 101b suggest that metal-to-metal and metal-oxides-metal contact prevailed during the testing time.

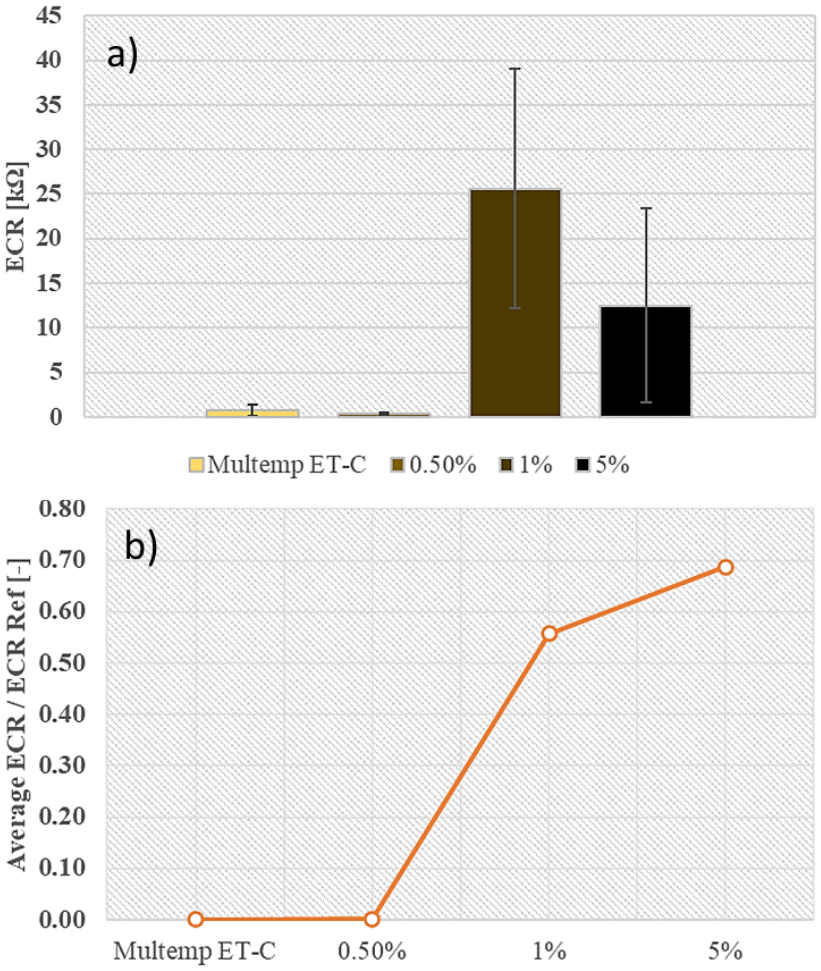

Figure 101. (a) Average ECR values recorded during pin-on-disk tests; (b) Ratio between the average ECR value and the grease bulk conduction value.

Regarding the thermal behaviour, the blue curves in Figure 92 represent the heating-up of the pin and the grease accumulated at the leading edge of the sliding contact. The data are plotted as increments above the ambient temperature signal. The two temperature trends were firmly cross-correlated with the trend of the friction curve, as was expected because the energy loss due to friction caused the temperature at the contact interface to rise. This correlation showed that the effect of graphene on the thermal behaviour of the system was indirect. Temperature rise lowered if graphene could mitigate its cause, i.e., friction. However, a direct beneficial effect could not be identified. It would be there only if the high-conductive additive affected the average conduction of the tribological interface. It is interesting to consider the ratio between the average friction power P_f and the average temperature increase ΔT. Friction power is calculated as per equation (33) and is converted almost entirely to heating power [23].

$$P_f = \frac{F_N}{t_{TOT}} \cdot \int_0^{d_{TOT}} \mu(x) \cdot dx \tag{33}$$

The ratio $P_f/\Delta T$ represents a global thermal conductivity of the tribological interface, including grease. Figure 102c suggests that only 5% GNPs could be responsible for a direct beneficial effect on the thermal behaviour of the system because the $P_f/\Delta T$ ratio is higher than the corresponding ratio estimated with base grease. Unfortunately, frictional heating from the unfavourable lubrication regime prevailed, and the average temperature with 5% GNPs (Figure 102a) was almost double as high as base grease (Figure 102b).

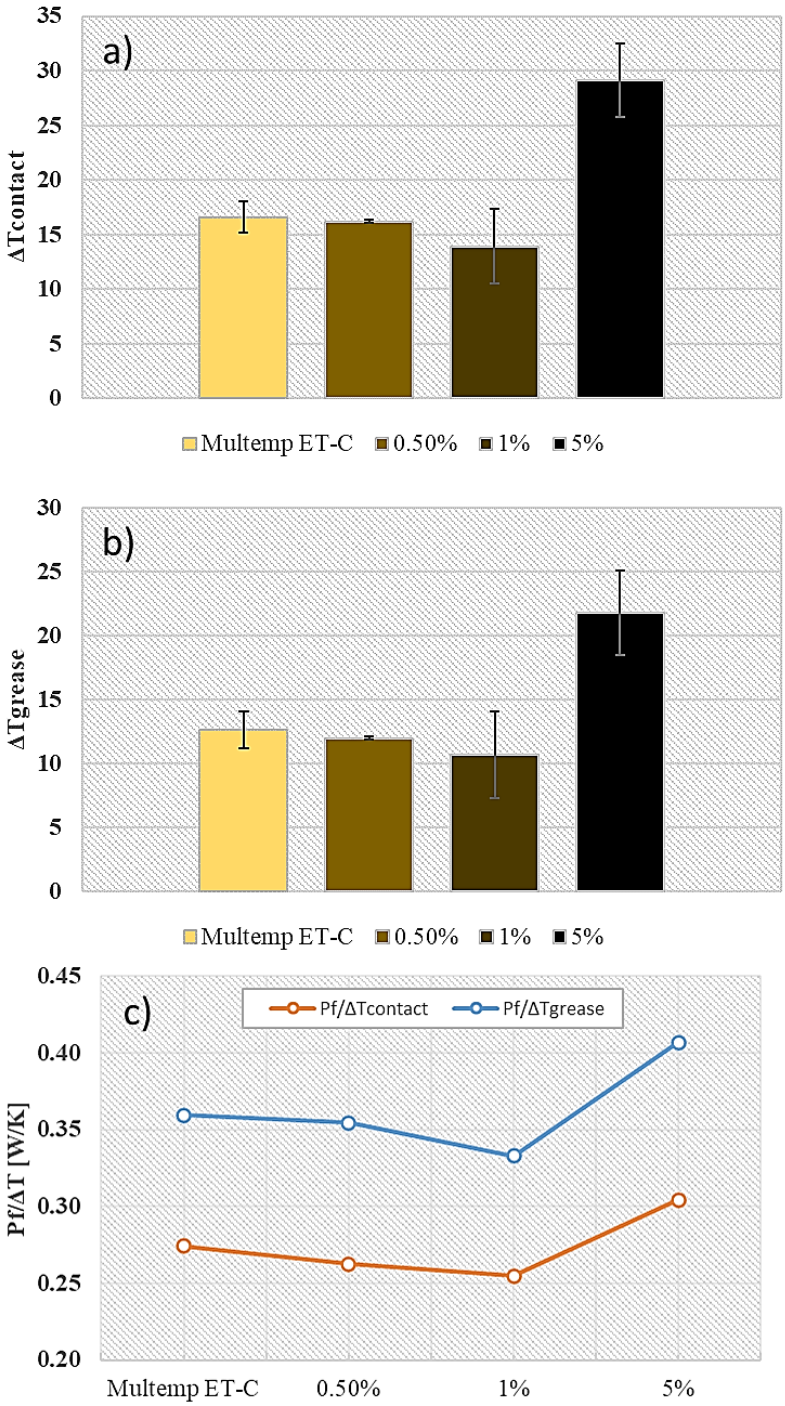

Figure 102. (a) Average temperature rise on the pin; (b) average temperature rise inside the grease build-up; (c) $P_f/\Delta T$ ratio.

5.2.2 Reduction of sliding wear

The addition of graphene also impacted wear, which was in line with friction. Figure 103 shows that graphene reduced the volume of material lost by the system, except with 5% GNPs, where the wear damage was about three times higher on average. 0.5% GNPs grease exhibited the best performance in terms of wear, and the average wear volume decreased by 46% w.r.t base grease. With 1% GNPs, the average wear reduction was 29%, but the scattering of the results was relatively high. The related confidence interval is superposed to that of base grease and 0.5% GNPs; therefore, it is hard to distinguish the performance of this compound from the statistical point of view.

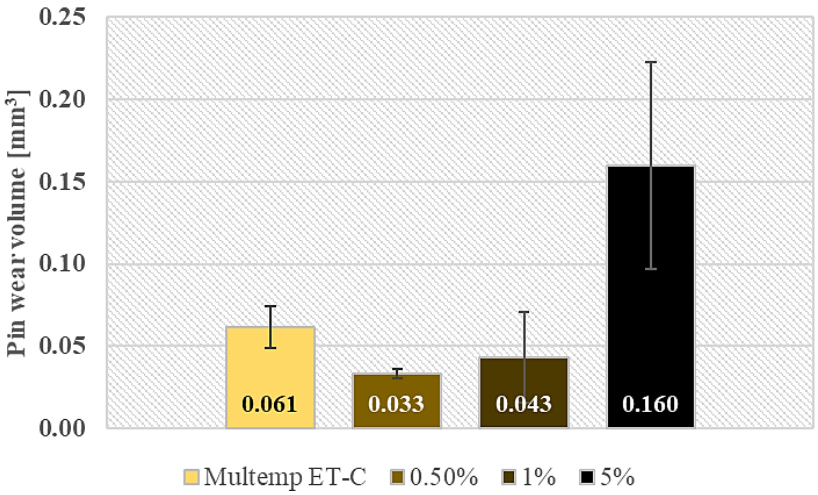

Figure 103. (a) The volume of removed material from the pin due to wear with the four grease compounds.

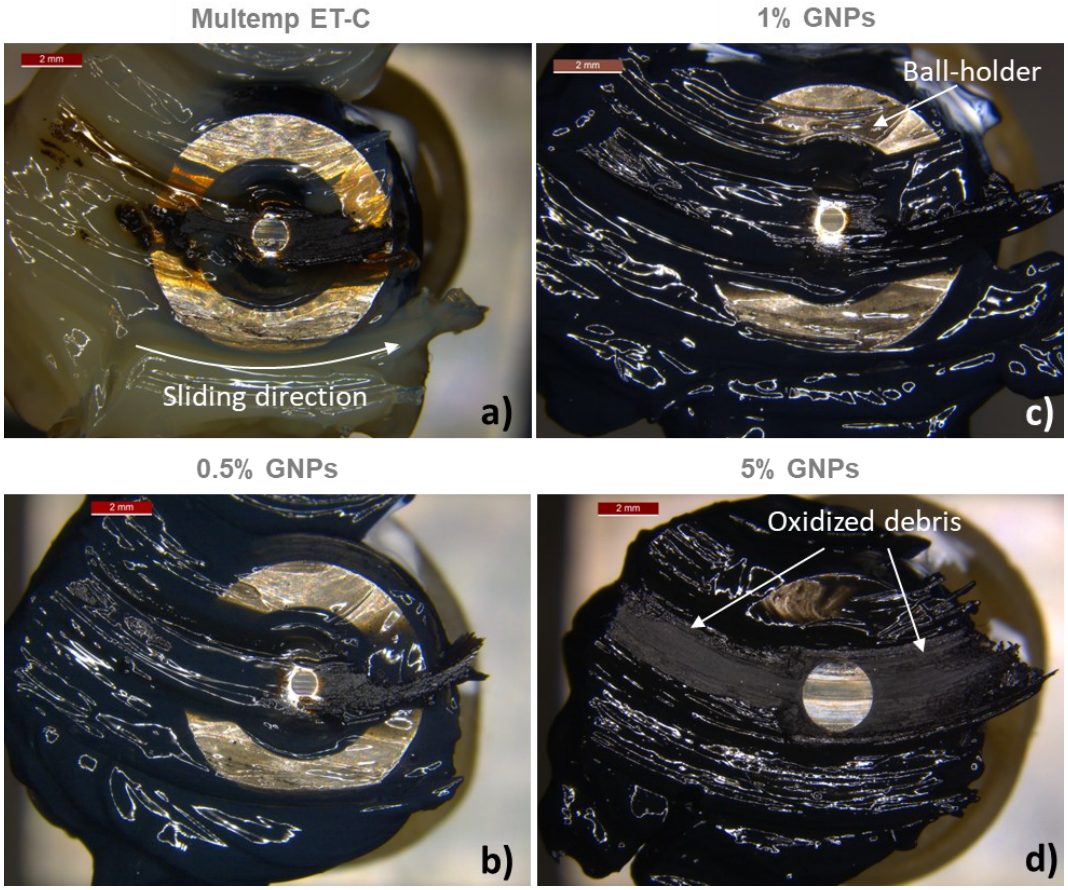

Figure 104. The worn region and waste grease on the steel sphere right after the tribological tests with the four grease compounds.

Figure 104 shows the appearance of the worn sphere right after the tribological test corresponding to the results presented in Figure 99. As discussed in Section 5.2.1, oxidized debris was found in the grease build-up, mainly at the trailing edge of the contact. A notably high quantity of debris was observed at the end of the tests with 5% GNPs grease, whereas a little debris was generated during the tests with 0.5% GNPs. This evidence correlates very well with the results of Figure 103, the friction curves in Figure 99 and the ECR values in Figure 100.

Figure 105 shows the worn region on the sample under the optical microscope and SEM. Even if the sliding path was visible on the flat sample, the amount of wear was overly tiny to be measured by surface profilometry. The wear damage was essentially limited to modifications of the surface roughness pattern because the samples were harder than the sphere. The sliding path featured a series of

relatively deep circular abrasion scratches with pure grease and 5% GNPs and a reaction layer formed in the outer region of the track where speed was maximum.

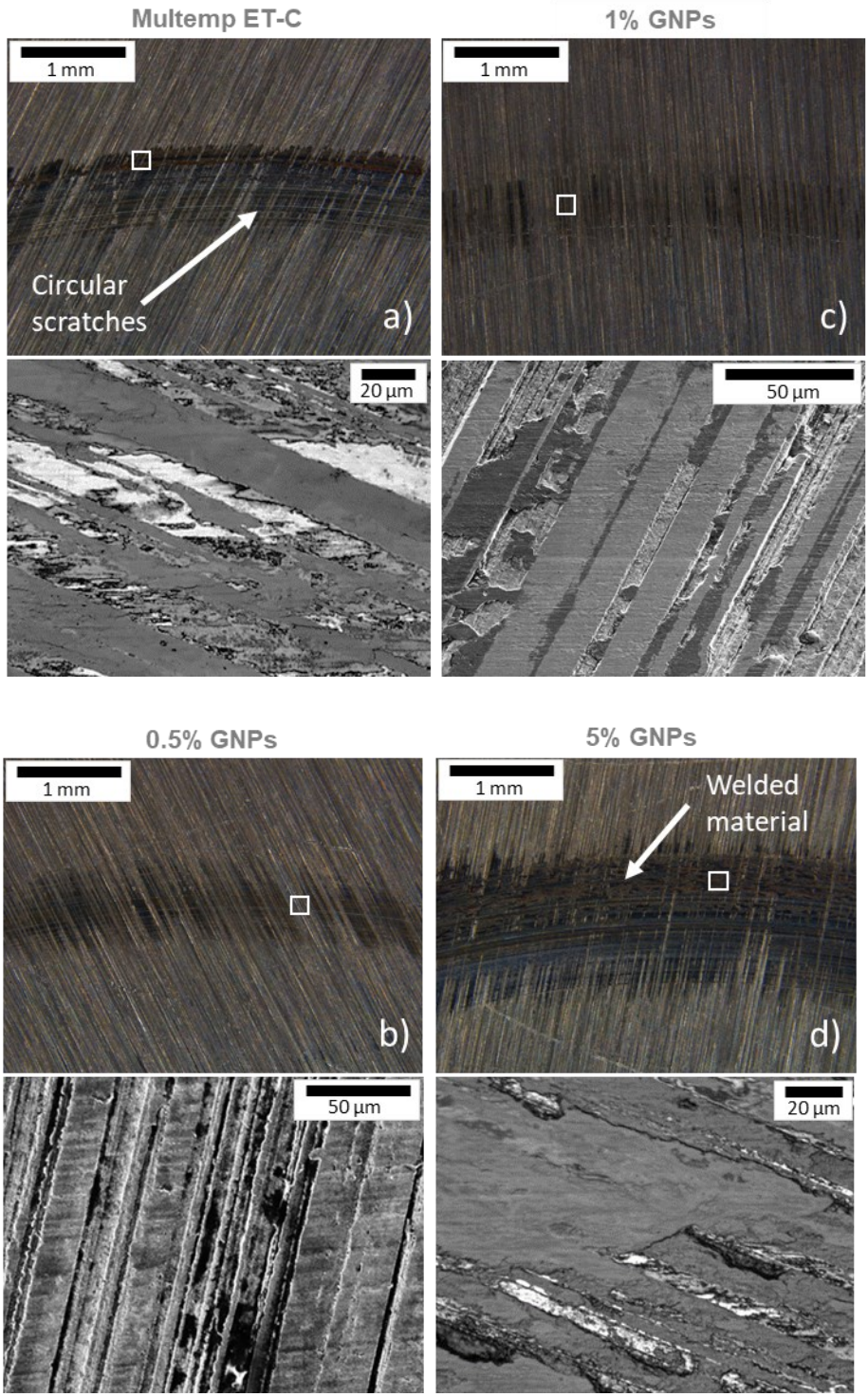

Figure 105. The appearance of the wear traces on the AISI 52100 flat sample under the optical microscope. Insets show the micro topography visible with SEM analysis corresponding to the position in the wear track highlighted by the white squares.

According to some researchers, among others, Singh et al. [103] and Niu et al. [95], the improvement of the anti-wear properties of the grease involves many physical aspects. Graphene does not only participate in boundary lubrication, thus promoting a thicker carbon-rich boundary layer, but in the presence of wear, it can be incorporated into the chemical reaction layer rich in oxides and carbides welded to the steel surfaces. If this occurs, graphene promotes the formation of lubricious carbides, e.g., F_3C, and may play a role as a solid lubricant, offering planes of easy sliding between the asperities.

With the other two graphene-enriched grease compounds, a light crushing of the rough ridges and some shallow scratches were visible after the test. As discussed in Section 5.2.1, a boundary lubrication film protected the steel surface during the tests here, thus limiting the deposition of a reaction layer (sporadic traces are visible in the inset of Figure 105c).

5.3 Rolling-in-raceway simplified tests

5.3.1 Special test setup

A special experimental setup was developed to carry out rolling friction tests with a standard pin-on-disc tribometer by reproducing the operating mode of ball bearings in a simplified way. The tribometer used for the tests was a TRB tribometer (Anton Par TriTec, Corcelles, CH) already used for the standard pin-on-disk test presented in Section 6.2. The bearing selected for tests was a 51105 thrust ball bearing with 16 spheres of diameter 6 mm, spaced 22.5° from one another into the cage. The lower ring was fixed to the rotating spindle of the instrument, and the set of rolling elements was placed above it. A pad cut out from the upper ring of the thrust bearing (a sector of the upper ring) was fixed to a cylindrical pin and installed onto the sensorized arm of the tribometer to measure the reaction force due to rolling friction. The contact load was applied to the pad by calibrated dead weights as with standard pin-on-disc tests. The contact between the rotating lower ring and the static upper pad is achieved through the spheres in between. The spheres were then free to roll inside the raceway of the lower ring, and the cage could rotate unrestrictedly about the axis of the bearing, as they do in

actual operating conditions. Figure 106a shows the peculiar setup for rolling friction measurement referred to as *rolling-in-raceway* tests hereinafter.

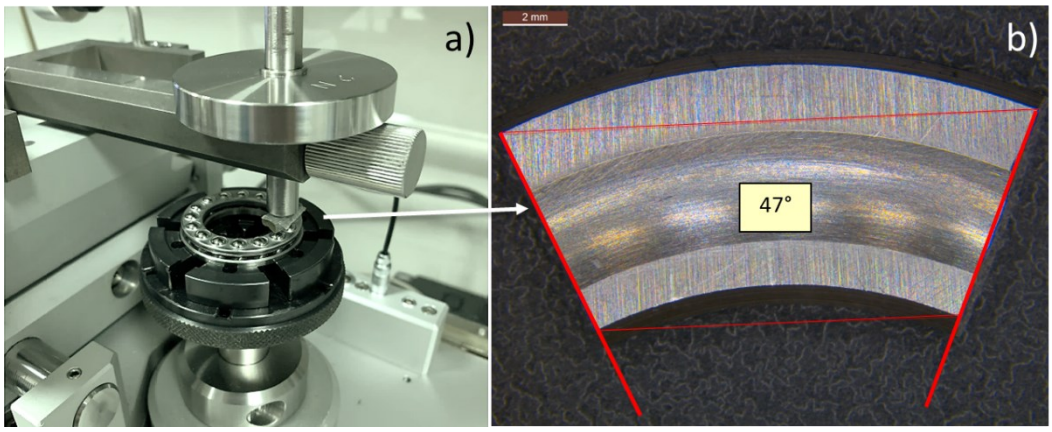

Figure 106: (a) Special setup of the rolling test installed on the pin-on-disk tribometer; (b) Sector cut from the upper ring of the thrust ball bearing by EDM. From [122].

To have at least 2 spheres in contact under the pad, the angular width of the pad should be equivalent to double the angular span between two consecutive spheres. However, the machining tolerance of the cutting process should be accounted for. A slightly larger angular width was chosen operatively to avoid transitory where only one sphere supports the load because only one sphere under the pad would misalign the friction pair during the measurement. The pads prepared for these tests were sectors 47° wide. Figure 106b shows the angular width measured under the optical microscope. The pads were manufactured by electrical discharge machining (EDM) to minimize the amount of material lost during the cutting process. One single bearing was used to carry out all the tests. Due to rolling motion and moderate applied loads (see Section 2.3), no signs of wear were ever detected inside the raceway groove either under the optical microscope or by profilometric inspection.

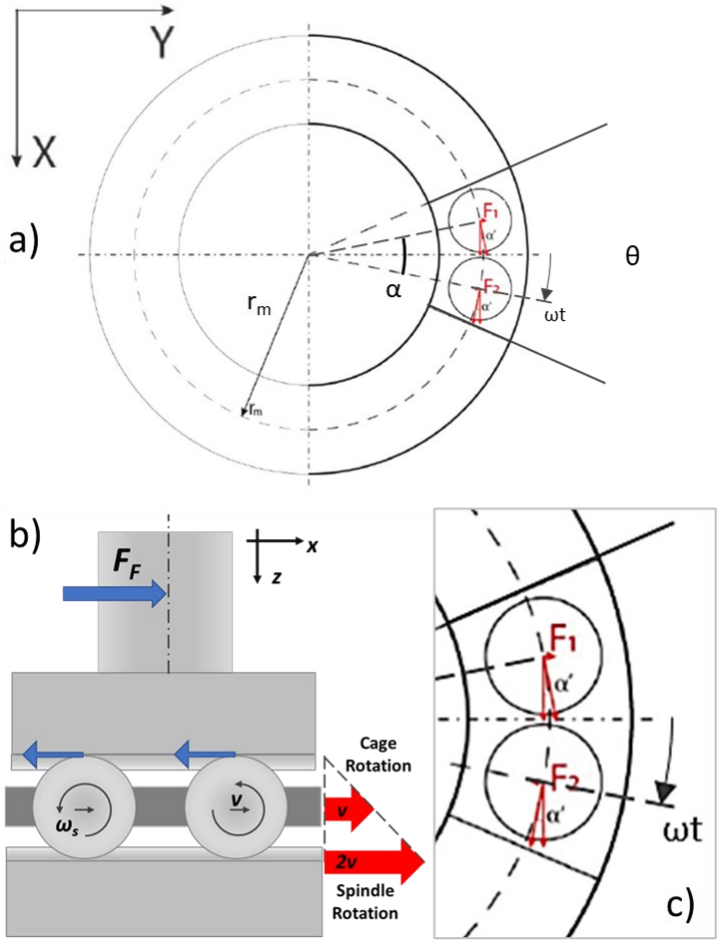

Figure 107: (a) Free-body diagram of the spheres in contact with the upper pad (θ is equal to 47°) in the case of two spheres in symmetrical contact, where α' = ωt – α; (b) Detail of the set of force at the contact site of the sphere against the pad. From [122].

Modelling the equivalent bearing friction torque

A system of tangential forces resulting from the frictional torque that drags the spheres to roll acts on the pad according to the free-body diagram of Figure 107a. The resulting frictional force F_f on the pad (Figure 107b) is the quantity measured by the force sensor of the tribometer during the tests. The frictional torque of the entire bearing can be estimated through a suitable analytical model that correlates the tangential forces F_1, F_2 at each contact site to the total reaction force F_f on the pad.

Only the force component along the x-axis contributes to the friction force measured by the tribometer. The components along the y-axis generate a

momentum that was neglected during these tests since the torsional stiffness of the measuring arm was supposed to be high enough. Since the angular width θ of the pad (47°) exceeds double the angular span α (22.5°) between two consecutive spheres, a transitory where three spheres are in contact under the pad exists. The analytical model neglects this transitory condition as it vanishes immediately after a new sphere enters the contact region.

Equation (34) correlates the total frictional force F_f with the contact forces in the generic case where two spheres lie under the pad (Figure 2). In the equation ωt is the generic contact angle which evolves as a function of the rotation of the cage itself. Supposing that the contribution of each sphere is constant, i.e. $F_1 = F_2 = F$, the tangential force at the contact sites is formulated according to equation (35) where F_f is the known quantity measured by the tribometer

$$F_f = F_1 \cos(\omega t - \alpha) + F_2 \cos \omega t\,; \qquad \omega t = \left[0, \frac{\theta}{2}\right] \tag{34}$$

$$F = \frac{F_f}{\cos(\omega t - \alpha) + \cos \omega t}; \qquad t = \left[0, \frac{\theta}{2\omega}\right] \tag{35}$$

The equivalent friction torque T_{sphere} needed to let each sphere roll is related to F through equation (36), where r_m is the pitch radius of the rolling path.

$$T_{sphere} = F \cdot r_m \tag{36}$$

The contribution of each sphere is to be multiplied by N, i.e., the total number of spheres, to obtain the estimate of the overall friction torque expected for the full bearing in the equivalent working conditions. The equivalent bearing torque $T_{bearing}$ is calculated by equation (37). Noteworthy, such equivalent friction torque for the full bearing represents the frictional behaviour of a bearing loaded by a correspondingly higher axial load $F_{Nbearing}$ defined by equation (38). $F_{Nbearing}$ is higher than the load F_N applied to the pad because during rolling-raceway tests only a sector of the bearing was subjected to loading.

$$T_{bearing} = N \cdot T_{sphere} = N \cdot F \cdot r_m \tag{37}$$

$$F_{Nbearing} = \frac{2\pi}{n \cdot \alpha} \cdot F_N \tag{38}$$

In equation (28), n is the number of spheres simultaneously in contact with the pad ($n = 2$ for the given setup).

5.3.2 Friction results of rolling-raceway tests

Rolling-raceway tests were carried out in lubricated conditions by applying *1g* of grease to the bearing. The lubricant selected for this investigation was MULTEMP ET-C grease and the three graphene-grease compounds used for pin-on-disc tests (see Section 5.2). The effect of graphene on rolling friction was investigated in terms of comparison with the base grease.

Two kinds of rolling tests were carried out: short-term and long-term. The short-term tests lasted 16 minutes; they were intended to investigate the coupled effect of increasing load, speed and graphene content on rolling friction. The overview of the parameters of the test campaign is presented in Table 35. Long-term tests were carried out to investigate the effect of the graphene concentration inside the grease over a longer running time. They lasted 3 hours and ran under a load of 30 N and a rotational speed of 600 rpm. Higher speed was not explored to avoid measurement instabilities because of the peculiar test setup. Three repetitions were performed with each set of testing parameters, and the results were averaged.

Table 35: Map of testing parameters for the rolling-raceway tests carried out with the four concentrations of graphene-enriched greases (0%, 0.5%, 1%, 5%). Marks ‘x’ indicate short-term tests; marks ‘#’ indicate long-term tests.

	Speed [rpm]			
Load [N]	**30**	**150**	**300**	**600**
5	x	x		
10		x		
20		x		
30		x	x	x #

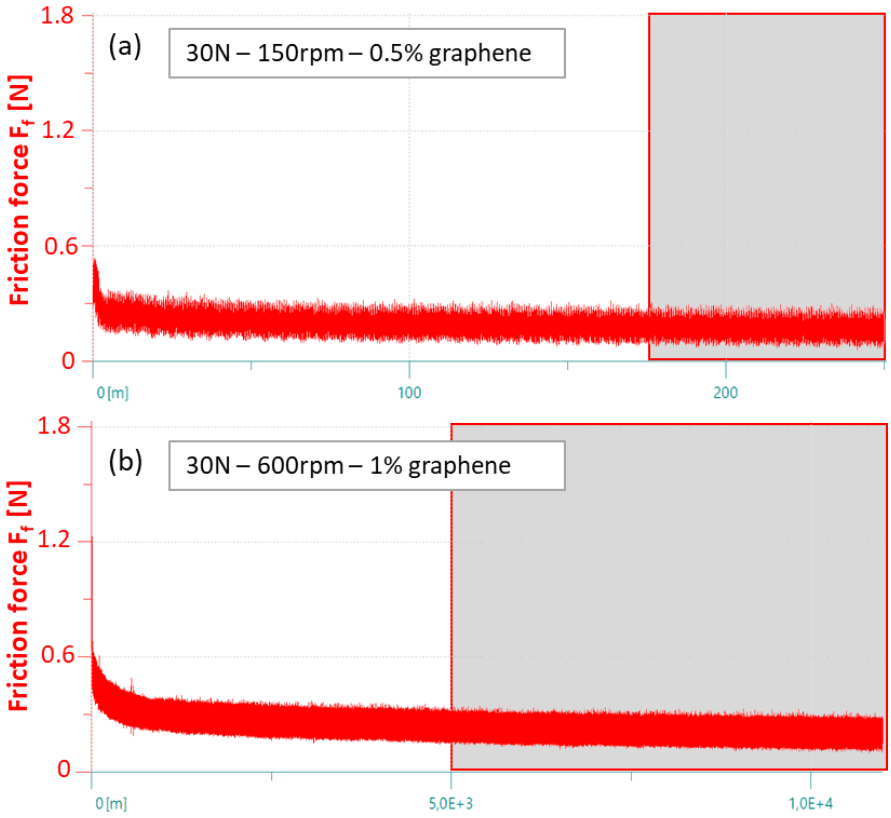

Figure 108: (a) CoF curve acquired during a short-term test with lubrication by the 0.5% graphene grease; (b) CoF curve acquired during a long-term test with lubrication by the 1% graphene grease. The greyed region of the diagram marks the portion of the curve considered to calculate the statistical quantities. From [122].

Figure 108a shows, for instance, the friction curves acquired during short-term tests, and Figure 101b is a friction curve from long-term rolling-raceway tests. A moving average filter filtered the rough signals to reduce noise. Considering the last part of the friction curve, the average CoF values and the related standard deviation values were estimated for both short-term and long-term tests. The frictional behaviour was unstable at the beginning of the tests because grease needed some time to distribute along the rolling path properly. Shaded areas in Figure 108 indicate the portion of friction curves considered for averaging, i.e. 10% of the total test duration for short-term tests and 50% for long-term tests. The authors decided to consider a wider portion of the friction curve in long-term tests because stabilization was not reached by the stop time of the tests.

The diagram in Figure 109 shows the results of the tests with a duration of 16 minutes. As a general trend, the friction force F_f increased with increasing load

and rotational speed for both base grease and grease enriched in graphene. The rolling-raceway tests carried out at a fixed speed of 150 rpm and increasing load produced very similar results in terms of friction. The friction force F_f underwent a weak increase from about 0.12 - 0.15 N to about 0.16 - 0.18 N in the range from 5 N to 30 N. On the other hand, when speed was reduced or increased under constant applied load, the friction force measured by the tribometer varied more. For instance, the friction force measured under a constant load of 30 N almost doubled when the speed was raised fourfold. This evidence suggests that speed is a major parameter influencing rolling friction, at least within the conditions explored in this research.

Under medium to low load and speed, up to 20 N and 150 rpm, the grease compounds with 0.5% and 1% graphene disclosed a fluctuating behaviour, sometimes decreasing and sometimes increasing the average rolling friction force. The grease compound with 5% graphene performed worst and always produced the highest rolling friction force. The consistency of the lubricant is expected to grow by increasing the amount of nano-additive in the grease. A higher consistency due to the excessive graphene quantity may have promoted the sticking of the spheres to the surrounding grease, thus negatively affecting friction. Moreover, the average temperature of the pad and the average temperature of the grease around it did not increase during the tests, so thermal softening of grease did not play a role (thermal softening would instead occur in the actual operative condition of bearings). Lack of thermal softening is expected to make it more challenging for grease to enter the rolling contact by dragging effect. The temperature at the contact was monitored by an IR camera (Radiamatic XT, IRTech) placed in front of the pad, as Figure 110 shows. The measured temperature during the tests ranged from 25 to 30 °C, on average, depending on speed.

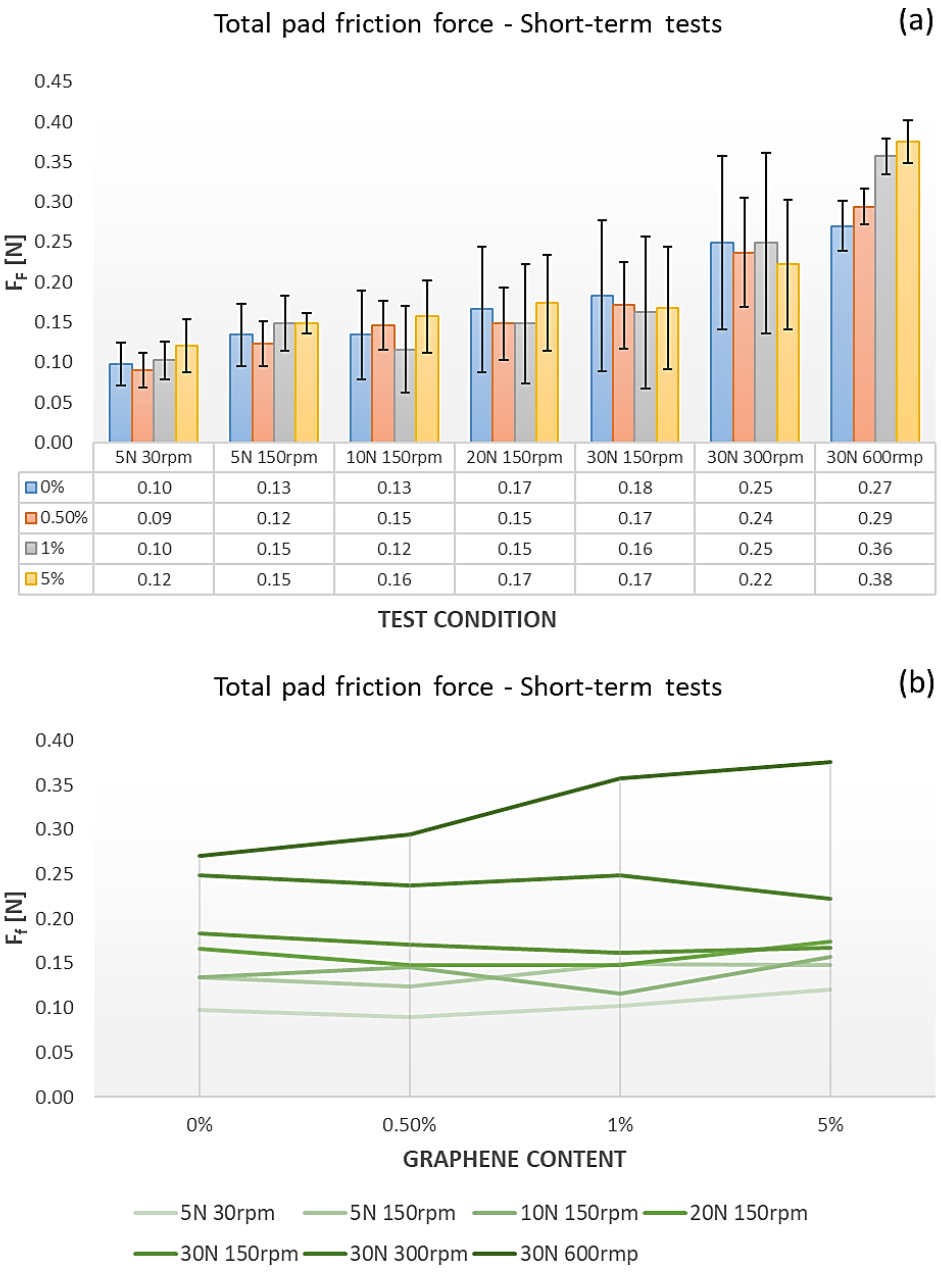

	5N 30rpm	5N 150rpm	10N 150rpm	20N 150rpm	30N 150rpm	30N 300rpm	30N 600rmp
0%	0.10	0.13	0.13	0.17	0.18	0.25	0.27
0.50%	0.09	0.12	0.15	0.15	0.17	0.24	0.29
1%	0.10	0.15	0.12	0.15	0.16	0.25	0.36
5%	0.12	0.15	0.16	0.17	0.17	0.22	0.38

Figure 109: Average Ff trend measured with increasing load and speed according to Table 35. Uncertainty bands at the 95% confidence level were estimated equal to 3σ, where σ is the standard deviation of the results. The corresponding CoF values ranged from 0.005 to 0.03. From [122].

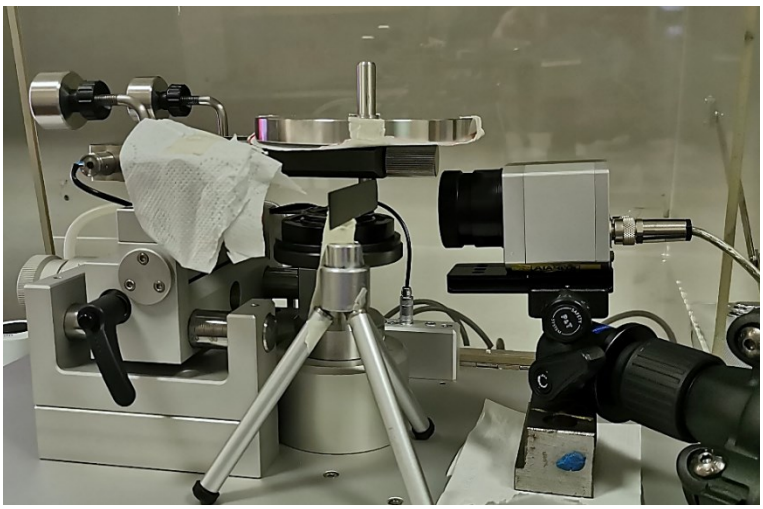

Figure 110: Setup for monitoring the temperature rise during rolling-raceway tests by IR thermography. From [122].

Besides, rolling traction transferred by the lower rotating ring to the spheres may fail under low load, thus amplifying the tendency of the rolling bodies to stick to the surrounding grease. Applying a vertical load of 5 N on the pad would correspond to a working condition where the full bearing is loaded by an axial load equal to just 40N, according to equation (38). This value was slightly higher than the minimum load of 18N suggested by the SKF Bearing Catalogue [123]. Therefore, some micro-slip at the contact points could not be excluded. As a reference value, the average Hertzian contact pressure under 5 N was calculated to be equal to 383 MPa by the software HertzWin (Vink System Design & Analysis), considering the effect of roughness. The surface roughness of the spheres and the raceway grooves was measured randomly with a stylus roughness measuring instrument (RTP80, SM Instruments, Volpiano). Roughness was *Ra* 0.085 µm and *Ra* 0.190 µm, respectively.

The trend was reversed for high load and medium speed, i.e. 30N and 150 to 300rpm. The addition of graphene seemed to have a weakly positive effect on rolling friction, and the value of the resulting friction force was slightly reduced compared to the base grease, whatever the content in graphene. The authors found no reasonable explanation for this trend reversal, however. The uncertainty range associated with friction tests carried out under load up to 30N coupled to speed up to 300 rpm largely overlapped, and the relative difference was hardly discernible from the statistical viewpoint.

At the highest load and speed, i.e. 30N and 600 rpm, the presence of graphene had a significant effect on friction, and the higher the content in graphene, the greater the friction losses. Interestingly, the results of the rolling-raceway tests lasting 3h, which run under the same load and speed, were in line with those from short-term tests. F_f measured with the 5% GNPs graphene-grease compound was about 1.5 times higher than base grease in both cases. The average value of the friction force measured during the 3h tests is presented in Figure 111. The uncertainty bands at the 95% confidence level were not overlapping here, which evidences a systematic effect related to the content of graphene in grease.

This unexpected result obtained by increasing the percentage of nano-additive could be ascribed once again to the increase in grease consistency. The temperature rise at the contact was almost null even in tests with extended running time, and the working of grease accumulated around the track was very gentle. Without thermal softening, the high-consistency greases may have struggled to feed the contact site after the grease was cleared from the rolling track. A lower lubrication performance may have resulted. Besides, Fu et al. [92] proved that the apparent kinematic viscosity increases with increasing the percentage of graphene nano-particles in the grease. At a speed of 600 rpm, an additional contribution to F_f due to viscous drag of the grease might have become significant.

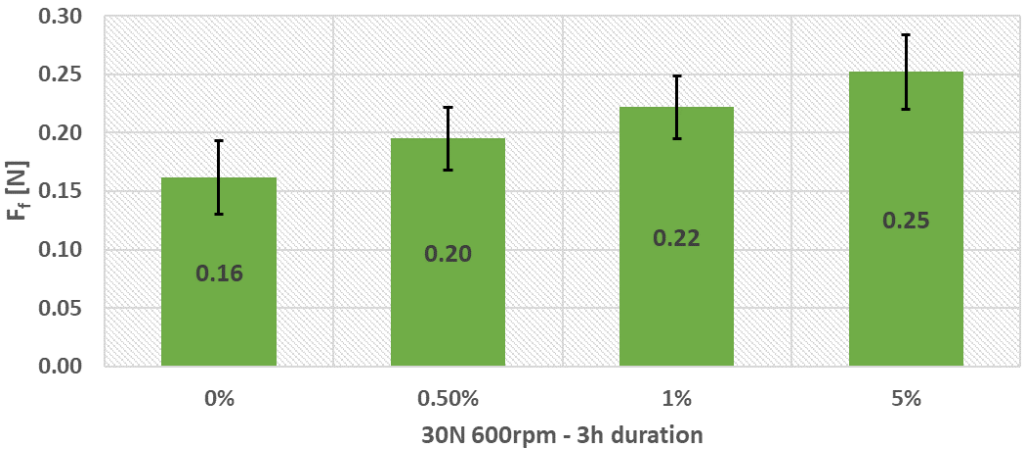

Figure 111: Average pad friction force measured during long-term tests (30N load and 600rpm speed) with increasing the graphene content into the grease. From [122].

The results of the long-term tests presented in Figure 111 were exploited to have an estimate of the equivalent friction torque $T_{bearing}$ expected for the bearing under test, based on equation (37). The results shown in Figure 112

confirmed the systematic increase in the friction torque with increasing graphene content, up to a maximum of 34 Nmm with 5% GNPs.

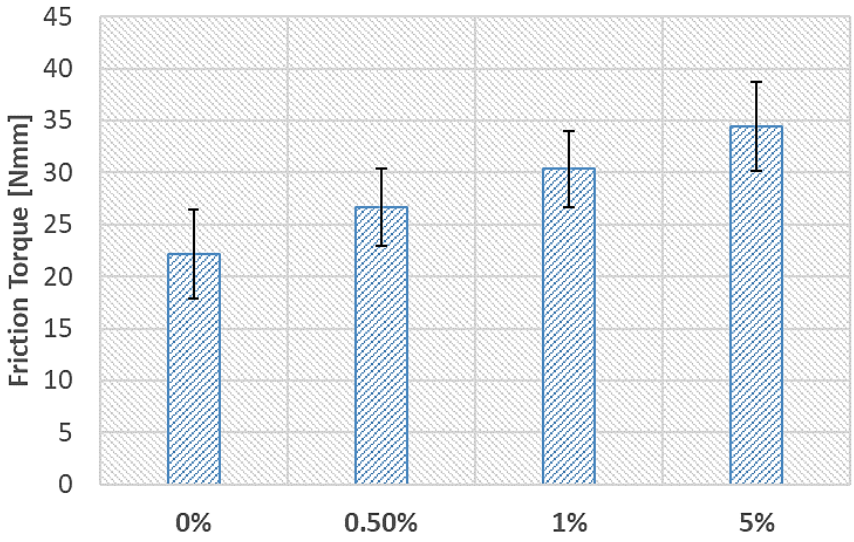

Figure 112: Equivalent friction torque $T_{bearing}$ calculated by equation (37) corresponding to the outcome of the long-term rolling-raceway tests with increasing GNPs content. From [122].

5.3.3 Validation of the testing method

Since experimental values of friction torque obtained by component tests in equivalent testing conditions are unavailable, the testing method proposed in this paper was validated by comparison with the value calculated through the SKF Model of Friction [123]. The semi-empirical model for T_{SKF}, i.e. Equation (39), is based on extensive experimental testing with many bearings, and thus the corresponding value can be taken as a reference value.

$$T_{SKF} = \beta \cdot \left(M_{rr} + M_{sl} + M_{seal} + M_{drag}\right) \tag{39}$$

In equation (39), M_{rr} is the rolling frictional moment, M_{sl} is the sliding frictional moment, M_{seal} is the contribution seals (if present), M_{drag} is the frictional moment of drag losses, churning, and splashing of lubricating oil, and β is a correction factor that considers the extra contribution to friction due to grease churning, if applicable. T_{SKF} was calculated by SKF Bearing Select, an online tool for the calculation of rolling bearings provided by SKF [124]. An equivalent

operating condition to long-term tests was considered for the calculation, i.e. 600 rpm of speed, 240 N of axial load, an average temperature of 30°C, and a contamination factor of 0.79 (as per ISO 281:2007 guidelines). The reference viscosities at 40°C and 100°C of the grease base oil were considered, according to the technical sheet provided by Kyodo Yushi Co. Ltd. As to the correction factor Table 32, β = 1 applies for:

- ❖ grease-lubricated bearings where the free volume is filled approximately 30% with grease
- ❖ bearings operated in steady-state conditions.

In all other cases, the SKF Model of Friction prescribes β = 2 for light series bearings and β = 4 for heavy-duty series bearings. This correction applies, for instance, during the running-in phase after a lubrication or relubricated event. In the rolling-in-raceway tests performed for this research, the load was low, the speed was moderate and almost no temperature rise was observed at the contact. Provided that a steady state was attained, it was not comparable to the actual operative conditions of most industrial applications. Steady-state lubrication is usually reached after many hours and usually involves thermal stabilization at a temperature higher than room temperature. Cousseau et al. [125] reported that grease generated higher bearing torque than the corresponding base oil in low-speed low-temperature conditions. Oil bleeding from grease reservoirs might not be the primary lubrication mechanism [4], and grease as a whole entity still plays a crucial role, including the thickener. Yet, the SKF Model of Friction takes into account just the viscosity of the base oil to calculate T_{SKF}. Moreover, the friction curve in Figure 108b shows a friction trend which is still decreasing at the end part of the 3h tests. A steady-state may require more than a few hours with a rolling-in-raceway setup (a few hours of running-in is typically observed with industrial bearings). Given the above observations, the authors decided to validate the method considering β = 2, as if running-in did not vanish yet. β higher than unity is also justified by considering that the whole free volume of the bearing was virtually filled out with grease, and a grease build-up accumulated at the leading edge.

Figure 113 compares the value of T_{SKF} and $T_{bearing}$ with reference to the case of lubrication with the base grease (without nano-additives). The values of friction torque obtained by rolling-raceway tests were comparable to that estimated by the SKF Model of Friction because T_{SKF} belongs to the uncertainty band associated to $T_{bearing}$ at the 95% confidence level.

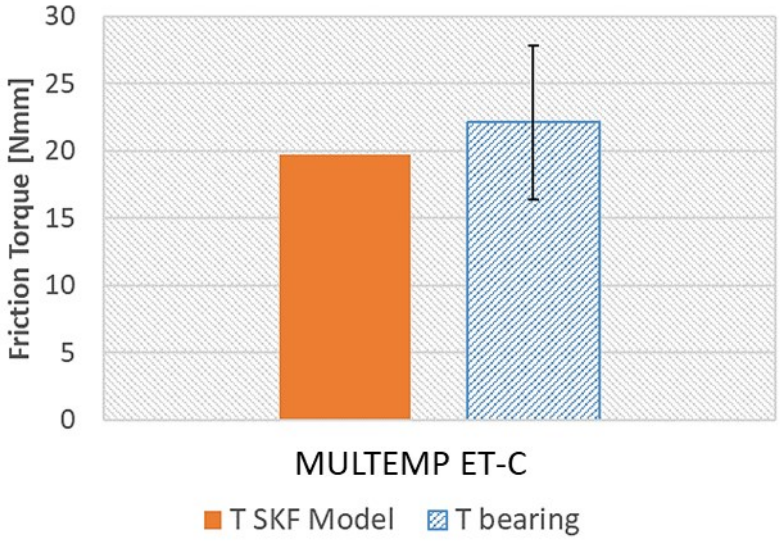

Figure 113: Equivalent frictional torque of the SKF 51105 bearing under 240 N load and 600rpm speed estimated based on the results of the rolling-raceway tests and compared to the values predicted by the SKF Friction model. T_{SKF} was calculated by the SKF Bearing Select online calculation tool (SKF Bearing Select, s.d.). From [122].

The results suggested that this simplified approach may apply to measuring friction in grease-lubricated thrust ball bearings. Further investigations will be necessary for the future, though, to eventually validate this method against experimental values of the friction torque by full component tests.

It is interesting to report here that a characteristic ticking sound was also perceived during the tests, as if recurring collisions were happening. A collision will likely occur between the spheres and the pad at the leading edge (Figure 114) whenever a sphere approaches the contact. Recalling the working principle of the test set-up presented in Figure 106, only a subset of the rolling elements is in contact with the pad in rolling-in-raceway tests and contributes to the measured friction force F_f. As soon as each sphere enters the contact region between the lower ring and the upper pad, a kinematic transition from prevailing sliding motion under no load (outside the contact) to rolling motion under applied load (inside the contact) occurs. This scenario is unusual for a fully loaded bearing where the spheres roll over a continuous raceway groove. The residual difference between the values of friction torque and the scattering of the experimentally determined friction torque might be associated with this phenomenon. However, it was apparently of minor importance since no dramatic extra contribution to the measured friction force was introduced into the system by these collisions

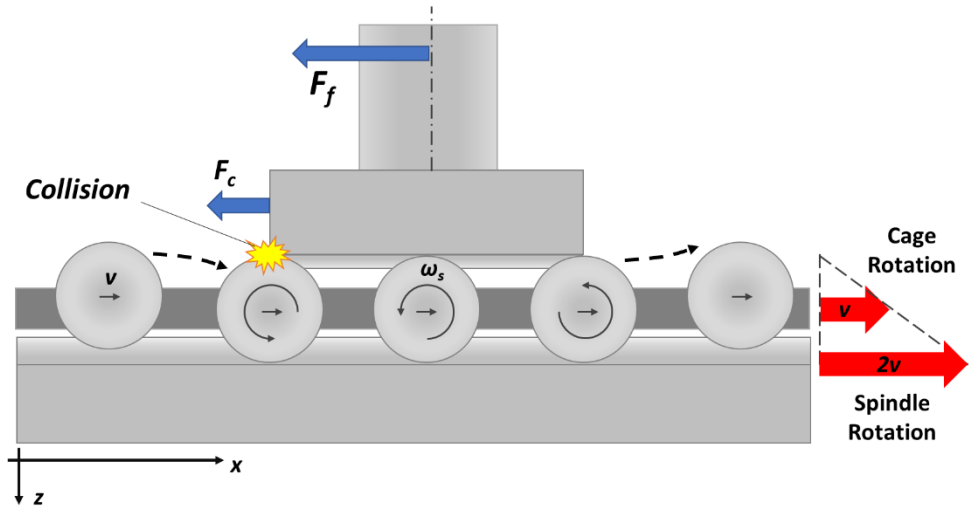

Figure 114: Schematic of the collision of the spheres with the upper portion of the raceway while entering the contact region where the tribometer measures the friction force F_f. From [122].

5.4 Conclusions and future perspectives

The research presented in Section 5 aimed to investigate whether adding graphene into a grease can enhance the lubricant performance and the tribological behaviour of rolling and sliding contacts.

Standard pin-on-disc tests were carried out to investigate the effect of graphene in grease-lubricated sliding contacts. Long-term tests under high load and high speed were intended to assess if graphene can serve as an EP solid additive for greases in heavy-duty conditions where the entrainment of lubricant into the contact is difficult. Rolling-in-raceway tests were exploited to investigate the effect of graphene in grease-lubricated rolling contacts. A special test setup was developed to replicate in a simplified way the operative condition thrust ball bearings with a pin-on-disc tribometer. Through this special setup, rolling friction force was measured in the presence of grease while reproducing the actual rolling motion of the spheres inside the bearing raceways. The friction torque expected for the full bearing in equivalent operative conditions was also estimated and turned out to be in line with the value calculated through the SKF Model of Friction.

Commercial MULTEMP ET-C grease from Kyodo Yushi Co. Ltd. was used to prepare graphene-grease compound with an increasing percentage of GNPs, i.e. 0.5%, 1% and 5%(wt.), and the performance of these compounds in terms of friction and wear was compared to that of base grease. A high-quality, high-performance, fully synthetic grease was selected to assess if graphene as a nano-additive can outperform the traditional molecular additive packages currently used by lubricant manufacturers to foster EP properties of greases.

The pin-on-disc test results proved that graphene positively affects sliding wear and friction if its concentration in the selected grease does not exceed 1%wt. Data augmentation by ECR measurement further confirmed the outcome of tribological tests. A moderate percentage of graphene in the grease reduced the average CoF and the contact temperature compared to base grease and suppressed most of the fluctuations of the friction curves related to an unsteady feed of grease to the contact. The results suggest that in pure sliding, the nano-additive made the starved boundary lubrication regime of grease more effective and protected the surface from adhesion. The presence of graphene reduced the amount of wear, and as such, it acted as an additional solid lubricant at the interface despite the intermittent feed of lubricant.

From the thermal point of view, 0.5% to 1% of GNPs improved the thermal state of the systems indirectly. Graphene reduced the heat source by reducing the frictional energy dissipation but could not affect the thermal diffusivity at the interface. On the other hand, a concentration of 5% GNPs increased the measured thermal conductivity of grease significantly, but such a high concentration turned out to be detrimental to the system in terms of wear and frictional energy dissipation. Consequently, any direct correlation between the improvement of the thermal properties of grease by graphene and the tribological behaviour of the system cannot be inferred based on the results presented.

Noteworthy, the results of the pin-on-disc tests were somewhat scattered, and more repetitions of the tests with the most promising grease compounds are necessary in the future. More repetitions were impracticable due to the very long duration of the tests (about 8h each) and the long setup time of combined tribological-thermal-electrical measurements. It would be interesting to investigate the effect of roughness and speed on graphene-grease compounds in the future. Roughness may interact with the additive promoting or discouraging some carbon deposits on the surfaces; speed may affect the feed of melted

lubricant towards the contact site, thus highlighting the degree of intervention of the nano-additive as a solid lubricant.

The results of rolling-in-raceway tests proved that enriching grease with GNPs is generally not beneficial on rolling friction, at least in the specific test conditions explored. The rolling friction force measured during short-term tests fluctuated significantly under low load and speed, and a beneficial or detrimental effect from graphene was not observed because friction was sometimes decreased and sometimes increased compared to base grease. The friction force observed during long-term tests under 30N load and 600 rpm (i.e. the highest load and speed here considered) was higher with every grease compound than with base grease. The 5% GNPs grease compound increased friction by 50% compared to base grease at the end of extended rolling tests.

This method could not still replicate the same operative conditions of grease-lubricated industrial bearings, although rolling-in-raceway tests simulated grease conditions in bearings better than other standard simplified tests. No temperature rise was observed at the contact site due to the limited load and speed allowed by the tribometer. Temperature is known to decisively impact grease consistency and lubrication mechanisms at a steady state. This issue might not have shed light on the full potential of graphene as an additive for greases in rolling conditions.

It will be interesting to compare in the future the results obtained by rolling-in-raceway tests with component tests performed through dedicated bearing testers with 51105 thrust ball bearings. This comparison is necessary to assess further the validity of the proposed method for measuring rolling friction torque in bearings. Moreover, the results of component tests will provide more insight into the impact of graphene on the rolling friction of grease-lubricated bearings operated in load, speed, and temperature conditions closer to industrial applications.

Chapter 6

Grease life modification by graphene nano-additive

The pin-on-disc tests presented in Section 5.2 revealed that graphene could effectively improve the tribological performance of the selected grease with a positive impact on both friction and wear. However, the grease working condition is far removed from any real-life application in any pin-on-disc test. Pin-on-disk involves pure sliding motion at the tribological interface according to the reference standards [62] and ASTM G133-05(2016) [126]. Pure sliding is the most burdensome working condition for any lubricant because shear stress is maximum and lubrication effectiveness is minimum due to shear thinning and low entrainment speed. In most industrial applications, the kinematics of the grease-lubricated tribological interface involves rolling or mixed rolling-sliding motion (e.g. bearings, gears, and others).

No type of '*model test'*, as per the definition provided by the DIN 50322 standard (now retired), can reproduce the same conditions of real applications, although representative values of speed, contact pressure and temperature can be reproduced at laboratory scale for higher significance. Ideally, laboratory testing should always allow rapid results with reduced test costs compared to component or field tests (Figure 115). Many widespread testing methods belong to the group of the simplified *model test*, for instance, the four-ball test (Shell VKA test machine), pin-on-disc test, Almen-Wieland test, SRV high-frequency reciprocating test, two-disc (or twin disc) test, to mention but a few. Some of

these methods are currently used in the development process of lubricants to allow rapid and economical determination of changes in the main lubricant characteristics through the development stages. It is hard to predict the actual performance of lubricants based on the results of simplified tests only because the correlation between these and the actual applications is not straightforward [117]. The testing machine can also constrain the contact shape and main testing parameters in model tests, so the simulated tribopairs may not directly represent the actual application under study. In other words, the more the tribological test is simplified, the less it can be susceptible to the whole set of influencing factors and phenomena involved in real applications[5].

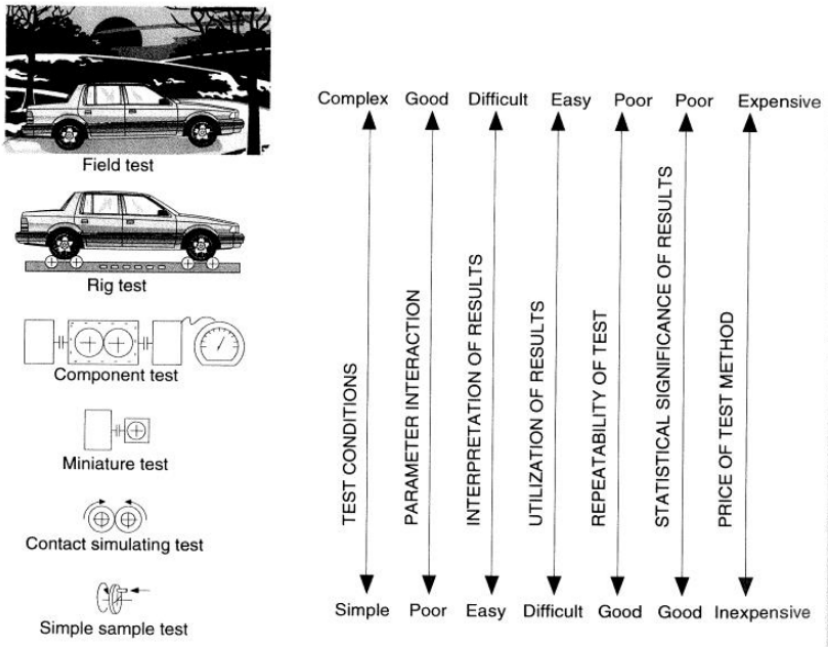

Figure 115: Classification of the tribological tests according to DIN 50322 (now retired). From [127]

It should also be noted that most of the experimental results on graphene-enriched grease available in the scientific literature (and revised in Section 4.2) are obtained through simplified laboratory testing, e.g., four-ball, pin-on-disc, SRV, disc-on-disc or others. These studies focused mainly on tribological issues

[5] The DIN 50322 standard proposes a classification of tribological tests where going from 'model tests' to 'field tests' the representativeness of the tests grows as they include many more variables, even if the generality of the result is reduced

related to sliding or rolling-sliding wear, i.e., adhesion and abrasion-related problems. Very little data have been made available in the scientific literature on the effect of graphene additives on the service life of components through component testing or field testing, for instance, the paper by Pape and Poll [100].

For a more reliable assessment of the benefits of graphene as an additive for grease, the lubricant must be tested in close-to-actual operational conditions of real applications, e.g. by component test. It is expedient to assess the performance of lubricants by exploiting a suitable component. Optimizing the lubricant performance for each application is possible only if the lubricants can be tested under conditions matching practical use. Rolling element bearings are a class of mechanical components particularly suited for testing grease performance. Many standardized lubricant testing methods, some of which are revised in Section 6.1, are based on rolling bearing test rigs. It is known from the extensive literature on the topic that roller bearings are susceptible to the lubrication regime (Lugt, Van den Kommer, Lindgren, & Roth) and the quality of the lubricant additive package. Grease "ages" in grease-lubricated bearings, and the service life of the component is very often determined by the life of the grease itself, making the grease and bearing duration closely interlinked.

For this research, a dedicated test rig was designed to test the performance of graphene-enriched grease through middle-sized thrust ball bearings and correlate the duration and effectiveness of lubrication in close-to-actual working conditions with the quantity of GNPs. Details on the test bench are provided in Section 6.2. Thrust ball bearings were chosen among other rolling element bearings because:

- Lubricating the component is straightforward.
- Inspection of the raceways where contact fatigue and damage accumulate is simple. Thrust ball bearings have indeed the rings and the rolling elements fully decoupled, making it easy to inspect the contact surfaces under the optical microscope and with the profilometer.
- The component is axially loaded only, making the layout of the test rig more simple than radial bearing subject to mixed radial and axial load.
- The number of influence factors that may affect the lifetime of thrust ball bearings is lower than radial bearings.

6.1 Review of the rolling bearing grease testers

Rolling bearings may be subjected to high mechanical and dynamic loads and require reliable working. Pursuing economic optimization and performance increase requires rolling bearing to withstand higher and higher loads while preserving reliability. In this scenario, the lubricant has a key role, and its functional behaviour can only be assessed by testing the component itself.

Several rolling bearing test devices are specifically conceived to investigate and model individual functions of the lubricant, such as its anti-wear capacity, vibration reduction capacity, protection from environmental agents, and others. This kind of component testing always aims to select test conditions such that the test duration is the shortest possible, but the lubricant must not be subjected to excessive load, which would falsify the test results. Some methods have been standardized according to the DIN standard organization [117]. What follows is a short review of the design of the rolling bearing grease testers primarily used in the industry as standard testing methods to assess the quality and performance of lubricants.

6.1.1 FE 8 Rolling bearing grease tester

The FE8 test rig is primarily used to determine the anti-wear behaviour of lubricating oils and greases by testing either point or line contact rolling element bearings. The test rig is standardized as per the DIN 51819 standard. Two sibling bearings (① in Figure 116) are loaded with a single axial load and tested simultaneously. The load is adjusted through a set of disk springs which provide compliance to the system to compensate for the temperature increase. The two testing bearings could be angular contact ball bearings, tapered roller bearings or thrust cylindrical roller bearings, and they should be the same type to distribute the load equally.

When thrust bearings have to be tested, a couple of additional support bearings (cylindrical or spherical roller bearings) might be added to the mechanical layout of the test rig. This option makes the two thrust bearing exploited for the test insensitive to the radial load from the own weight of the components, as shown in Figure 117b.

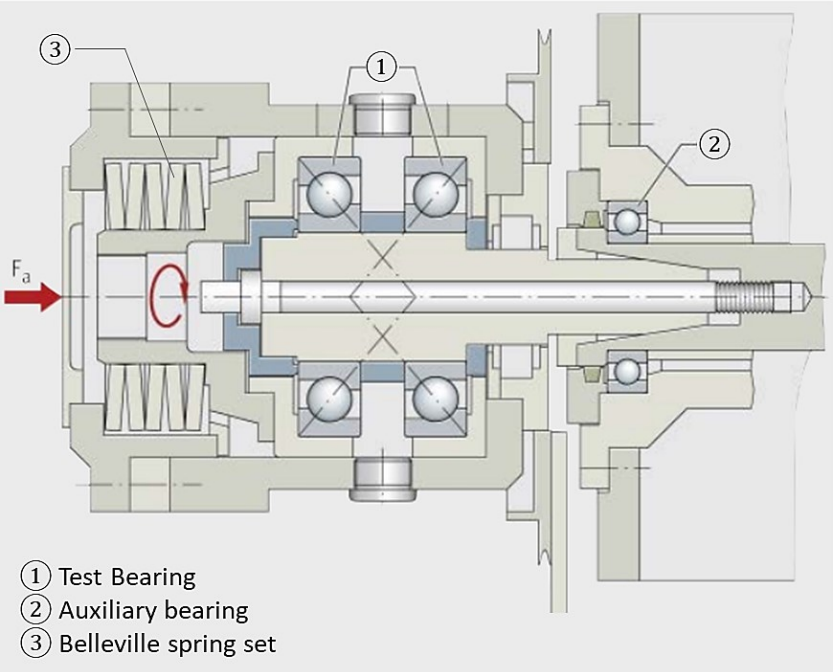

Figure 116: Schematic of the FE8 test rig as per DIN 51819 [117].

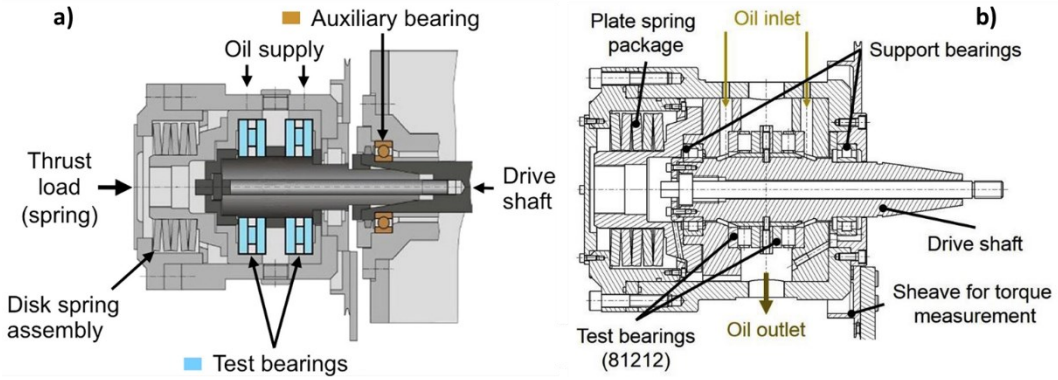

Figure 117: FE8 test rig equipped with two thrust test bearings, (a) without auxiliary support bearing [128]; (b) with auxiliary support bearing to bear radial loads. From [129].

Table 36 resumes the main testing parameters according to the standard guidelines. Axial loads from 5 kN to 100 kN and speeds from 7 rpm to 4500 rpm can be applied depending on the requirements of the application. DIN 51819 prescribes a series of duty cycles with appropriate load/speed combinations to reproduce a wide range of lubrication regimes with different bearing geometry. Many lubrication regimes can be replicated, from extremely mixed lubrication through moderate mixed lubrication to a full-film lubrication regime. If axial

cylindrical roller bearings are installed into the test rig, severe mixed lubrication and sliding can also be generated under high loads.

The friction torque curve and the temperature curve in the bearing can be monitored during the test run and correlated to the ageing of the lubricant. The amount of wear on the rolling bearing is determined by weighing the test bearings after proper cleaning. A single test may last 50 h to 1500 h depending on the type of lubricant, the type of bearing under test and the testing parameters.

Table 36: Testing conditions for FE8 rolling bearing lubricant test rig

Test bearing	Test conditions (DIN 51819)
• 2 Angular contact ball bearings • 2 Tapered roller bearings • 2 Cylinder roller thrust bearings • 2 Spherical roller bearings	*Duration of test* • 500 to 1500 h for greases • 80 h for oils *Speed* • 7 to 4500 rpm *Axial load* • 5 to 100 kN *Temperature* • ambient temperature to 150 °C

6.1.2 FE 9 Rolling bearing grease tester

The test rig FE9 is the evolution of the FE8 test rig presented in Section 6.1.1. It is exploited to determine the service life and the upper service temperature of lubricating greases in rolling bearings subject to medium speeds and axial loads. In the case of this testing method, however, only one high-precision angular contact ball bearing serves as a test bearing. The sibling bearing at the opposite side of the test rig (*n.4* in Figure 118) is necessary to withstand the axial load. The auxiliary bearing is usually oil lubricated with a dedicated oil recirculation system. The test bearing is filled with a defined quantity of grease and loaded by an axial force through a set of disk springs. Speed and temperature are set depending on the thickener and base oil of the grease. Usually, the test temperature is higher than the ambient temperature (100 °C up to 250 °C) and is adjusted through a resistance heating unit surrounding the seat of the test bearing.

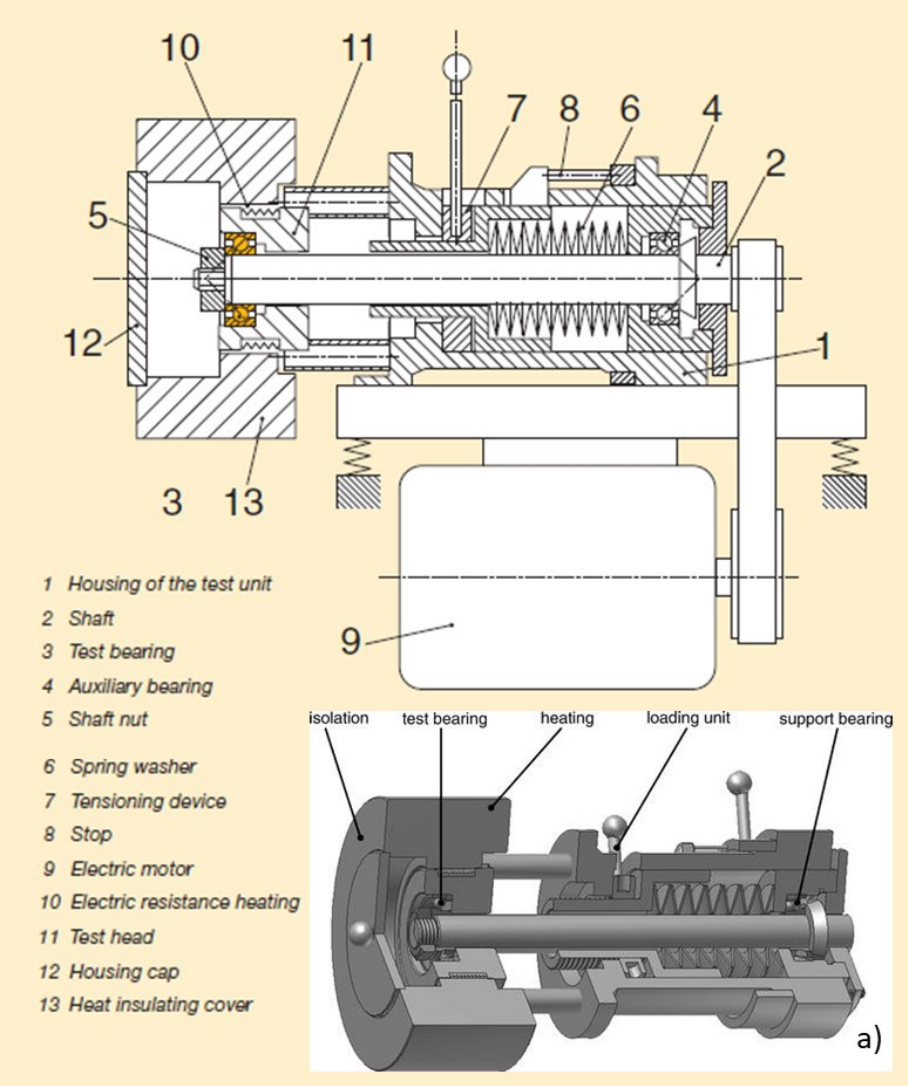

Figure 118: Schematic of the FE9 test rig as per DIN 51821 [130]. Inset (a) is the 3D view of the test rig from [131]. Five independent test heads are installed in the same test rig and driven by the same motor to run multiple tests simultaneously. Adapted from [130].

Three FE9 test setups are commonly used in industry; they are presented in Figure 119. Each testing assembly requires a different amount of grease into the test bearing, as per Table 37, which resumes the main testing parameters.

- *Assembly A*. It allows testing on open bearings. The test bearing is installed without a washer on either side, and the grease can freely emerge from the bearing. This setup is the most frequently used.

- *Assembly B*. The bearing is shielded on both sides with external washers that allow a gap facing the rotating shaft.
- *Assembly C*. Same as B, plus a grease reservoir on one washer. Instead of a front shield, an angular ring is positioned between the test bearing and the housing space. This ring can incorporate some further lubricating grease that generates a depot effect.

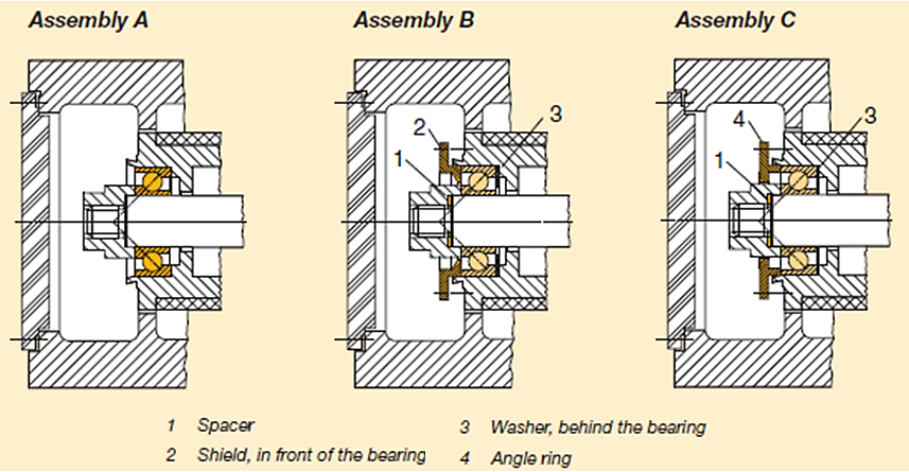

Figure 119: Assembly A, B and C of the FE9 test rig. Assembly A comply with the standardized testing procedure of DIN 51821-2. Adapted from [130].

DIN 51821-2 recognizes FE9 as a standard test method for lubricants and rolling element bearings, but only a specific testing procedure based on Assembly A is standardized. For the standard procedure, the test is carried out on the open bearing with an axial load equal to 1.5 kN at a speed of 6000rpm. The increase in friction determines the failure of the lubricant (or the bearing). The test is continued until the bearings require at least the double steady-state frictional moment for operation due to insufficient lubricity of the grease. The DIN 51825 standard specifies that the minimum running time to determine the grease service life with 50% probability (i.e. L_{50h}) must be at least 100 hours; otherwise, the test is considered invalid. If this duration is achieved, the test temperature can be stated as the upper operating temperature limit for the grease [117].

Table 37: Testing conditions for FE9 rolling bearing lubricant test rig

Bearing under test	Test conditions
• n.1 angular contact ball bearings (for each test head)	*Duration of test* • At least 100h (DIN 51825) *Speed* • 3000 rpm or 6000 rpm • DIN 51821: 6000 rpm *Load* • 1.5 kN, 3 kN or 4.5 kN • DIN 51821: 1.5 kN *Temperature* • 100 to 240°C • DIN 51821: 120-200°C *Grease quantity* • 2 cm^3 (Assembly A, B), • 10 cm^3 (Assembly C)

Figure 120 shows the Weibull diagram obtained at the end of a testing campaign based on a population of five grease bearings. In the example of Figure 120, the estimated L_{50h}, after which grease will likely fail, is equal to 200 h.

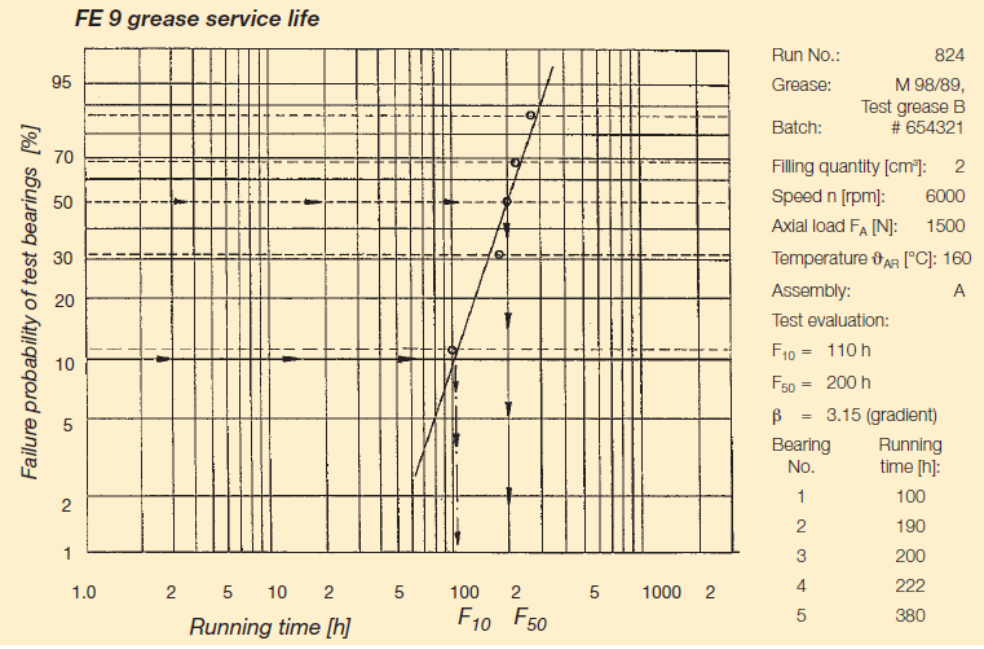

Figure 120: Example of a Weibull diagram obtained from a test campaign on 5 bearings with an FE9 test rig. From [130].

6.1.3 R0F/R0F+ Rolling bearing grease tester

R0F/R0F+ are simplified test rigs originally developed by SKF Industries to determine the service life and the upper service temperature of lubricating greases in rolling bearings at high speeds under mixed axial and radial loads. In the original version, the test rig could only test deep-grove ball bearings under fixed radial and axial loading. R0F+ test rigs came from a re-design of the R0F rig motivated by the need for greater flexibility in the load conditions and to make it possible to test roller bearings lubricated by their specific greases.

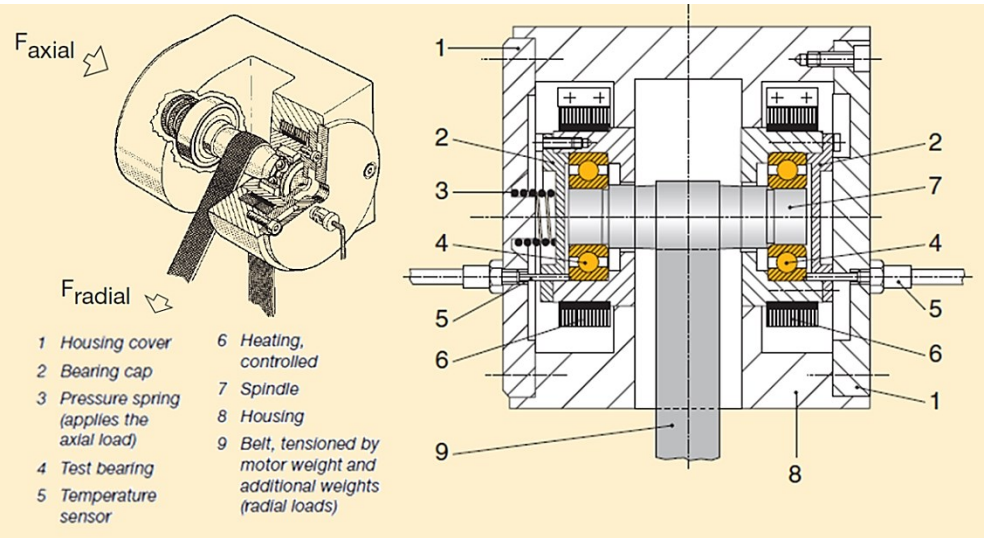

Figure 121: R0F rolling bearing grease tester schematic, from [130]. R0F stands for **R**ig with size **0** (i.e. small size) for **F**ett, a Swedish word for "Grease". Adapted from [130].

Lubricant testing is carried out at a constant speed from 5 000 rpm to 25 000 rpm. In the R0F+ version of this test rig, the axial load varies from 100 N to 1100 N per bearing, and the radial load is adjusted from 50 N to 900 N per bearing. A spring system with setscrews adjusts the axial load of the test. The radial load on the test bearings is applied through the belt drive and is controlled by controlling the tensioning of the belt itself (Figure 121). In the original R0F version, the radial and axial loads were adjusted at the beginning of the test and kept constant during the whole test run. With R0F+ test rigs, the axial load to the radial load ratio is adjusted pneumatically during the whole test duration to perform a series of test cycles out of a maximum of 20 test cycles per test. Lubricant test can be performed in conditions of self-induced heating or with active heating of the test bearing or at temperatures up to 230 °C through a resistance heating unit

surrounding the seat of the test bearings. The temperature of the static outer ring of each bearing is controlled by temperature sensors installed in the bearing seat [11]. Table 38 lists the typical test parameters of R0F+ tests.

Table 38: Testing conditions for R0F+ rolling bearing lubricant test rig

Bearing under test	Test conditions
• n.2 Deep Groove Ball Bearings • n.2 Angular Contact Ball Bearings • n.2 Tapered Roller Bearings • n.2 Spherical Roller Bearings	*Test time* • At least 500 h *Speed* • 10000 rpm to 30000 rpm *Axial Load per bearing* • 100 N (SKF-ERC standard) • 100 N to 1100 N *Radial Load per bearing* • 50 N (SKF-ERC standard) • 100 N to 900 N per bearing *Temperature* • Room temperature up to 230°C *Grease quantity* • 1.5 cm^3

The stop condition of the lubricant test is determined based on the temperature signal. Figure 121 shows a single test unit. Usually, R0F or R0F+ test rigs feature multiple test units to test many bearings at a time, as Figure 122 shows. Since bearings are tested in pairs in the R0F rig, the stop condition usually involves just one of the two bearings inside the test unit. However, as soon as one of the two bearings fails, the unit is stopped, and both bearings are considered failed. This test strategy, called Sudden Death Testing, is exploited to reduce the test time and increase safety. A minimum of five failures are usually collected to calculate the mean or median values and 90 % confidence intervals for the Weibull parameters and translated into median/mean values and confidence intervals for the life percentiles [11].

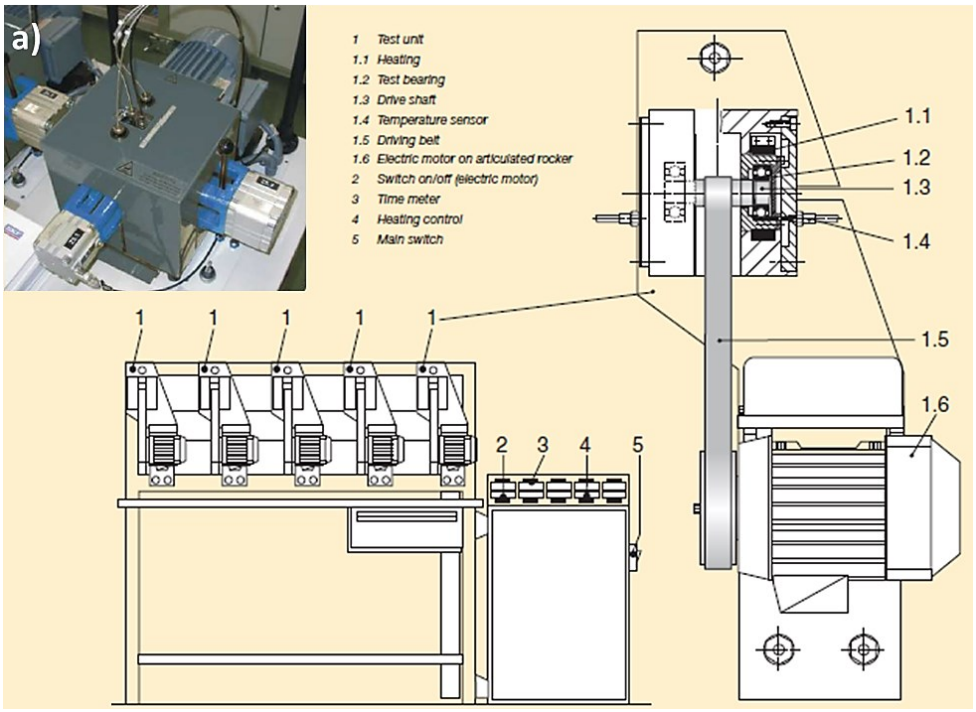

Figure 122: R0F industrial test rig with multiple test units. Adapted from [130]. Inset (a): modern SKF R0F+ test unit from [11].

6.1.4 LFT Rolling bearing grease tester

The LFT test rig from FAG is used to assess the anti-wear protection of oils and greases and to monitor the lubricant film formation. The schematic is presented in Figure 123. The test rig consists of an AC motor that rotates a vertical shaft supported by two auxiliary deep-groove ball bearing. The vertical shaft retains at the lower end the upper rotating ring of a thrust ball bearing or an axial cylindrical roller bearing. The static ring of the test bearing is fixed into a lubricant retaining cup, and the rolling element is partially immersed in the oil bath. Tests are carried out at speeds between 10 and 4000 rpm and under an axial load of 0.5 kN to 100 kN. The load is applied on the test bearing using either actuators or a dead-weight system attached to a lever arm system. Table 39 is the overview of the typical testing condition.

Some accelerometers are attached to the static ring of the test bearing to detect critical bearing faults such as spalling, and the bearing is considered failed when the vibration level exceeds a threshold level. The electrical contact resistance

between the static and rotating race of the bearing may also be measured to monitor the lubricant film thickness evolution during the test.

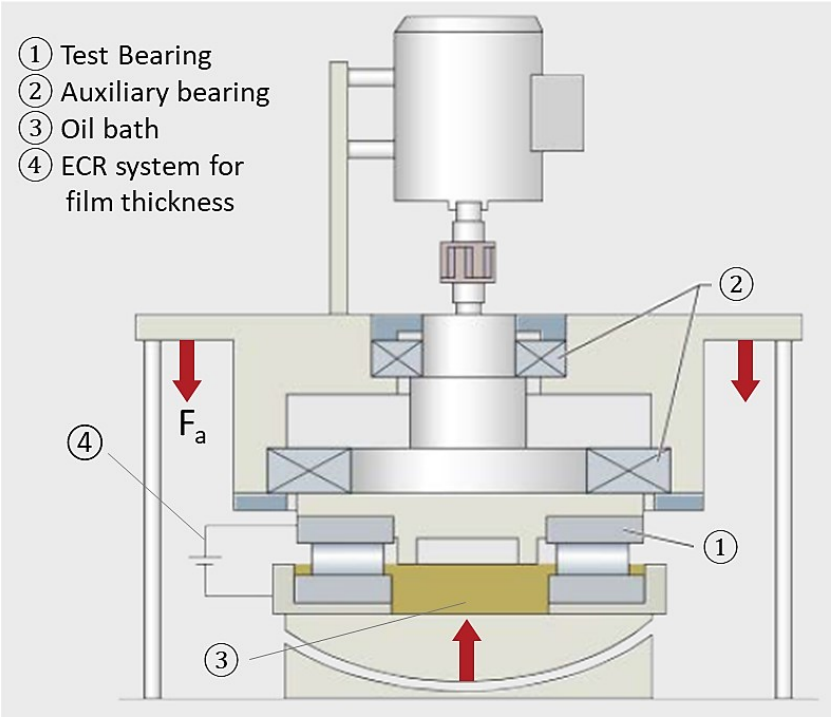

Figure 123: Schematic of the FAG-LFT rolling bearing test rig. Adapted from [117].

Table 39: Testing conditions for FAG-LFT rolling bearing lubricant test rig

Bearing under test	**Test conditions**
• n.1 Thrust ball bearings • n.1 Cylindrical roller thrust bearings	*Test time* • At least 500 h *Speed* • 10 rpm to 4000 rpm *Axial Load per bearing* • *800 N* *Temperature* • Room temperature *Grease quantity* • 1.5 cm^3

6.1.5 SNR-FEB2 Rolling bearing grease tester

SNR Roulements originally developed the SNR-FEB2 grease tester to study the anti-wear behaviour of lubricating greases in thrust rolling bearings subject to minor oscillating rolling and sliding movements and high load.

Two thrust bearings are loaded through a spring system with calibrated stiffness operated by a setscrew (Figure 124). Axial load ranges from 100N to 9 kN. The inner race of the test bearings is connected to a tilting arm driven by an AC electric motor. A crankshaft system generates a low-amplitude rotational oscillation to induce rolling-sliding fretting damage on the raceways. This test is often addressed as the "False Brinell Test" because the wear scar observed on the raceway at the end of the test is similar to the result of the Brinell hardness test. Figure 125 provides an example of laboratory equipment to perform SNR-FEB2 tests.

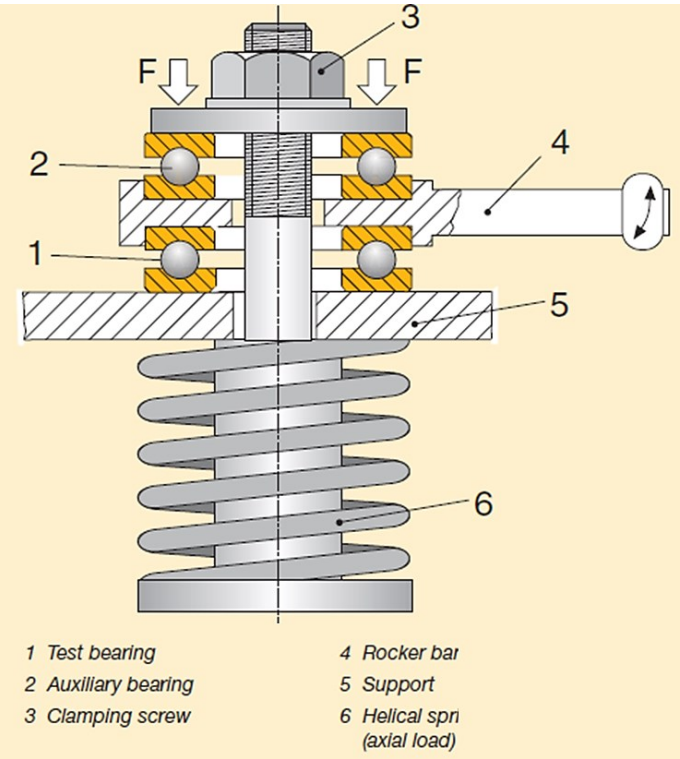

Figure 124: Schematic of the SNR-FEB2 rolling bearing fretting test rig. From [130].

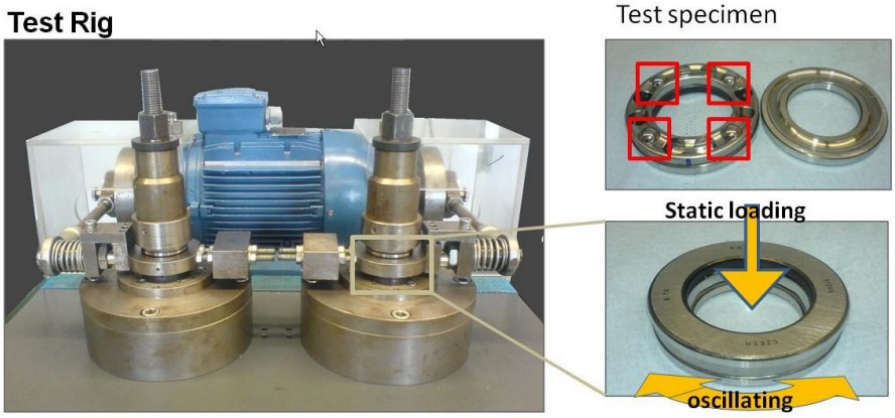

Figure 125: Example of laboratory equipment of the FEB2 type. From [132].

The user determines the test duration a priori, but it usually does not exceed 50 h. At the end of the test, the bearing rings are weighted with a high-precision scale to measure the material loss, and the groove depth is measured by profilometric inspection. Table 40 resumes the main testing conditions of the SNR-FEB2 test.

Table 40: Testing conditions for SNR-FEB2 rolling bearing fretting test rig

Bearing under test	Test conditions
• n.2 thrust ball bearings • n.2 cylindrical roller thrust bearings	*Test time* • 5 h to 50 h *Speed* • 5 Hz to 24 Hz oscillatory • 24 Hz standard • ±0.1 to ±3° amplitude • ±3° standard *Axial Load per bearing* • 100 N to 9000 N • 8000 N standard *Temperature* • Room temperature *Grease quantity* • 1.5 cm^3

6.2 Design of a test rig for grease life tests

Part of the research work of this PhD thesis has been devoted to designing and implementing a customized test rig to test the performance of greases through the testing of bearings. Sections 6.2.1 and 6.2.2 provide insight into the mechanical layout of the rig, optimized for the specific research purpose, and the implementation of the customized data acquisition and control system.

The development of the whole test rig took about 1 year before the prototype could be operated. The mechanical layout described in Section 6.2.1 represents the final version of the test rig used to run the grease life tests presented in Section 6.3.3. This final version of the test rig received adjustments in the mechanical layout to fix some drawbacks of the first prototype identified during the preliminary testing phase.

The main requirements defined in the conceptualization stage are listed as follows.

1. The test rig should allow the testing of a small-sized thrust ball bearing. Testing on overly large bearings is avoided to minimize costs, reduce complexity in design and simplify the in-house assembly on the test rig itself.
2. The applied load must be high enough to accelerate the accumulation of damage on the bearing and reduce the duration of the tests, i.e. the bearing must be tested above its fatigue load limit P_u.
3. The driving motor and the support bearings should be able of medium-to-high speed regimes, i.e. at least 1500-2000rpm, representative of typical industrial applications such as small grease-lubricated gearboxes. However, the overly high rotational speed is usually not of interest for grease-lubricated bearings under high loads due to excessive viscous heating and thermal instability above the thermal reference speed of bearings.
4. The temperature of the bearing under test must be measured during the tests, and ECR should monitor the lubrication regime.
5. Vibration and noise levels from running the endurance tests should be minimized.
6. The bearing under test should be visible to monitor the grease redistribution by sight and to make non-contact temperature measurements

by IR camera possible on the static ring, rotating ring and grease reservoir directly.
7. The test rig should feature a flexible mechanical layout for simple adaptation to testing of other types of bearings, e.g. small-sized radial ball bearings to be loaded with combined axial and radial loads.
8. The support bearings and the other auxiliary bearings of the test rig should be large enough to carry the test loads without any significant damage during the whole testing campaign, even considering off-design scenarios.
9. The test rig, the acquisition software and the control system should allow long-term unsupervised 24/7 accelerated tests.

6.2.1 Mechanical layout

The mechanical layout of the test rig specifically designed for this research activity was inspired by the industrial rolling bearing grease testers presented in Section 7.1 and some dedicated bearing test rigs for research purposes found in the scientific literature. Among the others, it is worth citing similar test rigs implemented by Alegranzi et al. [133], Niknam et al. [134], He et al. [135], Cao et al. [136], Fan et al. [137] and the one recently appeared in the paper by Nassef et al. [138].

Figure 126 shows the section view of the test rig, while Figure 127 presents the CAD model in full axonometric view. The main shaft (① in Figure 126) is supported by two bearing units DODGE P2B-GTMAH-50M. The main technical specs of the support bearings are listed in Table 41. Pillow block bearing units were selected to reduce the manufacturing cost of the test rig dramatically. The selected bearing units are manufactured according to the requirements of air-handling applications, i.e. they feature reduced vibration and noise level, improved shaft guidance for high-speed running and can operate cooler for longer grease life. Contact seals limit the maximum speed of these bearing units to 4300 rpm, but the same bearing units featuring labyrinth seals guarantee smooth running up to 6700 rpm. However, the target rotational speed for these tests is much lower than the limiting speed of these bearing units. The location of the shaft into the bearing was assured by a pull/push adapter system (Dodge grip-tight®) that enables fully concentric positioning of the shaft. It is optimized for higher rotational speed to reduce vibrations due to misalignments.

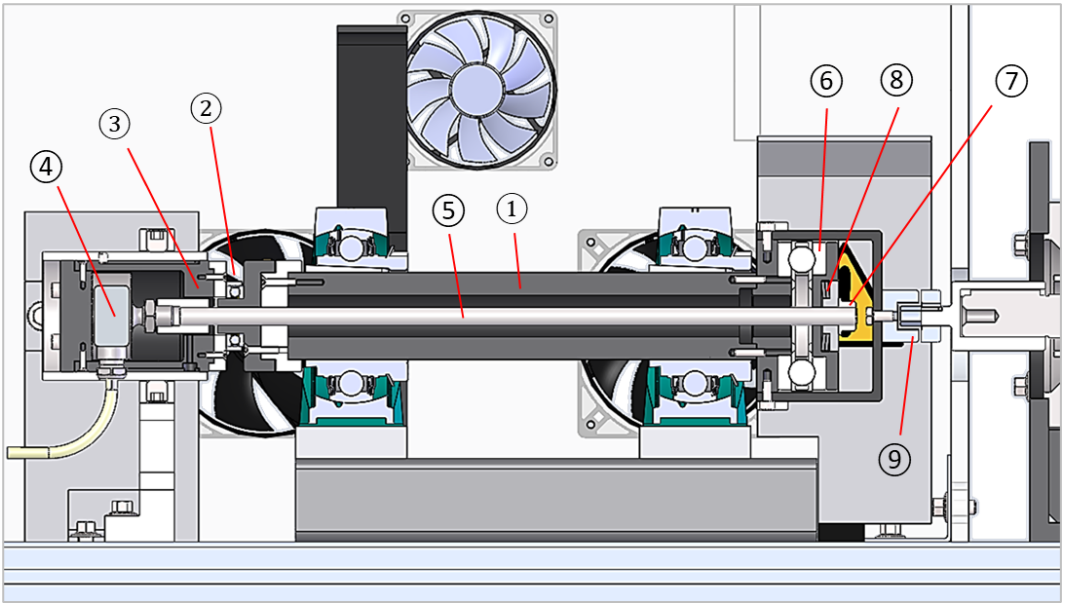

Figure 126: Section view of the test rig.

Table 41: Technical specs of the P2B-GTMAH-50M support bearings from DODGE Industrial Inc.

Performance data	Value
Bore diameter	50 mm
Basic dynamic load rating, C	43.4 kN
Basic static load rating, C_0	29.3 kN
Limiting speed	4300 rpm

At the left end of the hollow shaft, the thrust ball bearing under test ② (Figure 126) is installed coaxially to the shaft. The bearing under test is hereafter referred to as the device under test (DUT). The test rig was designed to allow testing on thrust bearings with a minimum bore equal to 20mm. The bell-shaped component ③ in contact with the fixed ring of the tested bearing applies the axial load of the test and is connected to a 10kN load cell (HBM U2B) ④. The threaded tie rod ⑤ coaxial with the main shaft connects the load cell with the static ring of a 51309 thrust ball bearing ⑥ installed on the right end of the shaft (whose specs are reported in Table 42). This auxiliary thrust bearing decouples the rotating parts of the test bench from the static loading system and allows for balancing the axial load without loading the two support bearings.

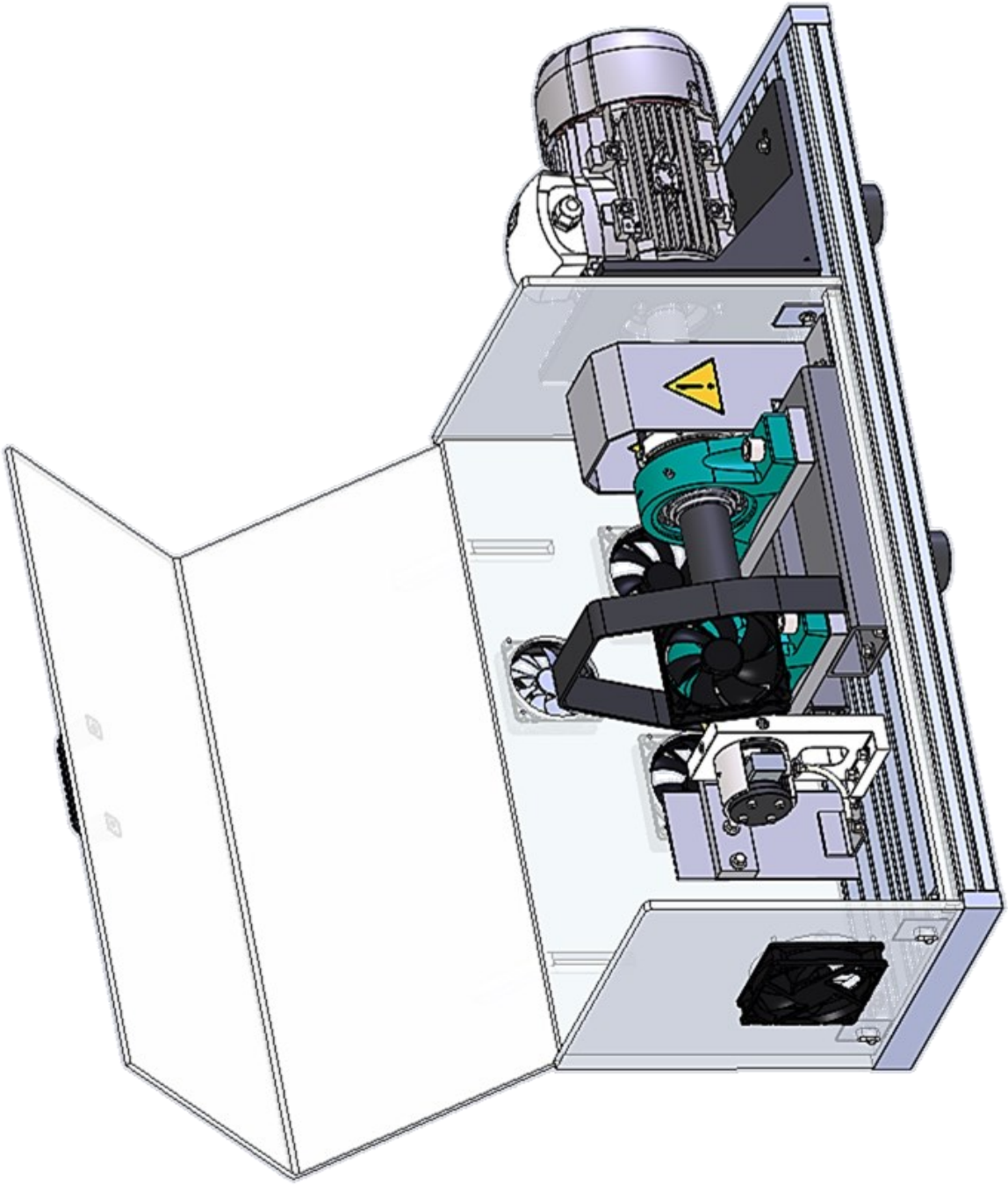

Figure 127: CAD model of the test rig for grease testing.

Figure 128: Pictures of the test rig for grease endurance tests at the Laboratory of Mechanics (DIMEAS, Politecnico di Torino).

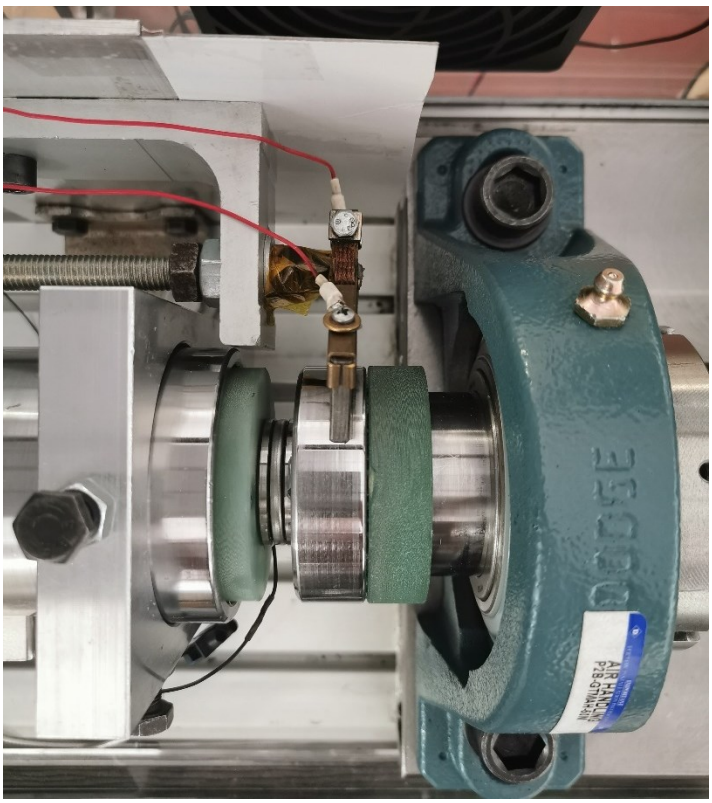

Figure 129: Detailed of the DUT installed on the test rig and connected to the ECR system.

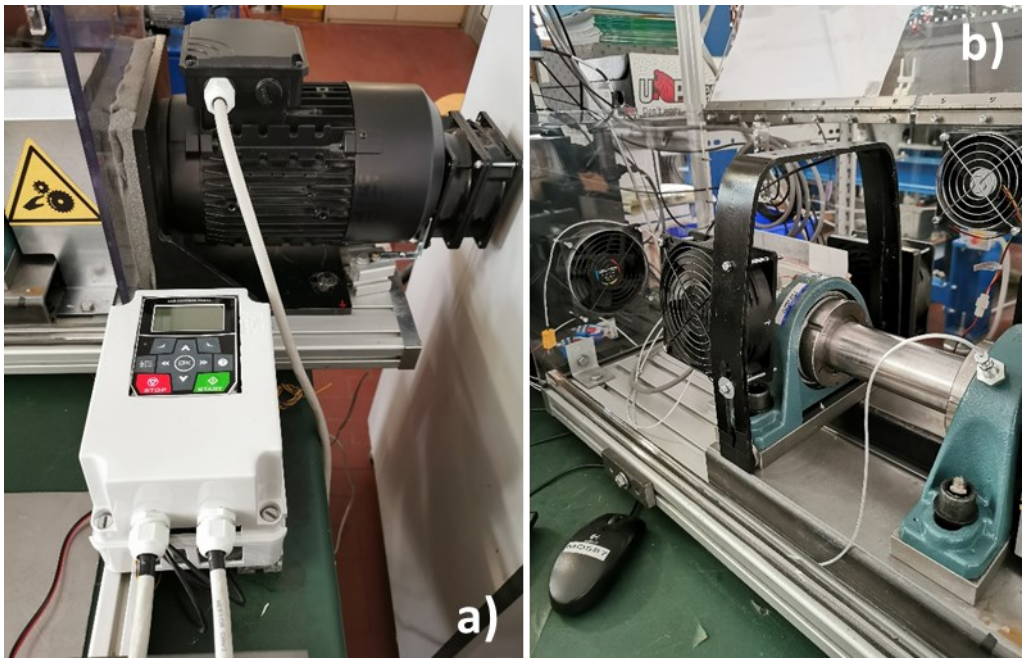

Figure 130: (a) Detail of the power system; (b) detail fo the air cooling system of the DUT.

Table 42: Technical specs and calculation parameters of the 51309 thrust ball bearings from SKF [139].

Performance data	Value
Bore diameter	45 mm
Basic dynamic load rating, C	76.1 kN
Basic static load rating, C_0	153 kN
Limiting speed	4000 rpm
Reference speed	2800 rpm
Fatigue load limit, P_u	5.6 kN

Fan et al. (Fan, Lee, Ouyang, & Yang, 2015) first proposed to apply an internally balanced axial load that exploited a dedicated four-rod loading frame surrounding the rotating part of their test rig. The solution adopted in the present test rig aims at simplifying this concept. The loading frame is replaced by the threaded tie rod coaxial to the main shaft, which guarantees compact dimensions and a significant reduction in the complexity of the layout. The load is not applied via an external actuator, but the user sets it via a lock nut ⑦ that forces the rolling elements and the thrust rings into close contact. Two Belleville springs⑧ (size 40x20.4x2mm, nominal load 5730N) are placed in a series arrangement behind the lock nut to add compliance to the loading line. The Belleville springs allow accurate setting of the initial thrust load and compensate for thermal expansion due to frictional heating during operation. Figure 131 compares the original solution by Fan et al. with the schematic representation of the simplified solution designed for this test rig. This simplified solution has some cons, in any case. Tight machining tolerances are required to guarantee the concentricity of components along the loading line; otherwise, undesired vibration would occur.

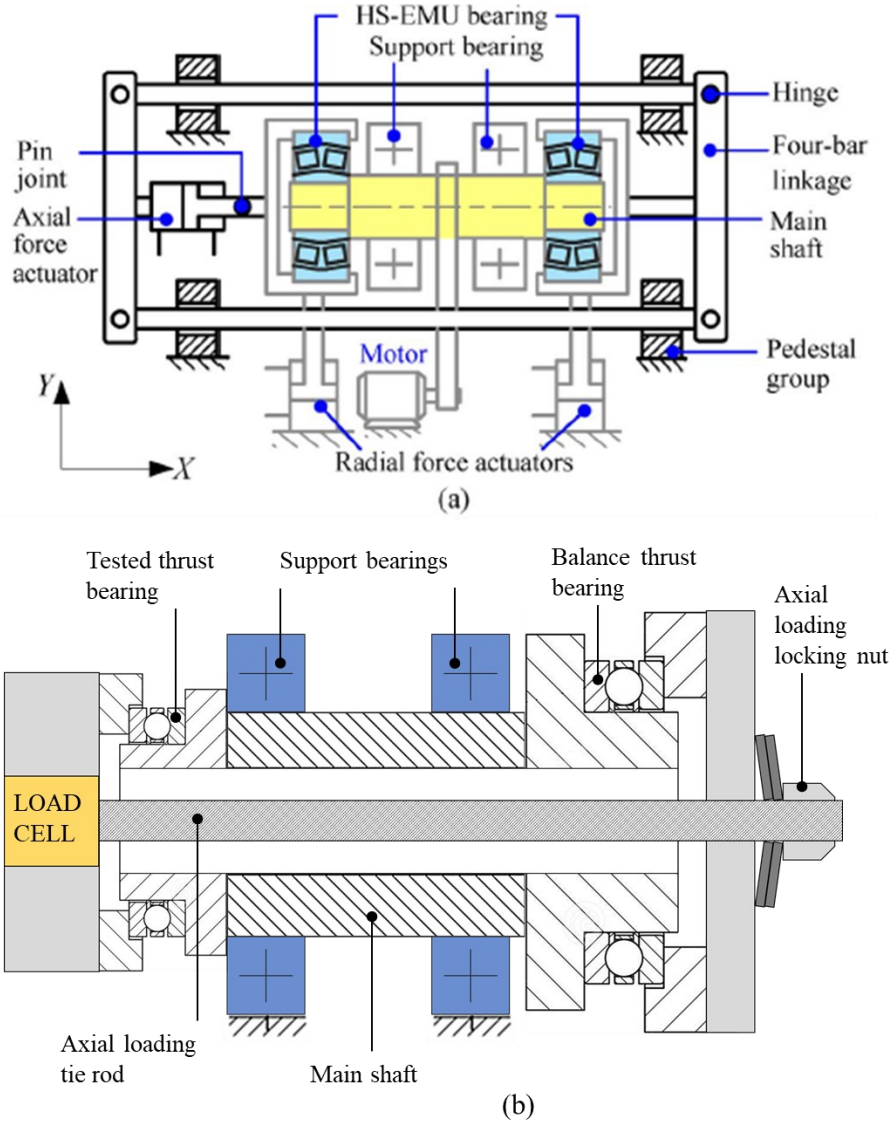

Figure 131: (a) Schematic of the test bearing for HS-EMU bearings by Fan et al. [137]; (b) schematic of the loading system of the test bearing designed for this PhD thesis research work.

The connection with the 3kW three-phase asynchronous electric drive Lafert AMPE 90L DA2 (whose specs are reported in Table 43) is provided by a flexible jaw coupling ⑨. The electric drive is operated with a 4kW inverter ES350-F0-2K2G/4K0P-3B from Cumark Co.Ltd that allows the continuous regulation of the motor speed from 25Hz up to 100Hz in open loop mode. Since the torque output of the drive is the result of the bearing friction only, the inherent rotor slip is supposed to be limited during operation. The actual rotational speed of the shaft

during tests bearing was then calculated according to equation (40), where 3000 rpm is the rotational speed of the magnetic field at a nominal excitation frequency of 50 Hz and 2865 rpm, the related idling speed of the rotor. The calculation is based on the simplifying assumption that the ratio between the nominal speed of the magnetic field and the rotor idling speed is constant at any excitation frequency.

$$\omega_{test} = f_{inverter} \cdot 60 \cdot \frac{2865}{3000} \, [rpm] \tag{40}$$

Table 43: Technical specs of the Lafert 3kW asynchronous electric drive installed into the test rig (https://www.lafert.com/it)

Tipo		kW	HP	min⁻¹	M_N Nm	IE3 η 50%	IE3 η 75%	IE3 η 100%	cos φ	I_N 400V	I_A/I_N	M_A/M_N	M_J/M_N	M_K/M_N	J 10^{-3} kgm²	kg
3000 min⁻¹ (2 poli) ALUMINUM CASE																
AMPE 90L DA	2*	3	4	2865	10.0	85.2	86.3	87.1	0.80	6.3	8.7	4.5	4.0	4.6	2.0	18.0

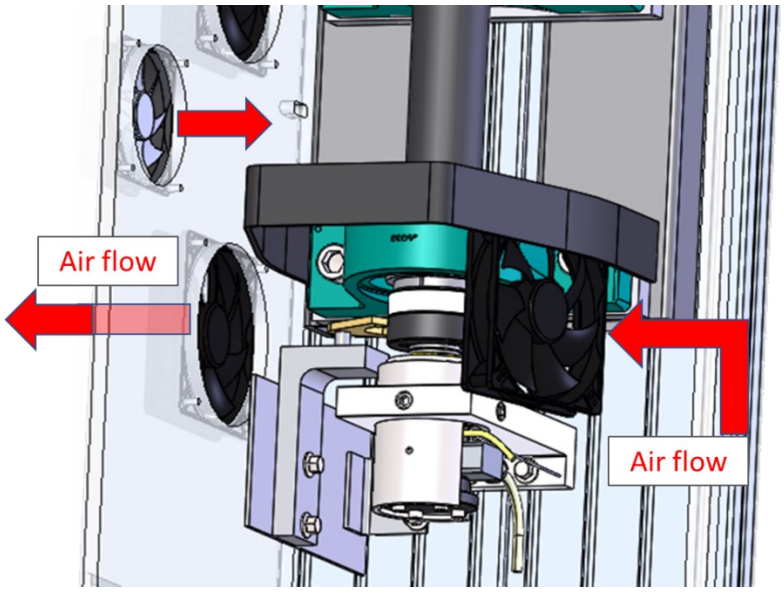

Figure 132: Schematic of the cooling system of the tested bearing to avoid overheating due to accelerated endurance test conditions.

A polycarbonate safety enclosure (visible in Figure 127) protects the rotating parts of the test bench and houses cooling fans. Preliminary testing showed that the tested bearing quickly ran into overheating at 1500 rpm inside the enclosure because the test speed was higher than the thermal reference speed of the bearing, and the applied load exceeded the rated fatigue limit. Therefore, an active air cooling system was designed with four 200 CFM cooling fans to control the temperature of the tested bearing. One cooling fan forces fresh air to enter the testing chamber from one side, two fans installed at the level of the pillow blocks take the hot air out of the test chamber, and one fan installed inside forces recirculation of fresh air around the bearing under test (Figure 132).

The support bearings of the bearing units work under no radial load except for the own weight of the components. They are insensitive to the axial load F_a by design, indeed. This feature makes the duration of these bearings theoretically unlimited. However, the concept behind the mechanical layout of the test rig was also allowing testing on radial bearings with minimum layout adaptations in the future. In the presence of external loading on a radial bearing under test, a couple of fixture reaction forces would rise on the support bearings. Therefore, the position of the support bearings was optimized to extend the bearing life, considering the presence of a virtual radial load F applied at one extremity of the shaft. In particular, the relative distance between the two support bearings SB1 and SB2 and the applied radial force, i.e. the l, l_1 and l_2 in Figure 133, was calculated to minimize the load on the most loaded bearing (bearing SB2).

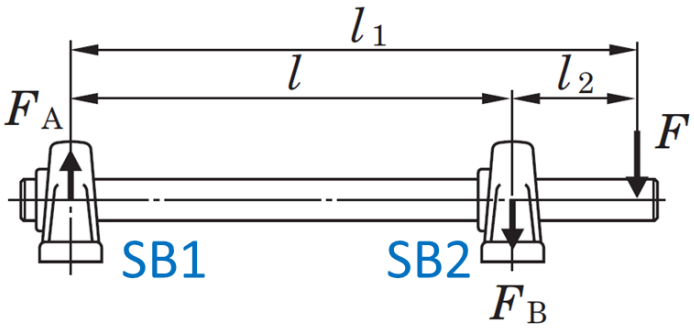

Figure 133: Schematic of the reaction forces on the support bearings SB1 and SB2 for the scenario where an external radial load acts on the bearing under test (adapted from KYH Mounted Bearing Units Catalogue, Nippon Pillow Block Co. Ltd., https://fyhbearings.com)

The testing parameters and the related estimated bearing rating life for the P2B-GTMAH-50M support bearings and the 51309 thrust ball bearing are presented In Table 44 and Table 45, respectively. The *Design scenario* in Table 44 refers to a testing condition where the speed is 1500rpm, as for the endurance tests presented in Section 6.3, and the tested bearing is a deep groove ball bearing with a 5 kN load applied radially. The estimated life of the support bearings in this testing condition is still virtually unlimited. The *Off-design scenarios* consider two hypothetical testing conditions where the support bearings operate under higher load and speed. The minimum estimated bearing life exceeds 200 days, which is satisfactory for a test bench.

Table 44: Equivalent bearing life calculations of P2B-GTMAH-50M bearings according to the SKF Bearing Calculations guidelines. A 0.5 kN thrust load was added to account for parasitic axial load due to the thermal expansion of the shaft (the support bearings are both locating by design).

Design scenario			Off-design scenario			Off-design scenario & high speed		
Axial force	0.5	kN	**Axial force**	0.5	kN	**Axial force**	0.5	kN
Radial force	5	kN	**Radial force**	9	kN	**Radial force**	9	kN
C/P	8.72	-	C/P	4.84	-	C/P	4.84	-
Speed	1500	rpm	Speed	1500	rpm	Speed	3000	rpm
Inner ring T	60	°C	Inner ring T	60	°C	Inner ring T	60	°C
Outer ring T	60	°C	Outer ring T	60	°C	Outer ring T	60	°C
SKF Grease	VT307		SKF Grease	VT307		SKF Grease	VT307	
etaC	0.85	-	etaC	0.85	-	etaC	0.85	-
Shaft	Horizontal		Shaft	Horizontal		Shaft	Horizontal	
aSKF	37.9	-	aSKF	9.6	-	aSKF	9.6	-
L10m SKF	$>2*10^5$	h	**L10m SKF**	12100	h	**L10m SKF**	6060	h
Estimated life	8000	days	**Estimated life**	504.2	days	**Estimated life**	252.5	days
Relubrication	13400	h	**Relubrication**	6470	h	**Relubrication**	3370	h
Power loss	99	W	Power loss	138	W	Power loss	290	W

The *Design scenario* in Table 45 refers to a testing condition where the DUT (either a thrust ball bearing or a hypothetical deep groove ball bearing) is loaded with the maximum allowable axial load of the load cell, i.e. 10 kN. The *Off-design scenarios* take into account operation at higher speed.

Table 45: Bearing life calculations for the thrust bearing SKF 51309 according to the SKF Bearing Calculations guidelines.

Design scenario			High speed-scenario		
Axial force	10	kN	**Axial force**	10	kN
Radial force	-	kN	**Radial force**	-	kN
C/P	7.61	-	C/P	7.6	-
Speed	1500	rpm	Speed	3000	rpm
Inner ring T	60	°C	Inner ring T	60	°C
Outer ring T	60	°C	Outer ring T	60	°C
SKF Grease	LGMT2		SKF Grease	LGMT2	
etaC	0.7	-	etaC	0.7	-
Shaft	Horizontal		Shaft	Horizontal	
aSKF	14.5	-	aSKF	16.3	-
L10m SKF	71000	h	**L10m SKF**	39200	h
Estimated life	2958	days	**Estimated life**	1633	days
Relubrication	7360	h	**Relubrication**	2460	h
Power loss	65	W	Power loss	147	W

6.2.2 Data Acquisition and control system

The control and the data acquisition system of the test rig presented in Section 6.2.1 were self-developed using a Nation Instrument LabView® application software specifically written for the purpose. The Front Panel of the LabView routine developed for this test rig is shown in Figure 134. The logical framework of the control and the data acquisition system is schematized in Figure 135.

The testing parameters being monitored while running the endurance tests are:

- the temperature of the static ring of the DUT
- the temperature of the static ring of the support bearing on the shaft
- the Electric Contact Resistance (ECR) through the bearing under test
- the applied axial load
- the axial vibration at the level of the seat of the tested bearing

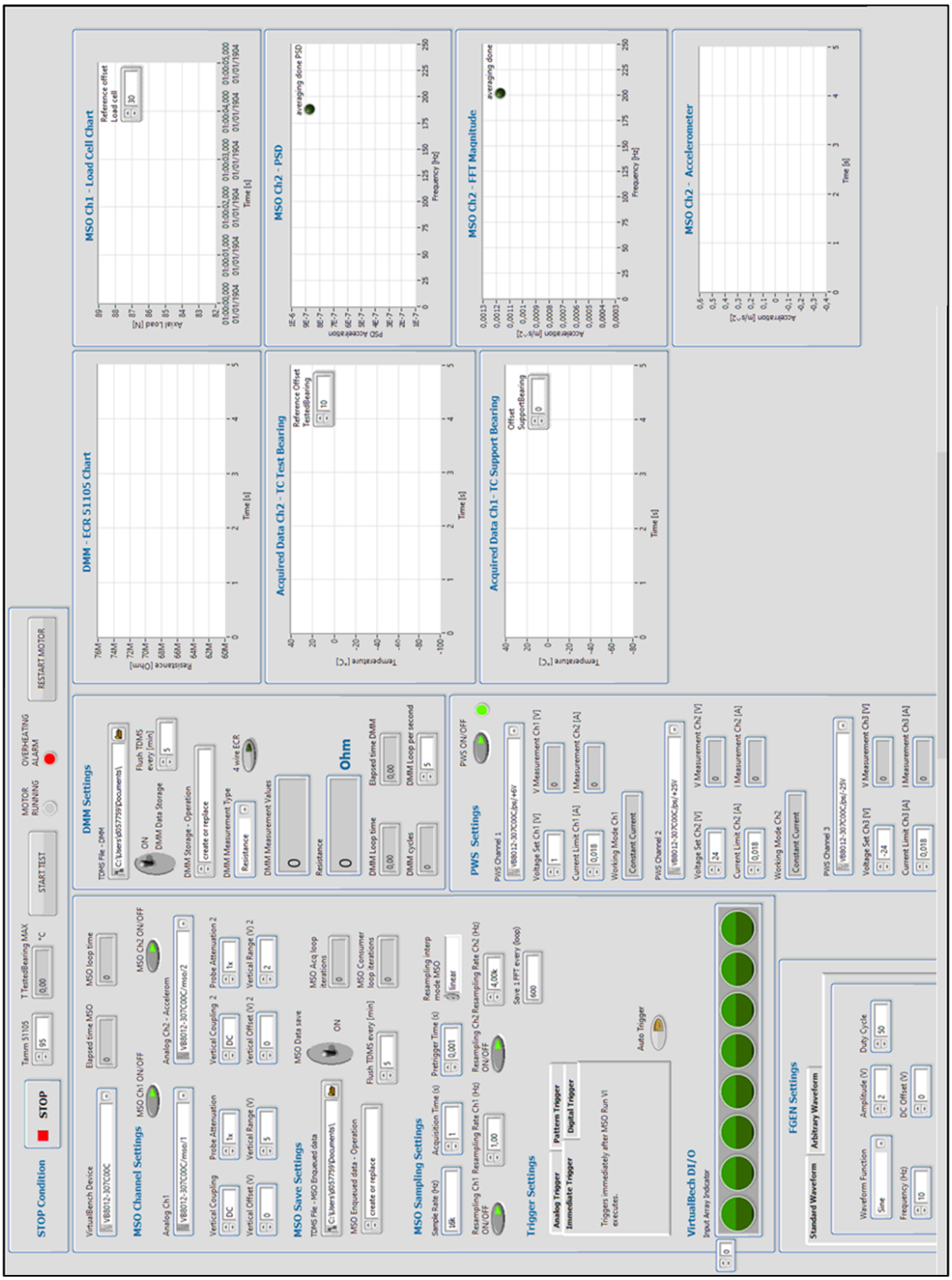

Figure 134: Front Panel of the LabView routine developed to run the tests.

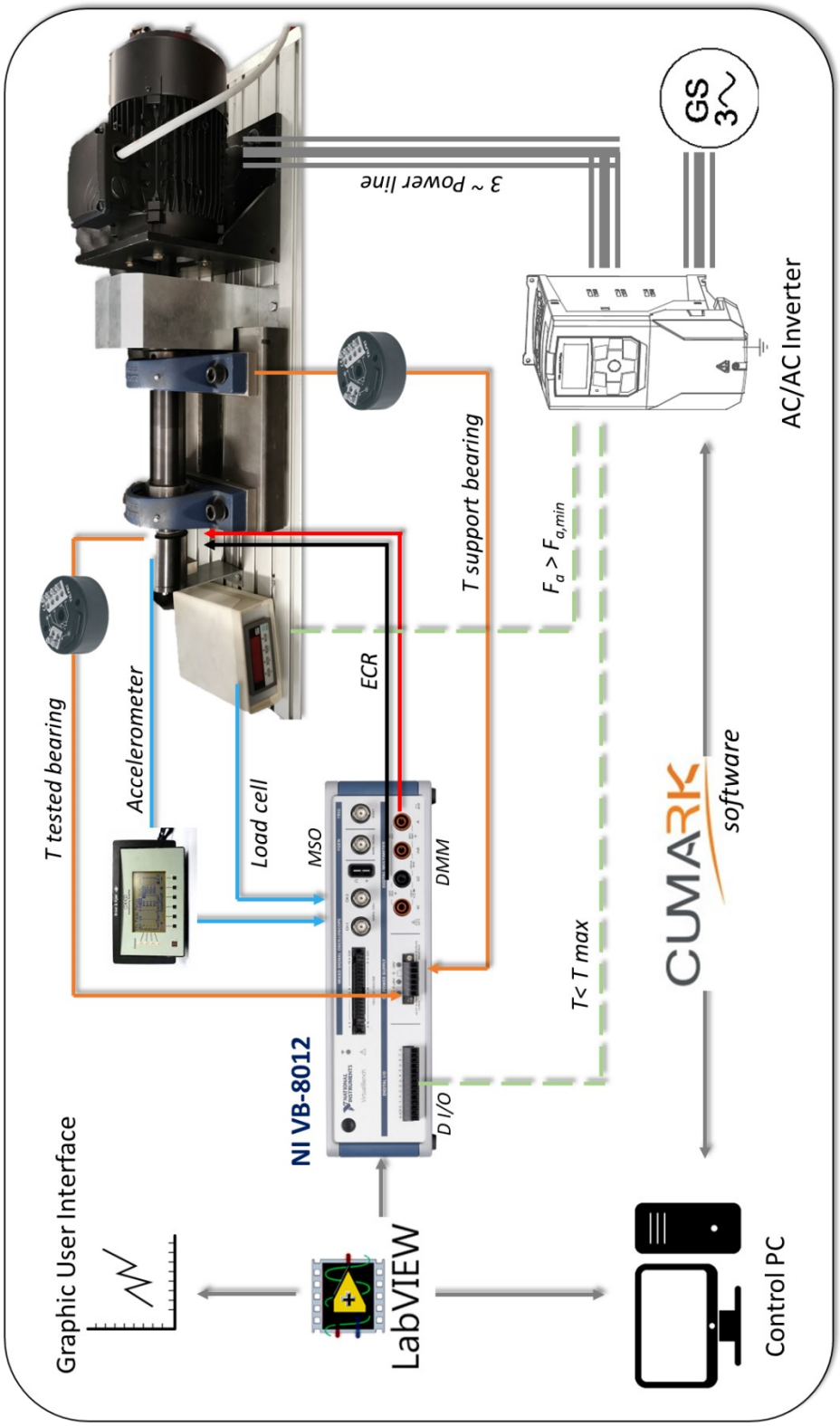

Figure 135: Control and data acquisition system of the test rig

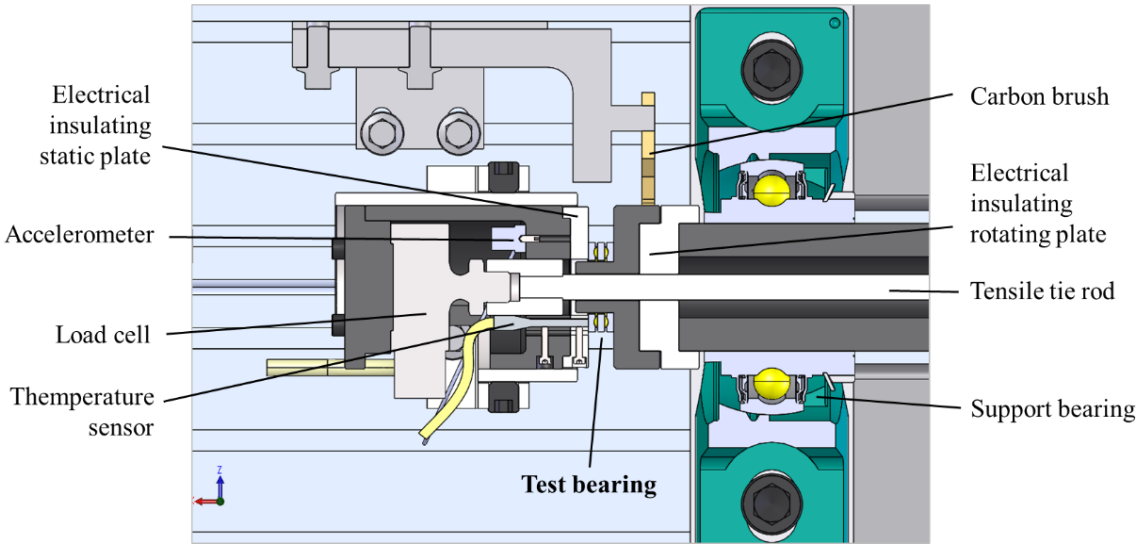

Figure 136: Section view of the test rig for grease testing.

Figure 136 is the detailed view of the seat of the bearing under test. The temperature of the bearing under test and the support bearing were sensed by a couple of small-sized Resistance Temperature Detector (RTD) of the Pt100 type. Tests were run not under controlled temperature conditions but under self-induced frictional heating, contrary to typical testing conditions of standardized bearing endurance tests. Figure 137 lists the main characteristics of the temperature sensor according to the manufacturer's datasheet. The tiny size of the sensor guarantees good responsiveness to limited temperature variations and a relatively fast response time. Figure 138 shows how the temperature sensor was installed at the level of the bearing seats into a blind hole and in direct contact with the static ring of the test bearing.

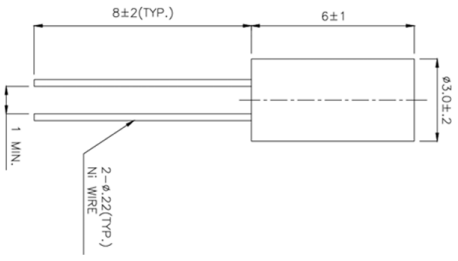

Resistance	100Ohm
Tolerance	kl.B 0.2%
Size	φ3x6mm
Temp factor	3850ppm/°C
Temp range	-50…500°C
Length cables	8mm

Figure 137: Technical sheet of the Pt100 RTD sensor installed into the test bench

This kind of temperature sensor was chosen due to the high stability of the measured values and the high immunity to EM disturbances. Each thermocouple

was conditioned by a 24V DC-powered temperature transducer, which converts the electrical resistance fluctuations in a 4-20 mA current signal from 0 °C to 300 °C. The current level associated with the temperature values was acquired with the amperemeter integrated into the high-performance DC power supply of the National Instruments VirtualBench VB-8012 device with a sampling rate equal to 5Hz. The resolution of the electrical current reading was ±30 µA which allows measuring the temperature level with a resolution of about ±0.5 °C. A digital safety stop condition based on temperature was coded inside the Labview-based control software to avoid undesired overheating of the bearing under test. The safety stop criterion activates a DO channel of the VirtualBench wired to a DI channel of the inverter, and it stops the test in case of overheating.

A uniaxial accelerometer was installed close to the temperature sensor to detect the axial vibration behind the bearing seat. Data from the accelerometer were acquired at 4kHz through a Bruel & Kjier Nexus 2693 amplifier and analyzed in real time during the test. The PSD of the acceleration signal in the time domain was calculated in the frequency range from 0 Hz to 2 kHz.

The average of 10 subsequent PSD charts was stored in memory every 10 minutes to track the evolution of the power spectrum during the test. Figure 139 shows the series of the average PSD signal in the frequency domain from the beginning to the end of one of the tests performed with pure grease presented in Section 6.3.3.

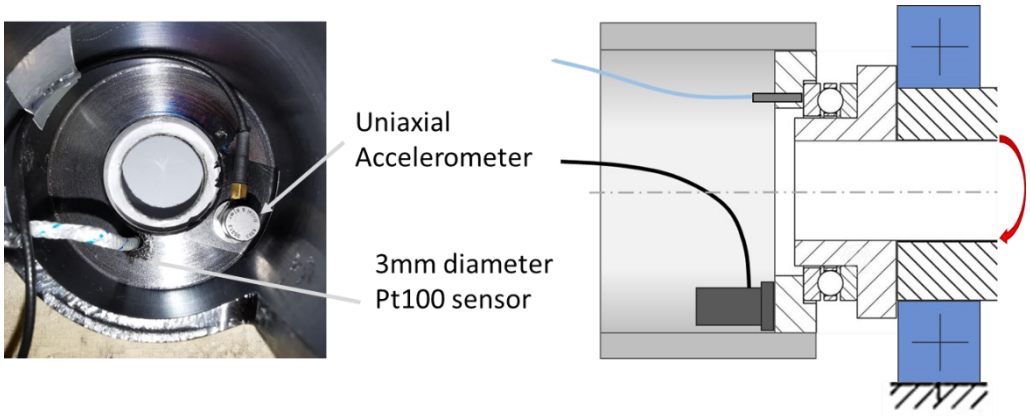

Figure 138: Sensorized seat of the bearing under tests featuring a temperature sensor and a uniaxial accelerometer.

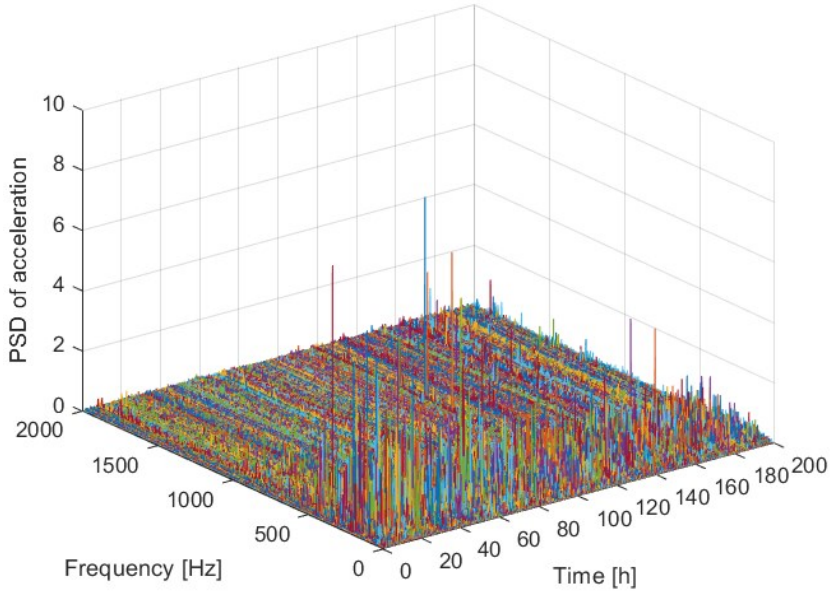

Figure 139: Series of the average PSD signal in the frequency domain recorded from the beginning to the end of Test 2.

The ECR system was intended to monitor the electric resistance through the lubricated rolling contacts between the spheres and the raceway. The 2-wire measurement of the electric resistance is performed through the Digital MultiMeter (DMM) integrated into the same NI VirtualBench VB-8012 device, whose measuring specs are reported in Table 46.

Table 46: Measuring range and accuracy of the Digital MultiMeter in DC Resistance mode installed into the National Instrument VirtualBench VB-8012 multifunction card.

DC Resistance Accuracy (2-Wire)*, 1 V Open Circuit Voltage

Range	Short-Circuit Current	1-Year Accuracy[13] ± (% of Reading + % of Range)	Temperature Coefficient[13] ± (% of Reading + % of Range)/°C
100 Ω	170 µA	0.018 + 0.050	0.0010 + 0.0005
1 kΩ	170 µA	0.018 + 0.005	0.0010 + 0.0005
10 kΩ	70 µA	0.018 + 0.005	0.0010 + 0.0005
100 kΩ	10 µA	0.018 + 0.005	0.0010 + 0.0005
1 MΩ	1.1 µA	0.035 + 0.005	0.0040 + 0.0005
10 MΩ	1.1 µA	0.150 + 0.005	0.0100 + 0.0005
100 MΩ	1.1 µA	1.3 + 0.005	0.1000 + 0.0005
* Perform offset nulling.			

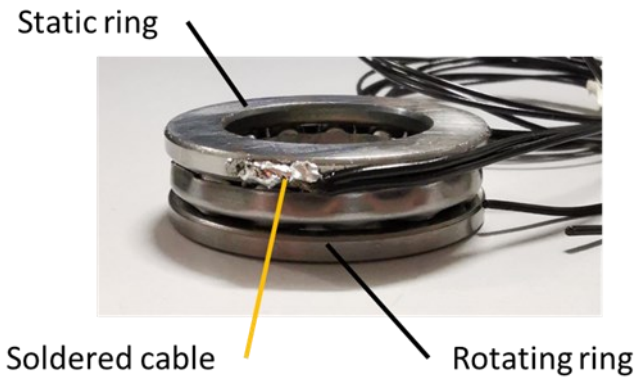

Figure 140: ECR wire tin soldered to the static ring of a 51104 bearing.

A couple of carbon brushes for electrical application slide against a mirror-finished steel surface next to the seat of the bearing under test. The carbon brush allows the closing of the measuring electrical circuit at the rotating side of the bearing. The rotating ring of the bearing is glued to its seat with a special electrically conductive glue rich in Ag powder to improve conduction at the bearing-seat interface. The static ring was connected to the DMM through a wire directly soldered to the side of the ring, visible in Figure 140. Soldering was necessary to avoid disturbances and interference in the electrical measurement due to vibrations and grease nearby.

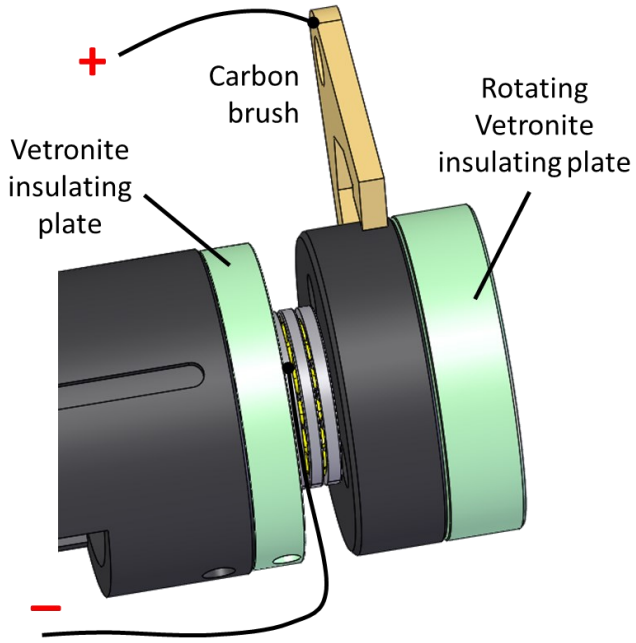

Figure 141: FR4 Vetronite insulting plates for ECR measurement.

Two insulating plates made of FR4 Vetronite are placed behind the static and rotating ring of the DUT, as shown in Figure 141. These plastic plates made of high-strength and high-thermal-stability engineering polymer insulate the region where the ECR measurement is performed from the rest of the test bench to avoid any electrical current dispersion.

The HBM U2B load cell is connected to a Druck DPI 280 transducer which linearizes the 0 – 10kN measuring load range into a 0-5V voltage signal. The oscilloscope acquires the voltage signal (MSO) integrated into the VirtualBench device and sampled at 1Hz. An additional safety emergency stop criterion was implemented by wiring a DO port of the Druck process transduced to one of the DI channels of the inverter. If the axial load lowers below a given threshold set by the user, the drive stop running to protect the test bench in the event of failure of the axial tie rod or load loss due to other misfunctioning.

6.3 Grease endurance tests

This section presents the experimental campaign with the test rig described in Section 6.2. Grease tests were carried out with thrust ball bearings of size 51105 and 51104. All the bearings being tested were purchased from the same manufacturer and belonged to the same production batch to minimize reproducibility issues of the results due to unavoidable manufacturing differences. Bearings are manufactured by SKF Industries AB, and the related manufacturing data are provided in Table 47.

Table 47: Manufacturing data related to the SKF bearings purchased for the experimental campaign.

Size	Manufacturer	Country of origin	Lot number	Quantity
51105	SKF Industries AB	CZ	013T	20 pcs
51104	SKF Industries AB	CZ	159U	20 pcs

SKF 51105 thrust ball bearings were initially selected for the whole experimental campaign with graphene greases. However, they were discarded after some preliminary tests because the test duration was too long, as discussed in

Section 6.3.2. Therefore, the remaining endurance tests were carried out with thrust bearings of size 51104. The main dimensional and mechanical specs of these bearings are reported in Table 48. All the tests were carried out at a fixed speed of 1500 rpm for this research.

The radial profiles of the raceways on the bearing rings were acquired before each test through a stylus profilometer (PGS200, SM Instruments, Volpiano), and the contact radius was calculated by fitting an osculating circle, as shown in Figure 142. Four profiles were taken at 90° from each other (Figure 142b), and the values were averaged to obtain one representative value of the contact radius to be used in the calculation of the Hertzian contact stress

Table 48: Dimensional and mechanical specifications of thrust ball bearings size 51104 and 51105.

Data	**51104**	**51105**
	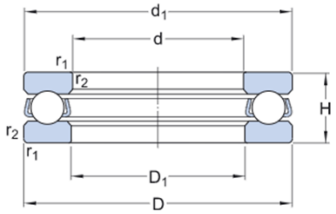	
Bore diameter, d	20 mm	25 mm
Outside diameter, D	35 mm	42 mm
Height, H	10 mm	11 mm
Pitch diameter, d_m	27.5 mm	33.5 mm
Basic dynamic load rating, C	15.1 kN	18.2 kN
Basic static load rating, C_0	29 kN	39 kN
Fatigue load limit, P_u	1.08 kN	1.43 kN
Reference speed	7500 rpm	6300 rpm
Limiting speed	10000 rpm	9000 rpm

The radius of the spheres was also verified by performing random profilometric acquisition on the set of spheres. The Hertzian contact pressure was calculated by the software HertzWin [140] by considering the simplified case of a sphere loaded against a cylindrical straight groove. The surface roughness inside

the raceways was measured randomly with a stylus roughness measuring instrument (RTP80, SM Instruments, Volpiano), and its average value equal to *Ra 0.190 μm* was considered in calculating the contact pressure. Profiles of the raceways were taken at the same positions after the tests to verify the evolution of the contact geometry due to surface fatigue.

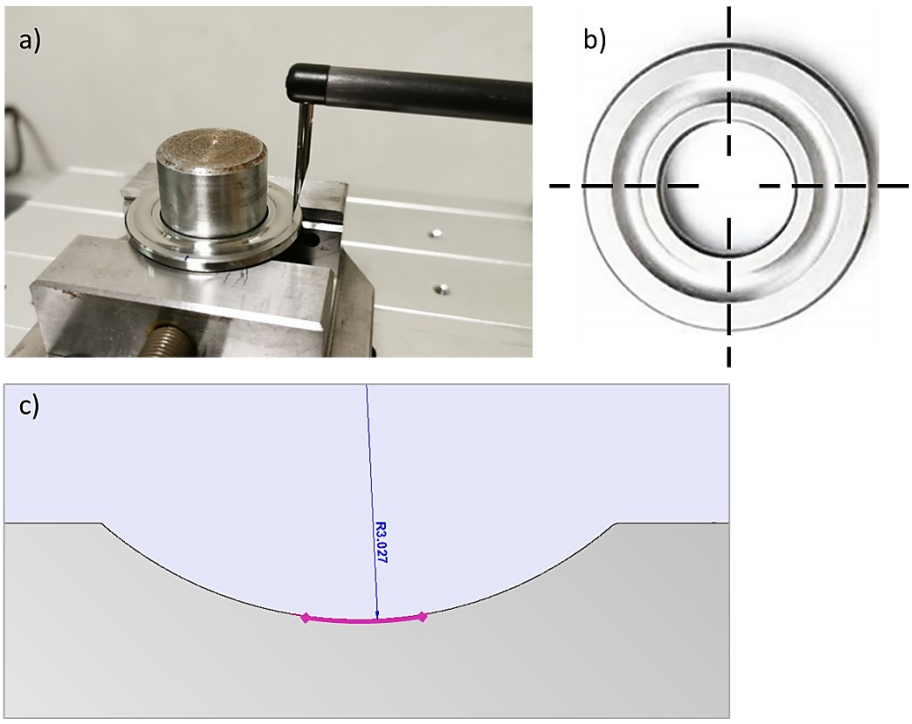

Figure 142: Profilometric inspection of the bearings before running the tests. (a,b) Four profiles equally spaced were acquired on each ring; (c) analysis of the profiles and measurement of the local osculating circle radius.

The rotating ring, the stationary ring and the row of rolling elements were weighted before and after the tests with a precision scale (Kern, ALJ 220-4NM) to identify the mass lost due to wear. Before any weighting, the rings and the rolling elements were thoroughly cleaned in a bath of chloroform and acetone to remove any trace of residual grease and debris. Figure 143 exemplifies the weighting procedure of the rolling elements and the thrust bearing rings.

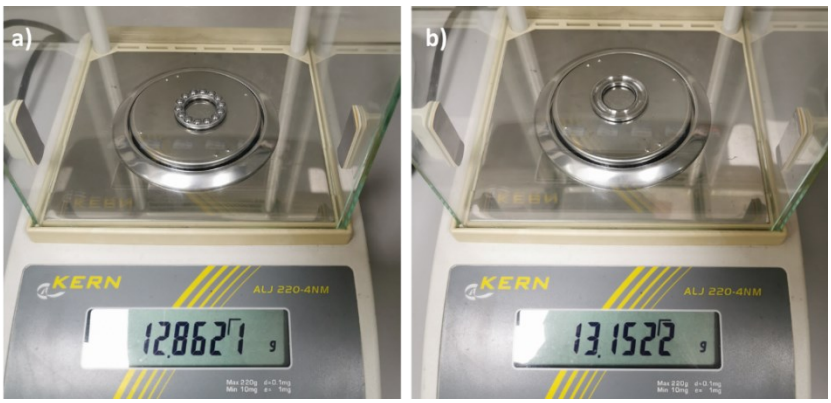

Figure 143: Weighting with precision scale (resolution 0.1mg, precision 1mg) of the thrust ball bearings. (a) Rolling elements, (b) rotating ring of an SKF 51104 bearing after degreasing in chloroform and acetone bath.

The amount of lubricating grease applied to the bearing was the same for each test. Thrust ball bearings of size 51105 were greased with *2g* of grease, whereas bearings of size 51104 were greased with *1.7g* on average. The amount of grease was determined according to the quantity suggested by the SKF Bearing Select online calculation tool [124]. Figure 144a shows the greasing procedure of a bearing installed in its seat on the test rig. The corresponding volume was determined by weighting with a precision scale featuring 0.1mg resolution (KERN ALJ220-4NM). Endurance tests were performed with the same graphene-grease compound used in the pin-on-disk test whose results are presented in Section 6.2, i.e. with 0.5%wt. GNPs, 1% GNPs, and 5% GNPs. No relubrication was applied to the bearings during the test run.

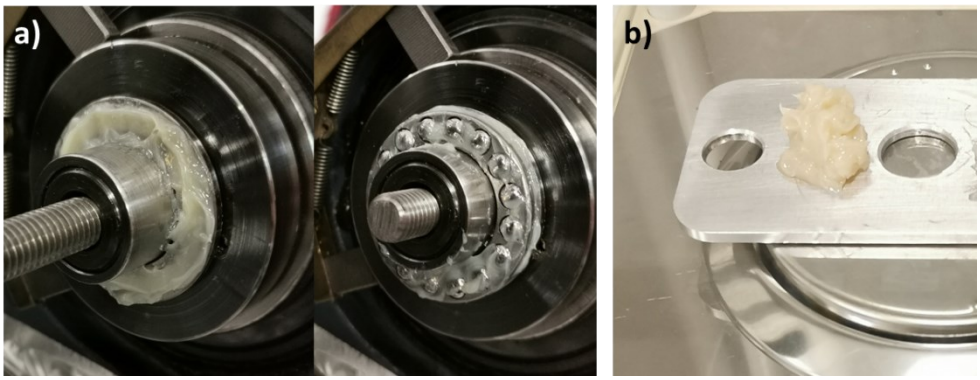

Figure 144: (a) Greasing of a 51105 thrust ball bearing installed in its seat on the test rig with 2g of MULTEMP ET-C lubricating grease before starting an endurance test; (b) the corresponding grease quantity measured with precisions scale.

6.3.1 Estimated Wohler curves

This experimental work focuses on the lubricating grease rather than the bearings as structural elements. As stated at the beginning of Section 6, rolling bearings are exploited to carry out the tests on graphene-additive greases. The structural strength of the component is of limited interest in the scope of this study. Therefore, the bearing rating life proposed by the ISO 281:2007 standard (described in Section 4.3) is calculated as a reference value to design the tests and select the testing parameters, and it is compared to the grease rating life described in Section 4.4.

The ISO standard assumes a 10% probability of failure, i.e. L_{10m}, to be the reference probability level to estimate the lifetime of a bearing for safety reasons. The purpose of the standard is to provide a conservative (not overly conservative, though) calculation method to select the proper bearing size according to the specific working condition. Bearing size should be selected to replace the component before structural damages like spalling or other catastrophic failures eventually appear during the lifetime of the bearing. Therefore, a reasonable margin is to be considered for safety. On the other hand, for testing purposes, one would desire to foresee the actual lifetime of the bearing as accurately as possible to plan the whole testing campaign thoroughly. Also, the desired lifetime of the bearing (or the grease) is as short as possible to limit the time waste while maintaining the representativity of the tribological phenomena involved in real applications. For this research the L_{50mh} Bearing Rating Life was calculated according to the guidelines of the ISO/TR 1281-2:2008 and considered for the setup of the testing parameters. The rating life was evaluated for a wide range of applied load *P* to obtain the Wohler curve of the bearing.

As to the L_{50mh}, the calculation was carried out by three methods, and the results compared:

- Automatic calculation through *Bearing Select,* the online tool developed by SKF Industries [124]
- Automatic calculation by *Bearing Solve*, an online independent calculation tool for bearings [141]
- Direct application of the detailed equations provided by the ISO 281:2007 standard.

Bearing Select is an application-oriented tool where many specific manufacturing data of the bearings are handled in the background, for instance, the radius and number of the spheres, the shape and radius of the raceways, the average surface roughness, and material properties. The user cannot be aware whether the values of these parameters of the endurance model (as long as other characteristics of the bearings, like the dynamic load rating *C*) stick closely to the guidelines of the ISO 281 standard or whether modifications are introduced based on the specific knowhow of the manufacturer and extensive experimental testing. In principle, the data provided by the SKF *Bearing Select* tool should be regarded as the reference data when testing SKF bearings. However, since industrial users care mostly about reliability and safety, the bearing manufacturers' calculation tools might consider precautionary safety factors that underestimate the lifespan of bearings.

Many paid software is available on the market to perform accurate bearing life calculations, for instance, Romax Spin® or Mesys Rolling Bearing Analysis®. This paid software has a powerful calculation kernel able to take into account the effect of the bearing clearance, the change of clearance because of interference fit and temperature, the effect of centrifugal forces, the profiles of rolling elements, load spectra, elastic expansion of the bearing rings, and many others. Since this software was unavailable for this research, the free *Bearing Solve* online calculator was chosen. This calculation tool allows the user to customize some manufacturing parameters that can be experimentally determined, e.g. the actual conformity between rolling bodies and raceway and the material properties. This approach is much more suited for a research-oriented calculation of bearing life.

Table 49: Overview of the input data needed by *SKF Bearing Select, Bearing Solve and ISO 281:2007 formulas* to perform rating life calculation. Grey-shaded regions indicate input data needed by the specific calculation method.

Calculation input	**51104**	**51105**	**Bearing Select**	**Bearing Solve**	**ISO 281 formulas**
Load, P	$0.5 \cdot P_u \div C$	$0.5 \cdot P_u \div C$			
Speed, n	1500 rpm	1500 rpm			
Pitch diameter, d_m	27.5 mm	33.5 mm			
Temperature, T	75 °C	70 °C			
Grease viscosity at 40°C	81.6 mm^2/s	81.6 mm^2/s			

Grease viscosity at 100°C	10.8 mm²/s	10.8 mm²/s
Lubrication parameter, κ	1.13	1.47
Contamination factor, η_c	0.45	0.61
Elastic modulus, E	210 GPa	210 GPa
Poisson ration, v	0.3	0.3
Sphere diameter, D_w	5.55 mm	6 mm
Number of spheres, Z	14	16
Raceway radius, R_e	3.028mm	3.195 mm
Raceway radius, R_i	2.976 mm	3.225 mm
Conformity	0.541	0.535
Material parameter, b_m	1.3	1.3
Geometry factor, f_c	90.2	87.4
Geometry factor, f_O (ISO 76:2006)	61.6	61.6
Reference viscosity, v_1	22.2 mm²/s	20.1 mm²/s
Weibull exponent, e	1.11	1.11
$a_{1,50}$	5.45	5.45

Figure 145 and Figure 146 show the Wholer curve estimated for thrust ball bearings with sizes 51104 and 51105. The diagrams are plotted considering a constant temperature, whatever the applied load, i.e., 70 °C and 75 °C for 51105 and 51104, respectively. The stabilization temperature of the bearing is here assumed to be a function of speed only. Therefore, the estimated rating life is assumed valid under the hypothesis of constant lubrication factor and constant contamination factor too. The contamination factor was calculated according to the Detailed Guidelines of ISO 281:2007. The life modification factor for reliability a_1 was calculated considering a Weibull exponent equal to *10/9*, accordingly to the results of Lundberg and Palmgren [109]. Table 49 is the overview of the input data used to estimate the Wholer curves and the related a_{ISO} diagrams of Figure 147 and Figure 148.

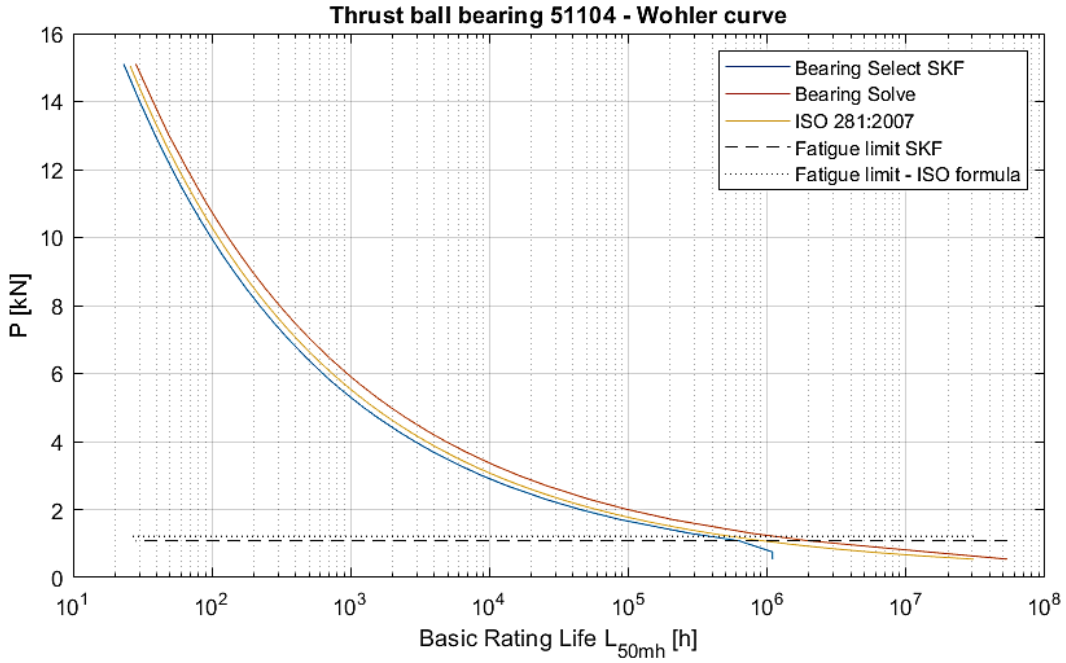

Figure 145: L_{50mh} of 51104 thrust ball bearing estimated at a constant temperature of 75 °C considering lubrication with pure MULTEMP ET-C grease.

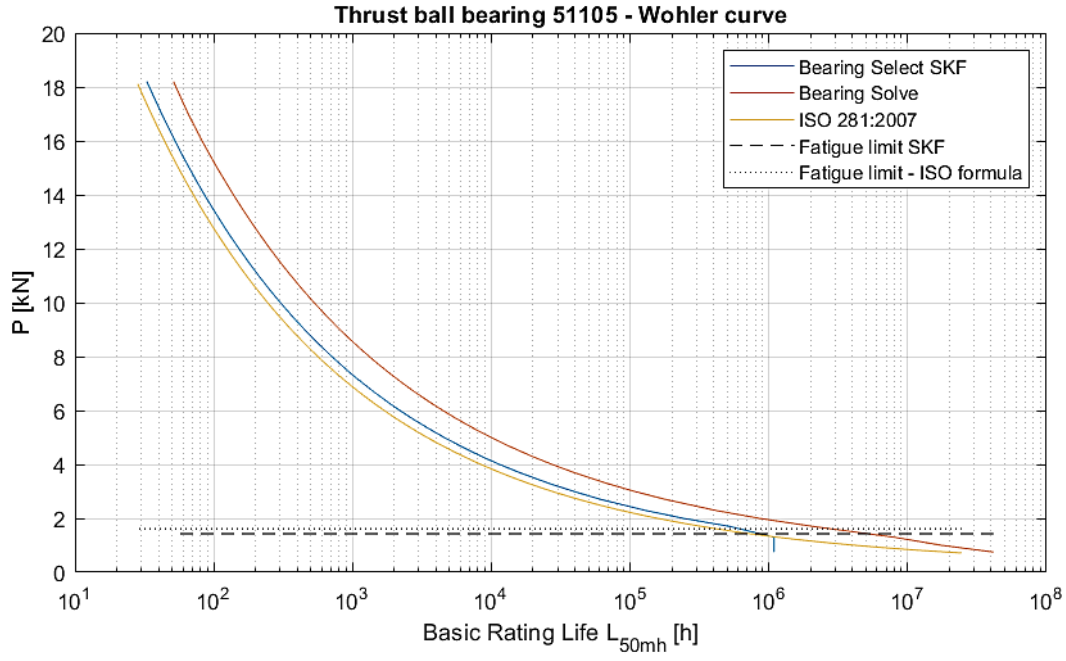

Figure 146: L_{50mh} of 51105 thrust ball bearing estimated at a constant temperature of 70 °C considering lubrication with pure MULTEMP ET-C grease.

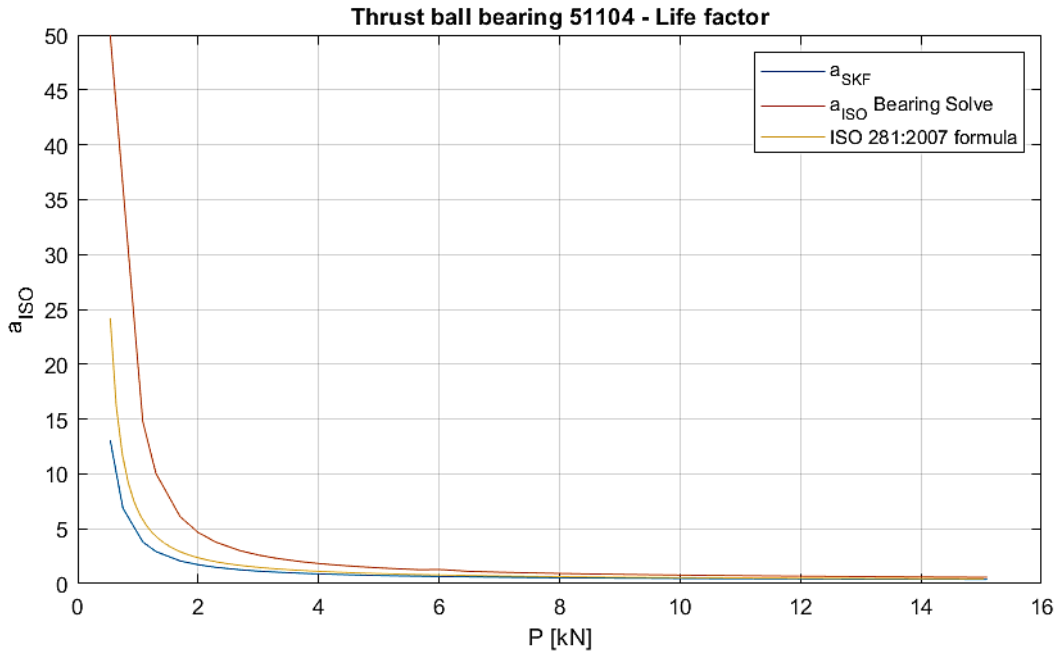

Figure 147: a_{ISO} of 51104 thrust ball bearing estimated at a constant temperature of 75 °C considering lubrication with pure MULTEMP ET-C grease.

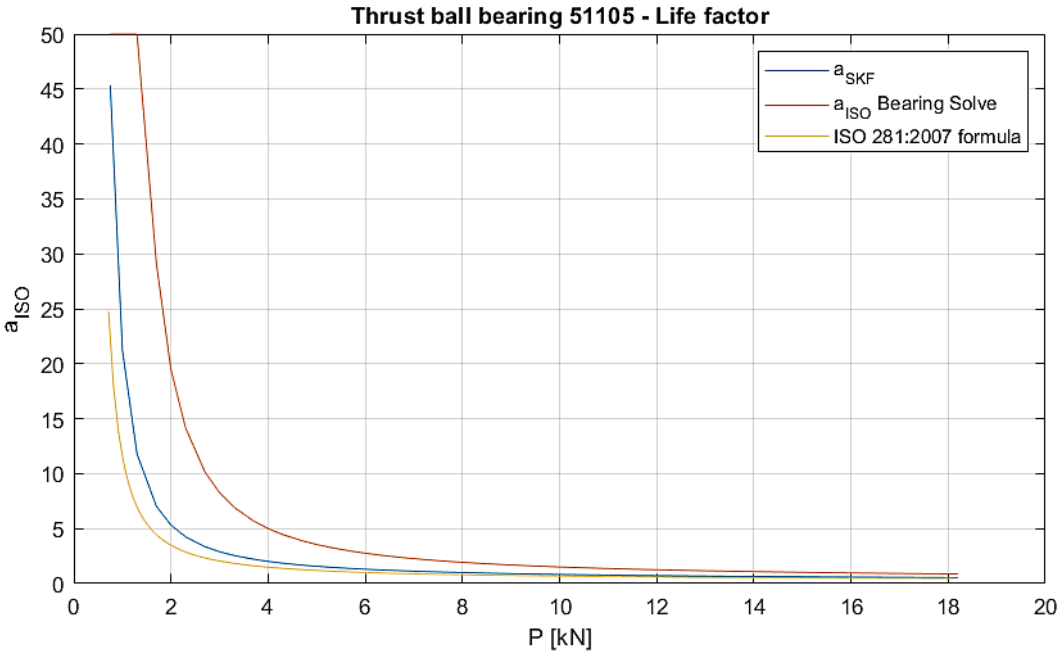

Figure 148: a_{ISO} of 51105 thrust ball bearing estimated at a constant temperature of 70 °C considering lubrication with pure MULTEMP ET-C grease.

The estimated values of the bearing endurance were also compared to the Grease Rating Life L_{fGh} and L_{50Gh} calculated as per the grease life models presented in Section 4.4. The equivalent Wohler curves of the lubricant were also obtained as if the lubricant were a mechanical component. The main input data of the models are summarized in Table 50 and Table 51.

Table 50: Main input data for the grease life model proposed by Schaeffler AG [117].

Input data	**51104**	**51105**
$L_{fGh} = K_T \cdot K_P \cdot K_R \cdot K_U \cdot K_S \cdot t_f$		
Rotational Speed, *n*	1500 rpm	1500 rpm
k_f	5.5	5.5
$k_f \cdot n \cdot d_m$	226875	276375
Load, *P*	$0.5 \cdot P_u \div C$	$0.5 \cdot P_u \div C$
K_t	1	1
K_R	1	1
K_U	0.9	0.9
K_S	0.5	0.5

Table 51: Main input data for the grease life model by Lugt and Berens [118].

Input data	**51104**	**51105**
$L_{50Gh} = GLF \cdot 52f \cdot \left(\frac{C}{P}\right)^{0.73} \cdot n_R^{-1.09} \cdot \left(\frac{1}{2}\right)^{\frac{T-T_r}{T_A}}$		
Rotational Speed, *n*	1500 rpm	1500 rpm
GLF	5	5
n_R	1.23	1.50
Load, *P*	$0.5 \cdot P_u \div C$	$0.5 \cdot P_u \div C$
T_A	19 °C	19 °C
T_r	120 °C	120 °C
f	≈ 0.3	≈ 0.3
T	75°C	70°C

As to the correction coefficients, K_T and K_R were set to unity because the bearing was operated under continuous rotation and at a temperature compatible with the work temperature range of grease. $K_U = 0.9$ was considered to take into account slight contamination (controlled laboratory conditions), and $K_U = 0.5$ accounts for grease expulsion from the bearing due to centrifugal forces and gravity because no seals and shielding were applied to the test bearing.

Figure 149 and Figure 150 show the Wohler curve estimated for the MULTEMP ET-C grease operated in thrust ball bearings of sizes 51104 and 51105 according to the equations presented in Section 4.4.

The unknown parameters for Lugt and Berens' model were estimated from [118]. Lugt and Berens identified the Arrhenius temperature and GLF value of a poly-urea grease with a mineral base oil (Pu/M); the values are 19 °C and 5, respectively. MULTEMP ET-C has a similar chemical composition, except for the fully synthetic base oil instead the mineral base stock. Therefore, these values were considered approximately valid for the grease used for these tests.

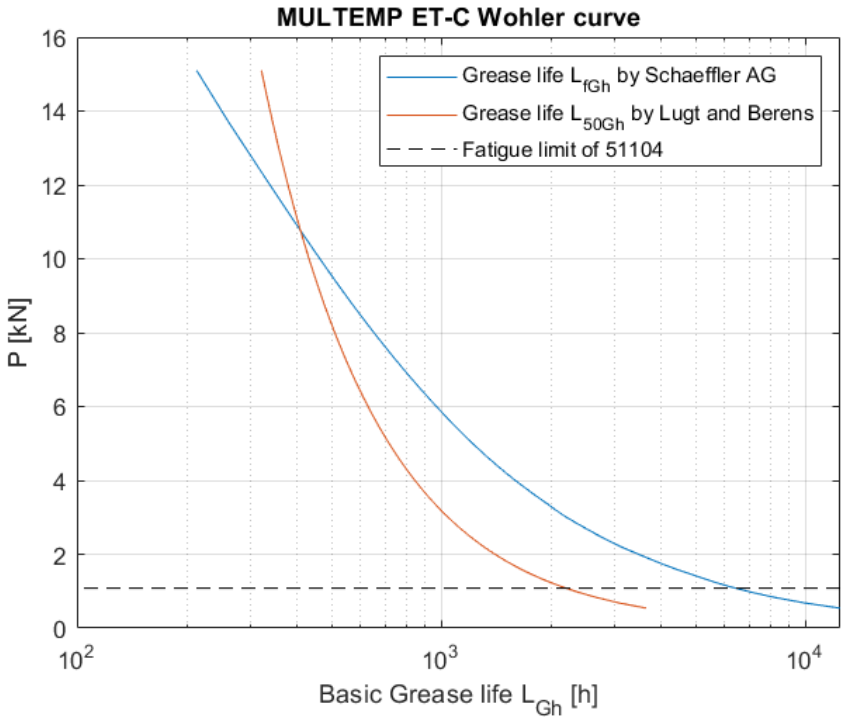

Figure 149: L_{fGh} Grease life curve estimated considering operation with a 51104 thrust ball bearing and constant operating temperature of 75°C.

The filling factor was set to 0.3 even though the nominal volume of grease applied to the bearings (*1.6 g* and *2 g,* respectively, see Section 6.3) was more significant than the free volume allowed between the rings and the tolling elements. This choice is motivated by observing the grease distribution evolution during the tests. A lot of grease flows out of the bearing when the load is applied, and the remaining part (that nominally fills 100% of the volume) is readily expelled as chunks in the first hours of running. Moreover, previous experimental observations [118] have shown that grease-lubricated bearings usually work with a filling factor of 0.27 to 0.4 at stabilization.

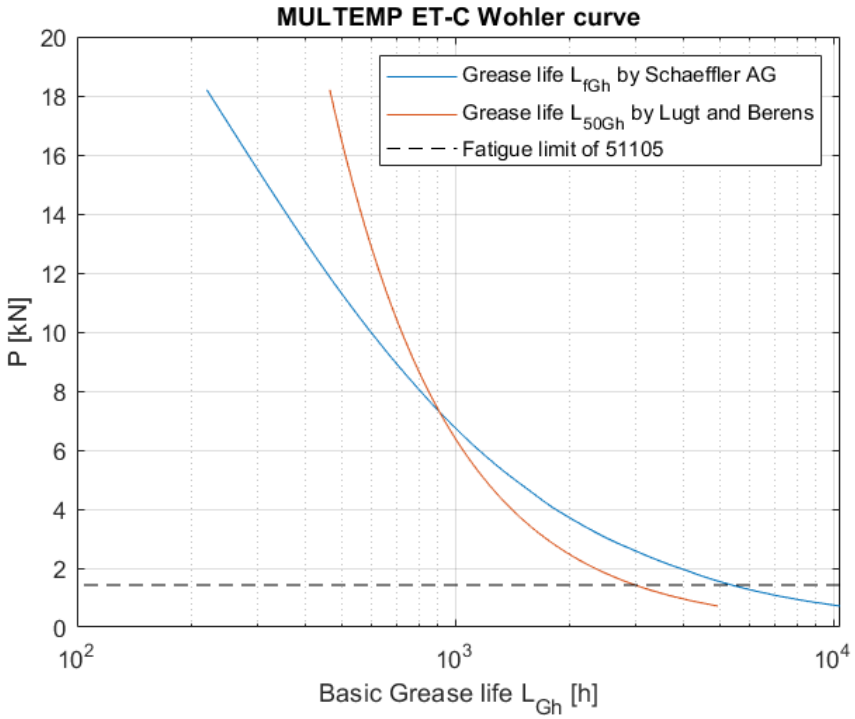

Figure 150: L_{fGh} Grease life curve estimated considering operation with a 51105 thrust ball bearing and constant operating temperature of 70°C.

6.3.2 Results of Preliminary tests

Preliminary endurance tests were carried out with commercial SKF 51105 thrust ball bearings. Bearings were tested as purchased. The tests were performed with pure MULTEMP ET-C high-performance grease without any nanoparticle additive. Before running the tests, the expected bearing life was estimated through the calculation tools presented in Section 6.3.1. The summary of the test

conditions and the estimated endurance is provided in Table 52. The table lists both the L_{10mh} and the L_{50mh} rating bearing life values since, in the first instances, the standard 10% probability failure was considered to predict the test duration.

Table 52: Theoretical bearing life rating for the preliminary endurance tests with SKF 51105 thrust ball bearings. "ISO 281" indicates data obtained by directly applying the formulas provided by the ISO281:2007 standard. The conformity value indicated in the tables is the average of the two raceways of the bearing.

	n [%]	**Preliminary test 1**	**Preliminary test 2**
Bearing size		51105	51105
Axial load, *P*		8.4 kN	9.3 kN
Temperature, *T*		70 °C	70 °C
C/P (SKF Catalogue)		2.17	1.96
Average conformity of the raceways		0.532	0.537
p_{Hertz}^{max}		2589 MPa	2707 MPa
L_{mh} Bearing Solve	L_{10mh}	211 h	130 h
	L_{50mh}	1149h	709 h
L_{mh} Bearing Select	L_{10mh}	107 h	73 h
	L_{50mh}	583 h	398 h
L_{mh} ISO 281	L_{10mh}	85 h	58 h
	L_{50mh}	465 h	318 h
Grease - Schaeffler AG	L_{10fGh}	139 h	121 h
	L_{50fGh}	758 h	661 h
Grease - Lugt e Berens	L_{10Gh}	150 h	140 h
	L_{50Gh}	820 h	761 h

The main results of the endurance tests are summarized in Table 53. The preliminary tests run at least for a twice as long time as the estimated L_{10} life rating by the theoretical models taken in the first instance as the reference prediction of actual test duration. Both the tests were periodically stopped and resumed to monitor the evolution of the interface state and the grease degradation.

Table 53: Test conditions and main results of the preliminary tests with SKF 51105 thrust ball bearings

Test #	Monitored parameters Average value	Stop at	Result
Preliminary Test 1	$\overline{F_a} = 8.38\ kN$ $\overline{T_{51105}} = 68.9\ °C$ $\overline{ECR} = 5.08\ M\Omega$	242 h	• *No apparent lubricant failure* • *No abnormal temperature rise* • *ECR > 1 MΩ* • *Carbonized residues around the rolling bodies*
Preliminary Test 2	$\overline{F_a} = 9.41\ kN$ $\overline{T_{51105}} = 70.4\ °C$ $\overline{ECR} = 2.73\ M\Omega$	330 h	• *No apparent lubricant failure* • *Occasional fluctuation of temperature in the central part of the test* • *ECR > 1 MΩ* • *Carbonized residues around the rolling bodies*

Figure 151 shows, as an example, the curves of temperature and ECR recorded during Preliminary Test 2. The diagrams show a slight variation of the monitored parameters was observed during the whole test after the running-in period. The working temperature of the test bearing stabilized at about 70 °C and featured occasional spikes to 75-80 °C during the central part of the test. No serious loss of grease performance was associated with these fluctuations because the corresponding ECR value always remained above 1 MΩ (Figure 152). No damages were detected on the raceways and rollers by the end of the tests, and no signs of structural failure. Figure 153 shows that the grease appearance and consistency changed due to the mechanical stress during the endurance tests. However, the grease performance was still sufficiently high to supply the contact with enough bleed oil even though many carbonised hard deposits were present at the raceway borders. Very similar results were observed in Preliminary Test 1.

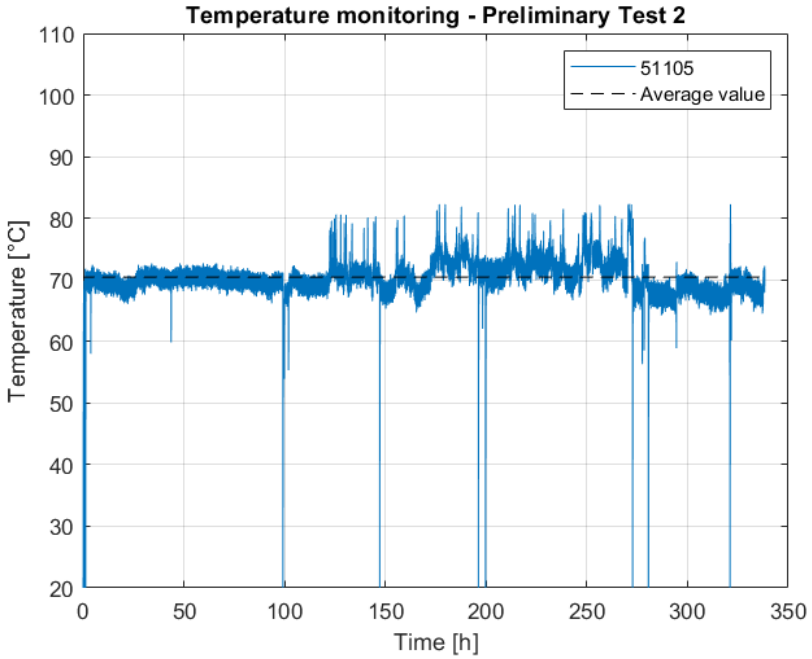

Figure 151: Temperature chart recorded during preliminary test 2.

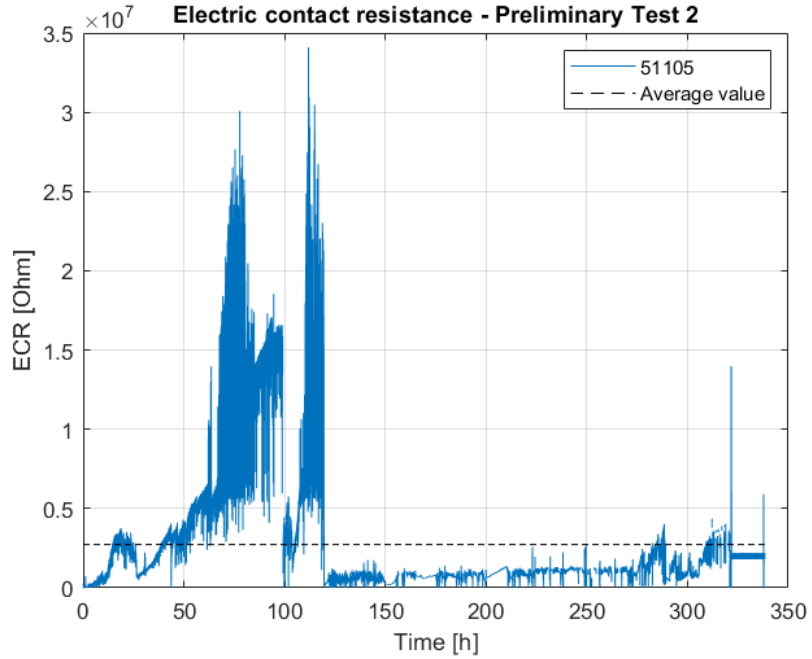

Figure 152: ECR chart recorded during preliminary test 2.

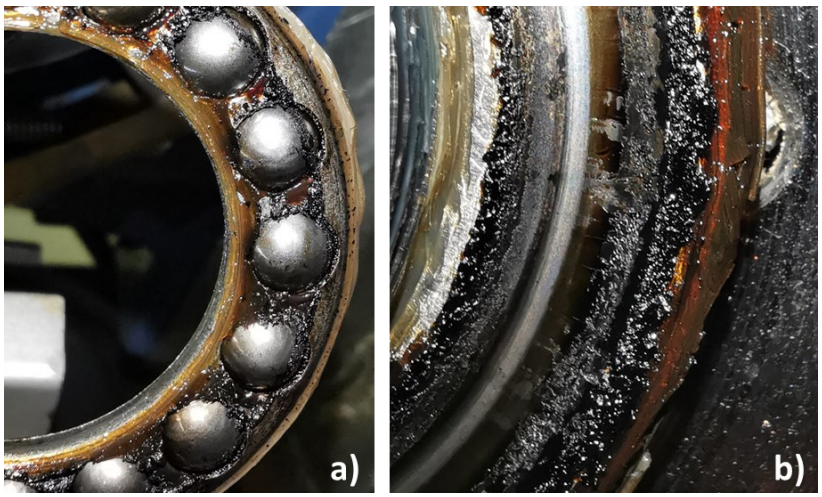

Figure 153: (a) Hard deposit on the cage and (b) at the raceway grove sides at the end of Preliminary Test 2 with base grease.

The two preliminary tests were stopped once the cumulative duration exceeded a threshold duration reasonable for laboratory tests and far higher than the theoretical L_{10} life ratings. However, in a second instance, L_{50} life ratings were considered a more statistically reliable prediction of the actual test duration. The values of L_{50mh} (reported in Table 52) suggested that it would probably take longer to produce any appreciable sign of failure due to either grease failure or rolling contact fatigue. Since the test load could not exceed 10 kN (i.e. the maximum allowable load of the load cell), it was decided to reduce the size of thrust ball bearings to handle endurance tests of shorter duration during the testing campaign. The following sections will present the results of the endurance tests carried out with bearings of size 51104.

6.3.3 Results with base grease

Three test repetitions were performed with three 51104 thrust ball bearing greased by MULTEMP ET-C lubricating grease to assess the reference performance with the base lubricant. Table 54 provides an overview of the leading testing parameters and the expected L_{50mh} bearing life estimated through the calculation tools presented in Section 6.3.1. Bearings were tested as purchased.

Table 54: Theoretical bearing life rating for the preliminary endurance tests with SKF 51105 thrust ball bearings. “ISO 281” indicates data obtained by directly applying the formulas provided by the ISO 281:2007 standard. The

average conformity used for calculations was estimated by averaging the raceway conformities of the 12 bearings under test.

	Selected test condition
Bearing size	51104
Target axial load, *P*	8.2 kN
Expected temperature, *T*	75 °C
C/P (SKF Catalogue)	1.84
Average Conformity of the bearings under test	0.542
p_{Hertz}^{max}	2946 MPa
L_{50mh} Bearing Solve	295 h
L_{50mh} Bearing Select	201 h
L_{50mh} ISO 281	228 h
L_{fGh} Schaeffler AG	631 h
L_{50Gh} by Lugt e Berens	501 h

The criterion to identify the stop condition of the endurance tests was determined based on the capability of the grease to lubricate the bearing adequately without any relubrication. The bearing operative temperature and the ECR value served as the monitoring parameters to assess the capability of grease to lubricate the contact. In line with standard practice, grease is assumed to have reached the end of its life as soon as a fluctuation exceeds a certain predetermined temperature level. Each test was stopped as soon as the bearing temperature exceeded 95 °C (i.e., about 25°C above the typical stabilization temperature observed in preliminary tests), and the ECR values dropped to an almost-conduction state. Since many factors influence the electrical contact resistance, the limiting ECR value for conduction was fixed at 0.1% of the average ECR of the test. Lugt et al. [3] remarked in their research work that grease life may depend strongly on the particular value of the maximum allowed temperature since the temperature of grease-lubricated bearings is expected to fluctuate as a result of the feed and loss mechanism [14]. Interestingly, these two stop conditions based on temperature and ECR were always met simultaneously, also because the unstable temperature rise and the resistance drop are both the consequence of the same lubricant film failure at the rolling interface.

Table 55: Test conditions and main results of endurance tests with on SKF 51104 thrust ball bearings. The conformity value indicated in the table is the average of the two raceways of each bearing.

Test ID	Monitored parameters Average value	Test Duration	Result
Test 1	$\overline{F_a} = 7.95\ kN$ $\overline{T_{51104}} = 75.9\ °C$ $\overline{ECR} = 0.78 M\Omega$ Conformity = 0.539	55 h	• *Chaotic temperature fluctuations at the of the test* • *Overtemperature limit of 95°C reached* • *Lubricant film failure due to ECR conduction*
Test 2	$\overline{F_a} = 8.13\ kN$ $\overline{T_{51104}} = 71.5\ °C$ $\overline{ECR} = 3.84\ M\Omega$ Conformity = 0.546	199 h	• *Chaotic temperature fluctuations at the of the test* • *Overtemperature limit of 95°C reached* • *Lubricant film failure due to ECR conduction*
Test 3	$\overline{F_a} = 8.17\ kN$ $\overline{T_{51104}} = 72.3\ °C$ $\overline{ECR} = 14.2\ M\Omega$ Conformity = 0.541	204 h	• *Chaotic temperature fluctuations at the of the test* • *Overtemperature limit of 95°C reached* • *Lubricant film failure due to ECR conduction*

Table 55 gives the observed test duration up to the stop condition with the base grease. Except for Test 1, which lasted just 55h, the other two tests featured a very similar duration of about 200 h. This observed duration is lower than the predicted grease rating life by Schaeffler's model and Lugt and Berens' model (Figure 154). Surprisingly, it is comparable to the L_{50mh} calculated by SKF Bearing Select tool although no signs of rolling contact fatigue were visible inside the raceway groves of the bearing. Being the duration of Test 1 far less than the other two tests, an unidentified difference in the testing condition should have occurred. More repetitions of the endurance tests are needed in the future to confirm the expected duration of MULTEMP ET-C grease more accurately, which were not carried out due to time reasons.

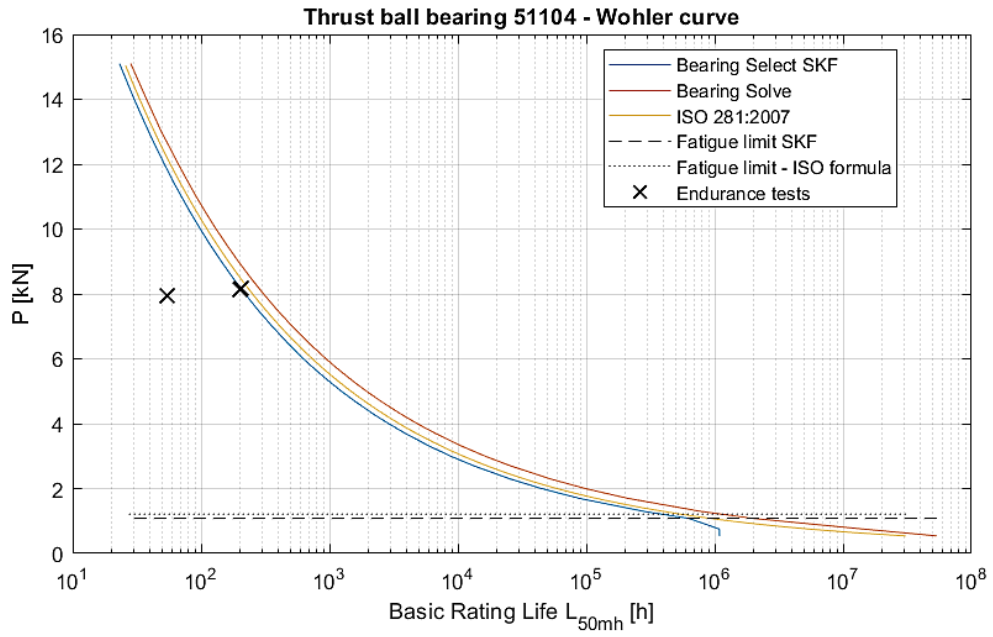

Figure 154: Duration of endurance tests with base grease compared to life rating curves.

Figure 155 shows the Weibull probability plots estimated through the results of the grease endurance tests. The Weibull statistics were applied even though it would generally require at least 5 observations of the same phenomenon [130]. The estimated parameters of the two-parameter Weibull distribution were used in equation (41) to determine the experimental L_{50}^{exp} value for each grease compound (i.e., with S = 50%), where η is the so-called characteristic duration and e is the Weibull exponent.

$$L_{100-S}^{exp} = \eta \left[\ln\left(\frac{100}{S}\right)\right]^{1/e} \tag{41}$$

Oil bleeding (see Section 1.1.2) appeared to be the dominant lubrication mechanism. Figure 156 shows the presence of base oil drained from the spheres and flowed back to the contact sites after the end of an endurance test. Droplets of oil expelled out of the rotating bearing were systematically found on the walls of the polycarbonate safety enclosure during the tests, and both are indicators that a film of liquid lubricant separated the solid surfaces of the bearing during the tests.

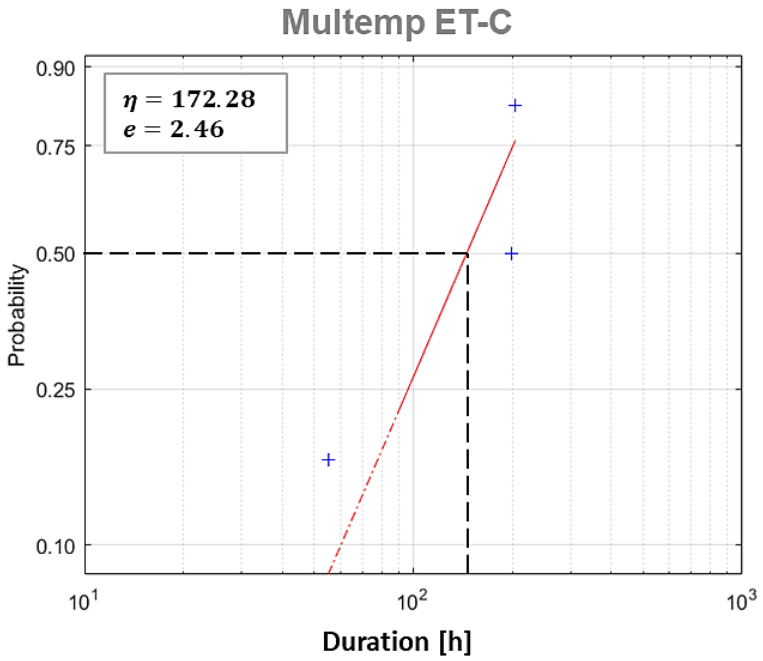

Figure 155: Experimental Weibull probability plot for MULTEMP ET-C grease duration. η and e are the parameters of the Weibull distribution.

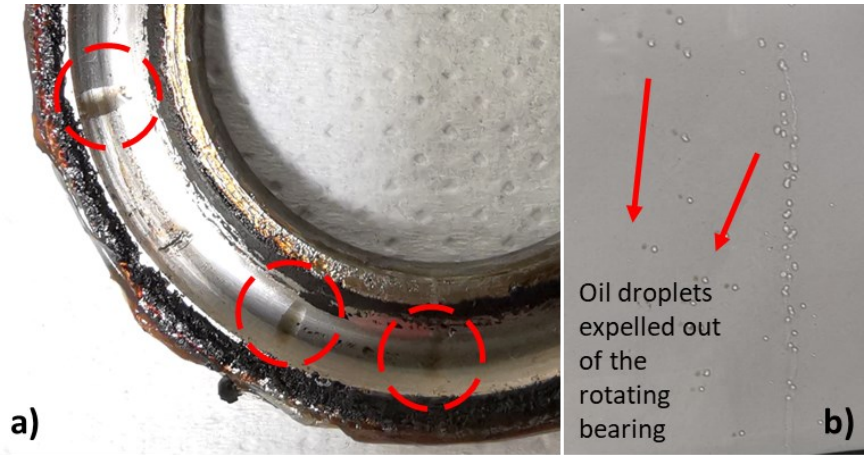

Figure 156: (a) Grease base oil drained from the spheres in static contact over the ring after the end of a test (Test 3); (b) Oil droplets expelled out of the DUT and accumulated on the safety enclosure of the test rig.

Figure 157 shows that the static ring temperature of the test bearing stabilized at about 71°C after 5h and remained almost constant up to 105h. The typical temperature peak in the first few hours of running due to grease migration out of the bearing (i.e. the so-called 'churning phase') was not observed. The favourable geometry of thrust bearings allows most grease to be squeezed out of the bearing

radially when the thrust load is applied, so drag losses from grease migration and churning are limited compared to radial bearings. Moreover, the shaft speed was gradually raised from 500 to 1500 rpm during the first 30 min of the test. A soft start lets grease find its position in the cage reservoirs and at the borders of the static and rotating rings. The soft start may have contributed positively to reducing overheating.

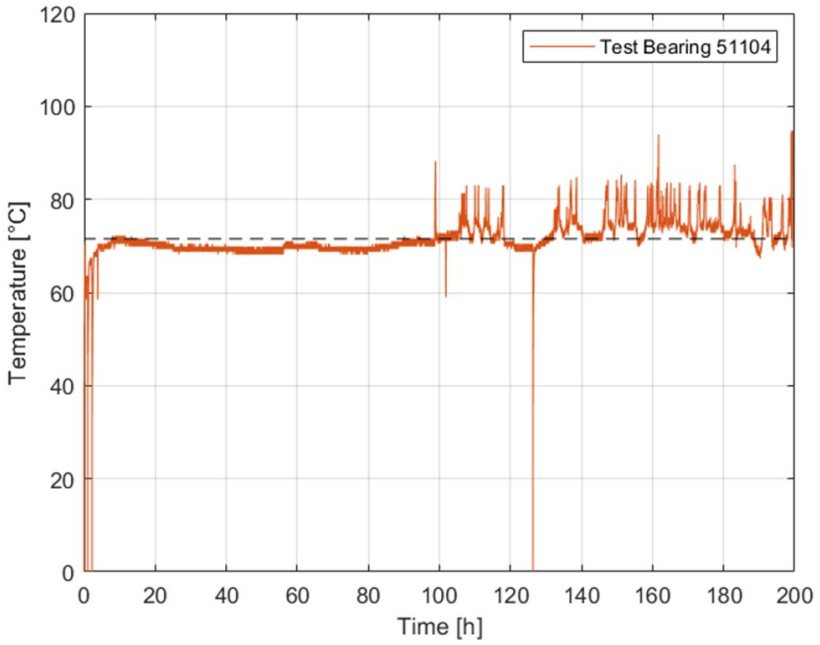

Figure 157: Temperature of the test bearing recorded during Test 2.

Wide temperature fluctuations up to 82°C to 85 °C dominated the thermal signal after 120 h. These fluctuations are similar to those reported by Lugt et al. [3], proving that the grease lubrication mechanism and the related thermal behaviour are *deterministically chaotic*. Grease lubrication is not a continuous process, as discussed in Section 1.1.2, and grease cannot continuously provide a sufficiently thick film to separate the solid surfaces. Lugt et al. argued that the dynamics of the thermal behaviour observed with grease-lubricated bearings under self-induced heating results from recurrent metal-to-metal contacts that cause transitory heat development. Softening of grease stored in reservoirs, which follows the peak of temperature, lets some lump of grease be released or increases the oil bleeding rate. Replenishment of the track restores a starved full-film condition and temperature drops. However, the film thickness progressively decreases over time, and another metal-to-metal contact is expected as soon as the film reaches a thickness of the order of or less than the surface roughness [3].

Such a self-healing mechanism at film breakdown occurs many times before the bearing can no longer recover from lubricant shortage. The thermal fluctuations lasted 80 h in the test of Figure 157 before the temperature rose above 95°C.

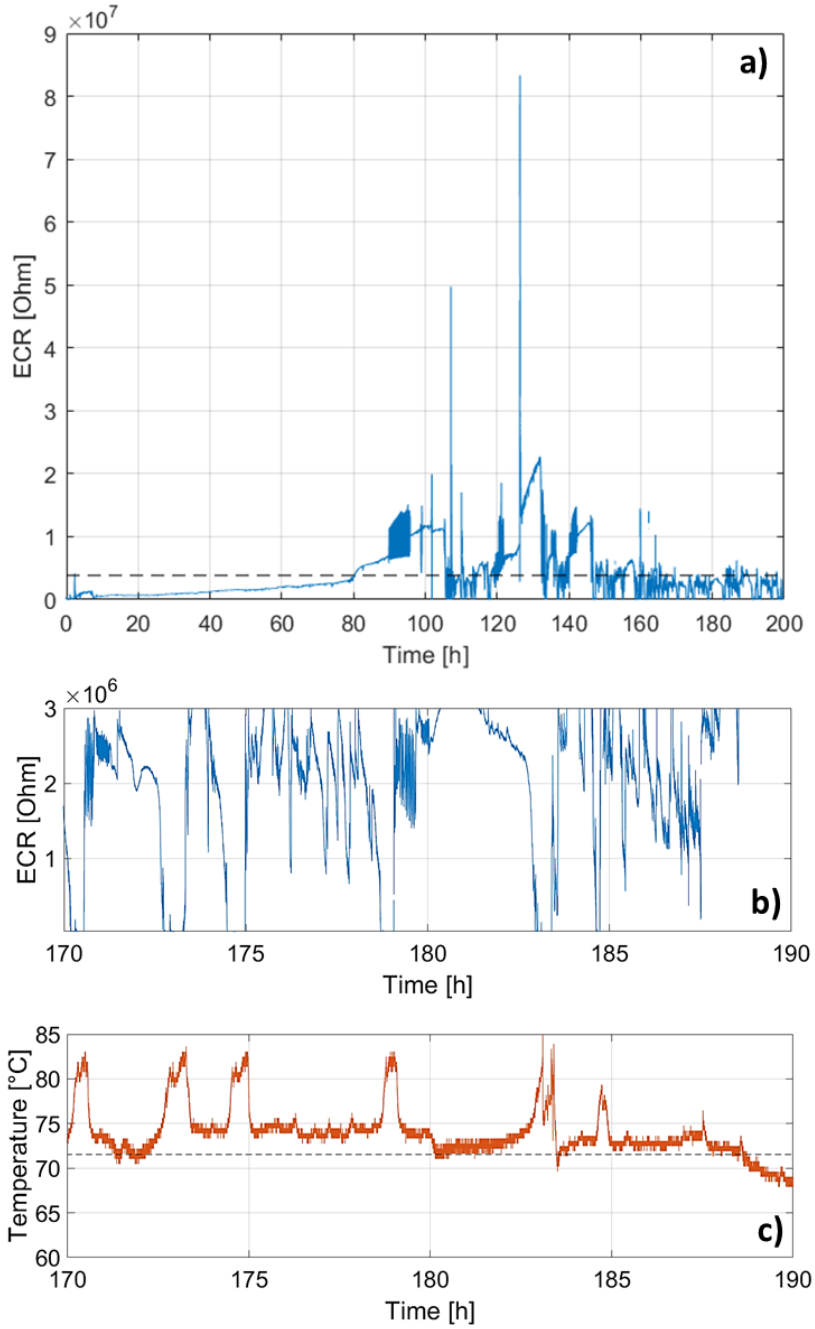

Figure 158: (a) ECR chart recorded during Test 2; (b-c) Detail of the ECR value between 170 h and 190 h where the resistance value followed the fluctuations of the bearing temperature and often dropped to conduction (few hundreds of Ω).

Figure 158a shows that the ECR value progressively increased whenever the temperature was steady as if the film thickness was growing. It is shown below that residual of a deposited layer (likely composed of degraded thickener) was found at the borders of the rolling track. The beneficial accumulation of broken thickener fibres into the lubricating film may be responsible for increasing contact resistance in steady-state oil bleeding. On the other hand, ECR underwent wide fluctuations whenever temperature fluctuated (Figure 158b). In the last part of the test, subsequent temperature excursions up to about 82°C well matched sudden drops of resistance to the conduction state (Figure 158c). This evidence supports the argumentation that recurrent metal-to-metal contacts were the root cause of the temperature fluctuations observed in these endurance tests. Similar behaviour was also observed during the other endurance tests.

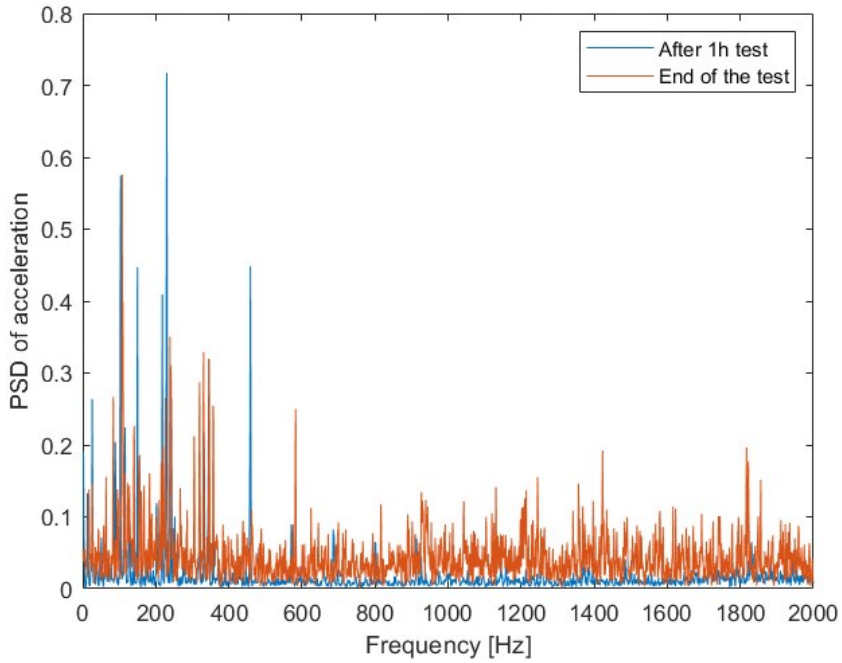

Figure 159: PSD of axial vibrations at the beginning and the end of Test 2.

Increased vibrations also indicated the unstable contact condition during the last part of the test. Figure 159 compares the average PSD chart of axial vibrations after 1h of the test and at the end of the test. A distributed increase of the PSD intensity in the whole frequency range justified the increased noise detected by the ear near the end of the test. Similar behaviour was also observed during the other endurance tests.

Figure 160 shows the evolution of the axial load recorded during Test 2. Temperature excursions were also the cause of minor fluctuations in the applied load, and this evidence is a side effect related to the specific loading system the test rig is equipped with. Any temperature peaks induced the local thermal expansion of the bearing under test. Since the characteristic time of these peaks was too short for the tie rod and the Belleville springs to elongate (see Section 6.2.1), the contact interference increased and resulted in a peak load.

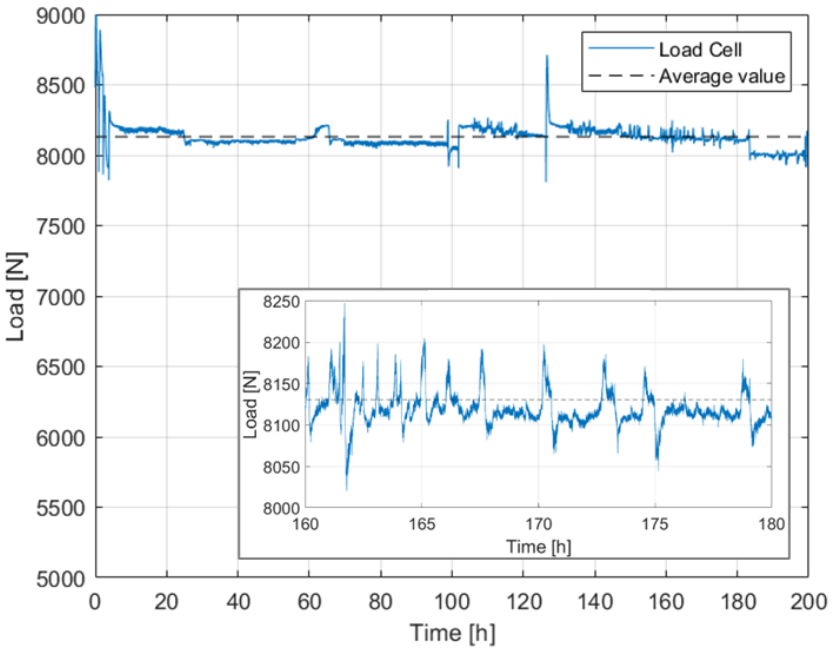

Figure 160: Axial load applied to the test bearing during Test 2. Tests were sometimes paused and restarted to manually adjust the value of the applied load in case of excessive drift of the preset value. Inset is the enlarged view of 20 h of test.

The bearings were inspected under the optical microscope at the end of the tests before and after cleaning. The rings and cage were degreasing by dipping into a bath of chloroform and acetone. Figure 161a and Figure 161b shows the appearance of the rotating ring and rolling elements after the end of the endurance test. As for the preliminary tests, carbonised deposits were observed inside the grease reservoir. Compositional analysis of the waste grease will be necessary to clarify if this carbonized matter is the consequence of grease oxidation. Traces of a deposited layer of dried grease was also visible at the borders of the rolling track. Part of this dark matter remained grabbed onto the steel surface after degreasing by dipping into the chloroform bath (Figure 161c) and was easily removed by rubbing the surface with a tissue soaked in acetone. It was probably

composed of degraded thickener fibres separated from the base oil compacted by over-rolling.

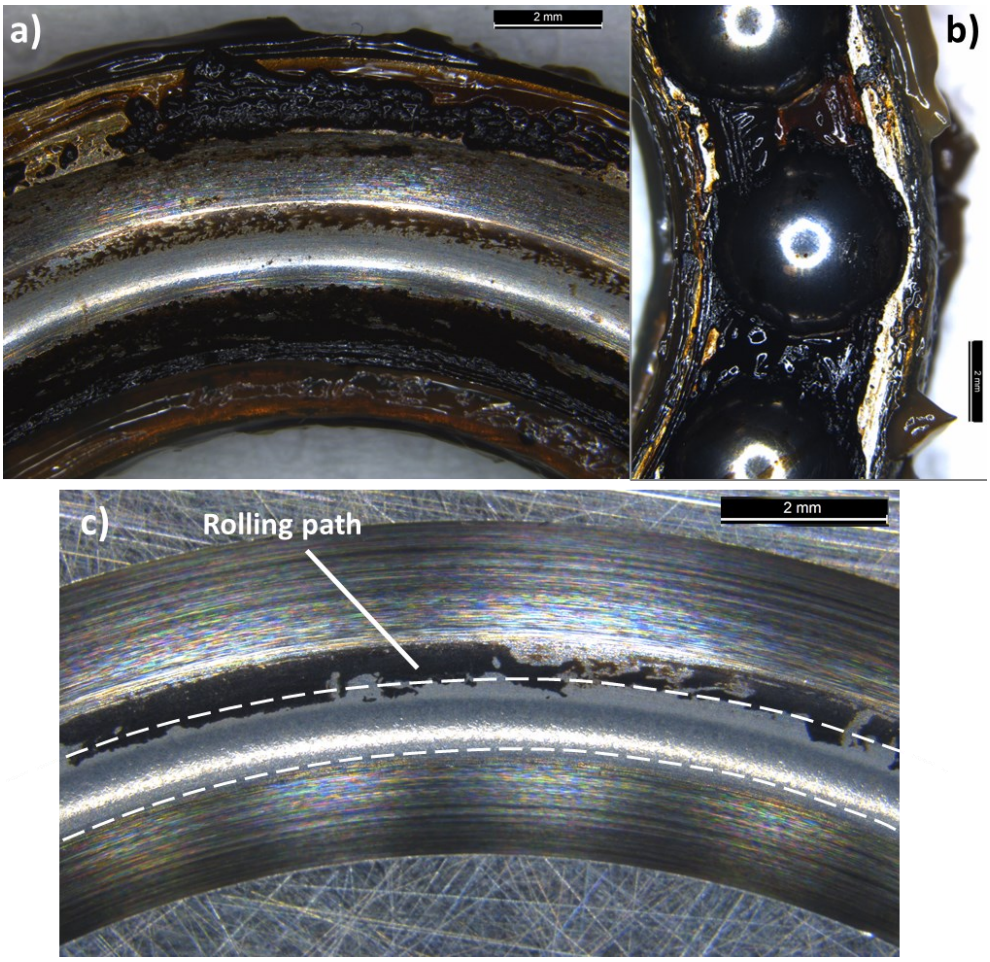

Figure 161: Inspection under the optical microscope of the rotating ring of the tested bearing (Test 2). (a) Distribution of waste grease just after the stop of the test; (b) distribution of waste grease on the cage; (c) appearance of the raceway after cleaning in a bath of chloroform and acetone.

Figure 162a shows that the surface morphology in the central part of the raceway groove is different than elsewhere and that region corresponds to the rolling path of the spheres. The grinding marks on the unworn surface (Figure 163) disappeared, and a matte wrinkled surface was observed after 200 h rolling. This appearance is likely due to fatigue at the level of the surface asperities and local plastic flow due to rolling motion and high load. The nominal contact pressure calculated by the Hertzian contact theory was about 2900 MPa.

However, the peak contact pressure of surface asperities is expected to be much higher [23].

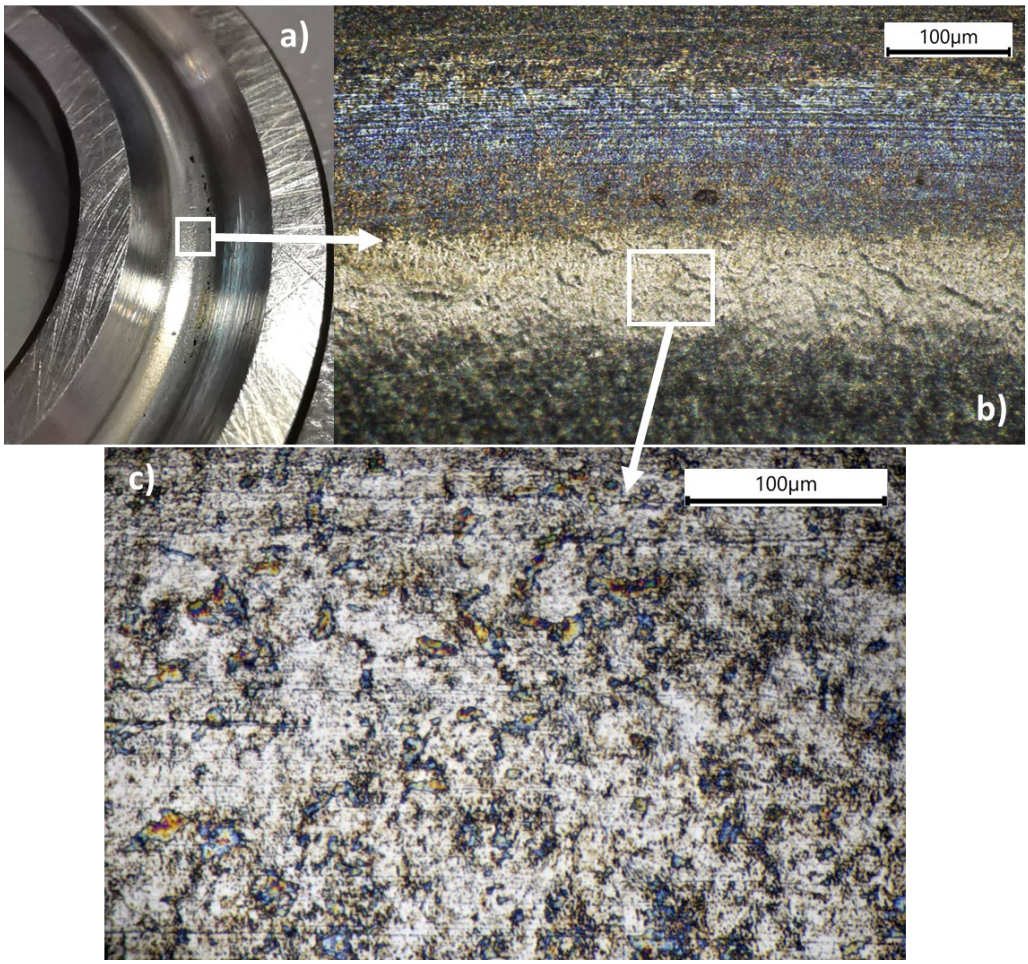

Figure 162: (a) Different surface finish inside the rolling track of the spheres visible after a deep cleaning with a tissue soaked in acetone to remove residues of the deposited layer; (b) plastically deformed region visible in the middle of the raceway groove under the optical microscope.

The profiles of the raceway grooves bearings were measured with the stylus profilometer after deep cleaning. Any trace of the third layer was carefully removed before profilometry to avoid distorting the analysis results. Profiles were taken in the exact location and compared with the profiles acquired before the endurance tests. The comparison was carried out via a dedicated tool of the instrument software. Figure 164a and Figure 164b show, as an example, the results of the profile analysis for the static and rotating ring of Test 2, respectively.

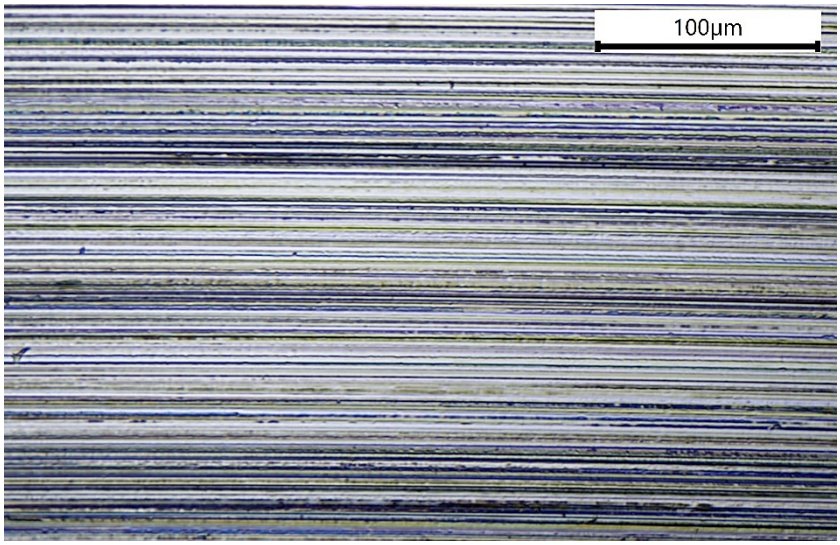

Figure 163: High magnification inspection of the surface of an unworn 51104 bearing under the optical microscope.

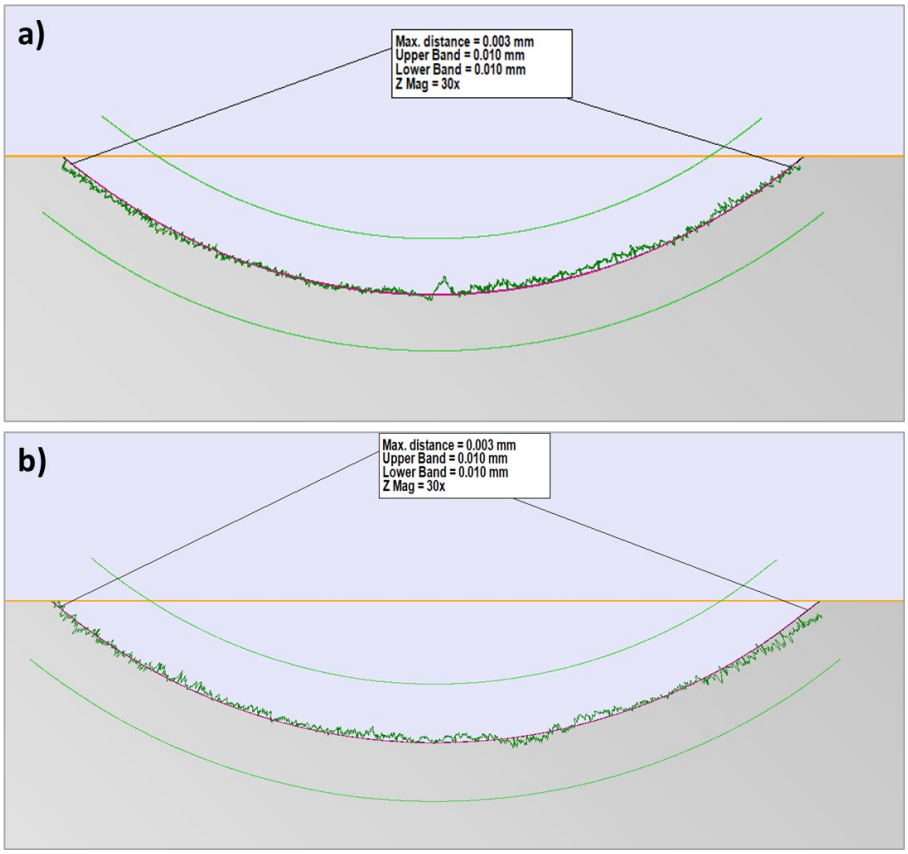

Figure 164: Example of profile comparison before and after the endurance test for (a) the rotating ring and (b) the static ring (Test 2).

Surprisingly, the results evidenced that the maximum deviation between the profiles was always in the order of a few micrometers, and no substantial modification of the profiles inside the contact region occurred due to over-rolling. Although a significant difference in the profiles was expected in the central part of the raceway groove, i.e. where surface yielding appeared, no measurable wear was detected. This evidence supports that Figure 162 represents a physiological reaction of the surface to a high surface and subsurface cyclic stress.

6.3.4 Impact of Graphene on the grease performance

The same test procedure and post-test analyses were repeated with 51104 bearings lubricated by the three graphene-grease compounds presented in Section 5, i.e. 0.5%, 1% and 5% wt, GNPs into MULTEMP ET-C grease.

Table 56: Test conditions and main results of endurance tests on SKF 51104 thrust ball bearings with 0.5% GNPs grease. Test 11 was suspended before grease failure.

Test #	Monitored parameters Average value	Test Duration	Result
Test 5	$\overline{F_a} = 8.23\ kN$ $\overline{T_{51104}} = 72.7\ °C$ $\overline{ECR} = 3.32\ M\Omega$ Conformity = 0.537	120 h	• *Chaotic temperature fluctuations at the of the test* • *Overtemperature limit of 95°C reached* • *Lubricant film failure due to ECR conduction*
Test 8	$\overline{F_a} = 8.24\ kN$ $\overline{T_{51104}} = 73.5\ °C$ $\overline{ECR} = 3.21\ M\Omega$ Conformity = 0.541	107 h	• *Chaotic temperature fluctuations at the of the test* • *Overtemperature limit of 95°C reached* • *Lubricant film failure due to ECR conduction*
Test 11	$\overline{F_a} = 8.23\ kN$ $\overline{T_{51104}} = 73.9°C$ $\overline{ECR} = 8.87\ M\Omega$ Conformity = 0.533	451 h	• ***No Chaotic** temperature fluctuations* • ***No** overtemperature* • ***No** Lubricant film failure* • *TEST SUSPENDED*

Table 57: Test conditions and main results of endurance tests on SKF 51104 thrust ball bearings with 1% GNPs grease.

Test ID	Monitored parameters Average value	Test Duration	Result
Test 4	$\overline{F_a} = 8.14\ kN$ $\overline{T_{51104}} = 73.7\ °C$ $\overline{ECR} = 15.9\ M\Omega$ Conformity = 0.541	254 h	• ***No Chaotic*** *temperature fluctuations* • *Overtemperature limit of 95°C reached* • *Lubricant film failure due to ECR conduction*
Test 7	$\overline{F_a} = 8.28\ kN$ $\overline{T_{51104}} = 76.6\ °C$ $\overline{ECR} = 5.31\ M\Omega$ Conformity = 0.540	136 h	• *Chaotic temperature fluctuations at the of the test* • *Overtemperature limit of 95°C reached* • *Lubricant film failure due to ECR conduction*
Test 10	$\overline{F_a} = 8.10\ kN$ $\overline{T_{51104}} = 76.7\ °C$ $\overline{ECR} = 1.45\ M\Omega$ Conformity = 0.537	125 h	• *Chaotic temperature fluctuations at the of the test* • *Overtemperature limit of 95°C reached* • *Lubricant film failure due to ECR conduction*

Table 58: Test conditions and main results of endurance tests on SKF 51104 thrust ball bearings with 5% GNPs grease. Just two repetitions were performed due to time constraints.

Test #	Monitored parameters Average value	Test Duration	Result
Test 6	$\overline{F_a} = 8.15\ kN$ $\overline{T_{51104}} = 76.7\ °C$ $\overline{ECR} = 2.76\ M\Omega$ Conformity = 0.535	389 h	• ***No Chaotic*** *temperature fluctuations* • *Overtemperature limit of 95°C reached* • *Lubricant film failure due to ECR conduction*
Test 9	$\overline{F_a} = 8.18\ kN$ $\overline{T_{51104}} = 75.1°C$ $\overline{ECR} = 9.24\ M\Omega$ Conformity = 0.543	392 h	• ***No Chaotic*** *temperature fluctuations* • *Overtemperature limit of 95°C reached* • *Lubricant film failure due to ECR conduction*

Table 57, Table 56, and Table 58 provide the results of the endurance tests with the three grease compounds. The average value of the monitored parameters during tests is also indicated. Due to time constraints, just two repetitions of the endurance tests with the 5% GNPs grease compound were performed within the framework of this PhD thesis because of their longer duration (about 20 days for each test). Figure 165 to Figure 167 show the Weibull probability plots estimated through the results of the grease endurance tests. Figure 168 compares the L_{50}^{exp} duration estimated by the Weibull distribution with the L_{50}^{exp} of base grease.

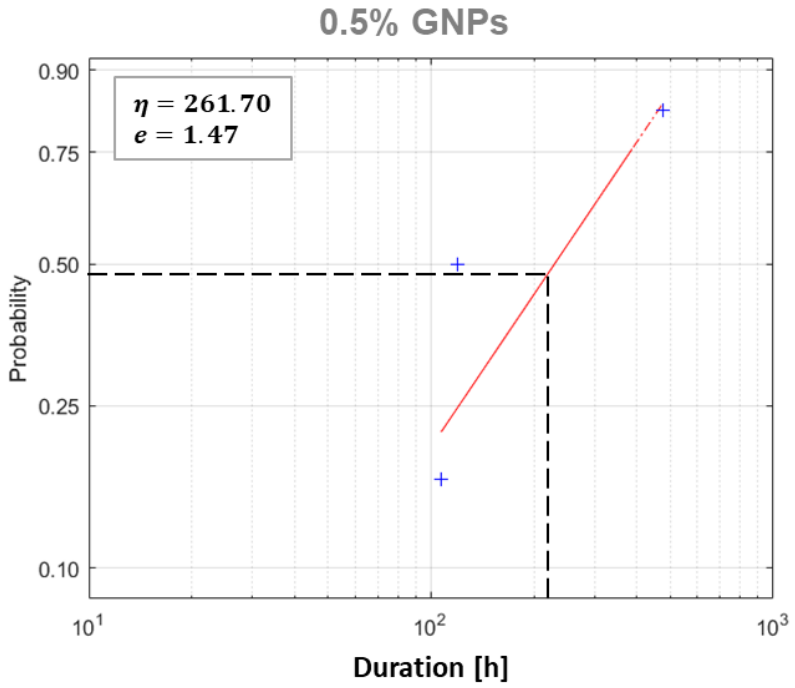

Figure 165: Experimental Weibull probability plot for the 0.5% GNPs grease duration.

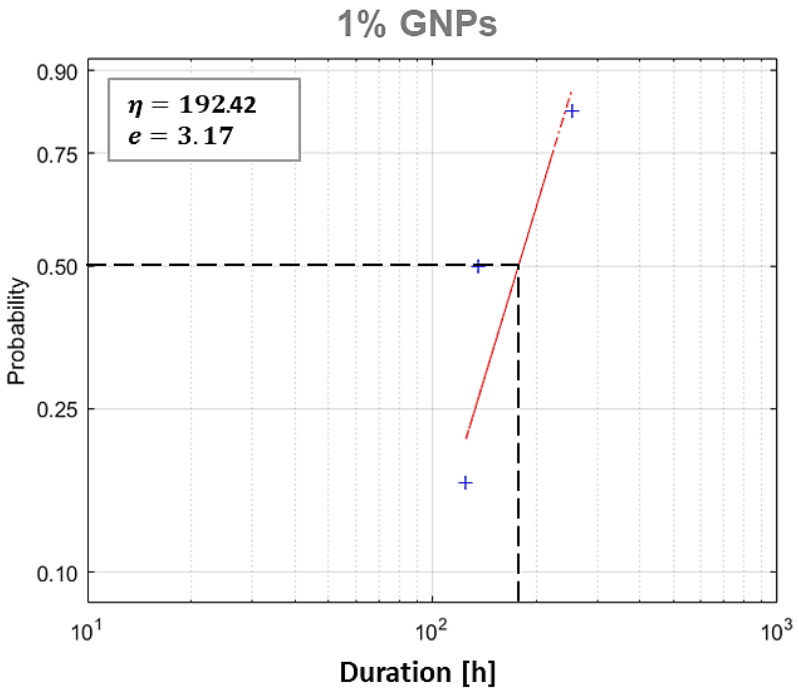

Figure 166: Experimental Weibull probability plot for the 1% GNPs grease duration.

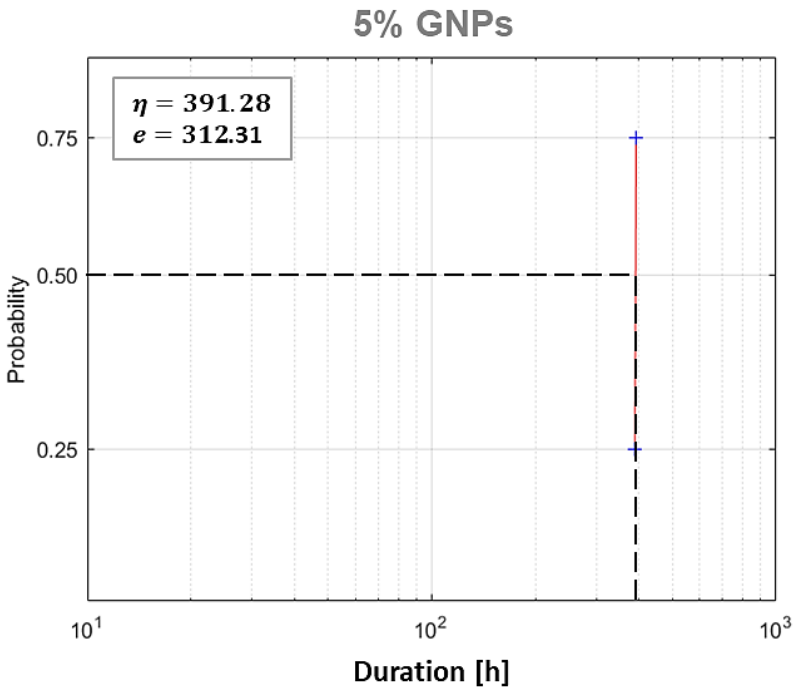

Figure 167: Experimental Weibull probability plot for the 5% GNPs grease duration.

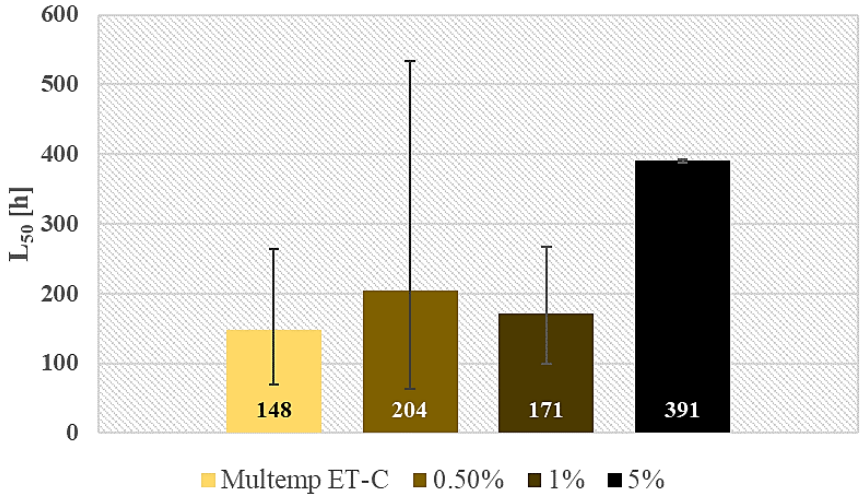

Figure 168: Effect of graphene on the average duration of the endurance tests. Error bars correspond to the 95% confidence intervals of the Weibull distribution.

Results suggested that adding 0.5% or 1 % GNPs produced scattered results. A moderate quantity of graphene could limit the test duration to about 100 h or extend it to over 450 h. The compound with 0.5% grease performed worse in terms of scattering of results: it produced both the minimum and the maximum test duration observed in the endurance tests. This effect could be related to the chaotic behaviour of grease, probably amplified by the role of the additive. On the other hand, 5% GNPs proved to be extraordinarily stable with high reproducibility of results, and the endurance tests with this compound always lasted about 400h.

To the best of the author's knowledge, this evidence was never reported in any previous research because most of the previous research on graphene greases relied on simplified laboratory tests (four-ball tests, SRV tests, or pin-on-disk tests) instead of grease endurance tests. This result also differs significantly from what was observed at the end of the pin-on-disc tests presented in Section 5.2. The effect of graphene on grease strongly depends on the kinematic of the relative motion at the interface, apparently. An optimum quantity of graphene in grease minimizes friction and wear in a pure sliding motion, and any excess of graphene worsens the tribological behaviour of the system. Instead, it seems that when rolling occurs, the higher the percentage of graphene in the grease, the more likely it is to observe a beneficial effect on the system. According to the results, a threshold quantity (between 1% and 5% GNPs) should exist for MULTEMP ET-C, above which the beneficial effect of graphene on grease life becomes systematic.

Many researchers, for instance, Niu et al. [95] Pape et al. [100], Kamel et al. [106] and Lin et al. [107], argued that graphene particles added to grease deposit onto the solid surface during the mechanical interaction producing a protective layer. Figure 169d and Figure 170d show that most of the rolling track was covered by a deposited black layer at the end of the endurance tests lubricated with the 5% GNPs grease. These deposits were easily solved with chloroform when the bearing was put into the cleaning bath, and therefore it is likely composed of dried grease thickener blended with graphene flakes. Figure 170e provides the high-magnification image of this black deposited layer taken under the optical microscope after a 5% GNPs grease test.

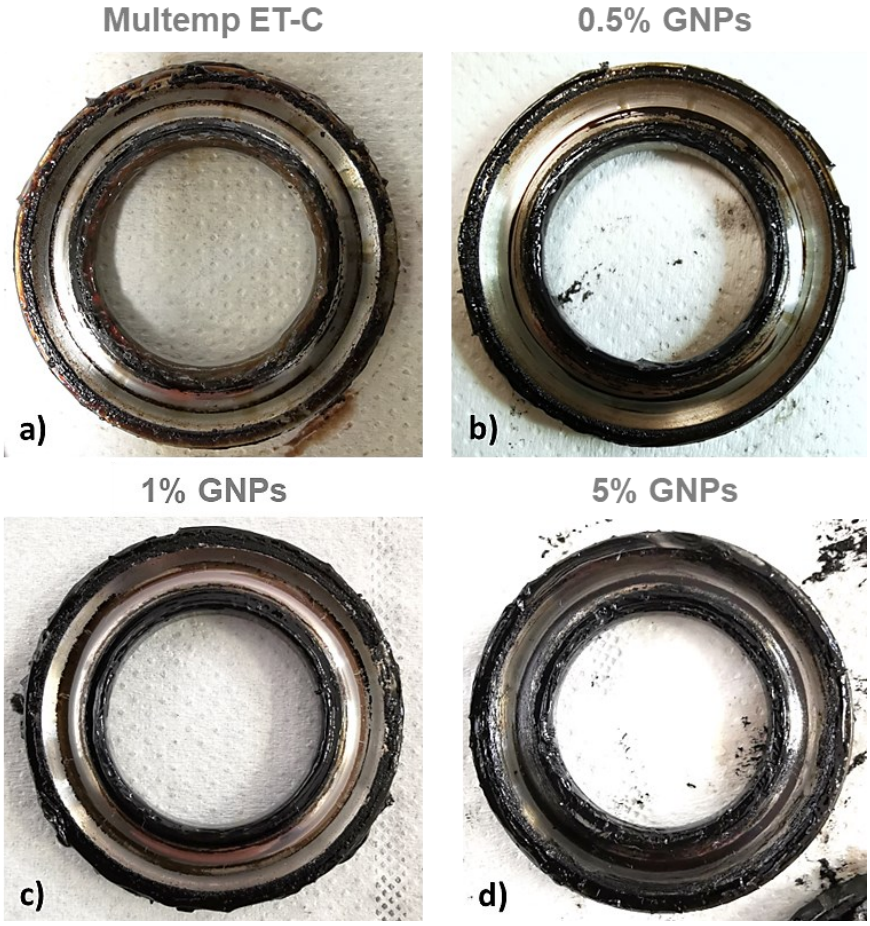

Figure 169: State of the raceway at the end of the endurance tests; (a) Test 3; (b) Test 8; (c) Test 10; (d) Test 9.

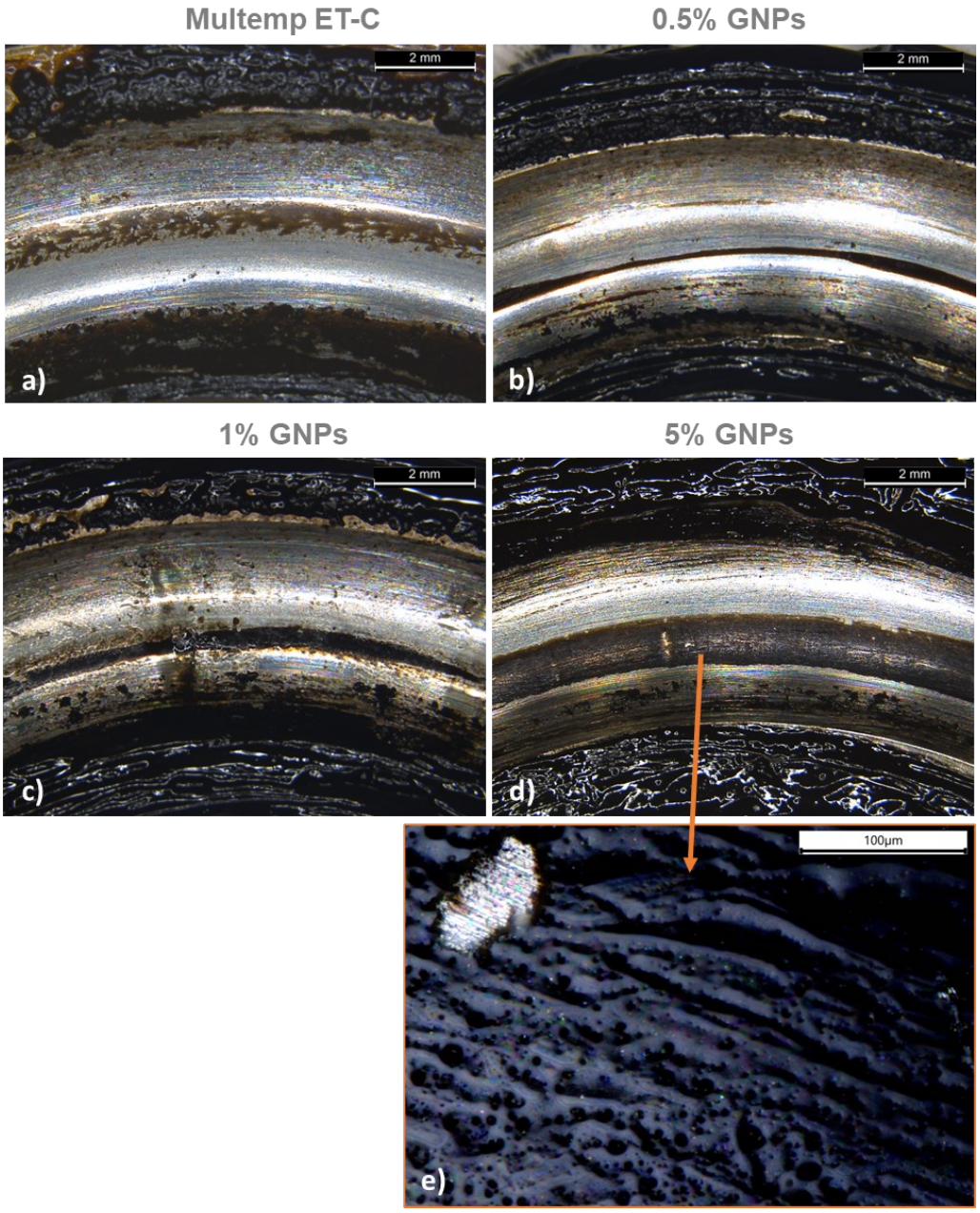

Figure 170: Detailed view of the raceway at the end of endurance tests; (a) Test 3; (b) Test 8; (c) Test 10; (d) Test 9; (e) high-magnification image of the black deposited layer likely composed of degraded thickener and graphene.

Traces of a black layer of degraded grease is also visible in Figure 169b and Figure 169c, corresponding to 0.5% and 1% GNPs in the grease. The main difference is the degree of coverage of the rolling path of the sphere. The black layer was visible mainly at the outer border of the rolling path, as with base grease

(Figure 169a is the appearance of the raceway groove at the end of a test with base grease for comparison). It is possible that by adding a moderate percentage of graphene, the layer of degraded grease did not settle inside the rolling path or failed before the end of the test, and traces survived just at the border of the rolling path. This scenario should be verified in the future by stopping the endurance test before the eventual grease failure to inspect the state of the raceway surface during steady-state lubrication. However, the fact that adding 0.5% and 1% GNPs sometimes reduced the grease lifetime remains somewhat surprising. It can be related to the inherent chaotic behaviour of grease lubrication, i.e., minimum yet uncontrolled differences in the initial conditions of tests. One might expect graphene to participate in lubrication even though no deposited layer settles. However, any interference with the grease lubrication mechanism by graphene should be verified in the future, although it seems unrealistic to the author. More repetitions of the endurance tests will clarify this aspect. Either Raman or IR Spectroscopic analysis inside the raceway grooves was not performed due to time constraints, and they will be performed in the future to determine the composition of the observed residual layers and the presence of graphene.

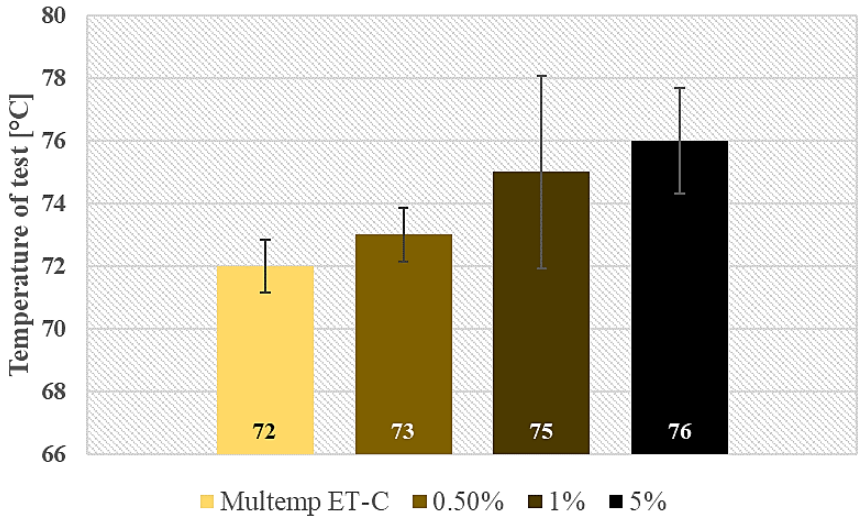

Figure 171: Effect of graphene on the average temperature of 51104 bearing during endurance tests.

As to temperature, Figure 171 indicates how the steady-state temperature of 51104 bearings is affected by the presence of graphene in the present testing conditions. It is worth recalling here that tests were carried out under active air cooling because the rotation speed selected to run the tests was higher than the

thermal reference speed of the bearing. Cooling was necessary to stabilize the temperature to a value comparable to the typical working conditions of industrial bearings. All the tests were performed with cooling fans operated at a fixed speed to ensure the repeatability of the test conditions.

It is possible to infer from Figure 171 that a systematic steady-state temperature increase resulted from the increased percentage of nano-additive. Although a reduction of the bearing temperature was expected due to the increased thermal conductivity (see Figure 90), viscous losses may have prevailed due to the increase in consistency and apparent viscosity determined by the nano-additive. The research works by Fu et al. [92], Wang et al. [102], Mohamed et al. [108], and Singh et al. [103] proved that the apparent viscosity of grease is expected to increase with increasing the percentage of a solid additive. Wang et al. [98] also pointed out that the addition of graphene flakes makes the fibrous microstructure of the thickener more compact, resulting in higher flow resistance. Higher rolling friction torque due to the increased flow resistance of dense grease may have caused higher losses during endurance tests.

Interestigly, Figure 171 also correlated with the results of rolling-raceways tests presented in Figure 112 (Section 5.3), although rolling-raceway tests were carried out under different loads and temperatures than grease endurance tests.

The temperature charts in Figure 172 and Figure 173 revealed that chaotic temperature fluctuations occurred with 0.5% GNPs and 1% GNPs grease before the eventual failure of the lubrication mechanism (similar to Figure 157). No chaotic fluctuations were observed when 5% GNPs grease was applied to the bearing (Figure 164), and grease failure followed a single progressive temperature increase until the stop condition was reached. The ECR chart of Test 9, shown in Figure 175, reflected the thermal behaviour of this grease compound closely. The contact resistance progressively increased throughout the test, and no conduction events were observed except at the test shutdown. This experimental evidence suggests that the black deposited layer of Figure 170c settled (and maybe progressively thickened) during the 5% GNPs test. It likely contributed to separating the rolling bodies and the raceway, thus extending the duration of grease.

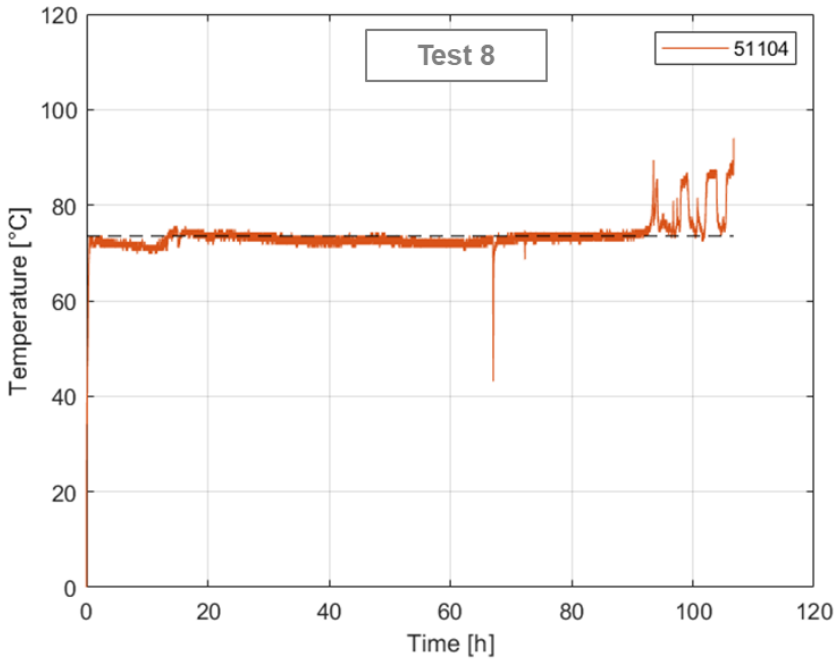

Figure 172: Temperature chart of Test 8 lubricated with 0.5% GNPs grease.

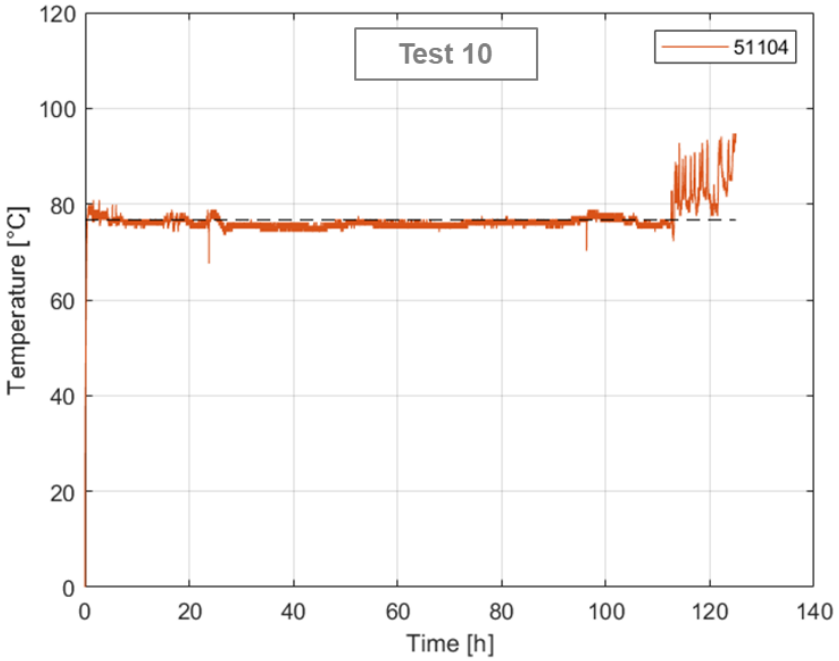

Figure 173: Temperature chart of Test 10 lubricated with 1% GNPs grease.

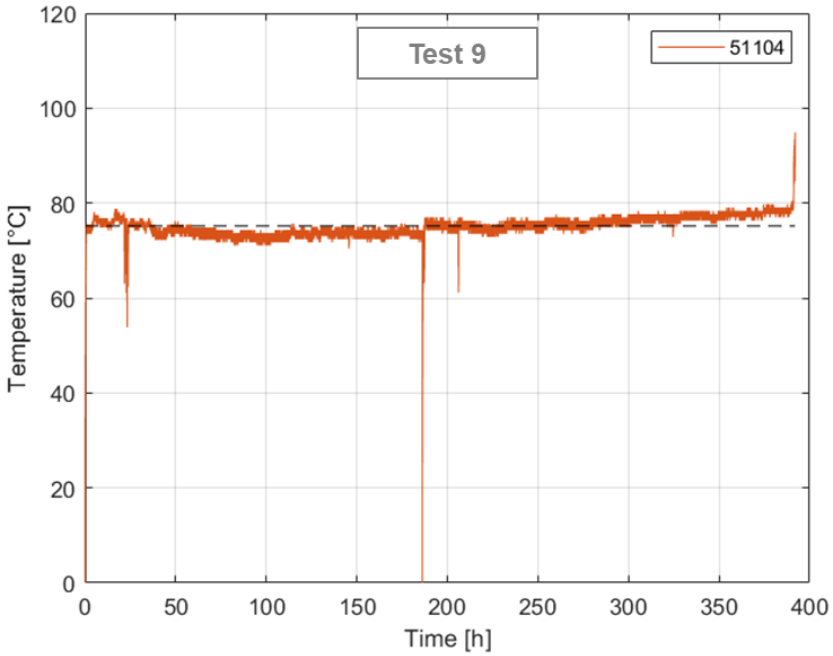

Figure 174: Temperature chart of Test 9 lubricated with 5% GNPs grease.

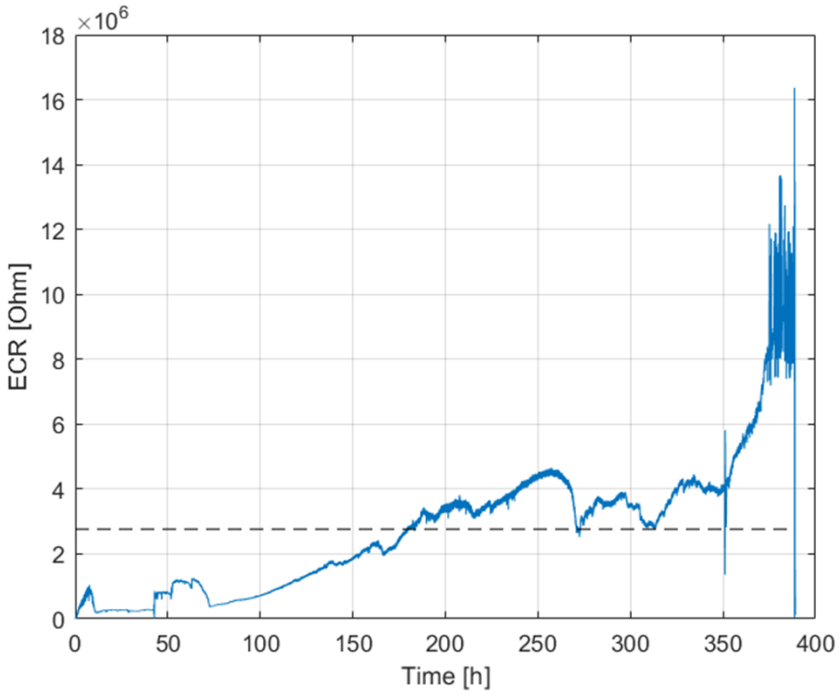

Figure 175: ECR chart recorded during Test 9. Contact resistance progressively increases as long as the temperature remains stable.

As already pointed out, the grease compounds with 0.5% and 1% GNPs produced high scattering in terms of grease endurance. Such scattering can be associated with the occasional formation of a deposited layer inside the rolling track. Figure 176 shows what was observed inside the raceway groove at the end of Test 4 and Test 7, whose duration was 254h and 136h, respectively. In both tests, the bearing was lubricated by the 1% GNPs grease, but a significant share of the rolling track of spheres was covered with a dark layer in Test 4, whereas most of the rolling track was not in Test 7.

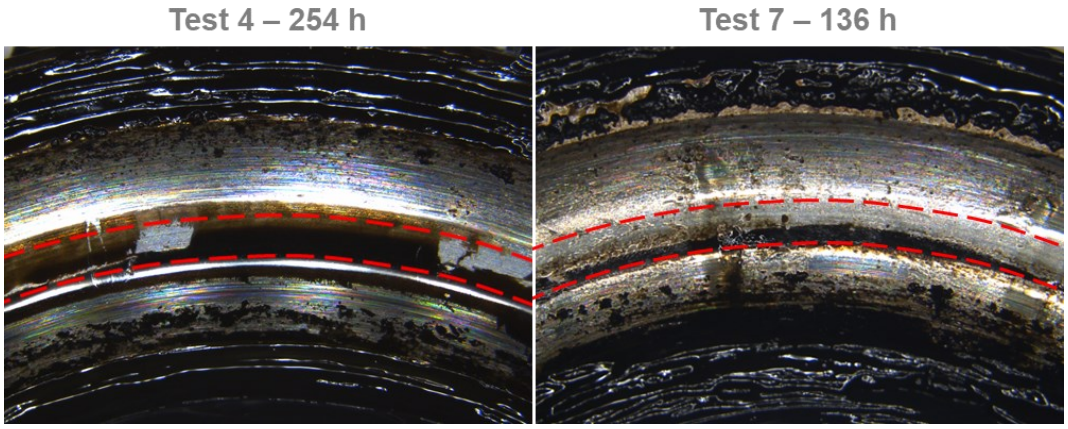

Figure 176: Traces of a deposited layer inside the rolling path of the spheres correlates with a longer useful grease life. Test 4 and Test 7 were both lubricated with 1% GNPs grease.

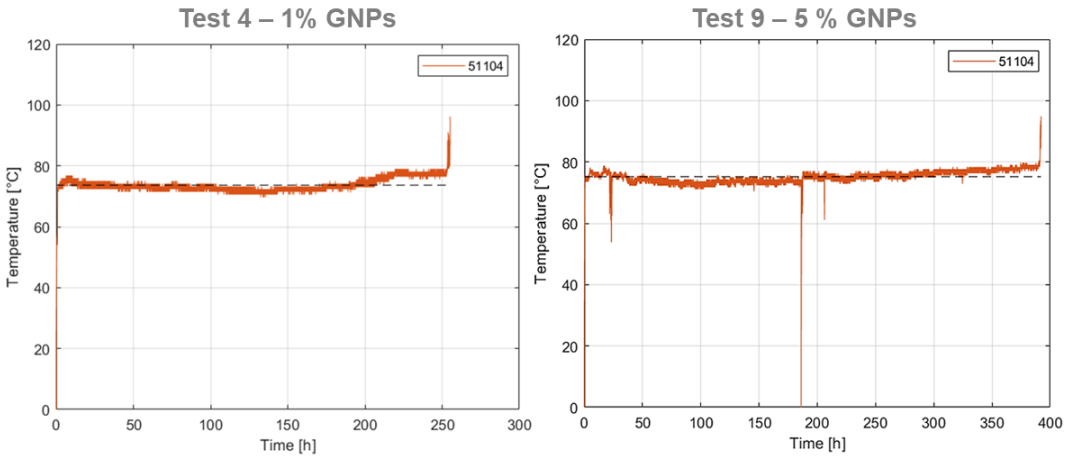

Figure 177: Chaotic temperature fluctuations did not occur when a deposited layer settled inside the rolling track.

The temperature chart of Test 4 was also extraordinarily similar to the tests lubricated by the 5% GNPs grease and featured a single temperature increment to 95°C by the end of the test. Besides, the same scenario appeared with Test 11

compared to Tests 8 and 5 running with the 0.5% GNPs grease. A significantly prolonged test duration with smooth running, stable temperature and increasing ECR values was obtained because of the settling of a deposited layer of dried grease rich in graphene flakes, which was not observed in Tests 8 and 5. These pieces of evidence further support the conclusion that a systematic dependence exists between the useful grease life, the enhancement of the lubrication mechanism and the formation of a deposited layer.

Microscopic inspection inside the raceway grooves and profilometric measurements were performed after a deep cleaning with chloroform and acetone. As to the raceway grooves profile, no differences were detected by comparing the profile before and after the test, like with base grease.

Under the microscope, the appearance of the rolling track strongly depended upon the percentage of graphene in grease. Figure 178 shows that plastic deformation and micro-adhesion occurred at the end of the tests with 0.5% GNPs grease (and short duration) as with base grease (see for comparison Figure 162c). On the other hand, the raceways of the bearings lubricated with the 1% and 5% GNPs grease maintained a surface texture like that before the tests (Figure 163). Machining marks remained visible inside the raceway groove, suggesting that graphene alleviated surface yielding. The similarities between the surface morphology observed in Figure 178d (Test 7 – 1% GNPs – 136h) and Figure 178f (Test 6 – 5% GNPs – 392 h) seemingly contradict the other outcomes of the endurance tests, i.e., the evolution of temperature, the ECR values and the time to failure of grease. This evidence supports the hypothesis that graphene plays a role in separating the rolling elements from the raceway if the percentage exceeds 1% wt., even without forming a deposited protective layer of dried grease. In other words, graphene nano-platelets should be dragged inside the contact site as suspended particles in bleeding oil and participate in the starved film lubrication mechanism preventing micro-adhesion between the asperities.

More repetitions of these tests and SEM analysis are needed to clarify these aspects related to the beneficial role of graphene.

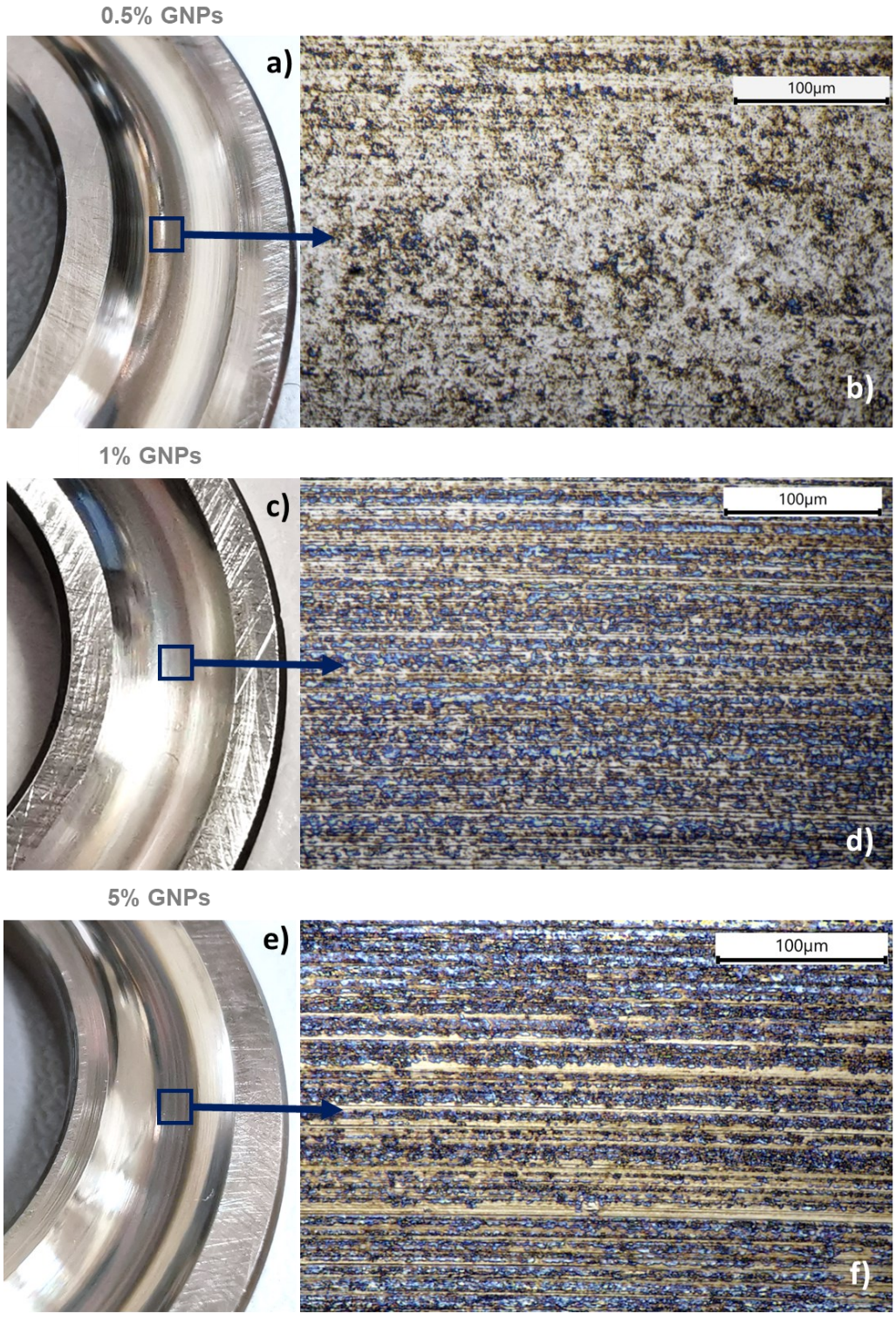

Figure 178: Appearance of the rolling track (in the middle of the raceway groove of the rotating ring) under the optical microscope; (a-b) Test 5, (c-d) Test 7, (e-f) Tests 6.

6.4 Conclusions and future perspective

The results presented in Sections 6.3.3 and 6.3.4 indicated that graphene impacts the useful life of grease. 5% GNPs was always highly favourable, and the useful life of the base grease increased to about 390 h consistently. This beneficial effect correlated with the settling of a deposited dark layer of dried grease (likely rich in graphene flakes) inside the rolling track, which avoided temperature fluctuations from metal-to-metal contacts and contributed to the lubrication mechanism of grease.

1% GNPs seemed to be a threshold percentage for MULTEMP ET-C grease. The solid nano-additive produced very scattered results when the content in GNPs was lower than or equal to 1%, especially with 0.5% GNPs. Sometimes the endurance was improved and sometimes reduced, following a chaotic behaviour. Stopping the endurance tests before the eventual grease failure is a promising strategy for inspecting the state of the raceway during steady-state lubrication. This verification will allow assessing whether a layer of degraded thickener ever forms if lubrication occurs with a moderate percentage of graphene in the grease. If so, this layer must have failed before the end of tests because few traces survived just at the border of the rolling track when the grease endurance was short.

EDS analysis and Raman (or FTIR) spectroscopic analysis should also be performed inside the rolling track in the future to determine the composition of the layer deposited inside the raceway groove. The results of these analyses will also clarify whether the settling of a deposited layer above 1% GNPs outweighs any other possible, yet unidentified, interplay between the oil-bleeding lubrication mechanism and the presence of graphene nano-platelets dragged into the contact.

In-line IR thermal measurements were planned but never carried out due to time constraints. Monitoring the temperature of grease reservoirs may provide an understanding of the replenishment mechanism of the track. Helpful information on the thermo-rheological behaviour of graphene-grease compounds is also expected.

Many more repetitions of the endurance tests are necessary to confirm the L_{50}^{exp} values thus obtained, in any case. The chaotic nature of grease lubrication [3] implies that grease life may strongly depend on slight variations in the initial conditions of the endurance tests, e.g., minor variations in initial filling quantity,

the initial distribution of grease, misalignments of the test bearing. Moreover, grease is systematically expelled radially from the bearing due to centrifugal effects, and in some tests, grease was ejected more than in others. The quantity of available grease clanged on the rotating ring and the cage might play a role in determining grease life, and this role should be verified in the future.

Conclusions

In this PhD thesis, graphene was investigated as a material to produce nano-coatings for dry sliding tribo-electrical application and as an additive for conventional lubricating grease.

Section 3 investigated the tribological performance of graphene-coated aluminum alloy and graphene-coated copper. Four synthesis methods were compared, including the direct growth of CVD graphene on the end samples for tribological tests, a technique rarely reported in the previous scientific literature. The results proved that graphene nano-sheets obtained from the self-assembly of GNPs are the most promising form of graphene among those investigated, whereas direct growth of graphene failed and was discarded in the end.

The improvement in terms of friction observed in sliding pin-on-disc tests was limited which suggests that these nano coatings are not suited for applications where gross sliding is involved. They may serve instead contacts subject to fretting and micro sliding, which will be the topic of future investigations beyond the results presented in this PhD thesis. The impact on sliding wear varied depending on the substrate material and the synthesis process, and a significative beneficial reduction of wear was observed with self-assembled coatings on copper substrate although the limited lifetime of the coating itself. The main issue which limits the performance of these nano coatings remains their low endurance due to the weak adhesion to the substrate. Therefore, enhancing adhesion is expected to be a promising strategy to let even thinner graphene layers last longer at the interface.

Sections 5 and 6 presented the results of an extended experimental investigation carried out with graphene-grease compounds based on a commercial bearing grease enriched with an increasing percentage of graphene nano-platelets as a functionalizing additive. The performance of these grease compounds in terms of friction and wear was compared to that of base grease through tribo-thermo-electrical pin-on-disc tests and through a special test setup developed for simplified friction tests on small-sized thrust ball bearings with a pin-on-disc tribometer. The latter method, developed within the framework of this PhD

project, was intended to allow measuring friction in grease-lubricated bearings without resorting to specific test rigs.

The original results of this research proved that a little quantity of graphene in the grease could reduce the average CoF of sliding point contacts and, consequently, the contact temperature compared to base grease. However, no significant correlation between the improvement of the grease thermal properties and the inherent tribological behavior of the system could be inferred. Augmentation of the tribological results by monitoring the ECR values suggested that the nano-additive made the starved boundary lubrication regime more effective and thicker and protected the surface from detrimental adhesion-abrasion degradation. However, an overly high graphene content must be avoided as it interferes with the lubrication mechanism.

The results of the rolling-in-raceway tests carried out through the special setup for friction in bearings were validated against the SKF model of friction and proved that enriching grease with GNPs is generally not beneficial on rolling friction. The higher the content of graphene in the grease, the higher the friction torque needed to rotate the bearing, at least in the specific test conditions being explored for this research. However, efforts are needed to improve this simplified method to simulate better the actual operative conditions of grease-lubricated industrial bearings, such as the operative temperature and the applied load.

Section 6 presented the in-house design of a test rig for grease endurance tests and the related results obtained from endurance tests with the same graphene-grease compounds. The mechanical layout of the test rig was optimized to simplify the system and to reduce costs while allowing a comprehensive monitoring of the bearings used to carry out the tests in terms of temperature, ECR, applied load and vibration level.

The results of the preliminary experimental campaign presented in this PhD thesis revealed that graphene impacts the useful life of grease and, as opposed to what was observed in laboratory tests, the highest content of the additive brought about the highest benefit in terms of grease life. When 5% wt. GNPs is added to grease the useful life of the lubricant increases from about 150-200 h to about 390 h. The post-mortem inspections and the ECR signal across the bearing showed that a beneficial layer of dried grease rich in graphene flakes deposited inside the rolling track; the higher the content in graphene, the more likely is the settling of this protective layer. Graphene was also able to limit the chaotic temperature

fluctuations due to metal-to-metal contacts in the event of failure of the lubrication mechanism.

To the best of the author's knowledge, no similar experimental results based on long-term endurance tests with graphene-grease compounds have ever been presented in the scientific literature. However, the original results presented in this work should be regarded as preliminary results because the dataset available due to time constraints was limited. Many more repetitions of the tests are necessary to confirm the L_{50}^{exp} values that were experimentally determined to consider the inherently chaotic nature of the grease lubrication mechanism.

References

[1] G. Stachowiak e A. Batchelor, Engineering Tribology, 4th Edition a cura di, Butterworth-Heinemann, 2013.

[2] F. Bowden e D. Tabor, Friction and Lubrication of Solids, Part 1, Oxford University Press, 1954.

[3] M. Lugt, S. Velickov e J. Tripp, «On the Chaotic Behavior of Grease Lubrication in Rolling Bearings,» *Tribology Transactions,* vol. 52, n. 5, pp. 581-590, 2009.

[4] P. Cann, «Thin-Film Grease Lubrication,» *Proc. Inst. Mech. Eng., Part J, Journal of Engineering Tribology,* vol. 213, pp. 405-416, 1999.

[5] E. Booser e D. Wilcock, «Minimum oil requirements of ball bearings,» *Lubrication Engineering,* vol. 9, 1953.

[6] H. O. J. H. E. Astrom, «Lubricating Grease Replenishment in an Elastohydrodynamic Point Contact,» *J. Tribol.,* vol. 115, n. 3, pp. 501-506, 1994.

[7] Y. Chiu, «An analysis and prediction of lubricant film starvation in following contact systems.,» *ASLE Trans.,* vol. 17, pp. 22-35, 1974.

[8] R. O'Halloran, J. Kolfenbach e H. Leland, «Grease Flow in Shielded Bearings,» *Lubrication Engineering,* vol. 14, pp. 104-107, 1958.

[9] P. M. Cann, «Starvation and reflow in a grease-lubricated elastohydrodynamic contact,» *STLE Tribology Transactions,* vol. 52, pp. 581-590, 2009.

[10] N. Scarlett, «Use of grease in rolling bearings,» *Proc. Instn Mech. Engr,* vol. 182(3A), pp. 585-593, 1967.

[11] P. Lugt, A. Van den Kommer, H. Lindgren e C. Roth, «The R0F+ methodology for grease life testing,» SKF Industries, 2013.

[12] S. Poon, «An Experimental Study of Grease in Elastohydrodynamic Lubrication,,» *Transactions ASME, Journal of Lubrication Technology,* vol. 94, pp. 27-34, 1972.

[13] P. Cann, J. Doner, M. Webster e e. al., «Grease degradation in ROF bearing tests,» *STLE Tribology Transactions,* vol. 50, n. 2, pp. 187-197, 2007.

[14] V. Wikström e B. Jacobson, «Loss of lubricant from oil-lubricated near-starved spherical roller bearings,» *Proceedings of the Institution of Mechanical Engineers. Part J: Journal of Engineering Tribology,* vol. 21, n. 1, p. 51–55, 1997.

[15] T. Cousseau, B. Graça, A. Campos e J. Seabra, «Grease Aging Effects on Film Formation under Fully-Flooded and Starved Lubrication,» *Lubricants,* vol. 3, n. 2, pp. 197-221, 2015.

[16] N. De Laurentis, A. Kadiric, P. M. Lugt e P. M. Cann, «The influence of bearing grease composition on friction in rolling/sliding concentrated contacts,» *Tribol. Int. 2016,* vol. 94, p. 624−632, 2016.

[17] OECD - Research Group on Wear of Engineering Materials, «Glossary of terms and definitions in the field of friction, wear and lubrication : Tribology,» Paris, 1969.

[18] F. Wood, «Summary on the Role and Analysis of Wear in Failures,» *J Test Eval,* vol. 22, n. 470–3, 1994.

[19] R. Bayer, Mechanical Wear Fundamental and Testing, New York, : Marcel

Dekker Inc., 2004.

[20] E. Whitenton e P. Blau, «A comparison of methods for determining wear volumes and surface parameters of spherically tipped sliders,» *Wear,* vol. 124, pp. 291-309, 1988.

[21] N. Fillot, I. Iordanoff e Y. Berthier, «Wear modelling and the third body concept,» *Wear,* vol. 262, p. 949–957, 2007.

[22] K.-H. Zum Gahr, Microstructure and wear of materials, Elsevier, 1987.

[23] G. Straffelini, Friction and Wear Methodologies for Design and Control, Springer International , 2015.

[24] B. Bhushan, Introduction to Tribology, 2nd Edition, John Wiley&Sons, 2013.

[25] K. Kato e K. Adachi, «Wear Mechanisms,» in *Modern tribology Handbook*, CRC Press, 2011.

[26] E. Rabinowicz, Friction and wear of materials, John Wiley & Sons, 1995.

[27] P. Uzoma, H. Hu, M. Khadem e O. Penkov, «Tribology of 2D Nanomaterials: A Review,» *Coatings,* vol. 10, n. 897, 2020.

[28] S. Zhang, T. Ma, A. Erdemir e Q. Li, «Tribology of two-dimensional materials: From mechanisms to modulating strategies.,» *Materials Today,* vol. 26, p. 67–86, 2019.

[29] K. Shinjo e M. Hirano, «Dynamics of friction: Superlubric State,» *Surface Science,* vol. 283, p. 473–478, 1993.

[30] M. Marian, D. Berman, A. Rota e e. al., «Layered 2D Nanomaterials to Tailor Friction and Wear in Machine Elements—A Review,» *Adv. Mater.*

Interfaces, vol. 9, n. 2101622, 2022.

[31] D. Berman, A. Erdemir e A. Sumant, «Graphene: a new emerging lubricant,» *Mater. Today,* vol. 17, n. 1, pp. 31-42, 2014.

[32] P. Shi, J. Guo, X. Liang e e. al., «Large-scale production of high-quality graphene sheets by a non-electrified electrochemical exfoliation method,» *Carbon,* vol. 126, pp. 507-513, 2018.

[33] J. Stafford, A. Patapas e N. Uzo, «Towards scale-up of graphene production via nonoxidizing liquid exfoliation methods,» *AIChE Journal,* vol. 64, n. 9, pp. 3246-3276, 2018.

[34] S. Mohammadi, Z. Kolahdouz, S. Darbari e e. al., «Graphene formation by unzipping carbon nanotubes using a sequential plasma-assisted processing,» *Carbon,* vol. 52, pp. 451-463, 2013.

[35] Y. Chen, H. Zhao e L. Sheng, «Mass-production of highly-crystalline few-layer graphene sheets by arc discharge in various H 2-inert gas mixtures,» *Chemical Physics Letters,* vol. 538, pp. 72-76, 2012.

[36] F. Caicedo, E. Lopez, A. Agarwal e e. al., «Ball-milling of graphite particles,» *Diamond and Related Materials,* vol. 109, n. 108064, 2020.

[37] A. Geim e K. Novoselov, «The rise of graphene,» *Nat. Mater.,* vol. 6, pp. 183-191, 2007.

[38] K.-Y. Shin, J.-Y. Hong e J. Jang, «Micropatterning of graphene sheets by inkjet printing and its wideband dipole-antenna application,» *Advanced Materials,* vol. 23, n. 18, pp. 2113-2118, 2011.

[39] D. Berman, S. Deshmukh, S. Sankaranarayanan e ., «Extraordinary Macroscale Wear Resistance of One Atom Thick Graphene Layer,» *Advanced Functionals Materials,* 2014.

[40] J. Lee, S. Park e J. Choi, «Electrical Property of Graphene and Its Application to Electrochemical Biosensing,» *Nanomaterials,* vol. 9, n. 297, 2019.

[41] X. Dong, W. Peng, W. Fang e e. al., «Growth of large-sized graphene thin-films by liquid precursor-based chemical vapor deposition under atmospheric pressure,» *Carbon,* vol. 49, n. 11, p. 3672–3678, 2011.

[42] O. Penkov, H.-J. Kim e D.-E. Kim, «Tribology of graphene: A review,» *Int. J. Precis. Eng. Manuf,* vol. 15, n. 3, pp. 577-585, 2014.

[43] R. Davis, H. Palmour e R. Porter, Emergent Process Methods for High-Technology Ceramics, New York, USA: Springer, 1984.

[44] B. Hu, H. Ago, C. Orofeo e Y. Ogawac, «On the nucleation of graphene by chemical vapor deposition,» *New J. Chem.,* vol. 36, pp. 73-77, 2012.

[45] M.-S. Won, O. Penkov e D.-E. Kim, «Durability and degradation mechanism of graphene coatings deposited on Cu substrates under dry contact sliding,» *Carbon,* vol. 54, pp. 472-481, 2013.

[46] Z. Ullah, S. Riaz, Q. Li e e. al., «A comparative study of graphene growth by APCVD, LPCVD and PECVD,» *Mater. Res. Express,* vol. 5, n. 3, 2018.

[47] P. Li, Z. Li e J. Yang, «Dominant Kinetic Pathways of Graphene Growth in Chemical Vapor Deposition: The Role of Hydrogen,» *J. Phys. Chem. C,* vol. 121, n. 46, p. 25949–25955, 2017.

[48] V. Pham, «Direct Growth of Graphene on Flexible Substrates toward Flexible Electronics: A Promising Perspective,» in *Flexible Electronics*, 2018, p. 122.

[49] A. Mura, H. Wang, F. Adamo e J. Kong, «Graphene coatings to enhance the tribological performance of steel,» *Mech. Adv. Mater. Struct.,* 2019.

[50] A. Mura, G. Canavese, E. Goti, P. Rivolo e e. al., «Effect of different types of graphene coatings on friction and wear performance of aluminum alloy,» *Mech. Adv. Mater. Struct.,* 2020.

[51] X. Li e e. al., «Large-Area Ultrathin Graphene Films by SingleStep Marangoni Self-Assembly for Highly Sensitive Strain Sensing Application,» *Adv. Funct. Mater.,* vol. 26, n. 9, pp. 1322-1329, 2016.

[52] A. Mura, F. Adamo, H. Wang e e. al., «Investigation about tribological behavior of ABS and PC-ABS polymers coated with graphene,» *Tribol. Int.,* vol. 134, pp. 335-340, 2019.

[53] S. Zhang, B. Arfaei e Z. Chen, «Friction force reduction for electrical terminals using graphene coating,» *Nanotechnology,* vol. 32, n. 3, 2021.

[54] B. Yildiz, A. Balkanci, I. Ovali e e. al., «Investigation of tribological behaviours of graphene-coated journal bearing,» *TRIBOLOGY - MATERIALS, SURFACES & INTERFACES,* 2018.

[55] D. Berman, A. Erdemir e A. Sumant, «Few layer graphene to reduce wear and friction on sliding steel surfaces,» *Carbon,* vol. 54, pp. 454-459, 2013.

[56] Z. Shi, P. Shum, A. Wasy e e. al., «Tribological performance of few layer graphene on textured M2 steel surfaces.,» *Surf Coat Tech.,* vol. 296, pp. 164-170, 2016.

[57] S. Bhowmick, S. Banerji e A. Alpas, «Role of humidity in reducing sliding friction of multilayered graphene,» *Carbon,* vol. 87, pp. 374-384, 2015.

[58] S. Novoselov, «Graphene: materials in the flatland (Nobel Lecture),» *Angew. Chem. Int. Ed. Engl.,* vol. 50, n. 31, pp. 6986-7002, 2011.

[59] C. Schoff, «Coatings clinic: Electrical properties II - Conductivity of solid coatings,» *CoatingsTech,* vol. 4, n. 7, 2007.

[60] S. Wu, S. Tian, P. Menezes e G. Xiong, «Carbon solid lubricants: role of different dimensions,» *The International Journal of Advanced Manufacturing Technology,* vol. 107, p. 3875–3895, 2020.

[61] «Difference Between Graphene Oxide and Reduced Graphene Oxide,» 2018. [Online]. Available: https://www.differencebetween.com/difference-between-graphene-oxide-and-reduced-graphene-oxide/.

[62] «ASTM G99-17, Standard Test Method for Wear Testing with a Pin-on-Disk Apparatus, ASTM International, West Conshohocken, PA, 2017, www.astm.org».

[63] R. Nair, P. Blake e A. Grigorenko, «Fine Structure Constant Defines Visual Transparency of Graphene,,» *Science,* vol. 320, n. 5881, pp. 1308-1308, 2008.

[64] A. Reina, X. Jia, H. Ho e e. al., «Large Area, Few-Layer Graphene Films on Arbitrary Substrates by Chemical Vapor Deposition,» *Nano Lett.,* vol. 9, n. 1, pp. 30-35, 2009.

[65] A. Ferrari, J. Meyer, V. Scardaci, C. Casiraghi e e. al., «Raman Spectrum of Graphene and Graphene Layers,» *Physical Review Letters,* vol. 97, n. 187401, 2006.

[66] C. Su, A. Lu, Y. Xu, F. Chen e e. al., «High-Quality Thin Graphene Films from Fast Electrochemical Exfoliation,» *ACS Nano,* vol. 5, n. 3, p. 2332–2339, 2011.

[67] R. Moharana, S. Sengar, B. Badhan e e. al., «Tribological Behaviour of Graphene Coated Bearing Steel (EN31),» *Phys.: Conf. Ser.,* vol. 1240, n. 012040, 2019.

[68] C. Park, D. Jung e E.-J. Chun, «Effect of laser shock peening without coating on fretting corrosion of copper contacts,» *Applied Surface Science,*

vol. 514, n. 145917, 2020.

[69] «https://www.italweber.it/files/catalogue/pdf/14_Isoflex.pdf».

[70] D. Berman, A. Erdemir, A. Sumant e e. al., «Reduced wear and friction enabled by graphene layers on sliding steel surfaces in dry nitrogen,» *Carbon,* vol. 59, pp. 167-175, 2013.

[71] D. Berman, A. Erdemir e A. Sumant, «Reduced wear and friction enabled by graphene layers,» *Carbon,* vol. 59, pp. 167-175, 2013.

[72] R. Leach, Characterisation of Areal Surface Texture, Berlin: Springer, 2013.

[73] A. Waterworth, Quantitative characterisation of surface finishes on stainless steel sheet using 3D surface topography analysis, 2006.

[74] Maculotti, G., E. Goti, G. Genta, L. Mazza e e. al., «Uncertainty-based comparison of conventional and surface topography-based methods for wear volume evaluation in pin-on-disc tribological tests,» *Tribology International,* n. 107260, 2022.

[75] F. Long, P. Y. W. Yasaei, A. Salehi-Khojin e R. Shahbazian-Yassar, «Anisotropic Friction of Wrinkled Graphene Grown by Chemical Vapor Deposition,» *ACS Applied Materials and Interfaces,* vol. Volume 9, n. Issue 24, pp. 20922 - 20927, June 2017.

[76] R. Paronyan, E. Pigos, G. Chen e A. R. Harutyunyan, «Formation of Ripples in Graphene as a result of Interfacial Instabilities,» *ACS Nano,* vol. 5, n. 12, p. 9619–9627, 2011.

[77] C. Comanescu, «Single-layer graphene Raman bands modifications as result of transfer from copper foil to oxidized silicon or quartz substrates,» *2016 International Semiconductor Conference (CAS),* pp. 49-52, 2016.

[78] Z. Huang, S. Chen, Q. Lin, Z. Ji, P. Gong, Z. Sun e B. Shen, «Microscopic Mechanisms Behind the High Friction and Failure,» *Langmuir,* vol. 37, pp. 6776-6782, 2021.

[79] C. Lee, Q. Li, W. Kalb, X.-Z. Liu e e. al., «Frictional Characteristics of Atomically Thin Sheets,» *Science,* vol. 328, 2010.

[80] Q. Li, C. Lee, R. Carpick e J. Hone, «Substrate effect on thickness-dependent friction on graphene,» *Phys. Status Solidi B,* vol. 247, n. 11-12, p. 2909–2914, 2010.

[81] X. Zeng, Y. Peng e H. Lang, «A novel approach to decrease friction of graphene,» *Carbon,* vol. 118, pp. 233-240, 2017.

[82] A. Ayyagari, K. Mutyala e A. Sumant, «Towards developing robust solid lubricant operable in multifarious environments,» *Nature,* vol. 10, n. 15390, 2020.

[83] S. Wu, S. Tian, P. Menezes e G. Xiong, «Carbon solid lubricants: role of different dimensions,» *The International Journal of Advanced Manufacturing Technology,* vol. 107, pp. 3875–3895,, 2020.

[84] B. G. A. J. A. Manu, «Tribological properties of 2D materials and composites- A review of recent advances,» *Materials,* vol. 14, n. 7, 2021.

[85] A. Rosenkranz, M. Righi, A. Sumant e e. al., «Perspectives of 2D MXene Tribology,» *Adv. Mater.,* vol. 35, n. 2207757, 2023.

[86] Z. Ali, A. Takhakh e M. Al-Waily, «A review of use of nanoparticle additives in lubricants to improve its tribological properties,",» *Materials Today: Proceedings,* vol. 52, pp. 1442 - 1450, 2022.

[87] A. Senatore, V. D'Agostino, V. Petrone e e. al., «Graphene oxide nanosheets as effective friction modifier oil lubricant: materials, methods,

and tribological results,» *ISRN Tribol,* pp. 1- 9, 2013.

[88] J. Mao, G. Chen, J. Zhao e e. al., «An investigation on the tribological behaviors of steel/copper and steel/steel friction pairs via lubrication with a graphene additive,» *Friction,* vol. 9, n. 2, pp. 228-238, 2021.

[89] G. Li, S. Yi, N. Li, W. Pan e e. al., «Quantitative analysis of cooling and lubricating effects of graphene oxide nanofluids in machining titanium alloy Ti6Al4V,» *Journal of Materials Processing Technology,* vol. 271, pp. 584-598, 2019.

[90] B. Chu, E. Singh, N. Koratkar e J. Samueal, «Graphene-enhanced environmentally benign cutting fluids for high-performance micro-machining applications,» *Journal of Nanoscience and Nanotechnology,* vol. 13, n. 8, pp. 5500-5504, 2013.

[91] H. Hong, D. Thomas e A. Waynick, «Carbon nanotube grease with enhanced thermal and electrical conductivities,» *Journal of Nanoparticle Research,* Vol. %1 di %212, Issue 2, pp. 529 - 535, 2010.

[92] H. Fu, G. Yan, M. Li, H. Wang e e. al., «Graphene as a nanofiller for enhancing the tribological properties and thermal conductivity of the base grease,» *The Royal Society of Chemistry,* vol. 9, p. 42481–42488, 2019.

[93] B. Hamrock, S. Schmid e B. O. Jacobson, Fundamental of Fluid film lubrication, 2nd Edition a cura di, New York: Marcel Dekker Inc., 2004.

[94] M. Xie, J. Cheng, C. Huo e G. Zhao, «Improving the lubricity of a bio-lubricating grease with the multilayer graphene additive,» *Tribology International,* vol. 150, n. 106386, 2020.

[95] M. Niu, J. Qu e L. Gu, «Synthesis of titanium complex grease and effects of graphene on its tribological properties,» *Tribology International,* vol. 140, n. 105815, 2019.

[96] X. Fan, Y. Xia, L. Wang e e. al., «Multilayer Graphene as a Lubricating Additive in Bentone Grease,» *Tribol. Lett.,* vol. 44, n. 3, pp. 455-464, 2014.

[97] J. Singh, D. Kumar e N. Tandon, «Tribo-Dynamics of Nanocomposite Grease Lubricated Point Contact Under Elastohydrodynamics Lubrication Regime,» *Journal of Tribology,* vol. 141, n. 031501, 2019.

[98] Y. Wang, X. Gao, J. Lin e P. Zhang, «Rheological and Frictional Properties of Lithium Complex Grease with Graphene Additives,» *Lubricants,* vol. 10, n. 57, pp. 1-13, 2022.

[99] J. Singh, G. Anand, D. Kumar e N. Tandon, «Graphene-based composite grease for elastohydrodynamic lubricated point contact,» *IOP Conf. Ser.: Mater. Sci. Eng.,* vol. 149, n. 012195, 2016.

[100] F. Pape e G. Poll, «Investigations on Graphene Platelets as Dry Lubricant and as Grease Additive for Sliding Contacts and Rolling Bearing Applications,» *Lubricants,* vol. 8, n. 3, 2020.

[101] L. S. Tang Z., «A review of recent developments of friction modifiers for liquid lubricants,» *Curr Opin Solid State Mater Sci,* vol. 18, n. 3, p. 119–139, 2014.

[102] J. Wang, X. Guo, Y. He, M. Jiang e K. Gu, «Tribological characteristics of graphene as grease additive under different contact forms,» *Tribology International,* vol. 127, p. 457–469, 2018.

[103] J. Singh, D. Kumar e N. Tandon, «Development of Nanocomposite Grease: Microstructure Flow and Tribological Studies,» *Journal of Tribology,* vol. 139, n. 5, p. 9 pages, 2017.

[104] B. Gupta, N. Kumar, K. Panda, S. Dash e A. Tyagi, «Energy efficient reduced graphene oxide additives: Mechanism of effective lubrication and antiwear properties,» *Scientific Reports,* vol. 6, n. 18372, 2016.

[105] T. Ouyang, Y. Shen, Yang, R., Liang, L. e e. al., «3D hierarchical porous graphene nanosheets as an efficient grease additive to reduce wear and friction under heavy-load conditions,» *Tribology International,* vol. 144, n. 106118, 2020.

[106] B. Kamel, A. Mohamed, M. El Sherbiny, K. Abed e M. Abd-Rabou, «Tribological properties of graphene nanosheets as an additive in calcium grease,» *Journal of Dispersion Science and Technology,* vol. 38, n. 10, pp. 1495 - 1500, 2017.

[107] B. Lin, I. Rustamov, L. Zhang, J. Luo e X. Wan, «Graphene-Reinforced Lithium Grease for Antifriction and Antiwear,» *ACS Applied Nano Materials,* vol. 3, p. 10508−10521, 2020.

[108] A. Mohamed, V. Tirth e B. Kamel, «Tribological characterization and rheology of hybrid calcium grease with graphene nanosheets and multi-walled carbon nanotubes as additives,» *Journal of Materials Research and Technology,* vol. 9, n. 3, pp. 6178-6185, 2020.

[109] G. Lundberg e A. Palmgren, «Dynamic capacity of rolling bearings,» *Acta Polytech. Mech. Eng. Ser. 1, R.S.A.E.E.,* vol. 3, n. 7, 1947.

[110] N. Londhe, N. Arakere e G. Subhash, «Effect of plasticity on the dynamic capacity of modern bearing steels,» *Tribology International,* vol. 133, p. 160–171, 2019.

[111] E. Ioannides, G. Bergling e A. Gabelli, «An analytical formulation for the life of rolling bearings,» in *Mechanical Engineering Series, Monograph 137*, Acta Polytechnica Scandinavica, 1999, p. 77.

[112] «ISO/TR 1281-2:2008 - Rolling bearings Explanatory notes on ISO281,» Geneva, 2008.

[113] T. Harris, Rolling Bearing Analysis, 4th Edition, John Wilsey & Sons Inc,

2001.

[114] D. Dowson e G. Higginson, «Elastohydrodynamics,» *Proc. Inst. Mech. Eng.,* vol. 182, n. 3A, pp. 151-167, 1967-1968.

[115] B. Hamrock e D. Dowson, «Isothermal elastohydrodynamic lubrication of point contacts — Part III — Fully flooded results,» *J. Lubric. Technol.,* vol. 99, pp. 264-276, 1977.

[116] D. Gonçalves, A. Vieira, A. Carneiro e e. al., «Film Thickness and Friction Relationship in Grease Lubricated Rough Contacts,» *Lubricants,* vol. 5, n. 34, 2017.

[117] Schaeffler Technologies AG & Co KG, «Lubrication of Rolling Bearings,» 2013.

[118] P. Lugt e F. Berens, «The Grease Life Factor concept for ball bearings,» *Tribology International,* vol. 169, n. 107460, 2022.

[119] «Kyodo Yushi - Rolling Bearing Grease,» [Online]. Available: https://www.kyodoyushi.co.jp/english/products/grease/rolling_bearing/.

[120] Y. Hu, «Conductivity and Tribological Properties of Conductive Polyaniline as Additives in Grease,» *Journal of Mechanical Engineering,* vol. 53, n. 109, 2017.

[121] Z. Cao, Y. Xia e X. Ge, «Conductive capacity and tribological properties of several carbon materials in conductive greases,",» *Industrial Lubrication and Tribology,* vol. 68, n. 5, pp. 577-585, 2016.

[122] E. Goti e F. Curà, «Friction torque in thrust ball bearings lubricated by graphene-enriched grease with a modified pin-on-disc method,» *International Journal of Mechanics and Control,* vol. 23, n. 1, 2023.

[123] SKF, Catalogo Generale Cuscinetti Volventi, SKF.com, 2021, p. 1155.

[124] «SKF Bearing Select,» [Online].

[125] T. Cousseau, B. Graça, A. Campos e J. Seabra, «Experimental measuring procedure for the friction torque in rolling bearings,» *Lubrication Science,* vol. 22, pp. 133-147, 2010.

[126] *ASTM Standard G133-05 (2010) Standard Test Method for Linearly Reciprocating Ball-on-Flat Sliding Wear. ASTM International, West Conshohocken, PA, 2016, www.astm.org.*

[127] Anton Paar TriTec SA, «Tribometer TRB User Manual,» Peseux, 2016.

[128] M. Evans, A. Richardson, L. Wang, R. Wood e W. Anderson, «Confirming subsurface initiation at non-metallic inclusions as one mechanism for white etching crack (WEC) formation,» *Tribology International,* vol. 75, pp. 87-97, 2014.

[129] H. Danielsen, F. Gutiérrez Guzmán e e. al., «FE8 type laboratory testing of white etching crack (WEC) bearing failure mode in 100Cr6,» *Wear,* vol. 434–435, n. 202962, 2019.

[130] Klüber Lubrication München SE & Co. KG, «Lubricant testing - Focusing on mechanico-dynamical tests,» München.

[131] G. Jacobs e M. Plogmann, «Rolling Bearing Lubrication and Materials,» in *Encyclopedia of Lubricants and Lubrication* , Berlin, Springer, 2014.

[132] M. Grebe e A. Widmann, «Combined Standstill Tests (Pre-damaging) and SNR-Tests,» Competence Center for Tribology - Mannheim University of Applied Sciences, 2018.

[133] S. Alegranzi, J. Gonçalves e H. Gomes, «BALL BEARING VIBRATION MONITORING FOR FAULT DETECTION BY THE ENVELOPE TECHNIQUE,» *Blucher Mechanical Engineering Proceedings,* vol. 1, n. 1, 2014.

[134] S. Niknam, V. Songmene e J. Joe Au, «Proposing a new acoustic emission parameter for bearing condition monitoring in rotating machines,» *Transactions of the Canadian Society for Mechanical Engineering,* vol. 37, n. 4, pp. 1105-1114, 2013.

[135] D. He, R. Li, M. Zade e J. Zhu, «Development and Evaluation of AE based Condition Indicators for Full Ceramic Bearing Fault Diagnosis,» *2011 IEEE Conference on Prognostics and Health Management,* pp. 1-7, 2011.

[136] L. Cao, F. Sadeghi e L.-E. Stacke, «A Wireless Sensor Telemeter for In-Situ Cage Vibration Measurement and Corroboration with Analytical Results,» *Tribology Transactions,* vol. 61, n. 6, pp. 1013-1026, 2018.

[137] B.-Q. Fan, K.-M. Lee, X. Ouyang e H.-Y. Yang, «Soft-Switchable Dual-PI Controlled Axial Loading System for High-Speed EMU Axle-Box Bearing Test Rig,» *IEEE TRANSACTIONS ON INDUSTRIAL ELECTRONICS,* vol. 62, n. 12, 2015.

[138] M. Nassef, M. Soliman, B. Nassef e e. al., «Impact of Graphene Nano-Additives to Lithium Grease on the Dynamic and Tribological Behavior of Rolling Bearings,» *Lubricants,* vol. 10, n. 29, 2022.

[139] «https://www.skf.com/uk,» [Online].

[140] Vink System Design & Analysis, «HertzWin,» Veldhoven.

[141] Bearing Solve, «https://www.bearingsolve.com/,» [Online].